ISBN 978-82-326-7752-8 (printed ver.)
ISBN 978-82-326-7751-1 (electronic ver.)
ISSN 1503-8181 (printed ver.)
ISSN 2703-8084 (electronic ver.)

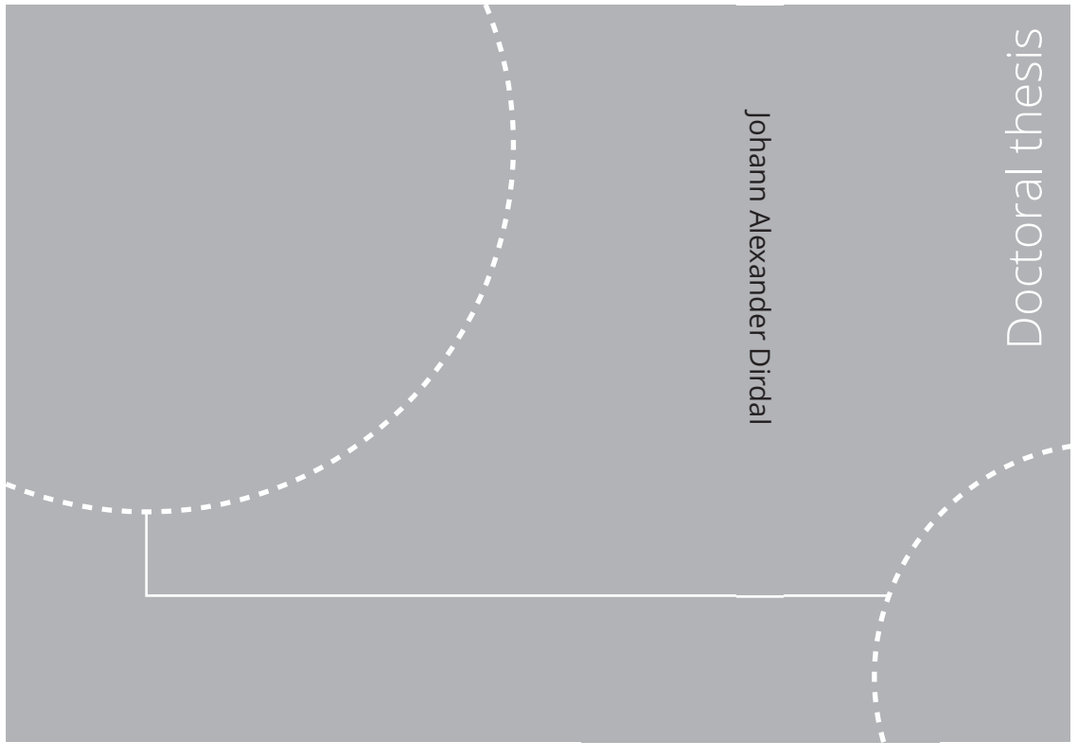

Doctoral theses at NTNU, 2024:79

Johann Alexander Dirdal

Signal-based sea state estimation: A phase-time-path-difference approach

A new shipboard wave estimation approach

Doctoral theses at NTNU, 2024:79

NTNU

NTNU
Norwegian University of
Science and Technology
Thesis for the degree of
Philosophiae Doctor
Faculty of Information Technology
and Electrical Engineering
Department of Engineering Cybernetics

NTNU
Norwegian University of
Science and Technology

Johann Alexander Dirdal

Signal-based sea state estimation: A phase-time-path-difference approach

A new shipboard wave estimation approach

Thesis for the degree of Philosophiae Doctor

Trondheim, March 2024

Norwegian University of Science and Technology
Faculty of Information Technology
and Electrical Engineering
Department of Engineering Cybernetics

NTNU
Norwegian University of
Science and Technology

NTNU
Norwegian University of Science and Technology

Thesis for the degree of Philosophiae Doctor

Faculty of Information Technology
and Electrical Engineering
Department of Engineering Cybernetics

ISBN 978-82-326-7752-8 (printed ver.)
ISBN 978-82-326-7751-1 (electronic ver.)
ISSN 1503-8181 (printed ver.)
ISSN 2703-8084 (electronic ver.)

ITK-report: 2024-02 -W

Doctoral theses at NTNU, 2024:79

Printed by Skipnes Kommunikasjon AS

Abstract

The safety and efficiency of marine operations at sea rely on accurate information about the sea state, which includes the dominant wave height, wave direction, and wave period. Unfortunately, many areas at sea lack this crucial data due to a scarcity of measuring instruments or inadequate measurement resolution. However, ships have the potential to address this issue since they are omnipresent at sea and situated near the waves, making them optimal platforms for both measuring and reporting wave conditions.

Shipboard sea state estimation uses sensor measurements of the sea surface from a vessel to determine important wave characteristics through model-based or signal-based approaches. Signal-based approaches have several advantages over model-based methods as they estimate waves directly from sensor measurements without the need for any complex ship model. However, these approaches often rely on expensive instruments and expert assistance for installation and maintenance.

This doctoral thesis investigates a relatively new and unexplored signal-based approach for shipboard wave estimation that is cost-effective and easy to implement. The approach uses the phase-time-path-differences (PTPDs) between an array of inertial measurement units (IMUs) to infer the directionality and frequency characteristics of waves. Only a few works have considered using a PTPD approach for wave estimation based on shipboard IMUs. However, these studies are restricted to model-ship wave tank testing in regular waves, and its application appears to overlook the differences between sensor delays on a rigid body and those directly obtained from sensors situated on the ocean. Moreover, it is presently unclear how many IMUs are needed, how far they should be separated, and how they should be geometrically arranged to determine the prevailing sea state.

The present study proves that the main wave direction and wave number can be uniquely determined from a minimum of two independent phase differences. Although measurements of the latter can be obtained from a minimum of three noncollinear

IMUs, this work demonstrates that a single IMU is sufficient by utilizing a rigid-body measurement transformation to generate the other measurements needed. Moreover, a comprehensive theoretical assessment of the validity of the PTPD approach is conducted, determining the conditions under which it may be safely applied to model rigid body sensor delays. These conditions are validated experimentally through extensive testing with a model ship in a wave tank.

As a ship moves forward in following seas, it is a well-known problem that each encountered wave frequency can correspond to three distinct absolute wave frequencies, making it challenging to accurately determine the correct wave frequency during movement. However, through the observability results presented in this thesis, we prove that the absolute wave frequency can be uniquely determined while the vessel is moving using the PTPD approach. This interesting result is validated experimentally in a wave tank with a model ship exposed to various regular and irregular waves.

An inherent drawback of using measured ship motions to determine wave characteristics is that they are susceptible to distortions caused by the effect of vessel low-pass filtering when the waves are sufficiently short. To address this challenge, a novel analytical expression of the frequency bandwidth of undistorted waves is derived based on the main vessel dimensions. This frequency bandwidth aids in identifying the wave components that are safe to consider and those to avoid. This frequency bandwidth is incorporated into our proposed methodology for implementing the PTPD approach, which comprises a fast Fourier transform and an unscented Kalman filter. Moreover, with our proposed methodology, we are able to yield estimates of the wave direction and wave number/period close to real-time, with updates given every three minutes after an initial six-minute startup period.

The validation of the proposed approach is carried out through model-scale and full-scale field experiments. The latter involves a research vessel with a commercial wave radar operating alongside various wave buoys under diverse sea state conditions. The results of these experiments show strong agreement with wave reference systems, confirming the competitiveness of our theory and method against existing wave measurement technology. Notably, our proposed method offers advantages in cost-effectiveness, simplicity, and environmental resilience, thereby establishing it as a promising alternative or complementary aid within the field.

Preface

This thesis is submitted in partial fulfillment of the requirements for the degree of Philosophiae Doctor (Ph.D.) at the Norwegian University of Science and Technology (NTNU), Trondheim. The work has been carried out at the Department of Engineering Cybernetics (ITK).

Professor Thor I. Fossen has been the main supervisor of this work, with the co-supervision of Professor Roger Skjetne, at the Department of Engineering Cybernetics and Department of Marine Technology, respectively. This work was sponsored by the Research Council of Norway through the Centre of Excellence funding scheme, project number 223254, AMOS.

Acknowledgments

This Ph.D. thesis concludes an almost five-year journey at the Norwegian University of Science and Technology. The realization of this thesis would not have been possible without the invaluable support of this institution and many key individuals, to whom I am immensely grateful.

First and foremost, I must sincerely thank my supervisor, Thor I. Fossen, for accepting me as a Ph.D. candidate and presenting me with the opportunity to study such a fascinating (and challenging) field as ocean wave estimation. Throughout this journey, you have given me the freedom to navigate my own research path while generously dedicating your time and energy to assist me whenever I need any help. Additionally, you have always provided me with all the necessary resources to complete my work. I am truly grateful for your unwavering support.

I must also warmly thank my co-supervisor, Roger Skjetne, for expanding my network and fostering collaborations. By being introduced to several of your master's students working on similar topics in the Marine Cybernetics Laboratory (MC-lab), I was able

to gain familiarity with the inner workings of the lab more quickly and efficiently. Moreover, I deeply appreciate your initiative in setting up a collaboration with your master's student on the research vessel Gunnerus, which proved pivotal for the results of this thesis.

Moving on to the Czech Technical University in Prague, I am immensely grateful to Associate Professor Jan Roháč. Our fruitful discussions and his thorough review of my work have been invaluable, shedding light on multiple important issues. I also want to thank him for his indispensable support in preparing the IMU wave measurement system for the full-scale experiments in Ålesund.

The technical staff at the MC-lab has been instrumental in my research journey. I extend my special thanks to Robert Opland, Terje Rosten, and Torgeir Wahl for their support and patience. They have not only helped me become familiarized with the instruments in the lab but also assisted in designing and setting up experiments, graciously tolerating my indecisiveness and unending stream of questions.

I also want to express my warm gratitude to Senior Engineer Stefano Brevik Bertelli at the Department of Engineering Cybernetics (ITK). Stefano always helped me locate tools and instruments in the basement workshop, showed me how to solder complicated wires, and brought me to the MC-lab, introducing me to Torgeir Wahl for the first time.

Moving on to my colleagues at ITK, I want to thank my office mates, Øystein Kaarstad Helgesen and Lars-Christian Ness Tokle, for creating an amazing office atmosphere. You really made the burden of the Ph.D. much easier to carry with your humor, pranks, and informal discussions. I must especially thank Øystein for also partaking in many of my spontaneous and adventurous missions during our time at the department. Moreover, I would like to thank Håkon Hagen Helgesen for being a close and trusted friend during this time.

Lastly, I would like to express my deepest gratitude to my dear wife, Hasti, for always being there for me. Whenever I have faced any difficulties, you have adopted my problems as your own and helped me find solutions to them. You have also generously helped me to finish this seemingly never-ending project by giving me invaluable feedback on my papers, coming with me to Ålesund as moral support for crucial experiments, and assisting me in the MC-lab for multiple days from morning until midnight when no one else could. Finally, I want to thank my parents and brother Christopher for all their love and support.

Trondheim, *Johann A. Dirdal*
December 2023

Contents

1 Introduction **1**

1.1 Motivation 1

1.2 Research objectives and scope 4

1.3 Contributions at a glance 8

1.4 Thesis outline 10

I Background **13**

2 Measuring and quantifying ocean waves **15**

2.1 Definition of sea state parameters 15

2.1.1 What is a wave? 16

2.1.2 Wave height 16

2.1.3 Wave period and wave number 18

2.1.4 Wave propagation direction 19

2.2 The wave spectrum 20

2.2.1 Spectral analysis of random waves 22

2.2.2 Practical considerations 24

2.3 Overview of measurement techniques 25

2.3.1 In-situ instruments 26

2.3.2 Remote sensing instruments 27

3 Shipboard wave estimation **29**

3.1 Model-based approaches 29

3.1.1 Frequency-domain formulation 31

3.1.2 Time-domain formulation 35

3.1.3 The effect of vessel low-pass filtering 38

3.2 Signal-based approaches 40

3.2.1 Radar and laser altimetry 41

3.2.2 Machine learning 42

4 Phase-time-path-differences: A new approach for shipboard wave estimation **45**

4.1 Main idea 45

4.1.1 Example from array signal processing 46

4.1.2 The PTPD concept applied to the sea surface 47

4.1.3 The PTPD concept applied to shipboard sensors 50

4.2 Main contributions 51

4.2.1 Theoretical assessment of the PTPD approach for rigid bodies 51

4.2.2 A forward speed PTPD model for surface vessels 52

4.2.3 Observability proof: Minimum sensor requirements 52

4.2.4 Determining the ambiguous wave frequency in following seas 53

4.2.5 Quantifying the frequency bandwidth of waves 53

4.2.6 Methodology: A measurement transform, an FFT, and a UKF 53

4.2.7 Model-scale and full-scale experimental validation 54

4.3 Wave height 55

4.3.1 Laser altimetry 56

4.3.2 Harmonic oscillator in heave and pitch 56

4.4 Summary and future recommendations 59

II Publications **61**

A Online wave direction and wave number estimation from surface vessel motions using distributed inertial measurement arrays and phase-time-path-differences 63

B A phase-time-path-difference approach for online wave direction and wave number estimation from measured ship motions in zero and forward speed using a single inertial measurement unit 85

References **113**

1 Introduction

"The basic law of the seaway is the apparent lack of any law."

– Lord Rayleigh, *Kinsman, B. (1965)*

1.1 Motivation

Observing waves has been an essential aspect of human activity for thousands of years, dating back to ancient times when sailors and fishermen relied on their knowledge of the ocean and its waves to navigate safely and make a living. The importance of this activity has not changed, and information about waves and the sea state continues to be paramount for the operational safety, efficiency, and sustainability of many ocean-related activities. For activities such as maritime navigation and shipping, significant waves may delay voyages and spell disaster for ships, their cargo, and personnel safety.[1] To avoid such disasters, real-time measurements of the prevailing sea state can facilitate real-time decision-making on ships to enhance safety and time and fuel efficiency.

Information about the local sea state is also vital for accurate weather forecasting, which, in turn, is crucial for the planning and execution of marine operations at sea. However, despite the importance of marine weather forecasts, there are vast areas at sea where information about local weather and waves is lacking and, as a result, represents a significant risk for ships traversing these regions. In such areas, satellites do not always provide the level of detail of the ocean conditions needed for meteorological institutions to give accurate and reliable weather reports. Although weather buoys do provide the level of detail needed, they are not everywhere and are

[1] As recent as 2015, the American-flagged cargo ship SS El Faro sank with its entire crew after hitting the eyewall of Hurricane Joaquin. Furthermore, in 2021, the bulk carrier MV Arvin broke in two and sank due to heavy seas, losing half its crew.

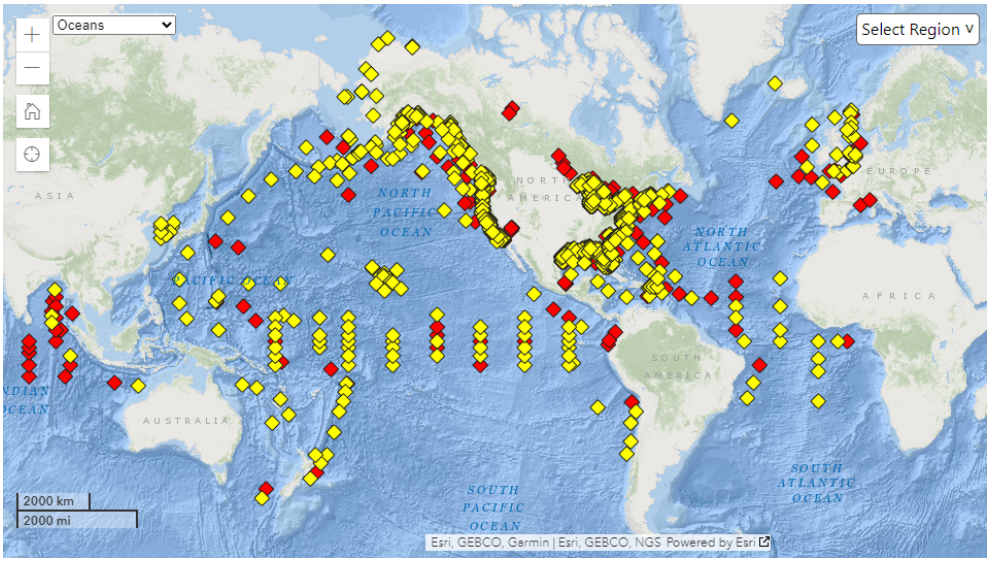

Figure 1.1: A screenshot of the National Data Buoy Center (NDBC) website displaying the current operational network of weather buoys [1]. Yellow buoys represent stations with recent data, while red buoys denote stations lacking data in the past 8 hours.

usually constrained to near-shore positions for cost-effective service and maintenance (Figure 1.1).

On the other hand, ships are everywhere, constantly traversing the high and deep seas (Figure 1.2). Employing voyaging ships to observe local weather and waves will significantly increase the availability of marine weather forecasts in the deep ocean, thereby enhancing overall safety and efficiency at sea. The Voluntary Observing Ship (VOS) program has applied this idea and enlists crew members around the world to report observations of the local weather conditions during their voyage [3]. Using various instruments and the naked eye, the crew members report values of the air temperature, sea temperature, *sea state*, visibility, barometric pressure, wind speed, and wind direction in a standardized format to meteorological institutions worldwide as an endeavor to enhance marine weather forecasting.

However, some significant drawbacks of the VOS program are: (i) observations are made every six hours, thus yielding scarce measurements; (ii) there are significant uncertainties in the parameters obtained through visual observations (e.g., the sea state), and (iii) it requires considerable human effort. In reality, for the weather forecasts to be reliable, they require frequent and accurate measurements of the local ocean conditions, which, in turn, requires a high degree of automation. As a preliminary attempt to facilitate frequent, accurate, and autonomous observations of the sea state,

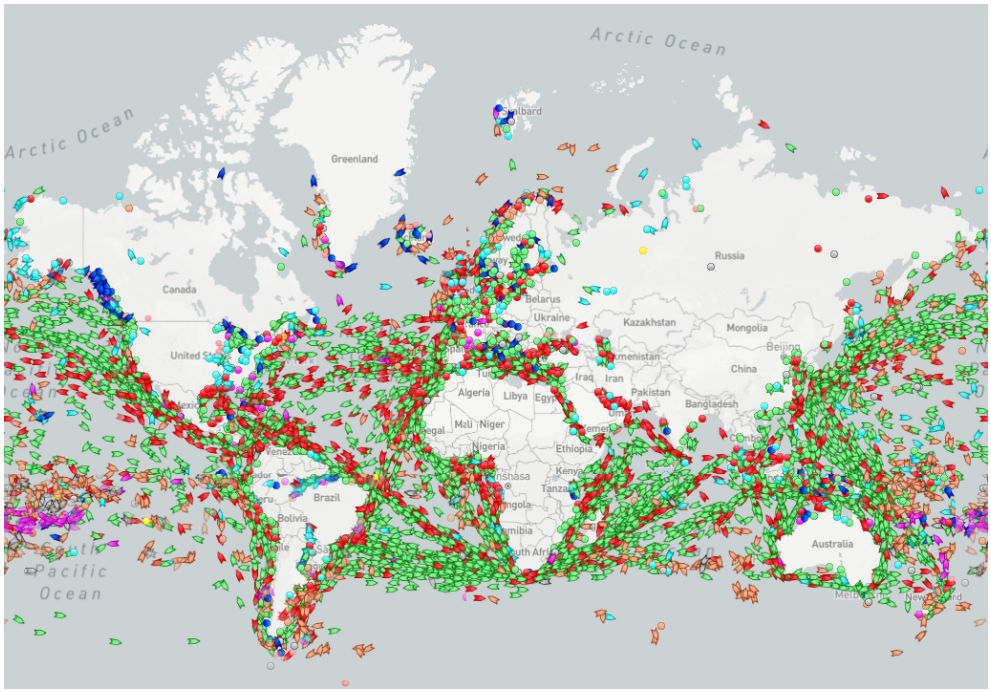

Figure 1.2: A snapshot of the global marine traffic based on AIS (automatic identification system) [2].

this thesis is concerned with utilizing the ship itself and its wave-induced motions. Instead of relying on visual observations by VOS observers to measure the sea state, a more effective method is to equip the ship with sensors that autonomously measure waves directly or indirectly.

Two types of approaches exist for measuring the sea surface from shipborne sensors: model-based and signal-based. Model-based approaches consider the vessel as a floating wave buoy and determine the sea state indirectly by using the measured wave-induced ship motions and a mathematical model of the ship. The wave-buoy analogy [4] dominates the research on sea state estimation from ships, mainly because these approaches only (in theory) require the measured ship responses, which can be obtained from inexpensive shipboard sensors. However, despite this advantage, they have failed to materialize in industrial applications due to several ongoing challenges [5], some of which include:

- **The need for response amplitude operators (RAOs):** RAOs are transfer functions that model the interactions between waves and vessel responses. These functions should generally be determined for each unique ship using hydrody-

namic software codes or extensive model wave tank testing, requiring substantial effort. Furthermore, since RAOs are transfer functions, their theoretical validity is constrained to linear systems, which correspond to mild and moderate wave conditions for ships at sea.

- **Time-delayed sea-state estimations:** The sea-state estimations yielded by methods based on the wave-buoy analogy can be delayed up to 10-15 min [6], as they usually require long time windows for the underlying spectral analysis. Given the dynamic and rapidly changing nature of the ocean, such delayed sea state estimates might not accurately capture the current ocean conditions. This, in turn, poses challenges for decision-support systems needing to promptly respond to real-time events.
- **The effect of vessel low-pass filtering:** If the waves are sufficiently short compared to the vessel size, the vessel will act as a low-pass filter and distort the waves passing through it. When this happens, the measured vessel responses will be nonlinear with the incident waves and cannot be relied upon for accurate sea state estimation.
- **Ambiguous wave-frequency estimation in following seas:** For a ship moving with forward speed, the experienced wave frequency will generally differ from the actual wave frequency due to the Doppler effect. Although, in most cases, the absolute wave frequency can be uniquely resolved from the encountered frequency, this is not always true for following seas. In such circumstances, the encountered wave frequency can map to three distinct absolute wave frequencies.

While model-based methods have many challenges, signal-based approaches for shipboard wave estimation are less susceptible to the issues above as most of these methods use a marine radar and/or laser altimeter to measure the ocean surface directly. Although such instruments are very accurate and commercially available, they tend to be expensive, sensitive to environmental impact, and challenging to install without expert help.

1.2 Research objectives and scope

The underlying motivation for this doctoral thesis is the challenge of autonomous sea state estimation from ships and the effective sharing of this information among ships and meteorological institutions to improve global maritime safety and efficiency. The primary concern during voyages is adverse weather conditions manifested as hazardous

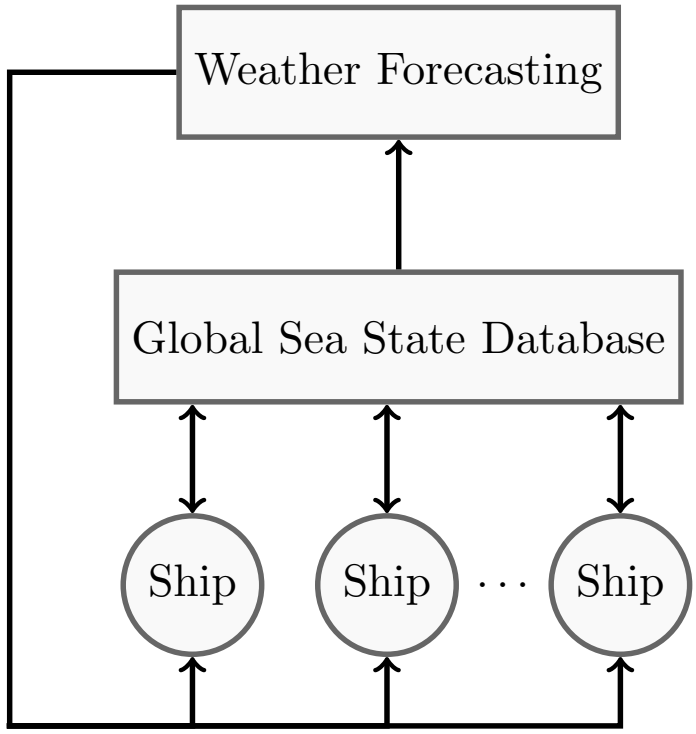

Figure 1.3: A network of ships sharing sea state and spatiotemporal information with a common global database. This data is also valuable for meteorological institutions to improve marine weather forecasts, which, in turn, can also be used by shipboard decision support systems.

ocean waves. To mitigate this risk, a proposal is made: If all ships worldwide measure the waves they encounter and share this data, the potential for disasters can be significantly reduced (Figure 1.3). This cooperative approach would allow ships to adapt their routes in real-time to avoid areas with reported or predicted dangerous wave conditions. However, making this idea a reality requires fulfilling two key conditions:

1. All ships need to measure and report local wave conditions close to real-time.
2. The accuracy of wave condition estimations must meet a satisfactory standard.

Presently, meeting these prerequisites is challenging due to the high cost and complexity associated with accurate shipborne wave measurement technology. To address these challenges and move closer to achieving the goal of globally distributed sea state information, the overarching objective of this doctoral thesis is as follows:

General objective

Develop a sea state estimation approach that is both affordable and feasible to implement on ships while still maintaining accuracy comparable to commercial wave measurement technologies.

As we shall see, this ambitious objective can be realized through the utilization of inexpensive inertial measurement units (IMUs) for shipboard wave measurement. IMUs are small, lightweight, compact, and robust sensors that can measure vessel motion responses when exposed to waves with a very high data sampling rate. The approach considered in this Ph.D. work involves distributing multiple IMUs across a ship and using the phase-time-path delays between these sensors to determine important wave characteristics.[2] This signal-based wave estimation approach is new and almost unexplored, which avoids many of the challenges faced with current model-based and signal-based methods. Although this concept has been applied to distributed sensors situated directly on the water, there has been limited research investigating this approach within the context of shipborne sensors. Given this research gap and the advantages of IMUs, the main research objective of this thesis emerges:

Main thesis objective

Develop and validate a novel shipboard sea state estimation method based on the phase-time-path-differences (PTPDs) between an array of inertial measurement units (IMUs). Investigate the feasibility and accuracy of this approach in determining the main wave propagation direction and wave number for various scenarios. Additionally, the performance of this approach should be compared to existing wave measurement technologies.

The proposed PTPD method is applicable across vessels of all sizes. However, when the waves are very short compared to the vessel size, the measured vessel responses will be nonlinear with the incident waves, making accurate wave estimation challenging. Consequently, the frequency bandwidth of waves unaffected by vessel-lowpass filtering is naturally narrower in large vessels compared to smaller vessels. As we shall see, one of the contributions of this Ph.D. work is explicit formulas (i.e., Eqs. (3.14) and (3.15)) quantifying the frequency bandwidth of ocean waves based on the main ship dimensions. These formulas serve as important tools for assessing the reliability of wave estimation across vessels.

The main thesis objective is realized through multiple smaller specific research objectives:

[2] Although model-based approaches typically employ such sensors, these approaches have important challenges that need to be addressed before they can be utilized in the industry (see Section 1.1).

Specific research objectives

1. Theoretically assess the validity of the PTPD approach to model sensor delays on a rigid body.
2. Derive a general kinematic PTPD model for vessels with constant forward speed.
3. Determine the minimum sensor requirements and configuration needed to successfully implement the PTPD method.
4. Develop a methodology to estimate the PTPDs between IMU measurements obtained in real ocean waves and determine the wave direction and wave number from the estimated PTPDs as close to real-time as possible.
5. Investigate the capability of the PTPD method to uniquely resolve the absolute wave frequency for vessels moving with constant forward speed in following waves.
6. Develop a strategy on how to handle high-frequency waves distorted by the effect of vessel low-pass filtering.
7. Assess the validity of the approach in a wave tank involving a stationary and moving model ship exposed to various regular and irregular waves.
8. Assess the validity of the approach in real ocean waves and compare its performance to commercial wave measurement systems, including a maritime wave radar and wave buoy.

The research scope of the present thesis encompasses the following aspects:

- **Main wave direction and wave number/period estimation:** The primary focus of this research is to estimate the main wave direction and wave number or period associated with the dominant wave component. The aim is to identify and quantify the key characteristics of the most significant wave within a given scenario. It is important to note that the scope does not extend to estimating the entire directional wave spectrum.
- **Vessels with constant forward speed and stationkeeping:** The study will specifically consider vessels that maintain a consistent forward speed and also engage in stationkeeping.
- **Wave tank experiments:** The research will involve conducting wave tank experiments encompassing a range of parameters, including various wave direc-

tions, wave frequencies, wave heights, and vessel speeds. These experiments will serve as controlled environments for systematic investigation and analysis.

- **Full-scale experiments:** The scope also includes full-scale experiments conducted in real-world conditions. These experiments will explore various wave directions and sea states to assess the applicability and accuracy of the proposed method in practical maritime settings. Also, the proposed method will be compared to commercial wave measurement technology such as a maritime wave radar and wave buoy.
- **Unimodal seas:** The performance of our proposed method is exclusively assessed in unimodal wave environments, i.e., long-crested waves. This limitation arises from the constraints of the wave basin in the MC-lab, which only allows the generation of long-crested waves. Additionally, during the full-scale field experiments, the prevalent wave conditions were mainly swell-dominant.

Notably, the estimation of wave height is excluded from the current research scope due to limited time. However, a potential strategy for estimating wave height within the existing framework is discussed in Section 4.3.2. The primary emphasis of the research remains on wave direction and wave number/period estimation.

1.3 Contributions at a glance

This doctoral thesis comprises two accepted journal papers, listed as Paper A and Paper B, respectively:

(A) Johann A. Dirdal, Roger Skjetne, Jan Roháč, and Thor I. Fossen. "**Online wave direction and wave number estimation from surface vessel motions using distributed inertial measurement arrays and phase-time-path-differences**." *Ocean Engineering*, vol. 249, 2022. DOI: 10.1016/j.oceaneng.2022.110760

(B) Johann A. Dirdal, Roger Skjetne, Jan Roháč, and Thor I. Fossen. "**A phase-time-path-difference approach for online wave direction and wave number estimation from measured ship motions in zero and forward speed using a single inertial measurement unit**." *Ocean Engineering*, vol. 288, Part 2, 2023. DOI: 10.1016/j.oceaneng.2023.116131

Collectively, these papers address the research objectives outlined in Section 1.2. The technical contributions of Papers A and B to the field of shipboard wave estimation are listed below.

1. A rigorous theoretical assessment of the validity of the PTPD method in modeling sensor delays on a rigid body is presented. It is shown that the proposed method is valid when sensor separations are sufficiently short, and ocean waves are sufficiently long. These conditions are experimentally verified with a model ship in a wave tank. (Paper B)

2. A novel PTPD model derivation for wave direction and wave number estimation based on measured inertial ship motions in zero and constant forward speed is introduced. (Papers A & B)

3. An observability analysis is provided in Paper A, demonstrating that the proposed PTPD state-space model is observable from a minimum of two independent phase difference measurements. Although three noncollinear shipboard IMUs can provide these measurements, it is shown in Paper B that a single IMU is sufficient by using a rigid-body transformation to generate the other measurements needed.

4. An observability analysis in Paper B shows that the absolute wave frequency can be uniquely resolved from a vessel with constant forward speed in following waves, addressing the mapping ambiguity between encountered and absolute frequency domains. This insight is experimentally validated during wave tank testing with a model ship in both regular and irregular waves.

5. A novel frequency bandwidth measure is proposed, quantifying when vessel filtering is likely to distort sensor measurements and indicating which wave components can be used for wave estimation. (Papers A & B)

6. A methodology that combines a fast Fourier transform, an unscented Kalman filter, and the frequency bandwidth threshold is introduced to successfully implement the PTPD approach for online wave direction and wave number estimation. (Paper B)

7. The proposed theory and method are experimentally validated on IMU data gathered from a model ship with zero and constant forward speed in regular and long-crested irregular waves. (Papers A & B)

8. The methodology is experimentally validated on full-scale IMU data involving the research vessel Gunnerus and several wave reference systems, including a commercial wave radar and multiple wave buoys. (Paper B)

A graphical overview of the research papers is shown in Figure 1.4, illustrating how they contribute to each of the outlined research objectives in Section 1.2.

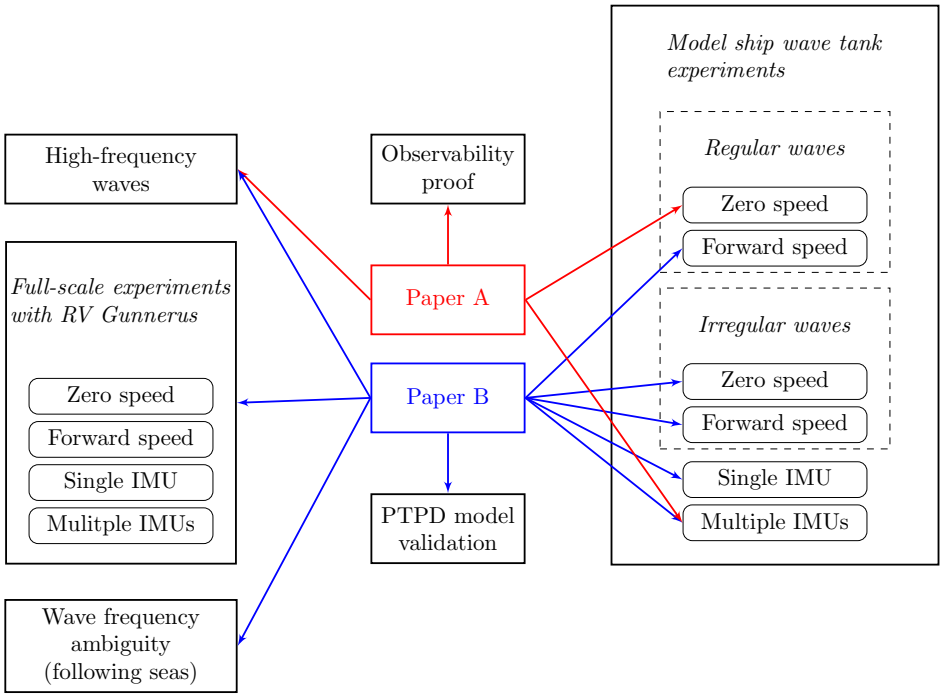

Figure 1.4: A graphical overview of the contributions of Papers A and B to the research objectives.

1.4 Thesis outline

The organization of this doctoral thesis is as follows:

- **Part I: Background.**
  - **Chapter 2: Measuring and quantifying ocean waves.**
    In this chapter, fundamental theory on ocean waves including formal definitions of a wave, sea state parameters, and the wave spectrum is presented. Furthermore, a brief account of existing techniques and technology for measuring waves is provided.
  - **Chapter 3: Shipboard sea state estimation.**
    In this chapter, current literature utilizing shipboard sensor measurements for sea state estimation is presented and reviewed. The advantages and disadvantages of existing approaches are addressed.
  - **Chapter 4: Phase-time-path-differences: A new approach for shipboard wave estimation.**

In this chapter, the PTPD approach is presented—our contribution to shipboard wave estimation—which includes the basic idea, the main contributions of this thesis, a discussion about the wave height, conclusive remarks, and comments about future work.

- **Part II: Publications.**
  In this part, the publications of this doctoral thesis are listed.

While this thesis is presented as a compilation of papers, its organization may occasionally resemble that of a monograph. This resemblance arises from the inclusion of certain chapters that provide foundational explanations about ocean waves and shipboard estimation techniques. The rationale behind this structure is to ensure that the thesis is self-contained, facilitating readers who are newcomers to the field of ocean wave modeling. By reading Part I initially, these readers can comprehend the content within the included papers without the need to refer to external sources. However, individuals already familiar with ocean wave basics and shipboard sea state estimation have the flexibility to skip Chapters 2 and 3 without disrupting the overall coherence of the material.

Part I

Background

2 Measuring and quantifying ocean waves

If we consider undulations of the sea surface to be ocean waves, the underlying causes for these vertical motions are the winds, the sun and moon, and underwater earthquakes. These natural forces constitute different portions or bands of the energy spectrum of ocean waves (Figure 2.1). From this spectrum, it is clear that most of the energy is contained in wind-generated surface waves and tides, which, in effect, are the waveforms commonly observed by the naked eye. When dominated by local winds, wind-generated waves take on an irregular short-crested shape, known as *wind sea*. After leaving the generation area, these waves become more regular and long-crested and are called *swell*. Wind-generated waves are the main subject of this thesis and are usually the prime focus of most research endeavors concerned with ocean modeling and sea state estimation.

2.1 Definition of sea state parameters

A *sea state* is a collective term used to describe the state or condition of the sea surface at a specific location and moment. It is usually characterized by parameters such as the main wave height, wave direction, and wave period. By *main*, we usually refer to the wave height, direction, and period associated with the primary modal period/frequency of the wave energy spectrum (i.e., the period/frequency in which the wave spectrum attains its maximum value). In this section, the definition of wave height, period, and direction is given based on a time series of the sea surface elevation to facilitate a more in-depth understanding of these quantities. However, before this can be done, a more precise definition of what a wave *is* needs to be provided.

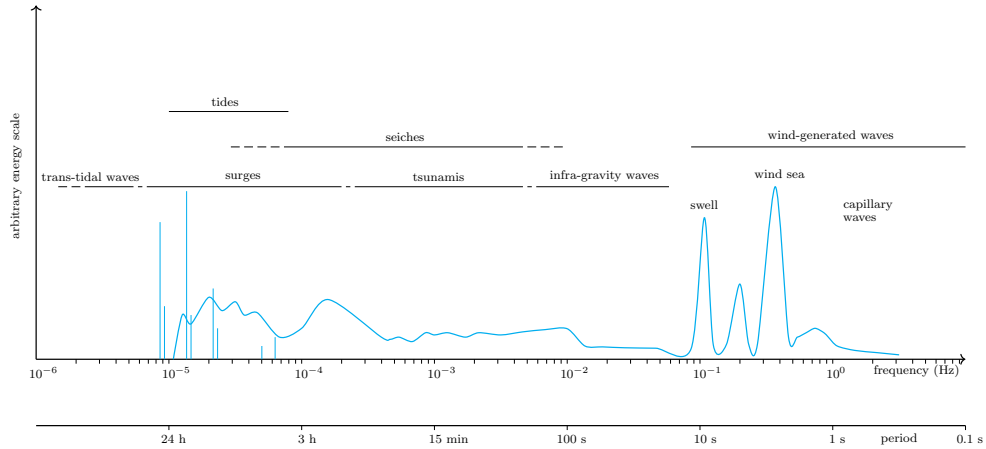

Figure 2.1: The vertical motions of the sea surface can be grouped into different wave categories depending on the range of wave periods/frequencies considered (after [7]).

2.1.1 What is a wave?

Many think of a wave as the instantaneous surface elevation relative to the mean equilibrium level of the water. However, this is false in the present context, and it is important to distinguish between a wave and surface elevation. A *wave* is defined as the surface elevation *profile* existing between two consecutive downward zero-crossings (Figure 2.2). In contrast, a surface elevation is a *number* (positive or negative) representing the elevation of the surface above some reference level at any moment in time. It is also possible to define a wave based on two successive upward zero-crossings instead; however, this definition does not include breaking waves and conflicts with visual estimates of the wave height, which is taken to be the relative distance between the crest and preceding trough [7].

2.1.2 Wave height

Based on the definition of a wave, the corresponding wave height H is defined as the vertical distance between the highest and lowest surface elevations in a wave (Figure 2.2). Hence, a wave has only one wave height.

In a time series of the surface elevation comprising N waves, the average wave height

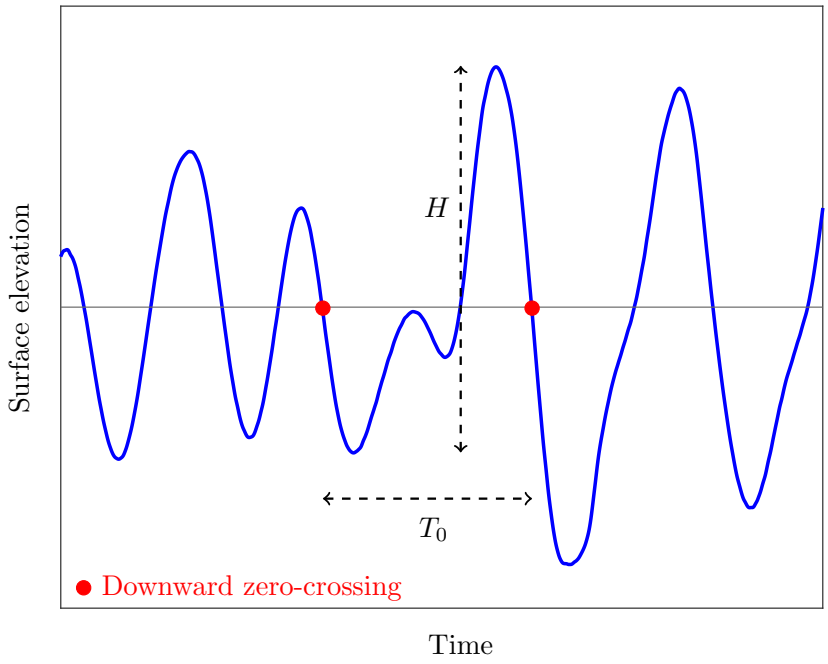

Figure 2.2: Definitions of a wave, wave height H, and wave period T_0.

$\bar{H}$ is simply

$$\bar{H} = \frac{1}{N} \sum_{i=1}^{N} H_i,$$

where i is the sequence number of each wave height H_i (i.e., $i = 1$ is the first wave height in the record, $i = 2$ is the second, etc.). In practice, however, the mean wave height is not so commonly used. Instead, most engineers and scientists refer to the *significant wave height* when addressing the magnitude of waves. The significant wave height is defined as the average wave height of the one-third highest waves in a surface elevation time series, i.e.,

$$H_{1/3} = \frac{1}{N/3} \sum_{j=1}^{N/3} H_j, \tag{2.1}$$

where $H_{1/3}$ is the significant wave height and j is the rank number of wave H_j (i.e., $j = 1$ represents the highest wave in the record, $j = 2$ the second highest, etc.). The

significant wave height is a popular metric as it agrees very well with the wave height obtained from visual observations of the ocean surface [7]. It is worth mentioning that there are several other metrics for quantifying the wave height; however, these are not considered in the works of the present thesis and have, consequently, been omitted.

2.1.3 Wave period and wave number

Following the same definition of a wave, the wave period is simply the duration of the wave, i.e., the time interval between the zero-crossings (Figure 2.2). Since the time period is based on zero-crossings, it is referred to as the zero-crossing period T_0. Following the same procedure as the wave height, the mean zero-crossing period $\bar{T}_0$ and significant wave period $T_{1/3}$ are defined, respectively, as

$$\bar{T}_0 = \frac{1}{N}\sum_{i=1}^{N} T_{0,i} \quad \text{and} \quad T_{1/3} = \frac{1}{N/3}\sum_{j=1}^{N/3} T_{0,j},$$

where i and j denote the respective sequence and rank numbers of the wave (based on the wave height). There are several other important wave periods that are defined in terms of the wave spectrum (see Section 2.2), which is a statistical representation of waves by considering them as a sum of a large number of harmonic wave components. One important such wave period is the *peak/modal* period T_p. The peak period is simply the wave component (frequency) that attains the highest spectral energy in the spectrum (see Figure 2.5).

The wave number is the spatial analog to the wave frequency and is defined as the number of complete cycles of a wave over its wavelength, i.e.,

$$k = \frac{2\pi}{\lambda},$$

where k is the wave number and λ denotes the wavelength. Linear wave theory shows that the wave number and wave period are connected through the dispersion relation, i.e.,

$$\omega^2 = kg\tanh(kd), \tag{2.2}$$

where $\omega = 2\pi/T$ is the angular frequency expressed in terms of the wave period T, water depth d, and gravitational constant g. For deep waters, the relationship above simplifies to

$$k = \frac{\omega^2}{g}.$$

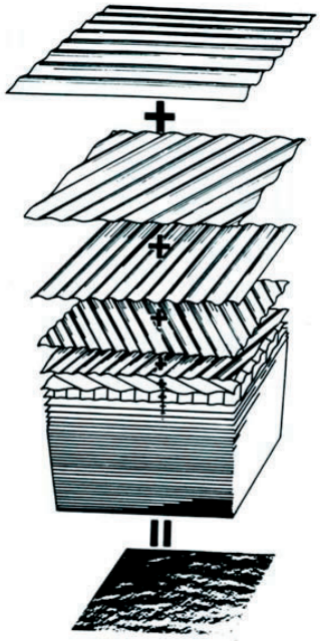

Figure 2.3: The structure of a random sea can be regarded as a sum of propagating cosine waves moving in different directions. Classical drawing from [8].

2.1.4 Wave propagation direction

Up to now, our study of waves has been based on a one-dimensional time series of surface elevation at a single geographical location. In reality, however, waves move in different directions through horizontal x, y-space. A common way to model the movement of short-crested ocean waves is to consider them a superposition of many propagating harmonic wave components with different wave amplitudes, frequencies, and directions (Figure 2.3). When the majority of wave components propagate in the same direction, the waves are regarded as long-crested. The wave propagation direction of a wave component is orthogonal to its wave crest and defined relative to the positive x-axis of an arbitrarily defined coordinate system in horizontal space (Figure 2.4). For wave observation systems, the relative wave propagation direction may be defined as the angle at which the waves approach or leave the observation instrument. In this thesis, we consider the wave direction to be the angle at which the waves leave the vessel in question.

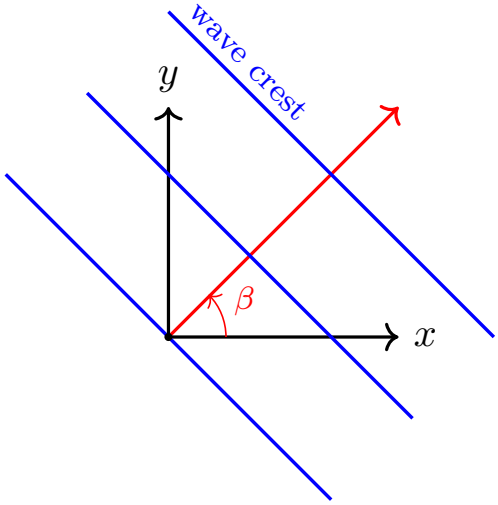

Figure 2.4: Definition of the wave propagation direction β.

2.2 The wave spectrum

Linear wave theory states that for deep waters, the sea surface elevation η at time t and spatial coordinates (x, y) is a superposition of many propagating regular harmonic waves (Figure 2.3) differing in amplitude a, frequency ω, direction β, and phase ϵ, i.e.,

$$\eta(x, y, t) = \sum_{i=1}^{N} \sum_{j=1}^{M} a_{ij} \cos(\omega_i t - k_i(x \cos \beta_j + y \sin \beta_j) + \epsilon_{ij}), \tag{2.3}$$

where k_i denotes the wave number and is related to the frequency ω_i through the dispersion relation (2.2). Due to the apparent complex and chaotic behavior of wind-generated waves, the surface elevation is regarded as a stochastic process, meaning that each individual observation (i.e., surface elevation time series) recorded at sea is treated as one possible realization of the random sea. The randomness of the surface elevation (2.3) is reflected in the phase component ϵ_{ij}, which is considered uniformly distributed between 0 and 2π. Hence, by assuming that the wave components in Eq. (2.3) are *independent* random variables, the central limit theorem tells us that the surface elevation η is a Gaussian random process with zero mean and variance σ^2

given by

$$\sigma^2 = \mathbb{E}[\eta^2] = \sum_{i=1}^{N}\sum_{j=1}^{M} a_{ij}^2 \mathbb{E}\big[\cos^2(\omega_i t - k_i(x\cos\beta_j + y\sin\beta_j) + \epsilon_{ij})\big]$$
$$= \sum_{i=1}^{N}\sum_{j=1}^{M} \frac{1}{2} a_{ij}^2, \tag{2.4}$$

where $\mathbb{E}[\cdot]$ denotes the mathematical expectation.

We want to evaluate the statistical characteristics of the random sea surface (2.3). This is usually done in the frequency domain by evaluating the wave spectral density function or wave spectrum as it is often called, which is the fundamental quantity used for analyzing the statistical properties of random ocean waves (wave-by-wave analysis in the time domain is difficult). The 2-D directional wave spectrum is defined by

$$E(\omega,\beta) = \lim_{\Delta\omega\to 0}\lim_{\Delta\beta\to 0} \frac{1}{\Delta\omega\Delta\beta}\mathbb{E}[\eta^2], \tag{2.5}$$

and shows how the variance of the sea surface elevation is distributed over a continuum of frequencies and directions. It is important to note that Eq. (2.5) is a modification of Eq. (2.4) as it considers a continuum of frequencies and directions to represent the fact that all frequencies and directions are present at sea. The variance is considered as it is closely related to the total wave energy—a physical property of great interest. In fact, the wave energy density spectrum is obtained by scaling Eq. (2.5) by ρg, where ρ represents the water density.

In order to completely describe the statistical properties of random ocean waves, the following two assumptions are needed:

(i) The waves are a wide-sense stationary process (i.e., its mean and variance are independent of time).

(ii) The waves are an ergodic random process (i.e., time averaging is the same as ensemble averaging).

Together, these assumptions ensure that a single time record of the sea surface elevation contains sufficient statistical variation that the statistical properties of the local ocean waves can be completely described at the location in which the measurement is taken. In reality, however, ocean waves are never really stationary, meaning that a wave record of the surface elevation needs to be divided into quasi-stationary segments and processed individually.

2.2.1 Spectral analysis of random waves

In general, there are two ways of computing the wave spectrum from a recorded time series of the surface elevation: (i) evaluating the auto-correlation function (single wave record) and/or cross-correlation function (multiple simultaneous wave records) and taking the Fourier transform of the result or (ii) taking the Fourier transform of the wave record(s) directly. In the following discussion, we only consider a single-point measurement of the sea surface, which contains the time history of all waves passing that location without reference to wave directionality. Hence, we do not consider any cross-spectral analysis, which is needed to evaluate the directional characteristics of ocean waves. The interested reader is referred to [9] for a detailed treatment of cross-spectral analysis from multiple simultaneous wave records.

The auto-correlation function is defined as

$$R(\tau) = \lim_{T\to\infty} \frac{1}{2T} \int_{-T}^{T} x(t)x(t+\tau)d\tau, \tag{2.6}$$

and expresses the degree of similarity between observations (random variables) as a function of the time difference τ. The Wiener-Khinchin theorem states that the auto-correlation function (2.6) and the spectral density $S(\omega)$ (i.e., the wave spectrum) with angular frequency ω are Fourier transform pairs, i.e.,

$$\begin{aligned} S(\omega) &= \frac{1}{\pi} \int_{-\infty}^{\infty} R(\tau)e^{-j\omega\tau}d\tau, \\ R(\tau) &= \frac{1}{2} \int_{-\infty}^{\infty} S(\omega)e^{-j\omega\tau}d\omega. \end{aligned} \tag{2.7}$$

Alternatively, the spectral density function can be obtained directly from the Fourier transform of $x(t)$, i.e.,

$$S(\omega) = \lim_{T\to\infty} \frac{1}{2T} \left|X_T(\omega)\right|^2, \tag{2.8}$$

where

$$X_T(\omega) = \int_{-T}^{T} x(t)e^{-j\omega t}dt$$

is the Fourier transform of $x(t)$. Whether Eq. (2.7) or (2.8) is used, the resulting wave spectrum will consist of either a single peak or multiple peaks depending on how many wave systems are present in the record. Figure 2.5 shows an example of a bimodal wave spectrum consisting of swell and wind sea. Wind sea refers to waves generated by the local wind, while swell is wind sea that has traveled from a distant storm and gradually dissipated some of its energy along the way. In general, the swell will manifest itself as a low-frequency, narrow-banded peak, symbolizing a regular

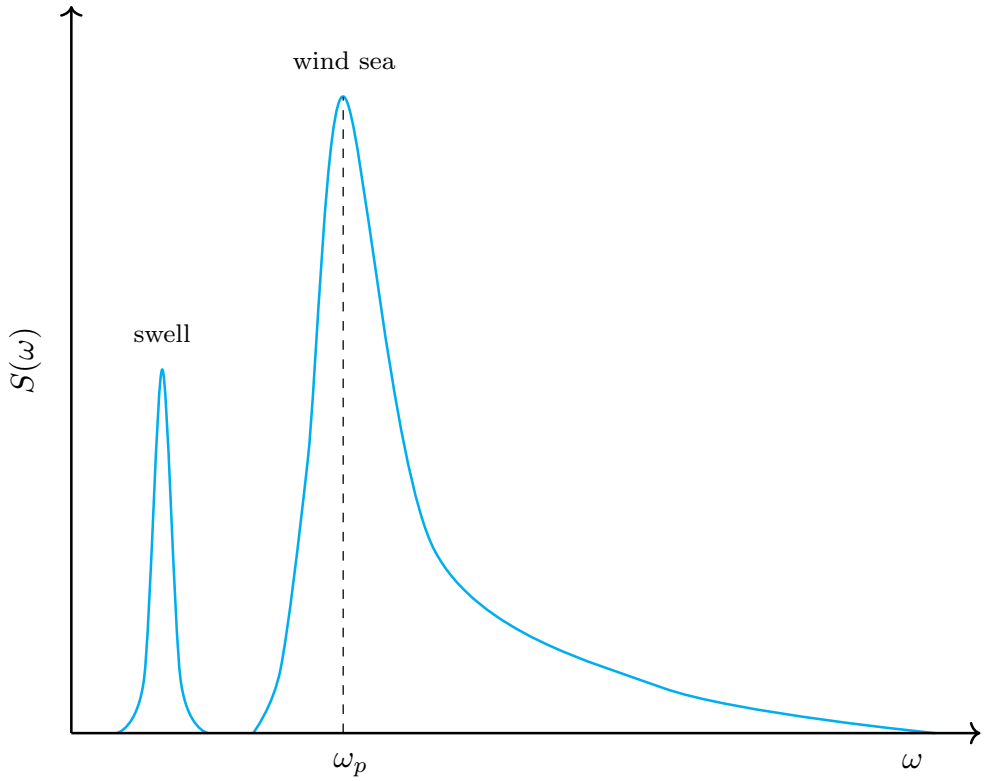

Figure 2.5: A one-dimensional bimodal wave spectrum $S(\omega)$ consisting of swell and wind sea. The peak wave frequency ω_p is the frequency in which $S(\omega)$ attains its maximum value.

and long-crested appearance. Wind sea, on the other hand, carries a broader shape and is usually higher in frequency, appearing as short-crested and irregular waves.

From the wave spectrum, several statistical parameters describing the sea state can be obtained. The most important parameter is the significant wave height, which, under the assumption that the wave height is Rayleigh distributed, is given by

$$H_s = 4\sqrt{m_0}, \tag{2.9}$$

where

$$m_0 = \sigma^2 = \int_0^\infty S(\omega)d\omega, \tag{2.10}$$

is the zeroth moment and also the total variance of the surface elevation. The significant wave height H_s is very important as it represents the sea severity. It is worth noting

that the significant wave height computed from its definition in Eq. (2.1) and from Eq. (2.9) will generally differ by a small amount (i.e., $H_{1/3} \neq H_s$) [7].

Other important parameters are the peak/modal period T_p, average period T_1, and average zero-crossings period T_z. The peak period T_p is obtained through

$$\left.\frac{dS(\omega)}{d\omega}\right|_{\omega_p} = 0, \tag{2.11}$$

with $T_p = 2\pi/\omega_p$, where ω_p is the peak frequency (Figure 2.5). The average wave period T_1 and average zero-crossings period T_z are defined by

$$T_1 = 2\pi\frac{m_0}{m_1} \quad \text{and} \quad T_z = 2\pi\sqrt{\frac{m_0}{m_2}}, \tag{2.12}$$

where m_0, m_1, and m_2 denote the zeroth, first, and second moments, computed by

$$m_n := \int_0^\infty \omega^n S(\omega) d\omega.$$

2.2.2 Practical considerations

In practice, an actual time record of the surface elevation differs in many ways from the theoretical formulation underlying the spectrum analysis in Section 2.2.1. Some of the differences are: (i) the measured wave record is a discrete quantity, (ii) the duration of the wave record is finite, (iii) there is usually only one wave record, and (iv) the wave record is contaminated with sensor noise. In the following, we give a brief account of each of these limitations and how they may be alleviated.

For a point measurement on the ocean surface, the discrete-time wave record is obtained by periodically sampling the surface elevation. It is important to sample the ocean at a sufficiently high rate to ensure that the effect of aliasing is minimized. Ideally, the sampling rate should be greater than or equal to twice the bandwidth of the process to avoid aliasing (Nyquist sampling theorem). However, since all frequencies are present at sea, there will always be some aliasing present in the wave spectrum. Nevertheless, the rapidly decreasing tail of ocean wave spectra implies that the ocean waves are almost bandlimited, meaning that aliasing is not a big issue, provided the ocean is sampled at a sufficiently high rate.

The fact that the wave record is of finite duration T (and not infinite as suggested in the equations in Section 2.2.1) implies that there will be details within the frequency interval or resolution $\Delta f = 1/T$ that cannot be seen. To ensure that most details

are seen, it is important that the duration T be sufficiently long while, at the same time, making sure the waves are stationary within T. For ocean waves, stationarity is generally maintained for up to 15-30 min [7].

A discrete and finite wave record also implies that the discrete Fourier transform (DFT) is needed to transform the record from the time to frequency domain. Since the record is finite, the DFT implicitly assumes that the entire data sequence is one period of a periodic signal. In most cases, there will be a discontinuity between the first and final data samples in the wave record, leading to spectral leakage (i.e., energy in one frequency bin is leaked into adjacent frequency bins). The effect of spectral leakage can be reduced by employing various window functions (e.g., Hanning window) to smoothly decrease the signal values to zero near the endpoints.

As seen in Eq. (2.8), the spectral density can be obtained by taking the Fourier transform of the wave record and squaring the result. However, since the wave record is discrete and finite, we rely on the DFT to carry out this transformation, which yields an *estimate* of the wave spectral density. This estimate is called the periodogram and is not a consistent estimator (i.e., the variance does not approach zero as the sample length approaches infinity). Since we usually only have *one* wave record, the variance can be improved by splitting the data into p blocks, computing the periodogram of each block, and averaging the result (Figure 2.6). However, care must be exercised when performing this operation, as increasing p leads to a decreasing frequency resolution.

In general, there will be a discrepancy between the true sea surface elevation and the corresponding measurement owing to the measurement technique, the instrument, and the processing of the raw signal. The discrepancy resulting from these factors is collectively termed noise and usually exhibits a low-frequency and high-frequency character. In some cases, the low-frequency behavior will manifest itself as a slowly varying bias, which may be mitigated by subtracting the average of the wave record from the record itself. The high-frequency behavior can be reduced by employing a low-pass filter with a cut-off frequency above the bandwidth of the considered waves.

2.3 Overview of measurement techniques

The wave height, wave direction, and wave period are generally computed directly or indirectly from time records of the surface elevation at one or more geographic locations. Time records of the ocean surface elevation may be obtained through various instruments, which can be classified as either *in situ* or *remote sensing* devices. In this section, we give a brief account of these instruments and the measurement principles they rely on.

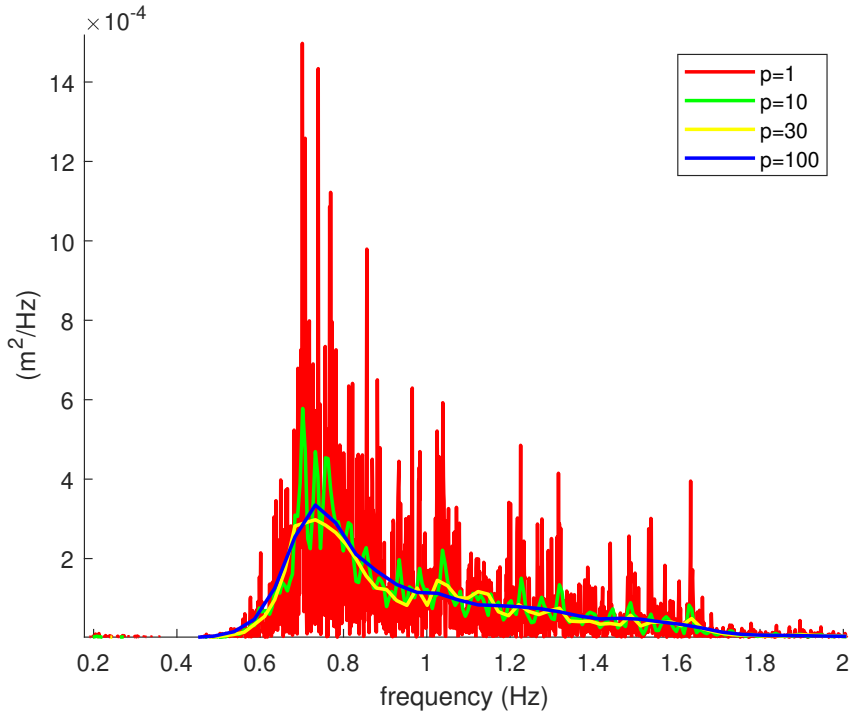

Figure 2.6: Dividing a wave record of duration T into p blocks, computing the periodogram of each block, and averaging the result leads to an improved estimate of the wave spectral density with the cost of reduced frequency resolution $\Delta f = p/T$.

2.3.1 In-situ instruments

In-situ wave measurement techniques comprise instruments such as wave buoys, wave poles/probes, pressure transducers, current meters, and echo sounders. A characteristic feature of these instruments is that they are in contact with the water, either at the sea surface (e.g., wave buoys), below the sea surface (e.g., pressure transducers mounted to a fixed underwater structure or inverted echo sounder installed on the seabed) or semi-submerged in the sea (e.g., wave poles extending from an offshore structure into the sea). Most of these instruments record the up-and-down motion of the sea surface at one geographic location.

The wave buoy is the most common instrument used for observing ocean surface waves. Situated at the ocean surface and anchored to the seabed, the vertical motion of the buoy is considered one-to-one with the ocean waves owing to its relatively small size and buoyancy. For this reason, the vertical buoy displacement and sea

surface elevation are generally regarded as equivalent. There are, in general, different techniques for obtaining the vertical buoy displacement. The most common approach is integrating the acceleration (computed from measurements of specific force) or velocity of the buoy to determine its vertical position. The acceleration and velocity are usually obtained from accelerometers (typically as part of an inertial measurement unit mounted inside the buoy) or through GPS by using the Doppler shift of the satellite signal. It is also possible to use the vertical position measurement from the GPS receiver directly as an estimate of the buoy displacement. However, for the latter to be accurate, a nearby base station is generally needed to enhance the received signal (this approach is known as differential GPS or DGPS).

Although the vertical buoy displacement is sufficient for determining the height and period of waves in the local region, this motion is not by itself sufficient to provide directional wave information. For this purpose, we need additional information about the roll and pitch motion or horizontal motion (surge and sway) of the buoy.

2.3.2 Remote sensing instruments

In contrast with in-situ instruments, remote sensing devices are not in direct contact with the water but are usually mounted remotely on a body, observing the ocean surface from afar. Remote sensing instruments include radars, laser altimeters, and cameras, traditionally installed on a fixed or moving platform, which may be an observation tower, satellite, airplane, or ship. These instruments emit electromagnetic radiation (visible light, infrared light, or radar energy) and use the reflections to produce spatial and temporal representations of the ocean surface. A concise account of marine radars and laser altimeters for wave measurement from ships is given in Section 3.2.1.

3 Shipboard wave estimation

Information about ocean waves is crucial for ships currently out at sea or for those charting a course for their next journey. As we have seen, when it comes to gathering information about the sea state, there are a variety of instruments at our disposal. In-situ instruments such as wave buoys are known for their accuracy, providing valuable data about wave heights, directions, and frequencies. However, wave buoys are often strategically placed near shore for cost-effective service and maintenance rather than covering vast areas. Satellites, on the other hand, offer a broader perspective, enabling us to gather information about the sea over extensive regions. However, they may not always provide the level of detail required at specific local sites.

Ships have the potential to combine the best of both worlds. They are omnipresent at sea and situated on the sea surface, which grants them the ability to capture detailed and localized information about ocean waves and distribute this information worldwide to other vessels and institutions in need of it. Indeed, many people and organizations have recognized the potential of this idea, sparking extensive research into using ships as platforms for measuring ocean waves. As we shall see, the research on shipboard wave estimation comprises several methods, each with its own advantages and disadvantages.

3.1 Model-based approaches

Ships, with their characteristic behavior resembling wave buoys, respond to the forces of the ocean by oscillating up and down. One early and successful attempt to exploit the wave-induced up-and-down motion of ships to measure waves was reported by Tucker [10]. He developed the first-generation shipborne wave recorder, a system comprising a pressure transducer and vertical accelerometer. The pressure transducer is located at a point inside the hull and measures the sea pressure to give the height of the water surface above the point, which is added to the vertical displacement of the

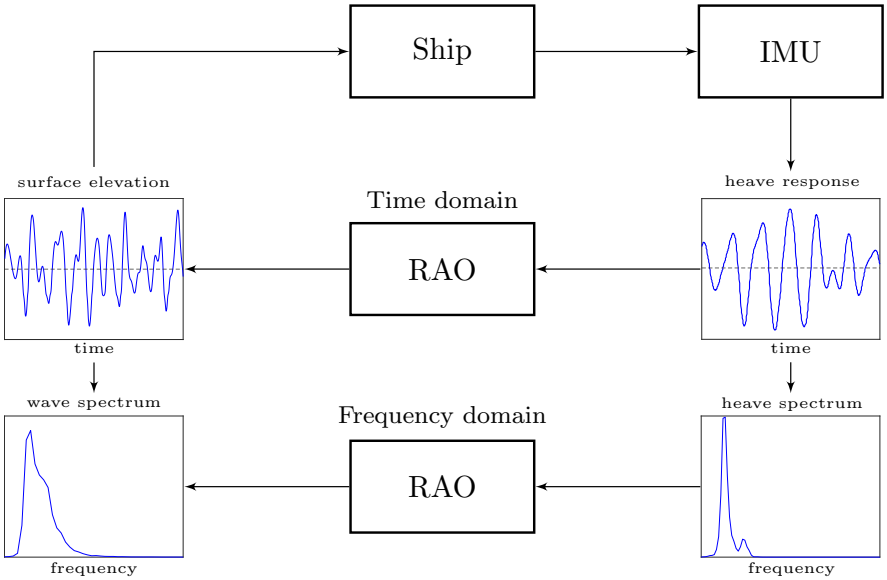

Figure 3.1: A conceptual illustration of model-based shipboard wave estimation. Waves, depicted as a surface elevation time series, cause ship motions recorded by an onboard inertial measurement unit (IMU). Ship motion responses, such as heave, combined with the ship response amplitude operators (RAOs), enable the inference of incident waves through an inverse problem-solving approach. This problem can be solved in either the time domain or frequency domain.

point, obtained by integrating the output from the heave accelerometer twice. These instruments are strategically positioned near the center of flotation to minimize the influence of vessel roll and pitch motions on the wave height measurements.

Although ships exhibit buoy-like behavior, their motion responses are usually not one-to-one with the incident waves owing to the ship's size and geometry. Unfortunately, shipborne wave recorders do not account for ship properties such as geometry and mass, which has led to inaccuracies in their wave height measurements [11]. Recognizing the limitations of shipborne wave recorders for measuring wave heights, Takekuma and Takahashi [12] explored the possibility of improving wave estimation by considering the ship's response amplitude operators (RAOs). RAOs are complex transfer functions that act as a type of scale factor between the incident waves and vessel responses but vary with different wave frequencies, amplitudes, and directions. If the RAOs in, e.g., heave, roll, and pitch are known for a specific ship, they can be combined with the corresponding measured ship response to determine the waves causing the motions (Figure 3.1). Since Takekuma and Takahashi's published

work [12], numerous studies have investigated using this model-based approach to extract information about the incident waves [13–17], which remains a key focus.

Recent literature on the subject can be divided into two categories: studies focusing on stationary vessels for wave estimation [18–25] and those considering vessels with forward speed [26–34]. When a ship is stationary at sea (zero speed), the frequency of its heave, roll, and pitch motions correspond to the wave frequency, simplifying the problem significantly. However, when the vessel is in motion, the encountered wave frequency is affected by the Doppler effect, resulting in a frequency shift. This effect introduces complexities, especially for following seas, where the encountered frequency may map to multiple absolute frequencies, making it challenging to determine the true wave frequency [35, 36].

Despite these challenges, the utilization of ships as wave measurement platforms, together with RAO analysis, continues to be a vibrant area of research. In the following subsections, we discuss the problem of estimating the sea state based on vessel RAOs in greater detail, which can be formulated either in the frequency or time domain [4].

3.1.1 Frequency-domain formulation

The waves and wave-induced vessel responses are generally considered linear for mild and moderate wave climates. The linearity assumption is essential as it allows the waves and vessel responses to be related through complex-valued transfer functions known as RAOs. Each ship generally has its own RAO model for each vessel response (e.g., sway, heave, roll, and pitch) and is usually obtained through computational methods or model tests. Computational methods involve using hydrodynamic codes based on strip theory (e.g., ShipX) or 3-D panel methods (e.g., WAMIT) to simulate the ship's behavior in waves for various amplitudes, frequencies, and directions. Model tests involve physically testing a scaled model of the ship in a wave basin or towing tank, measuring the responses, and extrapolating the results to the full-scale ship.

Let $\mathbb{J} = \{1, 2, 3, 4, 5, 6\}$ be the index set corresponding to the translational and rotational rigid-body motions $\{$surge, sway, heave, roll, pitch, yaw$\}$, respectively. Furthermore, let $\mathbb{I} \subseteq \mathbb{J}$ be the subset of vessel motion responses considered, which comprises a total of N_d responses. If the ship RAOs are known for the pair of vessel responses $\{i, j\} \in \mathbb{I}$, the relationship between waves (input) and vessel responses

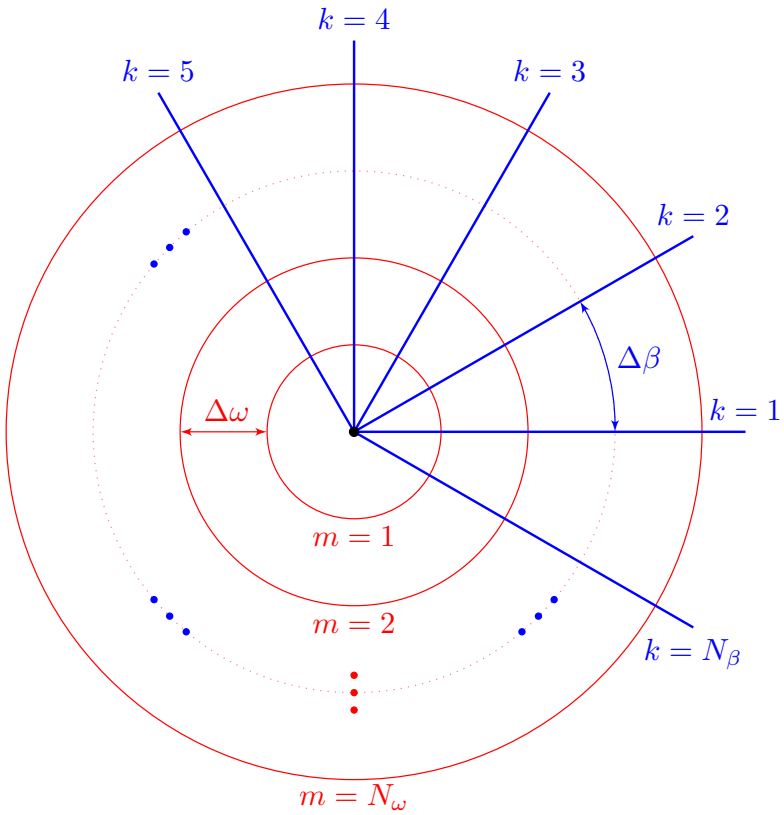

Figure 3.2: Polar diagram showing how the wavefield is discretized into N_ω frequencies and N_β directions.

(output) can be described mathematically in the frequency domain as

$$S_{ij}(\omega) = \int_{-\pi}^{\pi} \Phi_i(\omega, \beta)\overline{\Phi_j(\omega, \beta)}E(\omega, \beta)d\beta, \tag{3.1}$$

where $S_{ij}(\omega)$ denotes the cross-spectrum between the ith and jth vessel response at angular wave frequency ω, Φ_i and Φ_j represent the RAOs of the ith and jth vessel response, and $E(\omega, \beta)$ is the directional wave spectrum as function of ω and wave direction β. The response cross-spectrum $S_{ij}(\omega)$ is obtained by computing the cross-correlation between the time series of the measured vessel responses i and j. This result is then transformed to the frequency domain by application of a fast Fourier transform (FFT) or multivariate autoregressive (MAR) model.

The main goal is to retrieve the directional wave spectrum $E(\omega, \beta)$ from Eq.

(3.1) using the computed response cross-sprectra $S_{ij}(\omega)$ and known ship RAOs $\Phi_i(\omega,\beta)$ and $\Phi_j(\omega,\beta)$. To do this, the wavefield must be discretized into $N_\beta \times N_\omega$ points (Figure 3.2), where N_β and N_ω represent the number of respective wave directions and wave frequencies considered. Such a discretization implies that Eq. (3.1) can be rewritten into the following discrete form

$$S_{ij}(\omega_m) = \Delta\beta \sum_{k=1}^{N_\beta} \Phi_i(\omega_m,\beta_k)\overline{\Phi_j(\omega_m,\beta_k)}E(\omega_m,\beta_k), \tag{3.2}$$

where $\omega_m = \omega_0 + (m-1)\Delta\omega$ and $\beta_k = (k-1)\Delta\beta$ are the pre-computed discrete wave frequencies and wave directions for $m = 1,2,\ldots,N_\omega$ and $k = 1,2,\ldots,N_\beta$, respectively, and $\Delta\beta = 2\pi/N_\beta$ and $\Delta\omega = (\omega_f - \omega_0)/N_\omega$, where $[\omega_0,\omega_f]$ represents the considered frequency range. The cross-spectra $S_{ij}(\omega_m)$ can either be real (i.e., when $i = j$) or complex valued (i.e., when $i \neq j$), meaning that for each i and j, Eq. (3.2) can be divided into three separate parts: $S_{ii}(\omega_m)$, $\mathrm{Re}\{S_{ij}(\omega_m)\}$, and $\mathrm{Im}\{S_{ij}(\omega_m)\}$. Hence, for each frequency component ω_m, we can rewrite Eq. (3.2) into the following compact form

$$\mathbf{b}_m = \mathbf{A}_m\mathbf{f}_m, \tag{3.3}$$

where

$$\mathbf{b}_m := \underbrace{\begin{bmatrix} S_{ii}(\omega_m) \\ \vdots \\ \mathrm{Re}\{S_{ij}(\omega_m)\} \\ \vdots \\ \mathrm{Im}\{S_{ij}(\omega_m)\} \\ \vdots \end{bmatrix}}_{N_d^2\times 1}, \quad \mathbf{f}_m := \underbrace{\begin{bmatrix} E(\omega_m,\beta_1) \\ E(\omega_m,\beta_2) \\ \vdots \\ E(\omega_m,\beta_{N_\beta}) \end{bmatrix}}_{N_\beta\times 1},$$

$$\mathbf{A}_m := \Delta\beta \underbrace{\begin{bmatrix} \ldots & |\Phi_i(\omega_m,\beta_k)|^2 & \ldots \\ & \vdots & \\ \ldots & \mathrm{Re}\{\Phi_i(\omega_m,\beta_k)\}\,\mathrm{Re}\{\Phi_j(\omega_m,\beta_k)\} + \mathrm{Im}\{\Phi_i(\omega_m,\beta_k)\}\,\mathrm{Im}\{\Phi_j(\omega_m,\beta_k)\} & \ldots \\ & \vdots & \\ \ldots & \mathrm{Im}\{\Phi_i(\omega_m,\beta_k)\}\,\mathrm{Re}\{\Phi_j(\omega_m,\beta_k)\} - \mathrm{Re}\{\Phi_i(\omega_m,\beta_k)\}\,\mathrm{Im}\{\Phi_j(\omega_m,\beta_k)\} & \ldots \end{bmatrix}}_{N_d^2\times N_\beta}.$$

Generalizing Eq. (3.3) to account for *all* frequencies N_{ω_m}, yields the final affine equation

$$\mathbf{b} = \mathbf{A}\mathbf{f}, \tag{3.4}$$

where $\mathbf{b} = [\mathbf{b}_1^\top, \mathbf{b}_2^\top, \ldots, \mathbf{b}_{N_\omega}^\top]^\top \in \mathbb{R}^{N_d^2 N_\omega}$, $\mathbf{A} = \text{diag}\{\mathbf{A}_1, \mathbf{A}_2, \ldots, \mathbf{A}_{N_\omega}\} \in \mathbb{R}^{N_d^2 N_\omega \times N_\beta N_\omega}$, and $\mathbf{f} = [\mathbf{f}_1^\top, \mathbf{f}_2^\top, \ldots, \mathbf{f}_{N_\omega}^\top]^\top \in \mathbb{R}^{N_\beta N_\omega}$. The overall goal is to find an $\mathbf{f}$ that minimizes the difference between the left-hand and right-hand sides of Eq. (3.4), i.e.,

$$\min_{\mathbf{f}} ||\mathbf{A}\mathbf{f} - \mathbf{b}||^2, \tag{3.5}$$

where in this case, we have considered minimization in the least-squares sense, which is most common. However, in practice, the system (3.4) generally possesses fewer equations than unknowns (i.e., $N_d^2 N_\omega < N_\beta N_\omega$), rendering it an underdetermined system. To overcome this issue and make Eq. (3.4) uniquely solvable, some constraints must be imposed. The latter is achieved by realizing that the directional wave spectrum is positive, smooth, and diminishes to zero for sufficiently low and high frequencies. There exist two different approaches for incorporating such constraints into the optimization problem (3.5), which are termed parametric and nonparametric approaches. Parametric approaches [19, 29, 32, 37, 38] assume a predefined wave spectrum shape that depends only on a few parameters. For example, a 10-parameter bimodal wave spectrum is considered in [19, 38], where

$$E(\omega, \beta) = \frac{1}{4} \sum_{i=1}^{2} \frac{(((4\lambda_i + 1)/4)\omega_{p,i}^4)^{\lambda_i}}{\Gamma(\lambda_i)} \frac{H_{s,i}^2}{\omega^{4\lambda_i + 1}} A(s_i) \times \cos^{2s_i}\left(\frac{\beta - \bar{\beta}_i}{2}\right) \exp\left\{-\frac{4\lambda_i + 1}{4}\left(\frac{\omega_{p,i}}{\omega}\right)^4\right\}, \tag{3.6}$$

where H_s is the significant wave height, λ denotes the shaping parameter of the spectrum, $\bar{\beta}$ is the mean wave direction, ω_p is the peak wave frequency, s is a spreading parameter, Γ is the Gamma function, and

$$A(s) = \frac{2^{2s-1}\Gamma^2(s+1)}{\pi\Gamma(2s+1)}$$

is a normalization factor for the area under a $\cos^{2s}$ curve. The representation in Eq. (3.6) implicitly preserves the positiveness, smoothness, and boundary constraints above. On the other hand, nonparametric approaches [24–28, 39, 40] do not place any assumptions on the shape of the wave spectrum, and instead introduce the positiveness, smoothness, and boundary constraints directly into the optimization problem (3.5) and solve the system using convex optimization. Following such an approach, a typical

cost function with constraints is given by

$$\begin{aligned} \min_{\mathbf{f}} \; & ||\mathbf{A}\mathbf{f} - \mathbf{b}||^2 + ||\mathbf{C}\mathbf{L}\mathbf{f}||^2 \\ \text{s.t. } & \mathbf{f} \geq \mathbf{0}, \\ & \mathbf{f}_1 = \mathbf{0}, \\ & \mathbf{f}_{N_\omega} = \mathbf{0}, \end{aligned} \tag{3.7}$$

where $\mathbf{C}$ denotes a diagonal positive definite matrix of weights (penalty parameters) and $\mathbf{L}$ is a matrix containing the smoothness constraints [40]. For more details on the differences between parametric and nonparametric methods, the reader is referred to [28] and references therein.

It is worth stressing that the representation given in Eq. (3.1) applies only for stationkeeping vessels (i.e., zero forward speed). It is, however, possible to account for forward speed in Eq. (3.1) by considering the wave encounter frequency ω_e instead, i.e.,

$$S_{ij}(\omega_e) = \int_{-\pi}^{\pi} \Phi_i(\omega_e, \beta)\overline{\Phi_j(\omega_e, \beta)}E(\omega_e, \beta)d\beta, \tag{3.8}$$

where

$$\omega_e = |\omega - kU\cos\beta|, \tag{3.9}$$

with U denoting the vessel forward speed, ω the absolute wave frequency, k the wave number, and β the wave encounter angle (Figure 3.3). A drawback of Eq. (3.8) is that the directional wave spectrum $E(\omega_e, \beta)$ is formulated in the encounter frequency domain and not in terms of absolute frequency, i.e., $E(\omega, \beta)$. Although the computed significant wave height (and wave direction) is equivalent in both frequency domains due to the conservation of energy, the wave frequencies differ. The absolute wave frequencies can be obtained from the encounter domain by applying the transformation (3.9) to map the encounter frequencies to absolute frequencies [28]. However, for following seas (i.e., when the vessel is moving with the general propagation direction of the waves), each ω_e generally maps to three different ω (Figure 3.4). The 1-to-3 mapping problem implies that the integral (3.8) should map to three parts to maintain each potential absolute frequency, leading to an ambiguous solution. Some works have addressed this issue [35, 36], proposing various pseudo algorithms and optimization techniques based on parameterized wave spectra.

3.1.2 Time-domain formulation

Although most of the research using RAO-model approaches for shipboard sea state estimation is carried out in the frequency domain, there are some works [23, 24]

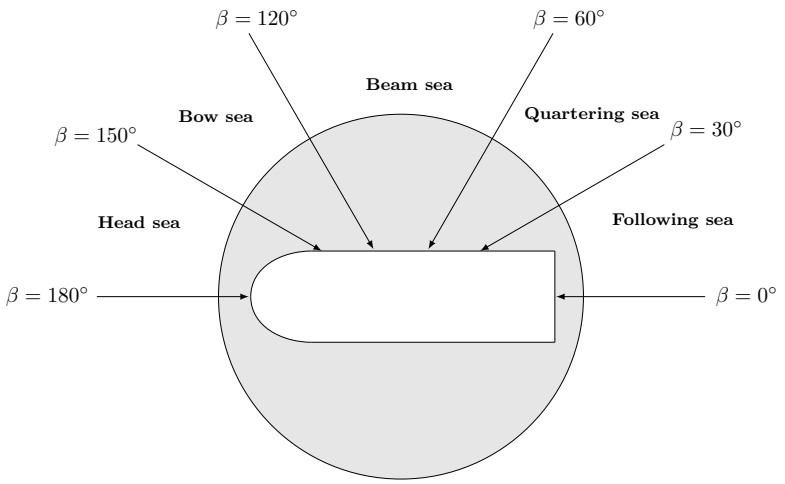

Figure 3.3: Definition of wave encounter angle β.

who have formulated the problem in the time domain as a state-space model and solved it using a Kalman filter. As we saw earlier, RAO approaches in the frequency domain usually involve minimizing an error cost function using iterative optimization procedures, which may require some computational effort. As we shall see, by instead formulating the problem in the time domain and employing a Kalman filter, the speed of estimation can be increased as cross-spectral calculations are not performed, and the wave amplitudes are estimated directly in real-time. In addition, with the Kalman filter framework, it is easy to fuse data from several sources and incorporate process and measurement noise into the estimation procedure. The latter is important as it provides an uncertainty measure in the estimated wave quantities, indicating whether they can be trusted or not.

Recall from Section 2.2 that the ocean surface elevation can be considered a superposition of a large number of harmonic wave components differing in amplitude, frequency, and direction. Assuming that the considered vessel response is linear with the incident waves, the response r can be modeled in the time domain as a weighted sum of harmonic wave components over a range of wave frequencies and directions [23, 24], i.e.,

$$r = \mathrm{Re}\left\{ \sum_{m=1}^{N_f} \sum_{n=1}^{N_\beta} \Phi(\omega_m, \beta_n) A(\omega_m, \beta_n) \big(\cos(\omega_m t + \epsilon_{mn}) + j \sin(\omega_m t + \epsilon_{mn}) \big) \right\}, \tag{3.10}$$

where $\Phi(\omega_m, \beta_n)$ denotes the RAO of the vessel response computed at discrete wave frequencies and directions ω_m and β_n, respectively, $A(\omega_m, \beta_n)$ represents the complex

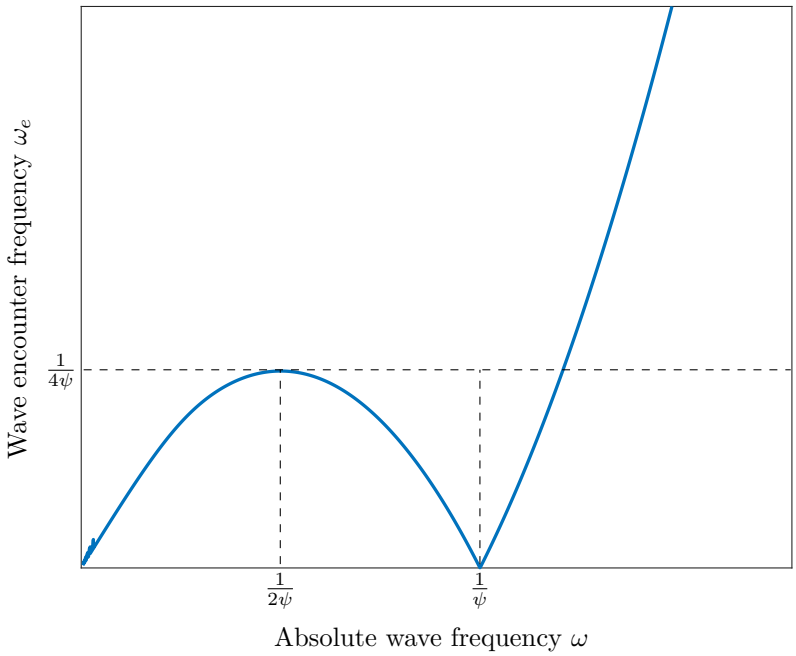

Figure 3.4: Relationship between wave encounter frequency ω_e and ω given by Eq. (3.9), where $k = \omega^2/g$ (deep waters) and $\psi := U/g \cos\beta$. If $\omega_e < 1/4\psi$, it maps to three different solutions of the wave frequency ω.

wave amplitude, and ϵ_{mn} is the random phase. Introducing state variables $x_{2m-1,n}$ and $x_{2m,n}$ to represent the real and imaginary parts of $A(\omega_m, \beta_n)$ and neglecting ϵ_{mn}, Eq. (3.10) can be rewritten as

$$\begin{aligned} r = \sum_{m=1}^{N_f}\sum_{n=1}^{N_\beta} \big(\operatorname{Re}\{\Phi_{mn}\}\cos(\omega_m t) - \operatorname{Im}\{\Phi_{mn}\}\sin(\omega_m t)\big)x_{2m-1,n} \\ - \sum_{m=1}^{N_f}\sum_{n=1}^{N_\beta} \big(\operatorname{Im}\{\Phi_{mn}\}\cos(\omega_m t) + \operatorname{Re}\{\Phi_{mn}\}\sin(\omega_m t)\big)x_{2m,n}, \end{aligned}$$

where $\Phi_{mn} := \Phi(\omega_m, \beta_n)$ for compactness. For N_r vessel responses, the discrete-time Kalman filter state-space model can be formulated as

$$\begin{aligned} \mathbf{x}_{k+1} &= \mathbf{x}_k + \mathbf{w}_k, \quad \mathbf{w}_k \sim \mathcal{N}(\mathbf{0}, \mathbf{Q}_k), \\ \mathbf{r}_k &= \mathbf{C}_k\mathbf{x}_k + \mathbf{v}_k, \quad \mathbf{v}_k \sim \mathcal{N}(\mathbf{0}, \mathbf{R}_k), \end{aligned} \tag{3.11}$$

where $\mathbf{x}_k = [x_{1,1}, x_{1,2}, \ldots, x_{1,N_\beta}, x_{2,N_\beta}, \ldots, x_{2N_f-1,N_\beta}, x_{2N_f,N_\beta}]^\top \in \mathbb{R}^{2N_fN_\beta}$ is the state vector consisting of wave amplitudes at sample number k, $\mathbf{r}_k \in \mathbb{N}_r$ is the measured vessel responses, $\mathbf{w}_k$ and $\mathbf{v}_k$ denote white Gaussian process and measurement noise with covariances $\mathbf{Q}_k$ and $\mathbf{R}_k$, respectively, and

$$\mathbf{C}_k = \begin{bmatrix} \mathrm{Re}\{\Phi_{1,11}\}\cos(\omega_1 kT) - \mathrm{Im}\{\Phi_{1,11}\}\sin(\omega_1 kT) \\ \mathrm{Re}\{\Phi_{2,11}\}\cos(\omega_1 kT) - \mathrm{Im}\{\Phi_{2,11}\}\sin(\omega_1 kT) \\ \vdots \\ \mathrm{Re}\{\Phi_{i,11}\}\cos(\omega_1 kT) - \mathrm{Im}\{\Phi_{i,11}\}\sin(\omega_1 kT) \\ \vdots \end{bmatrix}$$

$$\begin{matrix} -(\mathrm{Im}\{\Phi_{1,11}\}\cos(\omega_1 kT) + \mathrm{Re}\{\Phi_{1,11}\}\sin(\omega_1 kT)) & \ldots \\ -(\mathrm{Im}\{\Phi_{2,11}\}\cos(\omega_1 kT) + \mathrm{Re}\{\Phi_{2,11}\}\sin(\omega_1 kT)) & \ldots \\ \vdots & \\ -(\mathrm{Im}\{\Phi_{i,11}\}\cos(\omega_1 kT) + \mathrm{Re}\{\Phi_{i,11}\}\sin(\omega_1 kT)) & \ldots \\ \vdots & \end{matrix} \begin{bmatrix} \\ \\ \\ \\ \\ \end{bmatrix}$$

where $\mathbf{\Phi}_{i,mn}$ represents the RAO of the ith vessel response and $t(kT) := kT$ where T is the sampling time. In order for the Kalman filter to work, the state-space model (3.11) needs to be observable. However, as discussed in Section 3.1.1, the number of unknowns generally exceeds the number of measurements, leading to a singular or badly conditioned observability matrix. When this happens, the state estimates will fail to converge to the correct values. A solution proposed by [23, 24], is to include past measurements in the measurement vector, incrementing N_r in proportion to the number of lags. For details on the latter procedure and how the noise covariance matrices were tuned, the reader is referred to [23, 24] and references therein.

3.1.3 The effect of vessel low-pass filtering

Whenever the incident waves are sufficiently short, multiple wave crests (and troughs) will affect the vessel simultaneously as the waves move through it (Figure 3.5). When this happens, the vessel will distort the waves, and the observed vessel responses will generally no longer be linear with the incident waves. Indeed, this characteristic low-pass filtering ship behavior [33, 34, 41–43] implies that for waves of sufficiently high frequency, information about the prevailing sea state cannot be accurately obtained from measured ship motions. To understand when the measured vessel motions can be reliably utilized to determine the sea state, our recent study [44] proposed a frequency threshold quantifying the frequency bandwidth of waves not distorted by the vessel. The frequency bandwidth is based on the main vessel length L and breadth

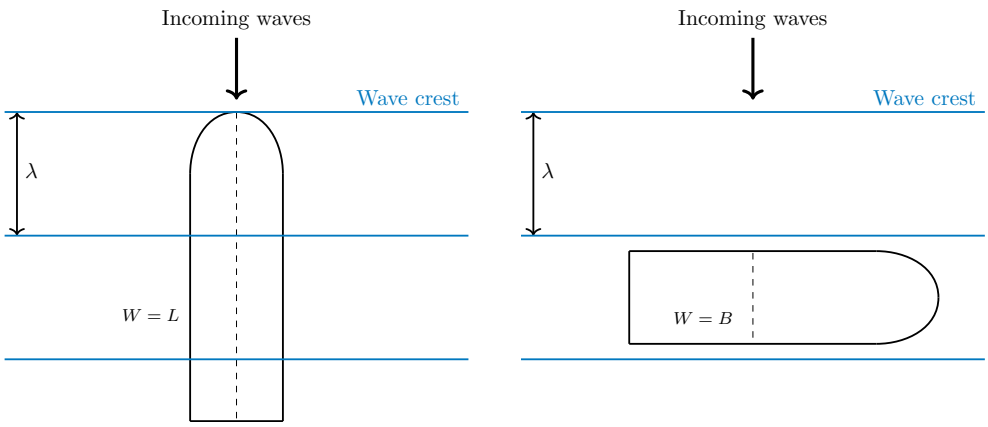

Figure 3.5: The wave trajectory distance W (represented by dashed lines) depends on the relative wave direction β. When $\beta = 180°$ (left), the vessel will filter the waves (shown in blue) passing through it as the wavelength $\lambda < W = L$, where L is the vessel length. However, when $\beta = 90°$ (right), the vessel motion responses will be unaffected by filtering as $\lambda > W = B$, where B is the vessel beam.

B dimensions and the relative wave direction β, quantified by

$$W = L|\cos\beta| + B|\sin\beta|, \tag{3.12}$$

where W is the projected wave trajectory distance through the vessel (Figure 3.5). Hence, whenever the wavelength λ exceeds Eq. (3.12), the vessel motions are deemed linear with the incident waves (i.e., the vessel behaves like a wave buoy). An easy and quick way to assess whether $\lambda > W$ holds for all β is to evaluate Eq. (3.12) when the wave trajectory distance is maximum, which for a box-shaped vessel occurs whenever it is parallel with the diagonal distance of the corners, i.e.,

$$W = \sqrt{L^2 + B^2}. \tag{3.13}$$

Hence, based on Eq. (3.13), the frequency of bandwidth of waves not distorted by the vessel in question becomes [45]

$$f_{\text{max}} = \sqrt{\frac{g/2\pi}{\sqrt{L^2+B^2}} \tanh\left(\frac{2\pi d}{\sqrt{L^2+B^2}}\right)}, \tag{3.14}$$

where g is the gravitational constant and d is the water depth. The relationship above was derived by equating (3.13) with $\lambda = 2\pi/k$, and inserting the resulting expression for k into the dispersion relation (2.2) and solving it in terms of the linear frequency

f. It is worth noting that Eq. (3.14) applies only for stationary vessels (i.e., $U = 0$). For vessels with constant forward speed $U > 0$, Eq. (3.14) can be extended to address such situations by considering the wave encounter frequency. Rewriting Eq. (3.9) in terms of linear frequency and substituting f_{max} into it, yields the adjusted maximum frequency threshold $f_{\text{e,max}}$ given in terms of forward speed [45], i.e.,

$$f_{\text{e,max}} = \left| f_{\text{max}} \pm \frac{UL}{L^2 + B^2} \right|, \tag{3.15}$$

where we have used $k = 2\pi/\sqrt{L^2 + B^2}$ and $\cos\beta = \pm L/\sqrt{L^2 + B^2}$ (worst case scenario in which the wave trajectory distance is maximum). The latter component on the right-hand side of Eq. (3.15) should be added or subtracted depending on whether the vessel is following or moving against the waves, respectively.

3.2 Signal-based approaches

Although most of the literature on shipboard sea state estimation is dominated by model-based approaches using the wave-buoy analogy, they have not yet materialized in industrial applications due to several challenges [5]. Firstly, they rely on RAOs, which should generally be determined for each unique ship, requiring substantial effort. Also, since RAOs are transfer functions, they require linearity between the waves and vessel responses to be valid, which is generally true for mild and moderate wave climates. Secondly, many of the sea state estimates from these methods are usually time-delayed by 10-15 min due to the underlying spectral analysis [6], posing challenges for decision-support systems requiring real-time data. Thirdly, high-frequency waves are effectively ignored when considering vessel motion responses for sea state estimation since the ship acts as a low-pass filter.

On the other hand, signal-based approaches are not constrained by the size of the waves and do not require any ship model, meaning they can be directly applied to any vessel. These approaches typically use shipboard wave radars and/or distance altimeters to measure the ocean directly by analyzing reflections of electromagnetic radiation from the sea surface, offering real-time estimations. Furthermore, these approaches are capable of measuring high-frequency waves, as they are not sensitive to vessel low-pass filtering. Some more recent studies have also investigated the possibility of using machine learning algorithms to determine the sea state by learning a direct mapping between the vessel responses and waves. In the following discussion, we will explore the advantages and disadvantages of these signal-based approaches, shedding light on their potential benefits and limitations.

3.2.1 Radar and laser altimetry

Most ships at sea are equipped with a marine X-band radar, which serves as a valuable tool for obstacle detection and collision avoidance. However, when the radar range setting is adjusted to measure objects within short distances, it often generates a noise signal called "sea clutter," which appears on the plan position indicator display. Sea clutter arises from the backscatter of electromagnetic waves by the ripples on the sea surface (i.e., capillary waves), primarily caused by local wind activity. These capillary waves are typically modulated by longer waves that carry the information we are interested in. By carefully examining the time evolution of recorded radar images, it becomes possible to discern the underlying low-frequency modulation pattern from the changes in the sea clutter.

To extract the directional wave spectrum, a common approach involves transforming the time series of radar images into the spectral domain using a three-dimensional Fourier transform. This transformation allows for the analysis of the various frequencies present in the radar data, helping to identify the characteristics of the waves and their directional properties. For a more detailed understanding of this procedure, interested readers are encouraged to consult [46–48] and the associated references within.

Although commercial marine X-band radars are popular tools for inferring information about the local waves, they are not perfect. Firstly, if there is little to no wind, the underlying low-frequency modulation pattern cannot be observed, and we get little to no wave information. Secondly, radar emissions and returns are susceptible to environmental influences such as precipitation (e.g., rain or snow). Thirdly, they are not very suitable for wave estimation near shore where landmasses and other obstacles may obstruct returns. Finally, the radars, installation, and associated software packages for wave processing are generally quite expensive. For instance, the Miros WaveX and RangeFinder radar-based systems employed in our experiments [45] cost roughly 20 000 dollars for a one-year leasing period.

Downward-looking distance altimeters are popular tools for measuring the sea surface directly [49, 50]. These altimeters, based on either radar or laser technology, are typically mounted over the bow of a vessel and measure the vertical distance from the instrument to the sea surface by a mechanism known as specular reflection. However, a drawback of these instruments is that they generally only provide one-dimensional wave spectra, meaning that only significant wave height and peak wave period can be obtained and not directional information. Also, the measurements from shipboard altimeters will generally be influenced by the roll and pitch motions of

the vessel. Although this unwanted influence can be corrected by employing an IMU separately to estimate the roll and pitch angles [49], the latter study shows that the wave estimation results were not very sensitive to the vessel roll and pitch motions.

3.2.2 Machine learning

Recently, there has been a significant surge of interest in shipboard wave estimation approaches based on machine learning [51–63]. These approaches are gaining attention due to their ease of application, ability to learn direct mappings from ship responses to sea state parameters without RAOs, and real-time estimation capabilities. Various types of deep neural networks, including convolutional neural networks and general adversarial networks, are commonly used in these approaches.

One key aspect that differentiates these methods is whether they treat sea state estimation as a classification or regression task. In the classification approach, the possible value ranges of sea state parameters are divided into discrete bins. For example, the wave direction parameter can be divided into 360 discrete bins, with each bin representing a possible wave direction. On the other hand, regression involves directly determining the continuous value of the sea state parameter. Another distinguishing factor among machine learning approaches for sea state estimation is whether they consider ship motion data in the time domain or frequency domain. This choice affects the model's ability to capture relevant features and extract meaningful information for accurate sea state estimation.

Despite the growing potential of machine learning approaches, there are still several challenges that need to be addressed before they can be practically implemented. The primary challenge lies in the availability of training data. Since machine learning models typically learn in a supervised manner, a substantial amount of training data with accurate reference sea state information is required to cover the wide range of scenarios possible at sea. However, obtaining such reference data is not straightforward. While marine wave radars have been used to collect sea state data, this technology is expensive and not feasible for all vessels. For this reason, the majority of the current research only considers simulated sea state and ship motion response data. Also, to ensure the generalization power of the models, it is necessary to collect ship motion data with corresponding sea state references from multiple vessels of different sizes and geometries. By doing so, a general sea state model can be trained using transfer learning techniques.

In summary, machine learning approaches are attractive as they do not require any ship RAO models, are easy to implement, and have real-time estimation capabilities.

However, the need for real training data poses a significant challenge in developing a general sea state model that can be applied to any ship. Acquiring the necessary training data is complex, requiring accurate sea state references, which are only available for some vessels typically using wave radars. While effective, wave radars are not universally accessible due to their cost.

4 Phase-time-path-differences: A new approach for shipboard wave estimation

As we have seen, model-based approaches for shipboard wave estimation assume linearity between vessel responses and incident waves, allowing the use of response amplitude operators (RAOs) to model wave-response interactions. However, this assumption generally holds true for mild to moderate wave conditions, and obtaining motion RAOs for each ship requires considerable effort. Conversely, signal-based approaches are ship-independent and not constrained by the size of the waves. Nonetheless, these methods also have their limitations. Machine learning approaches necessitate extensive training data sets, and wave radars and laser altimeters, while accurate, are often costly, prone to environmental influences, and challenging to install without expert assistance.

In this section, we introduce our contribution to shipboard wave estimation: A signal-based phase-time-path-difference (PTPD) approach, which utilizes the delays between a group of sensors on board a vessel to infer frequency and directional information about the incident waves. As we shall see, this approach only considers measurements from a *single* inertial measurement unit (IMU) as input, rendering the approach ship-independent (i.e., no vessel motion RAOs are needed), inexpensive, robust against environmental impact, and easy to implement on any vessel.

4.1 Main idea

The main idea or concept of this Ph.D. work is rooted in array signal processing. To provide a solid foundation for this concept, we begin by illustrating a simple example from the latter domain, allowing us to build intuition. With this foundation in place,

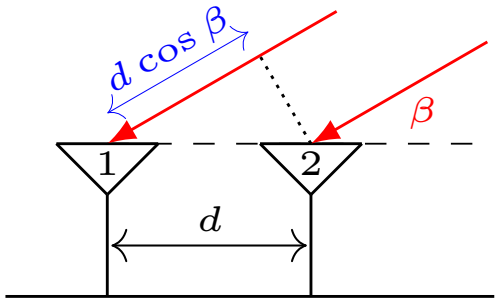

Figure 4.1: An antenna array consisting of two antennas separated by a distance d. The propagating waveforms (shown in red) approach the array at propagation angle β.

we then proceed to ocean waves, demonstrating how the concept can be applied there. Finally, we explain how this concept may be applied to shipboard IMUs, which, as we shall see, is considerably more practical.

4.1.1 Example from array signal processing

Array signal processing is a field within signal processing that deals with the analysis, processing, and interpretation of signals received by an array of spatially distributed sensors or antennas [64]. In array signal processing, the signals received by multiple sensors are combined and processed to extract useful information about the incident waveforms. A particularly important area of array signal processing is signal characterization, which aims to describe in a quantitative way the signals received by the array. One characteristic property of such signals is the direction of propagation, which is of fundamental importance in many applications measuring either electromagnetic, acoustic, or seismic waves. To show how the propagation direction of a propagating signal may be resolved from distributed sensor arrays, consider the antenna array illustrated in Figure 4.1. The array consists of two antennas separated by a distance d, receiving electromagnetic energy at an angle β relative to ground. Compared to antenna 2, we notice that the waveforms need to travel an additional distance to get to antenna 1. Using basic trigonometry, this extra path difference d_{12} can be expressed as

$$d_{12} = d\cos\beta. \tag{4.1}$$

The extra travel distance (4.1) will cause a corresponding time delay between the measurements in each antenna, given by

$$t_{12} = \frac{d_{12}}{c} = \frac{d}{c}\cos\beta, \tag{4.2}$$

where t_{12} is the time delay/difference between antenna 1 and 2, with c denoting the speed of light. It is more common to express the delay t_{12} as a phase difference Θ_{12} by using the fact that $\Theta_{12} = \omega t_{12}$, which together with Eq. (4.2), yields

$$\Theta_{12} = kd\cos\beta, \tag{4.3}$$

where we have used that $c = \omega/k$, with ω denoting the angular frequency and k the wave number. Hence, if we can measure the phase, time, or path difference (PTPD) between the measurements in each antenna, it is possible to determine the propagation direction β from one of the equations above.

4.1.2 The PTPD concept applied to the sea surface

If we substitute the electromagnetic waves and antennas from the previous example with physical ocean waves and sensors situated on the ocean, we can apply the same PTPD concept to resolve the propagation direction (and wave number) of ocean waves. To see this, consider a spatially distributed array of sensors (e.g., wave poles) in the ocean, as illustrated in Figure 4.2. The separation distance d_{12} between sensors $\{s_1\}$ and $\{s_2\}$ along the wave propagation direction causes a delay between the wave elevation time series recorded in each sensor. The path difference d_{12} is simply the x-component of the position vector $\vec{r}_{s_1 s_2}$ expressed in the wave tangent frame $\{w\}$, obtained by

$$\mathbf{r}^{w}_{s_1 s_2} = \mathbf{R}^{w}_{s_1}\mathbf{r}^{s_1}_{s_1 s_2}, \tag{4.4}$$

where $\mathbf{r}^{s_1}_{s_1 s_2} = [x_{12}, y_{12}, z_{12}]^\top$ denotes the coordinate position vector of $\{s_2\}$ relative to $\{s_1\}$ expressed in the sensor frame $\{s_1\}$ and $\mathbf{R}^{w}_{s_1}$ is the rotational transform between frames $\{s_1\}$ and $\{w\}$ given by

$$\mathbf{R}^{w}_{s_1} = \begin{bmatrix} \cos\beta & \sin\beta & 0 \\ \sin\beta & -\cos\beta & 0 \\ 0 & 0 & -1 \end{bmatrix}.$$

Carrying out the multiplication in Eq. (4.4) and extracting the x-component of the resulting vector, yields the path difference

$$d_{12} = x_{12}\cos\beta + y_{12}\sin\beta. \tag{4.5}$$

Following the same procedure as in Section 4.1.1, the corresponding time delay between the measurements in $\{s_1\}$ and $\{s_2\}$ then becomes

$$t_{12} = \frac{d_{12}}{c} = \frac{x_{12}\cos\beta + y_{12}\sin\beta}{c}, \tag{4.6}$$

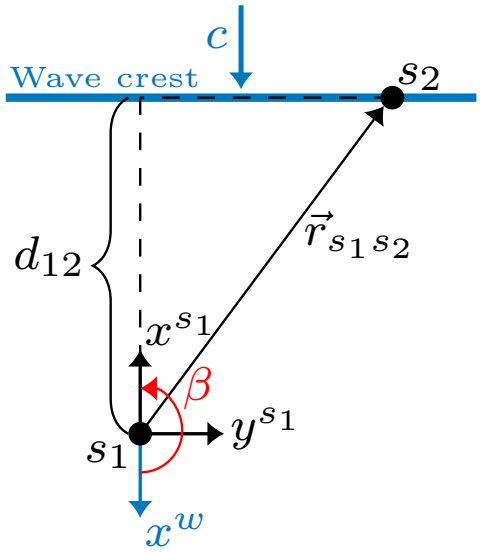

Figure 4.2: Two arbitrary sensors labeled s_1 and s_2 situated on the ocean surface with sensor axes $(x^{s_i}, y^{s_i}, z^{s_i})$ for $i = \{1, 2\}$ (z-axis not shown, but points down into the page) exposed to long-crested waves with propagation speed c. The wave tangent frame $\{w\}$ is defined with x^w-axis pointing in the same direction as the propagating waves, with the origin coinciding with the (arbitrarily chosen) reference sensor s_1. The wave propagation direction β is defined as the counterclockwise angle from x^w to x^{s_1} (chosen as $180°$ in this case). The position of s_2 relative to s_1 is denoted by the vector $\vec{r}_{s_1 s_2}$, where d_{12} is the x-component of the latter expressed in $\{w\}$.

where t_{12} is the time difference and c is the wave celerity or phase velocity as it is also called. Assuming a regular harmonic wave, the latter expression can be converted to a phase difference by substituting $c = \omega/k$, where ω and k denote the angular wave frequency and wave number, respectively, into Eq. (4.6), which yields

$$\Theta_{12} = k(x_{12} \cos\beta + y_{12} \sin\beta), \tag{4.7}$$

with $\Theta_{12} := \omega t_{12}$.

The phase difference (4.7) can also be derived directly from the definition of the surface elevation (2.3) by considering the surface elevation at two separate spatial locations. Let $\{s_1\}$ and $\{s_2\}$ denote two distinct locations on the sea surface with horizontal spatial coordinates (x_1, y_1) and (x_2, y_2), respectively. Assuming a propagating harmonic wave with relative wave direction β, the surface elevations at

$\{s_1\}$ and $\{s_2\}$ at time t can be expressed as

$$\eta(x_1, y_1, t) = a\cos(\omega t - k(x_1\cos\beta + y_1\sin\beta) + \epsilon),$$
$$\eta(x_2, y_2, t) = a\cos(\omega t - k(x_2\cos\beta + y_2\sin\beta) + \epsilon),$$

where a is the wave amplitude and ϵ is the random phase. The phase difference Θ_{12} is obtained by subtracting the arguments in the expressions above from each other, which yields

$$\begin{aligned}\Theta_{12} &= k\big((x_2 - x_1)\cos\beta + (y_2 - y_1)\sin\beta\big)\\ &= k(x_{12}\cos\beta + y_{12}\sin\beta),\end{aligned}$$

which indeed is identical to Eq. (4.7).

Unless prior information is known about the general propagation direction, the wave direction obtained from a pair of sensors will be ambiguous (it is unknown whether the waves approach the sensors from the left or right). To overcome such ambiguities, we introduce another sensor $\{s_3\}$ into the sensor array, which, in turn, gives us an additional phase difference Θ_{13}.[1] Grouping the phase differences into a vector, we can extend and express Eq. (4.7) more compactly as

$$\begin{bmatrix}\Theta_{12}\\ \Theta_{13}\end{bmatrix} = k\begin{bmatrix}x_{12} & y_{12}\\ x_{13} & y_{13}\end{bmatrix}\begin{bmatrix}\cos\beta\\ \sin\beta\end{bmatrix}. \tag{4.8}$$

Applying the 2×2 inverse matrix to the left and right-hand side above gives us

$$\begin{bmatrix}\cos\beta\\ \sin\beta\end{bmatrix} = \frac{1}{k(x_{12}y_{13} - x_{13}y_{12})}\begin{bmatrix}y_{13} & -y_{12}\\ -x_{13} & x_{12}\end{bmatrix}\begin{bmatrix}\Theta_{12}\\ \Theta_{13}\end{bmatrix}. \tag{4.9}$$

Hence, the analytical expression for the relative wave propagation direction becomes

$$\beta = \arctan\left(\frac{[x_{12}\Theta_{13} - x_{13}\Theta_{12}]/\mathrm{sgn}(D)}{[y_{13}\Theta_{12} - y_{12}\Theta_{13}]/\mathrm{sgn}(D)}\right), \tag{4.10}$$

where

$$D = k(x_{12}y_{13} - x_{13}y_{12}). \tag{4.11}$$

The above analysis shows that β can be uniquely resolved from Eq. (4.10) provided that (i) a minimum of three sensors are used, and (ii) they do not reside on a straight line—thus ensuring that Eq. (4.11) is non-zero.

[1] Actually, we get two additional phase difference Θ_{13} and Θ_{23}, but only one of them is needed for the present analysis.

The analytical solution (4.10) is widely considered the standard method for calculating the mean wave direction using arrays [65–72]. However, this approach has significant limitations that make it unsuitable for applications that need real-time or online wave direction estimates. One major drawback is that the analytical solution does not account for uncertainties in the wave direction estimates, even though there can be errors in the measured phase differences and sensor locations. Additionally, it does not provide an estimate of the wave number, even though this information can be derived from the same set of measurements [73]. Furthermore, the analytical solution lacks a convenient framework for incorporating additional measurements.

Most studies that focus on estimating wave direction using the PTPD concept primarily examine stationary arrays deployed in the ocean [65–68]. These arrays typically consist of sensors like pressure transducers, wave probes, lasers, echo sounders, and current meters, which are positioned either on the sea surface or the seabed. However, there are significant practical limitations associated with these arrays. They are often expensive, challenging to install, and geographically confined, offering limited flexibility for design modifications once installed.

4.1.3 The PTPD concept applied to shipboard sensors

A *shipboard* array of sensors offers many advantages over stationary sensor arrays on the sea surface or seabed. It is more cost-effective, flexible, easier to install, and considerably more practical as ships provide a portable platform for measuring waves. However, despite these advantages, there have been limited efforts [74–76] exploring the potential of using a group of sensors on board a vessel and the PTPDs between their measurements to extract important wave properties. For instance, in a previous study [74], an array of ultrasonic distance altimeters was mounted over the bow of the vessel, allowing phase-lagged measurements of surface elevation. Based on these measurements, the wave height and frequency were determined from the surface elevations themselves, whereas the wave direction was resolved from the PTPDs. Although this approach using ultrasonic altimeters is cheaper than stationary arrays embedded in the ocean, they still pose challenges in terms of cost, installation, and configuration.

On the other hand, IMUs offer an attractive alternative. IMUs are inexpensive, small, lightweight, robust, and compact sensors that are easy to install and integrate with existing systems (if not already present). Rigidly attached to the vessel, an IMU measures the angular velocity and specific force of the ship with a high data sampling rate. By employing an array of distributed IMUs around the vessel, it becomes possible to utilize the PTPDs between the specific force measurements to infer the frequency

and directional characteristics of the waves. However, despite the cost-effectiveness and practicality of using IMUs for wave measurement, only one study [75] has to our knowledge, attempted to investigate the potential capabilities of this approach. In the latter study, the author distributed multiple IMUs along the hull of a model ship and used the measured time differences between the estimated heave accelerations to determine the direction of incoming regular waves. Despite showing some success, the study above is far from complete. More work is needed to establish the theoretical foundation of the PTPD method to model sensor delays on a rigid body for both stationary and moving vessels in regular and irregular waves. Additionally, it is presently unclear from the previous study how many IMUs are needed, how far they should be separated, or how they should be arranged to obtain reliable wave estimates.

4.2 Main contributions

In this section, the main contributions of this Ph.D. work are presented. The contributions are listed as individual subheadings, followed by a brief but concise description. For a more in-depth treatment of each contribution, the reader is referred to the papers in Part II of this thesis.

4.2.1 Theoretical assessment of the PTPD approach for rigid bodies

The PTPD model derived in Section 4.1.2 was based on a group of sensors *directly* situated on the water. In such a situation, the sensor measurements are independent of each other as when a wave strikes the first sensor, the second sensor is unaware of this event until the wave strikes it a few moments later. However, for a group of sensors on a rigid body, all sensors will be simultaneously affected when the wave strikes the body. Although a sensor delay will be perceived between the measurements in both situations, the magnitude of the delay will generally differ. In the first situation, the delay is determined solely by the distance between sensors, the speed of the waves, and the angle at which the waves pass through them. In the second situation, however, the angular displacement of the body governs the perceived sensor delays. Despite the clear distinction between the situations above, previous studies [44, 75, 76] directly apply the PTPD approach for ocean-borne sensors to model sensor delays on a rigid body. In general, there can be significant deviations between the delays measured between a pair of sensors on a rigid body and a corresponding pair of sensors on the ocean. In [45], we rigorously assess the PTPD approach for modeling sensor delays on a rigid body and identify sufficient conditions for the method to be accurately applied. In short, for the PTPD approach to be applicable, the sensor separation distances need

to be sufficiently short and the wavelength of the ocean waves passing through the body containing the sensors sufficiently long.

4.2.2 A forward speed PTPD model for surface vessels

In most cases, it is more convenient for the captain and crew of a ship to measure ocean wave characteristics while the ship is in motion. Up to now, however, the application of the PTPD approach has been limited to stationary wave arrays or stationary ships. This limitation is addressed in [45], where a new PTPD model is derived to account for the forward speed of the vessel, enabling the estimation of waves both when the ship is moving and when it is stationary. Additionally, the model takes into consideration the vessel's roll and pitch motions induced by the waves, making it a time-varying model. Nevertheless, since the average roll and pitch motions of the vessel are typically close to zero, these motions can be neglected to simplify the PTPD model. For trimmed vessels with nonzero roll and pitch angles, it is possible to substitute the average offset values for these angles (if known) directly into the time-varying model and use this model instead.

4.2.3 Observability proof: Minimum sensor requirements

For wave arrays situated on the ocean, it is a well-known fact that a minimum of two independent phase differences (i.e., three sensors) are needed to resolve the wave propagation direction uniquely [65]. However, a lesser-known fact is that the wave number/frequency can also be uniquely resolved from the same PTPD data. We prove this interesting fact in [44] by showing that our nonlinear PTPD model is observable for a minimum of three noncollinear sensors (i.e., they do not lie on a straight line). The results from the observability analysis can be generalized to shipboard IMUs, provided that the IMUs are sufficiently close together and that the waves are sufficiently long. Also, if IMUs are considered primary sensors and assuming that the vessel can be regarded as a rigid body, then the minimum sensor requirements can be relaxed to a *single* IMU [45]. This important and exciting result significantly increases the practical utility of the PTPD method as additional hardware and time-synchronization between measurements are made redundant. Moreover, the latter result also implies that ships already equipped with an IMU may obtain directional and frequency characteristics of the waves today by implementing our proposed PTPD method. However, the validity of the rigid-body assumption should be assessed, e.g., by a hydroelastic analysis of the characteristic vessel.

4.2.4 Determining the ambiguous wave frequency in following seas

As discussed in Section 3.1.1, the encountered wave frequency in following seas will generally map to three distinct (absolute) wave frequencies, making it challenging to determine the correct one during forward motion [35, 36]. However, the observability results above imply that the absolute wave frequency can be uniquely resolved from the PTPDs of our proposed method in any sea by using the dispersion relation (2.2) to map the estimated wave number to the wave frequency. This interesting result is validated experimentally in a wave tank with a model ship exposed to various regular and irregular waves [45].

4.2.5 Quantifying the frequency bandwidth of waves

As discussed in Section 3.1.3, very short waves pose problems for ships relying on the measured vessel responses to infer important wave characteristics. When the waves are sufficiently short, the vessel acts as a low-pass filter and distorts the waves, causing a large discrepancy between the recorded vessel motion responses and the actual waves. When this happens, we cannot trust the measured vessel responses to yield the desired wave information. Although the effect of vessel low-pass filtering is a known problem [33, 34, 41–43], no one has to our knowledge, attempted to quantify explicitly when this effect is likely to occur based on the main vessel dimensions and the wave direction. In [44], we derive an explicit formula of the frequency bandwidth of waves, assuming a box-shaped vessel. The frequency bandwidth gives an upper limit of the wave frequencies unaffected by the effect of vessel filtering. Moreover, in [45], we incorporate this frequency bandwidth directly into our methodology (Figure 4.3) to avoid any wave components potentially distorted by the vessel (an irregular sea will always contain some wave components that are naturally high in frequency). The general expression of the frequency bandwidth for a vessel with forward speed is given by Eq. (3.15).

4.2.6 Methodology: A measurement transform, an FFT, and a UKF

Based on the outlined theory of the PTPD approach, we propose a novel methodology comprising a rigid body measurement transformation, a fast Fourier transform (FFT), and an unscented Kalman filter (UKF) to estimate the desired wave quantities (see Figure 4.3). As briefly mentioned in Section 4.2.3, we use a rigid-body measurement transformation to transform the measurements obtained from a single (physical) IMU to different locations on the vessel to represent measurements from the other virtual IMUs. A minimum of two additional measurements are needed to adhere to

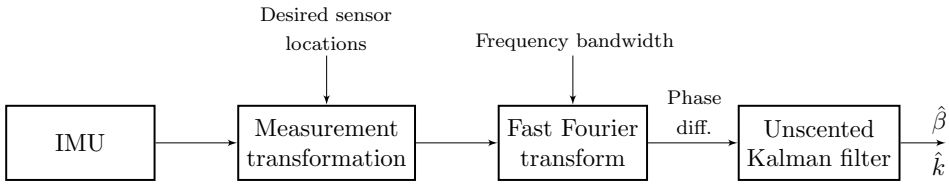

Figure 4.3: Our proposed PTPD approach comprises a rigid-body measurement transformation, a fast Fourier transform (FFT), and an unscented Kalman filter (UKF). The measurements from a single inertial measurement unit (IMU) are transformed to different locations on the vessel and supplied to the FFT. The FFT computes the phase differences within the desired frequency bandwidth, which are then given to the UKF. The UKF then estimates the wave direction and wave number, $\hat{\beta}$ and $\hat{k}$, respectively.

the minimum sensor requirements imposed by the observability analysis. After the measurements needed have been generated, an FFT is applied to obtain the phase response of each of them, from which the phase differences are estimated. The phase differences are then supplied as input to a UKF algorithm (recall that the PTPD state-space model is nonlinear), which estimates the wave direction and wave number.

The Kalman filter framework offers several benefits over the standard analytical solution presented in Eq. (4.10). Some of these benefits are: (i) the wave direction and wave number can be estimated simultaneously from the PTPD data; (ii) it is possible to include uncertainties in the PTPD measurements into the estimation procedure, which, in turn, yields an estimate of the error associated with the computed wave quantities, indicating whether they can be trusted or not; (iii) it is straightforward to incorporate and handle additional measurements from an arbitrary number of sensors.

With the methodology above, we are able to yield accurate estimates of the main wave direction and wave number/frequency in real ocean waves close to real-time, with updates given every three minutes after a initial six-minute startup period [45].

4.2.7 Model-scale and full-scale experimental validation

Previous studies [44, 75, 76] investigating the capabilities of the PTPD approach with shipboard IMUs are limited to a stationary model ship in a wave tank with regular waves. We extend experimental testing by considering a model ship with multiple IMUs advancing with forward and zero speed in a wave tank with regular and irregular waves. Motivated by the promising results from the wave basin testing, a full-scale experimental campaign was conducted outside the west coast of Norway with the research vessel Gunnerus (Figure 4.4) to assess the performance of our proposed

Figure 4.4: The research vessel Gunnerus used in the full-scale field experiments.

PTPD method in real ocean waves and different sea states [45]. The research vessel was also equipped with a marine wave radar and operated in proximity to several wave buoys, providing the necessary wave reference systems. The results from the experimental IMU data show very good agreement with the wave reference values provided by the wave radar and wave buoys, suggesting that our proposed PTPD approach is competitive with existing wave measurement technology while being cheap, easy to implement, and robust against environmental impact.

4.3 Wave height

The PTPD approach can only provide directional and frequency information about the waves. However, as previously mentioned, the wave height is a vital sea state parameter, and understanding it is paramount for evaluating the severity of ocean waves. To maintain a signal-based framework for estimating sea state parameters, we propose two additional methods in this section that can be employed alongside our PTPD method to gather information about the wave height.

4.3.1 Laser altimetry

One of the most precise approaches for acquiring wave height information involves installing a laser altimeter at the front of the vessel, which directly measures the vertical distance to the sea surface. To compensate for roll and pitch movements, a separate attitude heading reference system (AHRS) based on IMU measurements can be implemented to obtain the roll and pitch angles [77], which can be supplied to the motion correction formulas in [49, 50] to get the correct surface elevations. However, despite their accuracy, laser altimeters tend to be relatively expensive instruments and usually require expert assistance for installation.

4.3.2 Harmonic oscillator in heave and pitch

For mild and moderate waves, the wave-induced vessel responses in heave, roll, and pitch can be considered linear with the incident waves. Based on this notion, it is possible to express the vessel responses as decoupled analytical functions driven by a sinusoidal forcing term. If we assume regular harmonic waves, the general steady-state solution for heave z^n (expressed in the navigational frame $\{n\}$), roll ϕ, and pitch θ is given by [77] as

$$\begin{aligned} z^n &= \frac{F_3}{(m + A_{33}^{\mathrm{CF}}(\omega_3))Z_{m,3}\,\omega_e}\cos(\omega_e t + \epsilon_3), \\ \phi &= \frac{F_4}{(I_x^{\mathrm{CF}} + A_{44}^{\mathrm{CF}}(\omega_4))Z_{m,4}\,\omega_e}\cos(\omega_e t + \epsilon_4), \\ \theta &= \frac{F_5}{(I_y^{\mathrm{CF}} + A_{55}^{\mathrm{CF}}(\omega_5))Z_{m,5}\,\omega_e}\sin(\omega_e t + \epsilon_5), \end{aligned} \tag{4.12}$$

where F_i denotes the amplitude of the forcing terms, A_{ii}^{CF} represents the frequency-dependent added mass at the natural frequencies ω_i expressed in the center of flotation (CF), m is the mass of the vessel, I_x^{CF} and I_y^{CF} are the moments of inertia about the x and y axes, respectively, ω_e is the wave encounter frequency, and $Z_{m,i}$ and ϵ_i are the absolute impedances and phase shifts given by

$$\begin{aligned} Z_{m,3} &= \sqrt{(2\zeta_3\omega_3)^2 + \frac{1}{\omega_e^2}(\omega_3^2 - \omega_e^2)^2}, \quad \epsilon_3 = \arctan\left(\frac{2\zeta_3\omega_3\omega_3}{\omega_e^2 - \omega_3^2}\right), \\ Z_{m,4} &= \sqrt{(2\zeta_4\omega_4)^2 + \frac{1}{\omega_e^2}(\omega_4^2 - \omega_e^2)^2}, \quad \epsilon_4 = \arctan\left(\frac{2\zeta_4\omega_4\omega_4}{\omega_e^2 - \omega_4^2}\right), \\ Z_{m,5} &= \sqrt{(2\zeta_5\omega_5)^2 + \frac{1}{\omega_e^2}(\omega_5^2 - \omega_e^2)^2}, \quad \epsilon_5 = \arctan\left(\frac{2\zeta_5\omega_5\omega_5}{\omega_e^2 - \omega_5^2}\right), \end{aligned} \tag{4.13}$$

where ζ_i denotes the relative damping factors. However, despite the compactness of these expressions, they rely on frequency-dependent added mass, natural frequency, relative damping factors, and unknown driving force amplitudes, all of which are not trivial to obtain.

If we assume a monohull box-shaped vessel, the expressions (4.12) can be simplified to yield closed-form expressions for the heave, roll, and pitch responses in regular waves. The closed-form expressions are derived by [78] and only require the main vessel dimensions (length L, breadth B, draught T) together with the vessel speed U, relative wave direction β, and wave number k. The closed-form steady-state analytical expressions for heave and pitch are given by [77] as

$$\begin{aligned} z^n &= \zeta_a \frac{\omega_n^2}{Z_m w_e} F \cos(\omega_e t + \epsilon), \\ \theta &= \zeta_a \frac{\omega_n^2}{Z_m w_e} G \sin(\omega_e t + \epsilon), \end{aligned} \tag{4.14}$$

where ζ_a is the wave amplitude, and the impedance Z_m and phase shift are given by

$$Z_m = \sqrt{(2\zeta\omega_n)^2 + \frac{1}{\omega_e}(\omega_n^2 - \omega_e^2)^2}, \quad \epsilon = \arctan\left(\frac{2\zeta\omega_n\omega_e}{\omega_n^2 - \omega_e^2}\right).$$

The heave and pitch oscillators have a common relative damping ratio and natural frequency

$$\zeta = \frac{A^2}{B\alpha^3\sqrt{8k^3T}}, \quad \omega_n = \sqrt{\frac{g}{2T}},$$

where A is the sectional hydrodynamic damping

$$A = 2\sin\left(\frac{1}{2}kB\alpha^2\right)\exp\{-kT\alpha^2\},$$

where $\alpha = \omega_e/\omega$ is the ratio between the wave encounter frequency and absolute wave frequency. The forcing functions F and G are given by

$$\begin{aligned} F &= \kappa f \frac{\sin\sigma}{\sigma}, \\ G &= \kappa f \frac{6}{L\sigma}\left(\frac{\sin\sigma}{\sigma} - \cos\sigma\right), \end{aligned}$$

where $\sigma = k_e L/2$, $\kappa = \exp\{-k_e T\}$, $k_e = k|\cos\beta|$, and

$$f = \sqrt{(1 - kT)^2 + \left(\frac{A^2}{kB\alpha^3}\right)^2}.$$

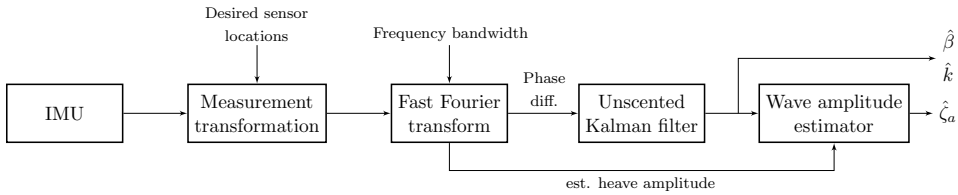

Figure 4.5: Cascaded signal-based framework for estimation of sea state parameters. The estimated parameters are the wave direction β, the wave number k, and the wave amplitude ζ_a. (Estimated quantities are indicated by a hat.)

Hence, if we measure the heave and pitch response of the vessel in question, we can obtain an estimate of the wave amplitude ζ_a by comparing the amplitude of the considered response with Eq. (4.14). The vessel pitch motion can be acquired by implementing an AHRS based on the IMU measurements, as briefly discussed in Section 4.3.1. Although the heave motion can be estimated from the specific force measurements of an IMU using a Kalman filter [79], it is more convenient to process the z-component of specific force to yield an estimate of the heave acceleration and compare this directly with the double derivative of z^n, i.e.,

$$\ddot{z}^n = -\omega_e^2 z^n = -\zeta_a \frac{\omega_n^2 \omega_e}{Z_m} F \cos(\omega_e t + \epsilon). \tag{4.15}$$

Based on Eq. (4.15) and the processed heave acceleration from an IMU, we can implement a wave amplitude estimator in cascade with our PTPD methodology as shown in Figure 4.5. The amplitude $\omega_n^2 \omega_e F / Z_m$ is computed using the estimated wave direction, wave number, and wave encounter frequency. The estimated amplitude of the heave acceleration is then divided by the latter result to obtain an estimate of the wave amplitude ζ_a. It is worth emphasizing that the signal-based framework illustrated in Figure 4.5 is also applicable to long-crested irregular waves as the FFT will extract a single sinusoid corresponding to the most dominant wave component within the specified frequency bandwidth.

Compared to using laser distance altimeters, the proposed wave amplitude estimation method is simple, cheap, and requires no additional hardware (all wave quantities are estimated from a single IMU). However, the proposed method is only theoretically valid for mild to moderate wave conditions and assumes a box-shaped vessel, implying that the estimation results will generally be less accurate than those obtained by direct measurement of the sea surface.

4.4 Summary and future recommendations

In this doctoral thesis, a novel and relatively unexplored signal-based approach for estimating the sea state from ships has been investigated. The approach considers the phase-time-path delays between an array of shipboard IMUs to determine the directionality and frequency characteristics of waves. As demonstrated, the proposed method is cost-effective and can be easily implemented on any vessel without ship RAOs, thereby avoiding many challenges associated with current model-based and signal-based approaches.

The potential capabilities of the PTPD approach were rigorously investigated in this thesis. Firstly, it was shown that the PTPD concept can effectively model sensor delays on a rigid body, given that the sensors are sufficiently close and the waves sufficiently long. Secondly, a novel PTPD model was derived for shipboard sensors, accounting for forward vessel speed. By conducting observability analysis on this model, it was shown that a minimum of three noncollinear arranged IMUs enables the wave direction and wave number/period to be uniquely determined. These results also imply that the wave period can be exactly identified in following seas, thereby resolving the 1-to-3 mapping ambiguity between encounter and absolute frequency domains. Moreover, it was demonstrated that the minimum sensor requirements could be relaxed to a single IMU by utilizing a rigid-body measurement transformation, significantly increasing the practical feasibility of the proposed method. Finally, the PTPD method and underlying theory were validated using IMU data from model-scale and full-scale field experiments involving a vessel at zero and forward speeds in various sea states.

While the PTPD method has shown great promise, several aspects still merit further investigation. As outlined in the accompanying papers, some of these future recommendations include:

- **Wave height estimation:** Although the proposed PTPD method can produce accurate estimates of the wave direction and wave number/period, it does not provide any information about the wave height, an essential sea state parameter. To preserve a signal-based framework that is cost-effective and requires minimal hardware, a simple wave amplitude estimation approach based on monohull box-shaped vessels was proposed in Section 4.3.2. However, due to limited time, it was not possible to test the performance of this approach.

- **More forward speed testing in real ocean waves:** In our full-scale field experiments with the research vessel Gunnerus, the forward speed trials were abruptly ended due to ship operational reasons. Therefore, we could not assess

the performance of our proposed method with forward speed in real waves for other boat headings except head sea. It would be interesting to confirm the validity of the approach for other wave angles in real seas, especially following sea, where the 1-to-3 mapping problem between the encounter and absolute frequency domains generally persists.

- **Investigation of other methods to improve real-time performance:** One of the main drawbacks of our PTPD method is that it relies on an FFT for the phase difference estimation. The FFT introduces a trade-off between real-time performance and accuracy, both of which are crucial for practical feasibility. This trade-off arises because the FFT requires windowed data segments as input. In order to enhance the practical utility of our method, it is recommended that future studies explore alternative procedures to the FFT that are less restrictive in this trade-off. Two promising approaches that warrant closer examination are the Hilbert-Huang transform (HHT) and a real-time phase difference tracking filter [80]. The HHT approach can provide instantaneous frequency and phase difference information for non-stationary data, while the latter approach yields the same information in real-time but relies on a single sinusoid.

- **Extending the PTPD framework to work in short-crested environments:** The primary wave environments studied in this doctoral thesis have been long-crested regular and irregular waves. It is important to note that the PTPD method can be extended to work in more short-crested wave environments comprising multiple modes by recursively applying the method to each modal frequency. The identification of modal frequencies can be achieved through various peak detection algorithms, such as those based on wavelet analysis [81].

Part II

Publications

A Online wave direction and wave number estimation from surface vessel motions using distributed inertial measurement arrays and phase-time-path-differences

Johann A. Dirdal, Roger Skjetne, Jan Roháč, and Thor I. Fossen. "Online wave direction and wave number estimation from surface vessel motions using distributed inertial measurement arrays and phase-time-path-differences". *Ocean Engineering* 249 (2022). DOI: 10.1016/j.oceaneng.2022.110760

Ocean Engineering 249 (2022) 110760

Contents lists available at ScienceDirect

Ocean Engineering

journal homepage: www.elsevier.com/locate/oceaneng

Online wave direction and wave number estimation from surface vessel motions using distributed inertial measurement arrays and phase-time-path-differences

Johann A. Dirdal [a,*], Roger Skjetne [b], Jan Roháč [c], Thor I. Fossen [a]

[a] Department of Engineering Cybernetics, Norwegian University of Science and Technology (NTNU), NO-7491, Trondheim, Norway
[b] Department of Marine Technology, Norwegian University of Science and Technology (NTNU), NO-7491, Trondheim, Norway
[c] Dept. of Measurement, Faculty of Electrical Engineering, Czech Technical University in Prague, Prague, Czech Republic

ARTICLE INFO

Keywords:
Kalman filter
Shipboard wave estimation
IMU
Phase-time-path-difference
Marine cybernetics

ABSTRACT

A common approach for finding the direction of ocean waves is to use the phase-time-path-differences (PTPDs) between a static array of various types of sensors mounted on either the sea surface or seabed. However, some practical drawbacks of such arrays are that they tend to be expensive, difficult to install, and fixed in location. We show that the PTPD approach can be generalized to a portable *shipboard* array of spatially distributed sensors rendering it more practical. In this respect, we derive a nonlinear PTPD model for shipboard sensor arrays and prove that the wave direction *and* wave number can be resolved from a minimum of three noncollinear sensors using observability analysis. Moreover, based on our PTPD model, we propose an unscented Kalman filter algorithm for online estimation of the wave direction and wave number, which offers a convenient framework for adding multiple measurements and incorporating uncertainties. Our experimental results from model basin testing with a model ship equipped with several inertial measurement units (IMUs) confirm that the wave direction and wave number can be estimated from the wave-induced motions of a surface vessel with a minimum of three noncollinear IMUs. In this study, we consider parameter estimation for regular waves and assume a dynamically positioned surface vessel with small roll and pitch angles.

1. Introduction

The physical separation distance between two local sensors embedded on the sea surface introduces a delay between the recorded waves passing through them. This delay manifests itself as either a phase, time, or path difference (PTPD) between the wave signals recorded in each sensor. A common technique for finding the direction of ocean waves is to use the PTPDs between the recorded wave signals from several such sensors (e.g., pressure transducers, wave staffs, wave probes, lasers, echo sounders, current meters) mounted on either the sea surface or seabed. This configuration of sensors in the ocean is generally called a wave array, and several works have been reported analyzing the capabilities of such arrays to resolve the wave direction (Esteva, 1976, 1977; Fernandes et al., 1988, 2000; Draycott et al., 2015, 2016, 2018; Luo et al., 2020). However, some important practical drawbacks of wave arrays are that they tend to be expensive, difficult to install, and fixed in location with little flexibility to changes in the design after installation.

Shipboard arrays, on the other hand, are more practical, offering a portable platform that is generally not location restricted and considerably more flexible when it comes to making changes to the installation. Furthermore, shipboard arrays can be used for wave estimation without ship information since the PTPD approach is inherently signal-based (i.e., estimation is done directly from sensor measurements). This useful feature distinguishes the PTPD approach from other signal-based methods using machine learning (Mak and Düz, 2019; Duz et al., 2019), which require ship-specific datasets, thus limiting its generalization to other vessels. The PTPD approach also differs from shipboard model-based methods, which are based on the wave buoy analogy (Waals et al., 2002; Tannuri et al., 2003; Nielsen, 2006; Pascoal and Guedes Soares, 2009; Nielsen, 2017; Brodtkorb et al., 2018) and use sensor measurements together with response amplitude operators (RAOs). RAOs are ship-dependent transfer functions that enable the estimation of the amplitude and direction of waves. However, without ship information, the wave amplitude cannot be estimated in the PTPD

* Corresponding author.
E-mail addresses: johann.a.dirdal@ntnu.no (J.A. Dirdal), roger.skjetne@ntnu.no (R. Skjetne), xrohac@fel.cvut.cz (J. Roháč), thor.fossen@ntnu.no (T.I. Fossen).

https://doi.org/10.1016/j.oceaneng.2022.110760
Received 6 May 2021; Received in revised form 31 January 2022; Accepted 1 February 2022
Available online 25 February 2022

approach with shipboard arrays. Moreover, to our knowledge, only a few studies have considered using a shipboard array of sensors for wave estimation (Fu et al., 2011; Udjus, 2017; Heyn et al., 2017), and these studies only consider the wave direction, although it is theoretically possible to obtain the wave number from the same PTPD data (Donelan et al., 1996; Fernandes et al., 2001).

A prerequisite for the success of both shipboard and standard wave arrays is accurate measurements of the PTPDs. The PTPD is susceptible to several sources of error such as sensor noise, sensor imperfections (e.g., nonlinear sensitivity character and non-orthogonality and misalignment character between the inner sensitive axes), inexact sensor locations and alignment when installed, and, most prominently, the sensor sampling rate. Although some of the literature mentioned above has shown awareness of some of these errors, only a few works have attempted a formal analysis investigating their quantitative impact (Pascal et al., 2009; Pascal and Bryden, 2011). However, those analyzes are mainly restricted to sensor positioning errors with little account taken for the other abovementioned sources. Additionally, despite the prevalence of these errors, there currently does not seem to exist a method indicating the expected uncertainty in the wave estimates.

One of the main goals of the present study is to promote some of the attractive features of inertial measurements units (IMUs) that make them particularly suitable as sensors for shipboard wave arrays. IMUs may add more design flexibility and PTPD accuracy since they are small, lightweight, cheap, easy to install, and have high sampling rates. Despite its attractive features, only a few works have, to our knowledge, considered using shipboard IMU arrays for wave direction estimation (Udjus, 2017; Heyn et al., 2017). In the latter, the authors mount multiple IMUs along the hull of a model-ship and use the PTPD from estimated heave accelerations to determine the direction of incoming harmonic waves. However, it is not clear from the previous study how many IMUs are needed, how far they should be separated, or how they should be arranged to attain reliable estimates of the wave direction.

In this paper, we extend earlier results by the following contributions: First, we derive a nonlinear PTPD model for surface vessels and prove using observability analysis that the wave number can, in addition to the wave direction, also be resolved from a minimum of three noncollinear sensors measuring regular harmonic waves, assuming a dynamically positioned surface vessel with small roll and pitch angles. Second, we propose an unscented Kalman filter (UKF) algorithm for online estimation of the wave direction and wave number. Third, we offer an extended error analysis discussing and quantifying several sources of error associated with shipboard arrays. Some of these errors are then reflected in the error covariance of the UKF, which gives an estimate of the uncertainty to be expected in the computed wave estimates. To our knowledge, we are the first to offer this type of error analysis and propose a method capable of yielding uncertainties in the wave estimates. Fourth, we highlight some important practical considerations regarding the number, separation, and arrangement of sensors from traditional wave arrays that should also be considered when designing shipboard arrays. Finally, the estimation results from several wave tank experiments considering regular waves and a model ship equipped with several IMUs are shown. The results, in general, verify that the wave direction and wave number can be estimated from a minimum of three IMUs.

2. Methodology

It takes time for a wave to travel from one location to another. This travel time induces a phase-time-path-difference (PTPD) between the wave elevation signals recorded at each (sensor) location, which, in turn, can be used to uniquely determine the wave direction and wave number. In this section, we derive a kinematic PTPD model for surface vessels and prove that the relative wave direction and wave number can be resolved uniquely from a minimum of three noncollinear arranged sensors, assuming regular harmonic waves and small roll and pitch angles. The small-angle assumption, which we deem appropriate for roll and pitch angles up to 2°, represents a first step in the research on wave estimation from shipboard sensor arrays utilizing the PTPD concept.

2.1. A phase-time-path-difference model for surface vessels

The PTPD between two signals recorded at two spatially separated locations on a surface vessel can be modeled by considering the distance a wave must travel to get from one sensor to another. The general scenario is depicted in Fig. 1: A dynamically positioned vessel is being struck by long-crested waves that must travel a distance d_{12} in the tangent plane $\{w\}$ to get from sensor $\{s_2\}$ to $\{s_1\}$, which, in turn, creates a delay between the signals in these sensors. The delay, represented by the distance or path difference d_{12}, is time-varying because of the wave-induced vessel roll and pitch motions (the distance between the sensors in the tangent plane $\{w\}$ changes as the vessel begins to tilt due to the wave passing through it; see Fig. 1b) and can be expressed mathematically by transforming the body-fixed position vector $\vec{p}_{s_1s_2}$ to the tangent plane and extracting the x-component of this vector, i.e.,

$$\mathbf{p}^{w}_{s_1s_2} = \mathbf{R}^{w}_{s_1}\mathbf{p}^{s_1}_{s_1s_2}, \tag{1}$$

where $\mathbf{p}^{w}_{s_1s_2}$ is the position of $\{s_2\}$ relative $\{s_1\}$ expressed in $\{w\}$, $\mathbf{p}^{s_1}_{s_1s_2}$ is the coordinate vector of $\{s_2\}$ relative $\{s_1\}$ expressed in $\{s_1\}$, and $\mathbf{R}^{w}_{s_1}$ is a rotation matrix representing a coordinate transformation from $\{s_1\}$ to $\{w\}$. The matrix $\mathbf{R}^{w}_{s_1}$ can be described by a sequence of principal rotations based on the zyx-convention (Fossen, 2021) with angles β, π, θ, and ϕ (Fig. 2). Following this convention, the resulting transform can then be expressed as

$$\mathbf{R}^{w}_{s_1} = \mathbf{R}_{z,\beta}\mathbf{R}_{x,\pi}\mathbf{R}_{y,\theta}\mathbf{R}_{x,\phi} = \begin{bmatrix} c\beta c\theta & c\beta s\theta s\phi + s\beta c\phi & c\beta s\theta c\phi - s\beta s\phi \\ s\beta c\theta & s\beta s\theta s\phi - c\beta c\phi & s\beta s\theta c\phi + c\beta s\phi \\ s\theta & -c\theta s\phi & -c\theta c\phi \end{bmatrix},$$

where $s\,\cdot = \sin(\cdot)$ and $c\,\cdot = \cos(\cdot)$. Using the rotational transform above, an expression for the position vector $\mathbf{p}^{w}_{s_1s_2}$ can be obtained by carrying out the multiplication given by (1), which yields

$$\mathbf{p}^{w}_{s_1s_2} = \begin{bmatrix} R_{12}\left(c\beta c\theta c\alpha_{12} + c\beta s\theta s\phi s\alpha_{12} + s\beta c\phi s\alpha_{12}\right) + z_{12}(c\beta s\theta c\phi - s\beta s\phi) \\ * \\ * \end{bmatrix}, \tag{2}$$

where the body-fixed coordinate vector $\mathbf{p}^{s_1}_{s_1s_2}$ is given in terms of cylindrical coordinates $(R_{12}, \alpha_{12}, z_{12})$ which, respectively, represent the radial distance, angular displacement in the horizontal plane, and sensor height separation of $\{s_2\}$ with respect to $\{s_1\}$. The path difference d_{12} is simply the x-component of (2) and the time it takes the wave to travel from $\{s_2\}$ to $\{s_1\}$ is given by

$$\begin{aligned} t_{12} &= \frac{d_{12}}{c} \\ &= \frac{R_{12}\left(c\beta c\theta c\alpha_{12} + c\beta s\theta s\phi s\alpha_{12} + s\beta c\phi s\alpha_{12}\right) + z_{12}(c\beta s\theta c\phi - s\beta s\phi)}{c}, \end{aligned} \tag{3}$$

where t_{12} represents the time difference between the recorded signals in $\{s_1\}$ and $\{s_2\}$. The wave celerity c (also known as the phase velocity) is given in terms of the wave frequency ω and wave number k by $c = \omega/k$. Using this fact, the time difference (3) can instead be expressed as a phase difference in the case of a harmonic wave, i.e.,

$$\Theta_{12} = kR_{12}\left(c\beta c\theta c\alpha_{12} + c\beta s\theta s\phi s\alpha_{12} + s\beta c\phi s\alpha_{12}\right) + kz_{12}(c\beta s\theta c\phi - s\beta s\phi), \tag{4}$$

where $\Theta_{12} = \omega t_{12}$ is the time-varying phase difference between $\{s_1\}$ and $\{s_2\}$ as a function of k, β, ϕ, and θ. For small ϕ and θ angles (characteristic of large vessels in moderate sea states), (4) reduces to the following expression

$$\Theta_{12} \approx kR_{12}\cos(\beta - \alpha_{12}), \tag{5}$$

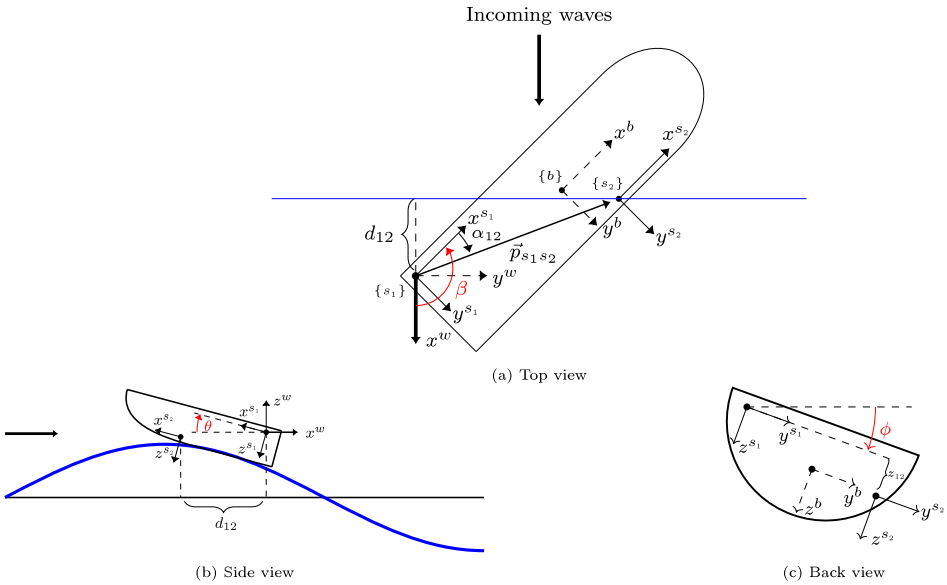

Fig. 1. Snapshots showing three independent situations of a dynamically positioned surface vessel being struck by long-crested waves. The induced rigid body vessel motions are recorded by two spatially distributed sensors denoted $\{s_1\}$ and $\{s_2\}$ with sensor axes $(x^{s_1}, y^{s_1}, z^{s_1})$ and $(x^{s_2}, y^{s_2}, z^{s_2})$ aligned with the body frame $\{b\}$. The position of $\{s_2\}$ relative to $\{s_1\}$ is denoted by the body-fixed vector $\vec{p}_{s_1 s_2}$ and angle α_{12}. The tangent plane $\{w\}$ moves up and down with the vessel and is defined by its x^w, y^w, and z^w axes with the origin coinciding with the chosen reference sensor (here $\{s_1\}$). The x^w axis is defined such that it points in the same direction as the propagating waves, the z^w axis points upwards, and the y^w axis completes the right-handed coordinate system. The distance d_{12} between $\{s_1\}$ and $\{s_2\}$ causes a delay in the recorded signals which depends on the roll (ϕ), pitch (θ), and relative wave direction (β) angles. The relative wave direction β is defined as the counterclockwise angle from x^w to x^{s_1} projected onto the tangent plane $\{w\}$. Starboard incident waves are defined by $\beta \in (-180, 0]°$, whereas port incident waves are defined by $\beta \in (0, 180]°$. When $\beta = 0°$, the waves hit the stern first as the boat heading axis (x^{s_1}) is oriented in the same direction as the waves (x^w).

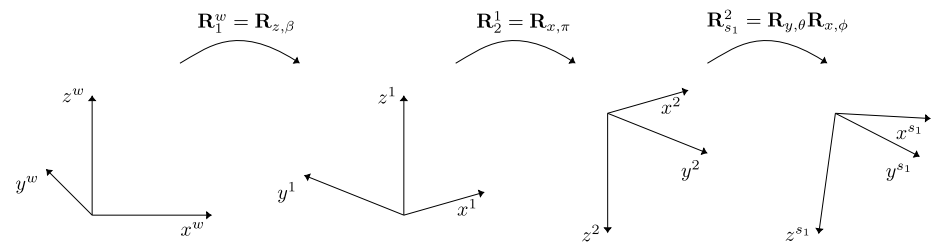

Fig. 2. The rotation matrix from $\{s_1\}$ to $\{w\}$ can be described by a combination of two rotation sequences based on the zyx-convention: A sequence from tangent plane $\{w\}$ to intermediate tangent plane $\{2\}$ (with z-axis pointing downwards) and a sequence from $\{2\}$ to $\{s_1\}$. The principal rotations are given in terms of angles β, π, θ, and ϕ.

which is the standard (constant) phase difference equation commonly found in the literature on wave arrays using the PTPD concept and is the main research focus of this article. Several experiments were performed verifying the correctness of the small-angle assumption. In all experiments considered, the vessel roll and pitch angles were within the range ±2° (Section 5.2), and the height separation between the lowest and highest sensor was measured to be around 16 cm. Together, these values justify the transition from (4) to (5), and our experimental results (Section 5.5.1) also confirm that the small-angle model worked well for those values. However, it is presently unclear how far the roll and pitch angles can be extended before the small-angle assumption is violated.

2.2. Analytical solution

For small roll and pitch angles, an analytical solution of the wave direction can be found by adding an additional sensor $\{s_3\}$ to the surface vessel in Fig. 1, which yields an additional phase difference measurement, i.e.,

$$\Theta_{13} \approx k R_{13} \cos(\beta - \alpha_{13}). \tag{6}$$

Expanding (5) and (6), and grouping the measurements into a 2×1 matrix, yields the system

$$\begin{bmatrix} \Theta_{12} \\ \Theta_{13} \end{bmatrix} = k \begin{bmatrix} R_{12}\cos\alpha_{12} & R_{12}\sin\alpha_{12} \\ R_{13}\cos\alpha_{13} & R_{13}\sin\alpha_{13} \end{bmatrix} \begin{bmatrix} \cos\beta \\ \sin\beta \end{bmatrix}.$$

The wave direction can be isolated by applying the 2×2 inverse to the right-hand side above, thus leaving us with

$$\begin{bmatrix} \cos\beta \\ \sin\beta \end{bmatrix} = \frac{1}{kR_{12}R_{13}\sin(\alpha_{13} - \alpha_{12})} \begin{bmatrix} (R_{13}\sin\alpha_{13})\Theta_{12} - (R_{12}\sin\alpha_{12})\Theta_{13} \\ (R_{12}\cos\alpha_{12})\Theta_{13} - (R_{13}\cos\alpha_{13})\Theta_{12} \end{bmatrix}.$$

Hence, the analytical expression of the wave direction becomes

$$\beta = \arctan\left(\frac{[(R_{12}\cos\alpha_{12})\Theta_{13} - (R_{13}\cos\alpha_{13})\Theta_{12}]/\mathrm{sgn}(D)}{[(R_{13}\sin\alpha_{13})\Theta_{12} - (R_{12}\sin\alpha_{12})\Theta_{13}]/\mathrm{sgn}(D)} \right), \tag{7}$$

where

$$D = kR_{12}R_{13}\sin(\alpha_{13} - \alpha_{12}). \tag{8}$$

The above analysis shows that the wave direction can be uniquely determined from (7) provided that (i) a minimum of three sensors are used, and (ii) they are arranged in a noncollinear configuration on the vessel—thus ensuring that (8) is non-zero.

Eq. (7) is arguably the de facto standard for computing the mean wave direction with arrays (Esteva, 1976, 1977; Fernandes et al., 1988, 2000; Draycott et al., 2015, 2016, 2018; Luo et al., 2020). However, this approach has some important drawbacks that render it unsuitable for applications requiring real-time or online estimates of the wave direction. In particular, the analytical solution (7) neither provides a measure of uncertainty in the wave direction estimates (despite the phase difference and sensor locations being subject to error) nor an estimate of the wave number, although, as we shall see, can be obtained from the same set of measurements. Also, the analytical solution does not offer a convenient framework for adding additional measurements. The Kalman filter framework will alleviate all these issues.

2.3. Kalman filter state–space model

Let R_{ij} and α_{ij} be the polar coordinates of sensor $\{s_j\}$ (slave) relative to sensor $\{s_i\}$, where $\{s_i\}$ is taken to be the chosen master/reference sensor. Using this notation, (5) and (6) can be expressed more generally as

$$\Theta_{ij} = kR_{ij}\cos(\beta - \alpha_{ij}), \tag{9}$$

where Θ_{ij} represents the phase difference between the heave signals recorded by sensors $\{s_i\}$ and $\{s_j\}$. Expanding (9) and introducing the state vector $\mathbf{x} = [x_1,\ x_2]^\top = [\beta,\ k]^\top$, the expression can be reformulated into

$$\Theta_{ij} = \begin{bmatrix} R_{ij}\cos\alpha_{ij} & R_{ij}\sin\alpha_{ij} \end{bmatrix} \begin{bmatrix} x_2\cos x_1 \\ x_2\sin x_1 \end{bmatrix}.$$

For $N \geq 3$ (number of sensors), the final Kalman filter state–space model becomes

$$\dot{\mathbf{x}} = \mathbf{0},$$
$$\mathbf{z} = \mathbf{h}(\mathbf{x}) = \underbrace{\begin{bmatrix} R_{12}\cos\alpha_{12} & R_{12}\sin\alpha_{12} \\ R_{13}\cos\alpha_{13} & R_{13}\sin\alpha_{13} \\ \vdots & \vdots \\ R_{1N}\cos\alpha_{1N} & R_{1N}\sin\alpha_{1N} \\ R_{23}\cos\alpha_{23} & R_{23}\sin\alpha_{23} \\ \vdots & \vdots \\ R_{2N}\cos\alpha_{2N} & R_{2N}\sin\alpha_{2N} \\ \vdots & \vdots \\ R_{(N-1)N}\cos\alpha_{(N-1)N} & R_{(N-1)N}\sin\alpha_{(N-1)N} \end{bmatrix}}_{\text{configuration matrix}} \begin{bmatrix} x_2\cos x_1 \\ x_2\sin x_1 \end{bmatrix}, \tag{10}$$

where $\mathbf{z} = [\Theta_{12},\ \Theta_{13},\ldots,\ \Theta_{1N},\ \Theta_{23},\ \ldots,\Theta_{2N},\ \ldots,\Theta_{(N-1)N}]^\top$. The dimension of $\mathbf{z}$ is given by the maximum number of distinct phase difference measurements associated with N, which can be calculated using (23).

2.4. Observability results

It was shown in Section 2.2 that a minimum of three noncollinear arranged sensors is needed to determine the wave direction uniquely. The analysis, however, does not show that the wave number may also be resolved from the same set of measurements, which—based on the reported literature (Donelan et al., 1996; Fernandes et al., 2001)—seems to be a less known fact. This interesting fact can be proved by showing that the state–space model in (10) is observable for a minimum of two distinct PTPD measurements (three noncollinear sensors). The results from the observability analysis (see Appendix A) are summarized in the following theorem:

Theorem 1 (*Minimum Sensor Configuration*). *Consider a single harmonic wave with wave number k and relative wave direction β (Fig. 1), then k and β can be uniquely determined from a dynamically positioned surface vessel with small roll and pitch angles using a minimum of three noncollinear spatially distributed sensors measuring the vessel's heave motion.*

Proof. See Appendix A.

3. Estimation algorithm and error analysis

The PTPD state–space model (10) is by nature nonlinear, indicating that nonlinear estimation techniques should be considered to find the wave direction and wave number. It is worth emphasizing that the wave number should be positive, which introduces a constraint on the state estimate. In this section, we look at two different methods for achieving the above goals, namely, the extended Kalman filter (EKF) and unscented Kalman filter (UKF) algorithms (Brown and Hwang, 1997; Julier and Uhlmann, 2004). Although the EKF is more renowned and conceptually easier to grasp, the UKF has advantages for highly nonlinear systems containing state constraints.

3.1. Extended vs. unscented Kalman filter

When a state–space representation contains nonlinearities in either the process model, measurement model, or both, the EKF algorithm has proven to be a viable option, capable of providing reliable state estimates for a wide range of applications. However, despite its success, the EKF suffers from some serious limitations.

In short, the EKF algorithm linearizes all nonlinear transformations related to the noise covariance progressions and inserts them in place of the linear transformations of a regular Kalman filter. While this estimation strategy has proven successful for many systems, in particular those whose dynamics can be considered almost linear, the EKF has not demonstrated the same level of success for highly nonlinear systems (Julier and Uhlmann, 2004). The reason for this is mainly due to its inherent use of linearization, which loses accuracy as the transformations become increasingly nonlinear.

When constraints are imposed on states, the state estimates from an EKF do not always converge to the true values (Kandepu et al., 2008). The standard way of handling constraints in the EKF is known as "clipping" (Haseltine and Rawlings, 2005), which involves projecting the estimates onto the boundary of the feasible region whenever they are outside it. The drawback of this strategy is that the constraint information has no effect on the covariances of the EKF estimates.

The UKF overcomes the aforementioned limitations by eliminating the need for linearization altogether, while simultaneously updating the covariances to account for constraints. In short, the UKF samples a fixed number of points around the mean (called *sigma* points) and propagates these points through the associated nonlinear transforms to obtain new sample points—from which new estimates of the mean and covariance are obtained. If the sampled points are outside the feasible region, they are projected onto the boundary, similar to "clipping", except that the updated covariance is based on these points instead.

3.2. UKF algorithm

The UKF may be applied to systems of the form

$$\begin{aligned} \mathbf{x}_{k+1} &= \mathbf{f}(\mathbf{x}_k) + \mathbf{w}_k, \quad \mathbf{w}_k \sim \mathcal{N}(\mathbf{0},\ \mathbf{Q}_k), \\ \mathbf{z}_k &= \mathbf{h}(\mathbf{x}_k) + \mathbf{v}_k, \quad \mathbf{v}_k \sim \mathcal{N}(\mathbf{0},\ \mathbf{R}_k), \end{aligned} \tag{11}$$

where $\mathbf{f}$ and $\mathbf{h}$ represent nonlinear vector fields, $\mathbf{x}_k := \mathbf{x}(kT_s)$ and $\mathbf{z}_k := \mathbf{z}(kT_s)$ constitute the sampled state and measurement vectors

with T_s and k being the respective sampling time and number (not to be confused with the wave number), and $\mathbf{w}_k$ and $\mathbf{v}_k$ represent white Gaussian process and measurement noise with covariance $\mathbf{Q}_k$ and $\mathbf{R}_k$, respectively. Discretizing (10) and comparing it with (11) shows that the former fits the required model form, with $\mathbf{f}(\mathbf{x}_k) = \mathbf{x}_k$ and $\mathbf{v}_k$ and $\mathbf{w}_k$ discussed in Sections 3.3 and 3.4.

Our UKF wave estimation algorithm is outlined in Algorithm 1; for relevant background material on the UKF and constraint handling, we refer to Brown and Hwang (1997), Julier and Uhlmann (2004), Kandepu et al. (2008) and Simon (2010) and references therein.

The UKF uses a deterministic sampling scheme to select its sample or sigma points, as it is commonly called. In this paper, we have chosen the following set of sigma points

$$X_k^{(i)} = \begin{cases} \hat{\mathbf{x}}_k^-, & i = 0 \\ \hat{\mathbf{x}}_k^- + \sqrt{(L+\lambda)\hat{\mathbf{P}}_k^-}, & i = 1, \dots, L \\ \hat{\mathbf{x}}_k^- - \sqrt{(L+\lambda)\hat{\mathbf{P}}_k^-}, & i = L+1, \dots, 2L \end{cases} \tag{12}$$

where

$\lambda = \alpha^2(L+\kappa) - L$

L = dimension of state $\mathbf{x}_k$

α = spread of samples about the mean

κ = scaling factor

If the sigma points are outside the feasible region, they are projected onto the boundary using the projection

$$P(\hat{x}_2) = \begin{cases} \epsilon, & \hat{x}_2 < \epsilon \\ \hat{x}_2, & \text{otherwise} \end{cases} \tag{13}$$

where $\hat{x}_2$ is the wave number estimate and ϵ is a small positive number representing the boundary of the feasible region. The sigma points are then propagated through the nonlinear transform (10) to yield a new cloud of transformed points. The statistics of these points are then computed by weighting them together using the following sets of weights

$$W_\mu^{(0)} = \frac{\lambda}{\lambda + L}, \; W_\mu^{(0<i\leq 2N)} = \frac{1}{2(\lambda + L)}, \tag{14}$$

$$W_\sigma^{(0)} = W_\mu^{(0)} + 1 - \alpha^2 + \gamma, \; W_\sigma^{(0<i\leq 2L)} = \frac{1}{2(\lambda + L)}. \tag{15}$$

Algorithm 1 Wave algorithm

procedure UKF($\hat{\mathbf{x}}_k^-, \hat{\mathbf{P}}_k^-, \mathbf{z}_k$)

$X_k^{(i)} \leftarrow \text{Sigma}(\hat{\mathbf{x}}_k^-, \hat{\mathbf{P}}_k^-)$ ▷ Compute sigma points using (12)

$X_c^{(i)} \leftarrow P(X_k^{(i)})$ ▷ Project sigma points using (13)

$\hat{\mathbf{x}}_k^- \leftarrow \sum_{i=0}^{2L} W_\mu^{(i)} X_c^{(i)}$ ▷ Compute the apriori state estimate with (14)

$\hat{\mathbf{P}}_k^- \leftarrow \{\sum_{i=0}^{2L} W_\sigma^{(i)} (X_c^{(i)} - \hat{\mathbf{x}}_k^-)(X_c^{(i)} - \hat{\mathbf{x}}_k^-)^\top\} + \mathbf{Q}_k$ ▷ Compute the apriori error covariance with (15)

$Z_k^{(i)} \leftarrow \mathbf{h}(X_c^{(i)})$ ▷ Propagation of sigma points using (10)

$\hat{\mathbf{z}}_k^- \leftarrow \sum_{i=0}^{2L} W_\mu^{(i)} Z_k^{(i)}$ ▷ Predicted measurement

$\hat{\mathbf{S}}_k \leftarrow \{\sum_{i=0}^{2L} W_\sigma^{(i)} (Z_k^{(i)} - \hat{\mathbf{z}}_k^-)(Z_k^{(i)} - \hat{\mathbf{z}}_k^-)^\top\} + \mathbf{R}_k$ ▷ Compute the innovation covariance

$\hat{\mathbf{P}}_k^{\mathbf{xz}} \leftarrow \sum_{i=0}^{2L} W_\sigma^{(i)} (X_c^{(i)} - \hat{\mathbf{x}}_k^-)(Z_k^{(i)} - \hat{\mathbf{z}}_k^-)^\top$ ▷ Compute the cross-covariance

$\mathbf{K}_k \leftarrow \hat{\mathbf{P}}_k^{\mathbf{xz}} \hat{\mathbf{S}}_k^{-1}$ ▷ Compute the Kalman gain

$\hat{\mathbf{x}}_k \leftarrow \hat{\mathbf{x}}_k^- + \mathbf{K}_k(\mathbf{z}_k - \hat{\mathbf{z}}_k^-)$ ▷ Compute posterior state estimate

$\hat{\mathbf{P}}_k \leftarrow \hat{\mathbf{P}}_k^- - \mathbf{K}_k \hat{\mathbf{S}}_k \mathbf{K}_k^\top$ ▷ Compute posterior error covariance

return $\hat{\mathbf{x}}_k, \hat{\mathbf{P}}_k$

end procedure

3.3. Error analysis

Several sources of error are associated with shipboard arrays that may inhibit high-quality wave estimates from the UKF. The errors can generally be grouped as (a) errors caused by sensor imperfections and oscillatory and/or transient effects on the sensors due to structural vibrations (e.g., from the engine) and external environmental conditions, and (b) errors caused by the array construction (e.g., inexact sensor locations and alignment). These errors ultimately affect the obtained phase differences, which, in turn, are used to estimate the wave direction and wave number. It is, therefore, essential to either remove these errors or quantify the uncertainties caused by them so that we may confidently decide whether or not to rely on the wave estimates. In Sections 3.3.1 and 3.3.2 we quantify and discuss strategies for removing the errors caused by (a) and (b), respectively.

3.3.1. Sensor errors

The noise $\mathbf{v}_k$ in (11) reflects the uncertainty associated with the measurement $\mathbf{z}_k$, which, in this case, is the measured phase difference Θ_{ij}. The error in Θ_{ij} can be linked to three primary sources: (i) high-frequency sensor noise and oscillatory and transient effects caused by structural vibrations and/or external environmental conditions, (ii) deterministic sensor imperfections such as axis misalignment, nonlinear sensitivity character, and stochastic bias behavior, and (iii) insufficient sensor sampling rate. Although temporal aliasing due to (iii) may also be a concern, the effect is usually minimized by the high inner sampling rates (typically ≥ 1 kHz) employed in today's IMU technology.

The high-frequency noise content related to (i) may be alleviated by applying a digital lowpass filter, which attenuates noise residing outside the predefined passband (in this application, the cut-off frequency was selected above the maximal wave frequency).

The effects of (ii) will generally manifest themselves as a bias in the specific force measurements of the accelerometers, further impacting the computed phase difference. One possible strategy to resolve the axis misalignment offset is to compare the measured specific force with the gravitational vector during some time when the average linear acceleration of the vessel is known to be zero, and the vessel is assumed to be well balanced (i.e., $\phi = \theta = 0$). This approach will work when the sensor biases can be considered negligible. Assuming that the above assumptions hold, the angle offset in roll and pitch between the sensor and body frames can then be estimated through

$$\delta\phi \approx \arctan\left(\frac{f_y}{f_z}\right), \quad \delta\theta \approx \arctan\left(\frac{f_x}{\sqrt{f_y^2 + f_z^2}}\right),$$

where $\delta\phi$ and $\delta\theta$ are the respective roll and pitch offset angles, and (f_x, f_y, f_z) denote the specific force measurements from the accelerometers (Fossen, 2021). The heading angle offset can, in general, not be determined from accelerometers alone, but may be estimated from a magnetometer. The error related to the nonlinear sensitivity behavior is deemed minimal due to the high-quality sensor technology being employed.

The error from (iii) can be quantified by examining in detail how the phase difference is defined and how it is actually measured. The phase difference between $\{s_i\}$ (master) and $\{s_j\}$ (slave) is defined through the relationship

$$\Theta_{ij} = \omega t_{ij}, \tag{16}$$

where ω is the frequency of the wave and t_{ij} is the time difference (i.e., the time it takes the wave to travel from $\{s_j\}$ to $\{s_i\}$). The time difference is estimated by measuring the lag (number of samples) D_{ij}

between the recorded signals and multiplying it by the sampling time T_s, i.e., $\hat{t}_{ij} = T_s D_{ij}$. Assuming that the effects from (i) and (ii) are handled and do not affect D_{ij}, the error resulting from the sampling time T_s can be bounded by

$$|t_{ij} - \hat{t}_{ij}| \leq t_{\max} := \frac{T_s(D_{ij}+1) - T_s D_{ij}}{2} = \frac{T_s}{2}.$$

The division by two is a property of the algorithm[1] we use to obtain D_{ij}. If we assume further that ω is known precisely, then the maximum phase error due to T_s can be quantified as

$$|\Theta_{ij} - \hat{\Theta}_{ij}| \leq \Theta_{\max} := \frac{\omega T_s}{2}. \tag{17}$$

The phase difference error bound to (17) implies that the *true* phase difference can be located within the interval $[-\omega T_s/2, \omega T_s/2]$ of the corresponding phase estimate. Based on this knowledge, it is possible to use a uniform distribution to model the worst-case phase difference error. However, when the error character can be considered rather similar to jitter, a Gaussian distribution is more appropriate over that specific interval and can be adopted with the same variance as the uniform distribution. The variance is computed as

$$\sigma^2_{\Theta_{\max}} = \frac{1}{12}\left(\frac{\omega T_s}{2} - \left(-\frac{\omega T_s}{2}\right)\right)^2 = \frac{1}{12}\omega^2 T_s^2, \tag{18}$$

and, hence, the measurement covariance $\mathbf{R}_k$ can finally be quantified as

$$\mathbf{R}_k = \sigma^2_{\Theta_{\max}} I_P,$$

where I_P is a $P \times P$ identity matrix with P denoting the number of distinct phase difference measurements.

3.3.2. Sensor positioning errors

In general, the exact position of each shipboard sensor will be subject to uncertainty. We can analyze how this uncertainty influences the predicted phase difference (9) by carrying out the analysis in Section 2.1 again, but with errors associated with each sensor location.

Consider again the vessel in Fig. 1 and let (x_{12}, y_{12}, z_{12}) denote the *exact* coordinate location of sensor $\{s_2\}$ (slave) with respect to sensor $\{s_1\}$ (reference/master), which forms the origin of the local frame with axes perfectly aligned with the vessel body frame. Further, if we define $(\hat{x}_{12}, \hat{y}_{12}, \hat{z}_{12})$ to be the corresponding *estimated* sensor location, then the coordinates of $\{s_2\}$ with respect to $\{s_1\}$ can be written as

$$x_{12} = \hat{x}_{12} + \epsilon_x, \quad y_{12} = \hat{y}_{12} + \epsilon_y, \quad z_{12} = \hat{z}_{12} + \epsilon_z,$$

where we have introduced Gaussian distributed errors ϵ_x, ϵ_y, ϵ_z with zero mean and variance σ^2 (representative of uncertainties of Type A, whereas Type B is considered negligible). The relationships above can be expressed more compactly using vector notation, i.e.,

$$\mathbf{p}^{s_1}_{s_1 s_2} = \begin{bmatrix} x_{12} \\ y_{12} \\ z_{12} \end{bmatrix} = \begin{bmatrix} \hat{x}_{12} \\ \hat{y}_{12} \\ \hat{z}_{12} \end{bmatrix} + \begin{bmatrix} \epsilon_x \\ \epsilon_y \\ \epsilon_z \end{bmatrix}.$$

Following the exact same derivation as in Section 2.1, the (time-varying) phase difference equation between $\{s_1\}$ and $\{s_2\}$ with location uncertainty becomes

$$\begin{aligned}\Theta_{12} = k\big(&\hat{x}_{12}c\beta c\theta + \hat{y}_{12}(c\beta s\theta s\phi + s\beta s\phi)\big) + k\hat{z}_{12}(c\beta s\theta c\phi - s\beta s\phi) \\ &+k\big(\epsilon_x c\beta c\theta + \epsilon_y(c\beta s\theta s\phi + s\beta s\phi)\big) + k\epsilon_z(c\beta s\theta c\phi - s\beta s\phi),\end{aligned}$$

and assuming small roll and pitch angles (i.e., $\phi \approx 0$ and $\theta \approx 0$), the expression above reduces to

$$\Theta_{12} \approx k(\hat{x}_{12}\cos\beta + \hat{y}_{12}\sin\beta) + k(\epsilon_x \cos\beta + \epsilon_y \sin\beta).$$

[1] For more details see: https://se.mathworks.com/help/signal/ref/finddelay.html.

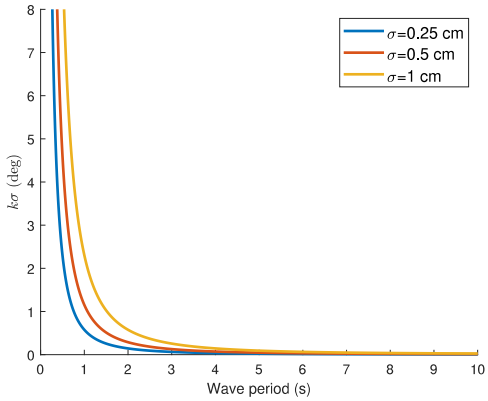

Fig. 3. Bias standard deviation of (20) vs. wave period for various σ. The wave number k is computed for the displayed wave periods using the dispersion relation (21) with constant water depth, $d = 1.5$ m. The results are almost identical for larger water depths.

If we let $\hat{\Theta}_{12} = k(\hat{x}_{12}\cos\beta + \hat{y}_{12}\sin\beta)$ be the estimated phase difference, then the phase error can be written as

$$\Theta_{12} - \hat{\Theta}_{12} \approx k(\epsilon_x \cos\beta + \epsilon_y \sin\beta). \tag{19}$$

From (19), it is clear that the location uncertainty of each sensor manifests itself as a constant bias in the estimated phase difference. In the following, we determine the noise characteristics (i.e., mean and variance) of (19) to have a better understanding of its impact on wave estimation.

If we let $b(k,\beta) = k(\epsilon_x \cos\beta + \epsilon_y \sin\beta)$ denote the state-dependent constant bias, then, when calibrated and compensated, the mean can be considered as

$$\begin{aligned}\mathbb{E}[b(k,\beta)] &= \mathbb{E}[k(\epsilon_x\cos\beta + \epsilon_y \sin\beta)] \\ &= k\cos\beta\mathbb{E}[\epsilon_x] + k\sin\beta\mathbb{E}[\epsilon_y] \\ &= 0,\end{aligned}$$

where we have utilized the Gaussian zero-mean assumption of the sensor positioning errors. Doing the same for the variance, yields

$$\begin{aligned}\mathbb{E}[b(k,\beta)^2] &= \mathbb{E}[k^2(\epsilon_x\cos\beta + \epsilon_y\sin\beta)^2] \\ &= k^2\Big(\cos^2\beta\mathbb{E}[\epsilon_x^2] + 2\sin\beta\cos\beta\mathbb{E}[\epsilon_x\epsilon_y] + \sin^2\beta\mathbb{E}[\epsilon_y^2]\Big) \\ &= k^2\sigma^2,\end{aligned}$$

where we have utilized that ϵ_x and ϵ_y are independent random variables. The noise characteristics above can be generalized to P measurements (assuming the same mean and covariance of the location error for each sensor pair), yielding the mean and covariance information

$$\begin{aligned}\mathbb{E}[\mathbf{b}(k,\beta)] &= \mathbf{0}_{P\times 1} \\ \mathbb{E}[\mathbf{b}(k,\beta)\mathbf{b}(k,\beta)^\top] &= k^2\sigma^2 I_P,\end{aligned} \tag{20}$$

where $\mathbf{b}(k,\beta) = [b_1(k,\beta), b_2(k,\beta), \ldots, b_P(k,\beta)]^\top$, $b_i(k,\beta) = k(\epsilon_{x_i}\cos\beta + \epsilon_{y_i}\sin\beta)$, ϵ_{x_i} and $\epsilon_{y_i} \sim \mathcal{N}(0,\sigma^2)$, and I_P is a $P \times P$ identity matrix.

The bias impact on wave estimation can be seen in Fig. 3, which shows that the standard deviation of the bias is inversely proportional to the wave period. This result suggests that, for sufficiently long wave periods (small frequencies), the biases may be neglected from analysis without incurring substantial errors in the phase difference estimates.

It is worth mentioning that the bias is, in general, not observable as each new sensor introduces another location error and, consequently, a new bias. This can be verified by augmenting the state–space

Table 1
A summary of the initial state estimates, covariances, and internal parameters used in the UKF.

UKF initialization	$\hat{\mathbf{x}}_0^- = [0,\ 0.05]^\mathsf{T}$ $\hat{\mathbf{P}}_0^- = \mathrm{diag}([\frac{\pi^2}{3},\ 2])$
Process and measurement covariance	$\mathbf{Q}_k = \mathbf{0}_{2\times 2}$ $\mathbf{R}_k = \left(\frac{1}{12}\omega^2 T_s^2 + k^2\sigma^2\right) I_P$
UKF parameters	$L = 2, \quad \alpha = 0.01, \quad \gamma = 2, \quad \kappa = 0$

model in (10) to include the bias as an unknown state and checking observability.

3.4. Summary

A summary of the initialization, covariance matrices, and internal parameters used in our UKF algorithm can be found in Table 1. It is worth stressing that faster convergence may be achieved by initializing the wave number to the value given by the dispersion relation, i.e.,

$$\omega^2 = kg\tanh(kd), \tag{21}$$

where g is the gravitational constant and d is the water depth. In this paper, however, we chose the initial values in Table 1 to demonstrate the validity of Theorem 1.

The initial estimated error covariance $\hat{\mathbf{P}}_0^-$ was selected by modeling the initial wave direction error as a uniform distribution over the interval $(-\pi, \pi]$ and approximating it by a Gaussian distribution with the same variance. The wave number variance was chosen heuristically but relatively large, reflecting our uncertainty in the actual value.

The process covariance $\mathbf{Q}_k$ was considered zero due to the states in the process model (10) and conditions of the experiments performed being (more or less) constant. However, this value is not universal as $\mathbf{Q}_k$ should, in general, be adapted to reflect any discrepancy between the state model and the properties of the sea environment being considered. The measurement covariance $\mathbf{R}_k$ was chosen based on our analysis in Section 3.3.1.

4. Shipboard wave array design

In this section, we highlight some important practical considerations when designing shipboard wave arrays. As we shall see, care must be exercised when selecting (a) the separation distance between each sensor, (b) the geometry of the sensor array, (c) sensor type, and (d) number of sensors. All these features ultimately contribute towards our desired end goal—the attainment of accurate estimates of the wave direction and wave number.

To facilitate analysis, we consider two different types of sensor arrays (Fig. 4). These arrays will aid us in demonstrating the key issues with some of the features mentioned above.

4.1. Barber and Doyle criterion

As pointed out by Fernandes et al. (1988, 2000), the criterion of Barber and Doyle (1956) plays a crucial role in the design and construction of wave arrays. The criterion states that the separation distance D between two wave sensors should not exceed half the wavelength λ of the wave passing through them, i.e.,

$$D < \lambda/2, \tag{22}$$

in order for the phase difference between these sensors to be resolved unambiguously. In other words, as long as (22) is satisfied, the theoretical phase difference between the sensors will be restricted to the interval $(-\pi, \pi)$, thus correctly representing the physical situation. The maximum sensor separation imposed by (22) ultimately implies that the wave direction and number cannot be resolved for a range of frequencies (Fig. 5). It is thus important to have an idea of the frequency range of the expected waves and design the separation distances accordingly using (22). For wind-generated surface gravity waves, the wave periods generally range between 0.25 and 30 s.

4.1.1. Case study

The problems associated with (22) are illustrated by considering the polygonal array in Fig. 4a and choosing a wave period for which we want to resolve the wave direction and number. If we select $T = 1.0$ s and $D = 1.33$ m as our desired wave period and separation distance, it can be seen that some of the phase differences associated with this frequency become ambiguous for certain choices of reference sensor (Fig. 6). When selecting sensor 1 as reference, the separation distance to sensor 2 and 4 exceeds the limit imposed by $T = 1.0$ s (i.e., $R_{12} = R_{14} = D = 1.33 > 0.7806$ m), whereas when sensor 3 is chosen as reference, all separation distances ($R_{31} = R_{32} = R_{34} = D' = 0.768 < 0.7806$ m) are within the boundary. Hence, if sensor 1 is naively chosen as a reference, a range of wave directions cannot be resolved no matter how the sensor pairs are selected. It is, however, worth emphasizing that the latter is valid in relation to the imposed period $T = 1.0$ s. There will always be a range of periods (and, consequently, wave directions) that cannot be resolved based on the sensor configuration (Fig. 5), which implies that the wave period(s) should also be considered a design criterion of the system.

4.2. Errors due to sampling rate and sensor location

Unfortunately, the satisfaction of (22) alone is no guarantee to avoid ambiguity in the computed phase difference. As we saw earlier in Section 3.3, the sensor sampling rate and location error will induce errors in the phase difference, which may cause it to exceed the interval $(-\pi, \pi)$—especially if the separation distance is close to the limit given by (22). The situation can be simulated by considering the case study in Section 4.1.1 and adding random Gaussian noise with variances given by (18) and (20) to the theoretical phase difference (9). The simulation results (Fig. 7) confirm that errors from the sampling rate and sensor locations can potentially "push" the phase difference outside the desired range, making it increasingly challenging to resolve the true wave direction and wave number. Therefore, one should consider using sensors with a sufficiently high sampling rate (e.g., IMUs) and ensure that their positioning is known accurately as possible when designing shipboard arrays. A high sampling rate (e.g., 1 kHz) will also reduce the amount of temporal aliasing.

4.3. Multiple measurements

We emphasize that although the wave direction and wave number can be resolved from a minimum of three noncollinear sensors, this number only represents a theoretical lower bound for harmonic waves and does not, in general, reflect optimality. It is, therefore, interesting to study how additional sensors and measurements may impact wave estimation.

Consider the polygonal array in Fig. 4a with $D = 1.33$ m again. The array consists of four sensors yielding a total of six distinct phase difference measurements, as calculated by

$$P_{\max}(N) = \frac{N(N-1)}{2}, \tag{23}$$

where N is the number of sensors and $P_{\max}(N)$ is the maximum number of distinct phase difference measurements associated with N (assuming nonlinear arrays). The phase measurements are generated using (9) for multiple wave directions, and Gaussian random noise with variances given by (18) and (20) is added to simulate the uncertainties caused by the sensor sampling rate and location errors (see Sections 3.3.1 and 3.3.2). By applying the UKF algorithm (Algorithm 1) to this data and inspecting the resulting error covariance $\hat{\mathbf{P}}_k$, it is possible to see

(a) Polygonal array (b) Linear array

Fig. 4. An illustration of the different sensor arrays considered in the analysis of Section 4. The sensors $\{1, 2, 4\}$ in (a) form an equilateral triangle on the horizontal plane with length D and a circumscribed circle at $\{3\}$ with radius $D' = D/\sqrt{3}$.

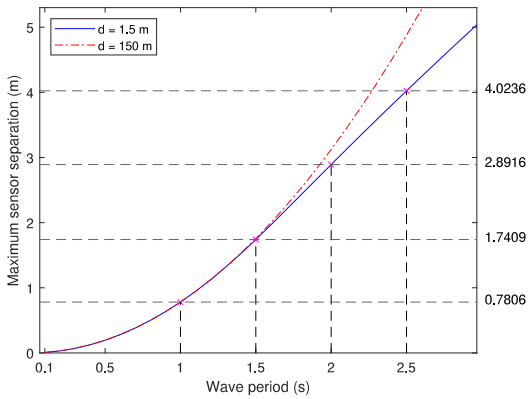

Fig. 5. Maximum sensor separation vs. wave period for water depths $d = 1.5$ and $d = 150$ m. The wave number $k = 2\pi/\lambda$ has been substituted into (22) and plotted against a range of wave periods using (21). The maximum separation distances for which the phase difference can be resolved unambiguously are indicated for wave periods $T = 1.0, 1.5, 2.0, 2.5$ s, and $d = 1.5$ m. The indicated periods and water depth were chosen to correspond with the periods and water depth used in experiments (discussed later).

Table 2
The standard deviation of the wave direction error estimates vs. # phase difference measurements (P) based on the polygonal array (Fig. 4(a)) with $D = 1.33$ m and $N = 4$. The particular sensor pairs considered in each simulation are indicated in the parentheses next to each number in the column P with (—"—) representing the sensor pairs in the above row. The standard deviations (deg) are computed from $100\times\sqrt{\hat{\mathbf{P}}_k(1,1)}$ at simulation time $t = 1000$ s, where $\hat{\mathbf{P}}_k(1,1)$ is the estimated error covariance of the UKF corresponding to the wave direction estimate. The multiplication factor of 100 is used to highlight the overall trend. For each wave direction, the UKF was applied to phase difference data generated by (9) with wave period $T = 2.0$ s and added Gaussian random noise with variances given by (18) and (20) with parameters $T_s = 0.1$ s and $\sigma = 1$ cm, respectively. The initial conditions and UKF parameters were identical for each run (see Table 1).

P	0°	30°	60°	90°	120°	150°	180°
2 : (1-2,1-3)	3.47	8.48	12.9	14.0	11.3	6.05	3.62
3 : (—"—,1-4)	3.41	4.62	5.17	4.65	3.42	2.67	3.43
4 : (—"—,2-3)	2.89	3.72	4.28	4.10	3.30	2.64	2.89
5 : (—"—,2-4)	2.58	2.67	2.77	2.85	2.79	2.59	2.58
6 : (—"—,3-4)	2.58	2.58	2.58	2.59	2.60	2.59	2.58

how the accuracy and covariance of the wave estimates change with the number of phase difference measurements. The simulation results (Table 2) indicate that the estimated error covariance decreases by increasing P, which corresponds to the number of independent phase difference measurements. The results also suggest that after a certain number of measurements, the improvement in the error variance is minimal. Hence, additional sensors may have benefits, but only up to a specific limit.

Furthermore, as P ($\leq P_{\max}(4) = 6$) increases, the estimated error covariances approach similar values on all wave directions, culminating in similarity at $P = 6$. It is worth emphasizing that this pattern is not general but a coincidence resulting from the geometry of the considered sensor array (Fig. 4a). Due to the symmetry of the sensors, the error covariance becomes progressively independent of the wave direction as $P \to 6$. This pattern is, in general, not duplicated for asymmetrical sensor arrays, which produce a greater spread of values.

4.4. Linear arrays

In general, the wave direction and wave number cannot be resolved uniquely from a linear shipboard configuration of two or more sensors. For instance, if a harmonic wave passes through two sensors at the same time, a zero phase difference will be detected and a third non-collinear sensor is needed to determine the direction. Without this third noncollinear sensor, there will be a 180° ambiguity in the direction since we do not know whether the wave is approaching from left or right. However, in the special case where information about the general wave direction is known beforehand (e.g., close to the shoreline such as in Hardisty (1988)), shipboard linear arrays may be used to find the wave direction (Fig. 8). As seen in Fig. 8, the wave direction can be determined from two sensors alone, provided that we know which side the waves are approaching. In this case, if the waves suddenly change direction to the other side (i.e., between 0 and $-\pi$), we get an ambiguity within a mirror symmetry (Fernandes et al., 1988, 2000). Also note that for linear arrays to work, the wave number should be known in advance.

5. Experimental verification

In this section, we give experimental verification of the UKF algorithm by applying it to experimental data from multiple shipboard IMUs. The raw IMU data needs to be processed through several steps such as data processing, choice of reference sensor, and wave frequency and phase difference estimation to ensure that the phase differences are

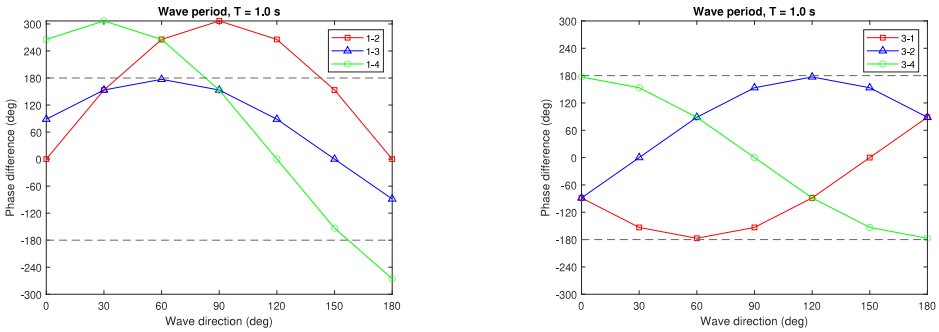

(a) Reference sensor = 1 (b) Reference sensor = 3

Fig. 6. The theoretical phase difference is plotted against the wave direction using (9) for two different choices of reference sensor in the polygonal array (Fig. 4a) with $D = 1.33$ m and $D' = 0.768$ m. For sensor pairs 1–2 and 1–4, several of the phase differences lie outside $(-\pi, \pi)$, whereas for sensor pairs 3-1, 3-2, and 3-4, all reside within $(-\pi, \pi)$.

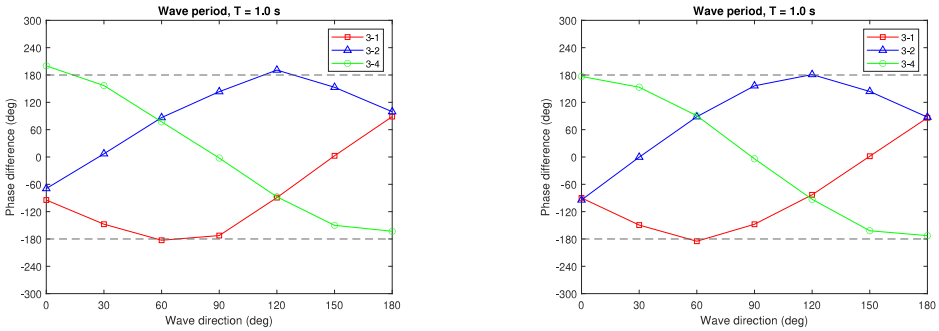

(a) $T_s = 0.1$ s (b) $\sigma = 1$ cm

Fig. 7. Gaussian random noise with variance given by (18) and (20) has been added separately to the phase differences in Fig. 6b. In (a) and (b) we can see how the sensor sampling time (T_s) and location error (σ), respectively, may cause some of the phase differences to become ambiguous.

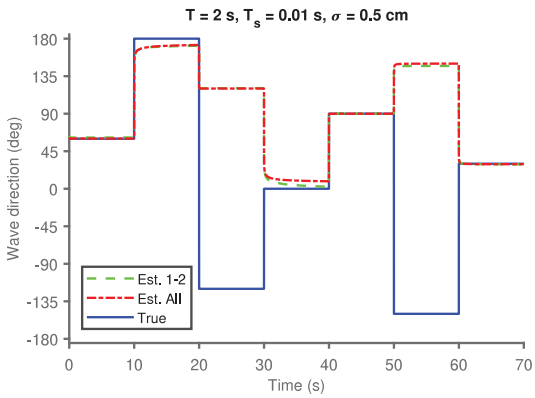

Fig. 8. Online estimates of the wave direction given by the UKF algorithm (Algorithm 1) with the linear array shown in Fig. 4b ($D = 0.5$ m). The phase differences were simulated using (9) with wave period $T = 2.0$ s and Gaussian random noise with variance given by (18) and (20) with $T_s = 0.01$ s and $\sigma = 0.5$ cm, respectively. The wave estimates are based on two sets of measurements (i.e., sensor pair 1–2 and all sensor pairs 1–2, 1–3, 1–4) with sensor 1 as reference. The wave number is assumed known.

obtained with as little error as possible. In the following subsections, we discuss each of these steps. The experimental data considered in this work was originally collected as part of the Master's thesis of Udjus (2017).

5.1. Experimental design

As explained in Udjus (2017), the authors equipped a 1:90 scaled model C/S Inocean Cat I Drillship (CSAD) (Fig. 9) with four spatially distributed ADIS16364 IMUs along the hull to record the vessel motions caused by waves. The IMU array configuration considered in the experiments is illustrated in Fig. 10. Each IMU is connected to an Arduino microprocesser, which is responsible for sampling the IMU data. The time synchronization of all four IMUs was handled by an interrupt signal from one (master) Arduino microprocessor to the other (slave) Arduinos. We refer to the Master's thesis of Udjus (2017) and references therein for additional details on the hardware and experimental design.

The experiments were carried out in the NTNU Marine Cybernetics laboratory, which contains a 1.5 m deep wave basin equipped with a wavemaker. The wavemaker is a 6-meter wide paddle operated by an electrical servo actuator and has a DHI wave synthesizer for producing regular and irregular waves.[2] The CSAD position and orientation was confined using ropes with 1 kg weights attached to each end (Fig. 9). This setup ensured that motions in surge, sway, and yaw were limited, while still allowing nearly free motions in heave, roll, and pitch.

A total of 52 regular wave experiments were carried out in the wave basin. For each relative wave direction {0°, 30°, 60°, 90°, 120°, 150°,

[2] For more details see: https://www.ntnu.edu/imt/lab/cybernetics.

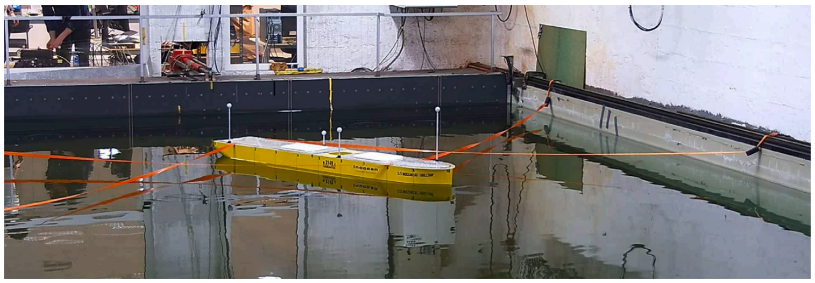

Fig. 9. The model ship C/S Inocean Cat I Drillship (CSAD) used in experiments. The position and orientation were held fixed by ropes with 1 kg weights attached to each end. Image reproduced with courtesy of Udjus (2017).

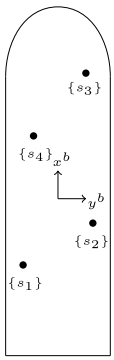

	x^b	y^b	z^b
s_1	-465	-184	-73
s_2	-244	184	-13
s_3	740	130	82
s_4	450	-160	82

Fig. 10. An illustration of the sensor configuration used in the wave experiments by Udjus (2017). IMUs 1, 2, 3, and 4 are denoted $\{s_1\}, \{s_2\}, \{s_3\}$, and $\{s_4\}$, respectively. The location of each sensor is given in millimeters with respect to the body-fixed reference frame $\{b\}$, which is defined midships with the z-axis pointing downwards (into the page).

180°}, regular waves with wave periods {1.0 s, 1.5 s, 2.0 s, 2.5 s} lying within the frequency range of wind-generated surface gravity waves (Holthuijsen, 2007), were tested. A wave height of 5 cm was considered in all wave basin experiments, which, in reality, corresponds to a 4.5 m wave height (using Froude scaling with model scale 1:90). Although a 4.5 m wave height can be considered a very rough sea state (Price and Bishop, 1974), the roll and pitch responses in the experiments were small owing to the large vessel size.[3] According to the authors, the beach was not functioning as intended during the day of experimentation and, to avoid the impact of reflected waves, experiments were stopped after approximately 50 s, which, consequently, became the time duration of the recorded IMU data.

5.2. Data processing

In this section, we discuss some data processing steps needed to obtain an estimate of the vessel heave acceleration from the specific force measurements of each IMU. As we shall see, the heave accelerations are needed to compute the phase differences, which, in turn, will be used to estimate the desired wave quantities.

The accelerometers in an IMU measure the specific force $\mathbf{f}^a$ with respect to the inertial reference frame $\{i\}$. The readings are expressed in the accelerometer frame $\{a\}$, defined by the orientation of the accelerometer-sensitive axes. The $\{a\}$-frame may be non-orthogonal and misaligned and can be compensated via the rotation matrix $\mathbf{R}_a^s$, which converts raw measurements into the IMU sensor frame $\{s\}$ defined by the IMU manufacturer. The $\{s\}$-frame may suffer from installation errors caused by the alignment and inner distances of the sensor array. In order to align the $\{s\}$-frame with the body frame $\{b\}$, which is the referential frame used in the evaluation of the following heave acceleration, an additional rotation matrix $\mathbf{R}_s^b$ is required. The matrices $\mathbf{R}_a^s$ and $\mathbf{R}_s^b$ can be respectively obtained via the calibration procedures available at the site of the IMU manufacturer and after the IMUs have been installed into the array on the vessel. The sensor array positioning errors and their effects are discussed in Section 3.3.2.

For an ideal three-axis accelerometer, the specific force is given by

$$\mathbf{f}_{is}^b = \mathbf{a}_{is}^b - \mathbf{g}^b = \mathbf{R}_s^b \mathbf{R}_a^s \mathbf{f}^a,$$

where $\mathbf{a}_{is}^b$ is the linear acceleration of the IMU sensor frame $\{s\}$ with respect to the inertial frame $\{i\}$ expressed in $\{b\}$, and $\mathbf{g}^b$ is the gravity vector expressed in $\{b\}$. In practice, after treating the deterministic sensor imperfections discussed in Section 3.3.1, the measurements from a three-axis accelerometer are, in general, still subject to several stochastic errors. A common approach is to separate these errors and model them, respectively, as additive zero-mean Gaussian white noise and a drifting bias term. Following this approach, we can use the standard three-axis accelerometer sensor model from Fossen (2021), i.e.,

$$\mathbf{f}_{is}^b = \mathbf{a}_{is}^b - \mathbf{g}^b + \mathbf{b}_{\text{acc}}^b + \mathbf{w}_{\text{acc}}^b, \tag{24}$$

where $\mathbf{b}_{\text{acc}}^b$ and $\mathbf{w}_{\text{acc}}^b$ denote the respective bias and noise of the three-axis accelerometer. In general, (24) should be transformed to the navigational frame $\{n\}$ such that the linear *heave* acceleration from each sensor can be extracted and used to compute the phase differences. However, since we are only considering small roll and pitch angles, it is sufficient in this case to only consider the z-component of (24), i.e.,

$$f_{z,is}^b = a_{z,is}^b - g\cos\phi\cos\theta + b_{z,\text{acc}}^b + w_{z,\text{acc}}^b, \tag{25}$$

where ϕ and θ are the roll and pitch angles between $\{n\}$ and $\{b\}$, and g is the gravitational constant. In the following, we walk through the steps needed to obtain an estimate of the linear acceleration $a_{z,is}^b$, which corresponds to the heave acceleration when assuming small angles.

As explained in Udjus (2017), a separate camera-based tracking system called Qualisys was used to obtain measurements of the roll and pitch angles. These measurements showed that, in all experiments, ϕ and θ were less than 1° during the first 15 s and less than 2° for

[3] The model drillship corresponds to a 232 m × 40 m × 19 m vessel which are the standard dimensions of many drillships.

Table 3
The separation distance R_{ij} in meters between sensors $\{s_i\}$ and $\{s_j\}$ for the experimental configuration in Fig. 10.

		j			
	R_{ij}	1	2	3	4
i	1	-	0.4293	1.2452	0.9153
	2	0.4293	-	0.9855	0.7746
	3	1.2452	0.9855	-	0.4101
	4	0.9153	0.7746	0.4101	-

the remaining time of the experiments with wave excitation. Since $\cos(2°)^2 \approx 1$, (25) can be approximated by

$$f^b_{z,is} \approx a^b_{z,is} - g + b^b_{z,\text{acc}} + w^b_{z,\text{acc}}. \tag{26}$$

The initial bias in each accelerometer was estimated by computing the expected value of (26) and assuming that the accelerometers were level and at rest. Applying these assumptions to (26), yields

$$\begin{aligned}
\mathbb{E}\left[f^b_{z,is}\right] &= \mathbb{E}\left[a^b_{z,is} - g + b^b_{z,acc} + w^b_{z,acc}\right] \\
\mathbb{E}\left[f^b_{z,is}\right] &= \underbrace{\mathbb{E}\left[a^b_{z,is}\right]}_{=0} - g + b^b_{z,acc} + \underbrace{\mathbb{E}\left[w^b_{z,acc}\right]}_{=0} \\
b^b_{z,acc} &= \mathbb{E}\left[f^b_{z,is}\right] + g,
\end{aligned} \tag{27}$$

where $w^b_{z,acc}$ vanishes due to the Gaussian zero-mean assumption. Since the vessel only underwent wave excitation for 30–35 s, it is assumed that the initial sensor bias remained more or less constant throughout each experiment. This assumption is validated by the accelerometer Allan Variance curve found in the ADIS16364 datasheet, which states that for a 30 s time interval the in-run bias stability is around ± 0.1 mg.

The high-frequency noise components were removed by lowpass filtering the specific force measurements above the maximal wave frequency, resulting in the final estimated acceleration signal

$$\hat{a}^b_{z,is} = \bar{f}^b_{z,is} + g + \hat{b}^b_{z,\text{acc}}, \tag{28}$$

where $\bar{f}^b_{z,is}$ is the lowpass filtered specific force and $\hat{b}^b_{z,\text{acc}}$ is the initial bias estimate obtained through (27).

5.3. Choice of reference sensor

To resolve the wave direction and wave number associated with all the experimental wave periods $\{1.0\text{ s}, 1.5\text{ s}, 2.0\text{ s}, 2.5\text{ s}\}$, care must be exercised when selecting the reference sensor. As we shall see, the appropriate reference IMU can be chosen by examining the criterion (22) for each wave period and checking which IMU has all its neighboring separation lengths within the imposed limits. As discussed in Section 4.1, abidance to this criterion ensures that the theoretical phase differences are restricted to $(-\pi, \pi)$, thus avoiding spatial aliasing.

A comparison between the separation distances given by the experimental configuration (Table 3) and the separation limits imposed by Barber and Doyle (Fig. 5) reveals that only some of the IMUs can be used to resolve waves with period $T = 1.0$ s. In particular, we see that IMU 2 or 4 should be considered as a reference along with sensor pairs 2-1 and 2-4 or 4-2 and 4-3. With these choices, the Barber and Doyle criterion (22) is (in theory) satisfied for all experimental wave periods with the given IMU configuration.

5.4. Wave frequency and phase difference estimation

We have in the analysis thus far tacitly assumed the wave frequency ω to be perfectly known. The reliance on ω can be seen in the computation of the phase difference (16), the measurement covariance related to (18) and (20), and implicitly in the lowpass filtered acceleration signals (28). Hence, the wave frequency is an important cornerstone and requires accurate determination in order for our wave algorithm to function optimally.

For regular waves it is reasonable to assume that the vessel acceleration (28) can be modeled by a single sinusoid and perturbation of the form

$$\hat{a}^b_{z,is}(t) = A\sin(\omega t + \epsilon) + \delta(t), \tag{29}$$

where A, ω, ϵ, and δ represent the respective amplitude, frequency, phase, and perturbation of the acceleration signal pertaining to sensor $\{s\}$. Hence, the task at hand is to find an accurate estimate of ω from $\hat{a}^b_{z,is}$ assuming it can be modeled according to (29) with unknown parameters A, ω, ϵ, and bounded perturbation $\delta(t)$. In the following three subsections, we describe three different methods that can be used to achieve this goal.

5.4.1. Averaging the time intervals between successive peaks

A straightforward approach to finding the frequency of a sinusoid is to average the time intervals between the (detected) successive peaks of the signal. The averaged time intervals should be identical to the period given that the signal in question is a simple sinusoid. A prerequisite for this approach to work on signals of the form (29) is that the amplitude of the perturbation term δ is significantly smaller than the amplitude A. In other words, the signal (29) should have a sufficiently high signal-to-noise ratio (SNR). A high SNR will help prevent noisy spikes from being detected and confused as the actual signal peaks. In cases where the signal is significantly corrupted by noise, the SNR may be improved through various filtering techniques.

5.4.2. The Aranovskiy frequency estimator

The frequency identification algorithm of Aranovskiy et al. (2007) is designed based on a sinusoid of the form (29) and is attractive for two reasons. First, it offers a real-time implementation, rendering it suitable for many applications in need of quick frequency estimates where the measured signal can be approximated by a sinusoid. Second, it has shown robustness in the presence of unaccounted perturbations in the measurement signal.

The algorithm comprises an auxiliary filter and an adaptive observer of the form

$$\begin{aligned}
\dot{\xi}_1 &= \xi_2, \\
\dot{\xi}_2 &= -2\omega_f \xi_2 - \omega_f^2 \xi_1 + \omega_f^2 w(t), \\
\dot{\theta} &= k\xi_1(\dot{\xi}_2 - \hat{\theta}\xi_1),
\end{aligned} \tag{30}$$

where $w(t) = \hat{a}^b_{z,is}(t)$ is the measured signal (here chosen as the estimated acceleration signal), ω_f is the user-specified filter cut-off frequency, $k > 0$ is the observer gain (not to be confused with the wave number), and $\theta := -\omega^2$. Both ω_f and k affect the convergence rate and steady state error of $\hat{\theta}$ to θ and should be selected based on the desired performance. In general, small ω_f and k will result in a slower convergence rate, whereas larger values will result in faster convergence but with some induced oscillation in steady-state (Belleter et al., 2015).

For marine craft operating in situations with little wave excitation, algorithm (30) can be modified to include an adaptive gain-switching mechanism for the observer gain k, as proposed by Belleter et al. (2015). This mechanism enables k to be switched between a high and a low gain depending on the amplitude of the measured roll, pitch, or heave responses, which may improve the convergence rate of the estimator. The reader is referred to Belleter et al. (2015) for additional theory and implementation details of the gain-switching mechanism.

5.4.3. The fast Fourier transform

In reality, ocean waves are usually irregular, exhibiting a broad spectrum of frequencies. In such situations, the time-averaging and Aranovskiy frequency estimator algorithms may be limited due to their inherent single-frequency model assumption. Unless the wave spectrum is sufficiently narrow, these approaches may struggle to identify the dominant (peak) frequency, which is the frequency component often

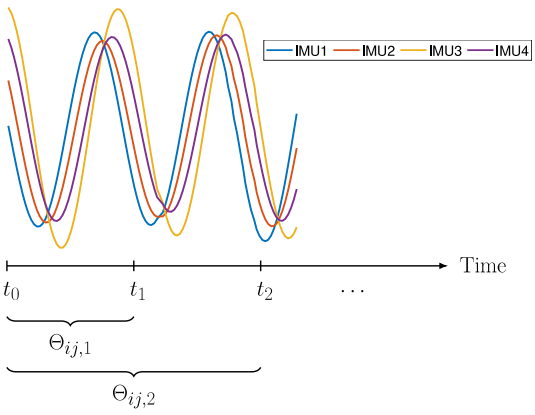

Fig. 11. The phase difference $\Theta_{ij,k}$ between IMUs $\{s_i\}$ and $\{s_j\}$ at time t_k can be estimated online by considering the linear heave acceleration signals within a window, before being passed on to the UKF. In this time window, the lag (i.e., the number of samples) between the respective heave signals is estimated by computing the cross-correlation between them and converting it to a phase difference using (16). The initial width of the window is set equal to the wave period and increases from t_0 as the signals continue to develop.

sought in marine applications. For a signal comprising multiple frequencies, the fast Fourier transform (FFT) can be used to deconstruct its spectral composition and identify any potential peaks. Unlike the above methods, the FFT does not make any assumptions on the structure or shape of the signals considered, thus making it a more viable option for analyzing signals comprising multiple frequencies. However, a drawback of this approach is that it cannot be implemented in real-time as it relies on back-dated information, which, as a consequence, produces a lag in the estimation.

Despite the attractive features of the Aranovskiy frequency estimator, the FFT was selected as the main method in this paper. This decision was based on two points: First, the FFT gave the most consistent frequency estimates for all experimental wave periods, in close agreement with the ground truth values, whereas the Aranovskiy estimator was somewhat less accurate and had difficulties identifying wave period $T = 1.0$ s (the reasons are discussed in Section 5.5.3). Second, as a proof of concept of Theorem 1 and in the compromise between accuracy and computational lag, we currently deem a higher accuracy in the wave estimates more important than real-time performance.

5.4.4. Phase difference estimation

After an estimate of the wave frequency has been obtained using either of the approaches described in Sections 5.4.1–5.4.3, the phase difference between the respective heave acceleration signals (28) can be estimated by computing the cross-correlation between them. This operation can be performed online by considering the heave acceleration signals within an increasing time window (Fig. 11).

5.5. Results and discussion

In this section, we present the results from our UKF wave algorithm on the experimental IMU data of Udjus (2017). The raw IMU data was processed according to the previous subsections to ensure that the phase differences could be obtained with as little error as possible and reduce the risk of ambiguities before being passed on to the UKF algorithm (Fig. 12). In the following results, the reference wave number was computed using the dispersion relation (21) with pool depth $d = 1.5$ m and the true wave period (i.e., the wave period used as input to the wavemaker machine). The reference wave direction was computed by fixing the boat heading (Fig. 9) and confirming this value with the Qualisys camera system.

5.5.1. Experimental verification of Theorem 1

The experimental results (Fig. 13) show that in 91% and 86% of experiments considered, the absolute wave direction and wave number errors based on three IMUs are less than 5° and 0.1 m^{-1}, respectively. These numbers provide strong evidence in favor of Theorem 1 and also validate the UKF capabilities in estimating those quantities. Experimental verification of Theorem 1 extends previous findings (Udjus, 2017; Heyn et al., 2017), which only seem to consider the wave direction, and not the wave number—although, as we have now shown, can also be determined simultaneously from the same data. Additionally, we have demonstrated that as few as three IMUs are in theory sufficient, provided that they are noncollinearly arranged and separated in accordance with (22).

The experimental results (Fig. 13) also show that in 71% and 52% of experiments considered, the measurement set $\{\Theta_{23}, \Theta_{24}\}$ (yellow) constitutes the largest error in each wave quantity, with some errors significantly exceeding the other sets of phases within each experiment. The large deviations observed can be linked to large errors in the estimated phase differences $\hat{\Theta}_{23}$ and $\hat{\Theta}_{24}$, which, in turn, are caused by several potential sources of error affecting IMUs $\{s_3\}$ and $\{s_4\}$. In general, the error between the estimated and actual phase differences can be attributed (either directly or indirectly) to one or more of the following sources: sensor imperfections, inexact sensor positioning and alignment, insufficient sensor sampling rate, shortcomings in the experimental design (e.g., from using ropes to confine boat heading and position), modeling errors due to small-angle approximation, wave frequency estimation, and oscillations and/or transient effects on the sensors due to structural vibrations and external environmental influences. From the above list, however, only inaccuracies in the sensor positioning and alignment of $\{s_3\}$ and $\{s_4\}$ may realistically explain the significant separation of errors within the sets of some experiments (we expect the errors caused by the other sources to manifest themselves roughly equally among the phase differences). As we have seen earlier, errors in the sensor locations can produce significant biases in the phase difference estimates (especially for short wave periods; see Fig. 3), which may translate to biases in the wave direction and wave number estimates. In order to test this theory, we have conducted a small simulation study investigating how the positioning errors of sensors $\{s_3\}$ and $\{s_4\}$ may impact the wave estimate errors associated with measurement sets $\{\Theta_{21}, \Theta_{23}\}$, $\{\Theta_{21}, \Theta_{24}\}$, and $\{\Theta_{23}, \Theta_{24}\}$. The results (Fig. 14) exhibit a similar error pattern to the results in Fig. 13, indicating that the location uncertainty of $\{s_3\}$ and $\{s_4\}$ is a plausible cause for the large separation of errors observed. This argument is further substantiated by Udjus (2017), which states that the sensor positions were obtained using a folding ruler and that some measurement errors may transpire because of this.

5.5.2. Multiple independent phase measurements

The experimental results also suggest that using additional independent phase measurements by adding more IMUs may reduce overall errors by having an "averaging" effect on the various measurement sets. Indeed, by studying the errors in Fig. 13 carefully, we see that the error obtained from the set of all six phase measurements is, in general, lower than the worst performing set constituting two phases. The reasons for this can be linked to the error variance, which is discussed in Section 4.3.

5.5.3. High-frequency waves

Contrary to wave periods $T = 1.5$ s, 2.0 s, and 2.5 s, obtaining accurate estimates of the wave direction and wave number proved difficult for the IMU data corresponding to $T = 1.0$ s (Fig. 15). The significant errors observed are caused by large errors in the estimated phase differences (Fig. 16), which, in turn, can be linked to several sources of error. In the following, we discuss some potential sources that we believe can have contributed to the deviations observed in Fig. 16.

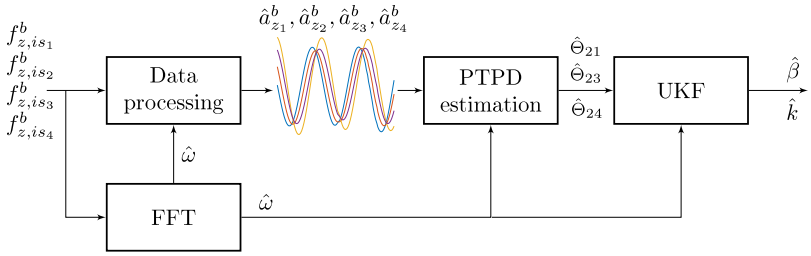

Fig. 12. A block diagram illustrating the general procedure of going from raw IMU measurements to obtaining estimates of the wave direction β and wave number k. The procedure can be summarized in three steps: (a) data processing, (b) PTPD estimation, and (c) state estimation. In (a) sensor biases and high-frequency (HF) noise are removed from the IMU measurements, yielding an estimate of the linear heave acceleration associated with each IMU (assuming small roll and pitch angles). The HF noise is filtered using a lowpass filter with cut-off above $\hat{\omega}$, obtained from a fast Fourier transform (FFT) applied to the entire data sequence. In (b) we estimate the phase difference $\hat{\Theta}$ online by following the procedure explained in Fig. 11. Finally, in (c) we apply the UKF algorithm to obtain the desired wave estimates.

A close look at some of the IMU data corresponding to $T = 1.0$ s (Fig. 17a) shows that the heave responses are non-sinusoidal, indicating that some distortion has taken place. This suspicion is confirmed by the corresponding FFTs of the data (Fig. 17b), which reveal additional frequencies in proximity to the expected single peak frequency. The existence of additional frequencies is a violation of the fundamental regularity/single-frequency assumption that our PTPD model is built on and may, as a result, be the reason for the poor estimation quality.

The distortion observed in Fig. 17a can most likely be attributed to the lowpass wave filtering characteristics of a ship (Nielsen, 2007, 2008; de Souza et al., 2018; Nielsen et al., 2019; Nielsen and Dietz, 2020), which occur whenever the waves are sufficiently short. For sufficiently short waves, multiple wave crests (and troughs) will affect the vessel simultaneously, resulting in a non-sinusoidal (filtered) response. This high-frequency filtering effect happens when the wavelength is shorter than the length of the wave trajectory through the vessel (i.e., the vessel length as seen by the waves). As seen in Fig. 18, the length of the wave trajectory depends on the orientation of the vessel relative to the waves, meaning that high-frequency filtering will not necessarily happen for all wave directions when considering waves of a given wavelength. It can be shown (see Appendix B) that the wave trajectory distance W through a box-shaped vessel along the wave propagation axis x^w (see Fig. 1 for definition) is

$$W = L|\cos\beta| + B|\sin\beta|, \tag{31}$$

where β is the relative wave direction, and L and B are the respective length and beam dimensions of the vessel. In order to avoid the high-frequency filtering effect, the wavelength λ should ideally be larger than W for a given β. This result can be generalized for all β if $\lambda > W$ for $\beta = \arctan(B/L)$ (see Appendix B for proof).

To quantitatively assess the potential occurrence of high-frequency filtering in our experiments, (31) was computed for all wave directions and compared to the wavelengths associated with each wave period (Fig. 19). In all the conducted experiments with $T = 1.0$ s ($\lambda = 1.5613$ m), except for $\beta = 90°$, W exceeds the wavelength, thus confirming the presence of high-frequency filtering in the vessel dynamics. Moreover, this result corresponds well with the observed estimation errors in Fig. 15, which shows significant errors for all wave directions except $\beta = 90°$.

The effect of high-frequency filtering is a known problem and, in general, a core limitation of wave estimation methods based on wave-induced vessel motions (Nielsen, 2007, 2008; de Souza et al., 2018; Nielsen et al., 2019; Nielsen and Dietz, 2020). Unfortunately, the problem can, as of now, only be alleviated by considering other responses that are less affected by filtering (Nielsen, 2008; de Souza et al., 2018). However, this requires additional complementary sensors not installed on the ship in the present study.

Phase ambiguities resulting from a precarious selection of sensor pairs represent another potential error source for wave period $T = 1.0$ s. As discussed in Section 5.3, only sensor pairs 2-1 and 2-4 will (in theory) satisfy the Barber and Doyle criterion (22), thus guaranteeing that phase differences Θ_{21} and Θ_{24} are within $(-\pi, \pi)$. This result can be seen from Fig. 16, which also shows that the theoretical phase difference Θ_{23} is outside $(-\pi, \pi)$ for wave directions $\{0°, 30°, 150°, 180°\}$, indicating that Θ_{23} should not be relied upon in the computation of those values. Nevertheless, the theoretical values of Θ_{23} were computed under the assumption that the sensor locations given in Fig. 10 are correct. However, as pointed out in Section 5.5.1, this is not necessarily true, meaning that the actual Θ_{23} may be within the range of $(-\pi, \pi)$ for several wave directions. In particular, we suspect that this may be the case for wave directions $\{0°, 30°, 150°\}$, since the estimated phases remain somewhat close to the theoretical values and should ideally have been wrapped to angles of opposite sign.

Table 4
The sum of wave direction $\tilde{\beta}$ and wave number $\tilde{k}$ errors corresponding to "All" phases in Figs. 13 and 15 for each respective wave period T. The total errors $\tilde{\beta}$ and $\tilde{k}$ are given in degrees and m^{-1}, respectively. Notice that the total errors decrease as the wave period gets longer and vice versa.

T	$\tilde{\beta}$	$\tilde{k}$
1.0	366.23	27.12
1.5	74.05	0.95
2.0	44.80	0.62
2.5	41.74	0.56

Recall from the analysis of Section 3.3.2 that inexact sensor positions produce a bias in the computed phase difference that grows exponentially as the wave period becomes smaller (Fig. 3). This effect may be one of the reasons for the overall growth of errors observed in the wave estimates when comparing them with the respective wave periods (Table 4). The bias caused by the sensor positioning may also render some of the phase differences ambiguous by "pushing" them outside the range $(-\pi, \pi)$, as discussed in Section 4.2. Studying Fig. 16 closely, it is possible that this may have occurred for Θ_{24} at wave directions $\{120°, 150°, 180°\}$ since the angles below the boundary $-\pi$ wrap to values in proximity to the estimates of Θ_{24}.

5.5.4. Future work

Today, most shipboard wave estimation methods are based on response amplitude operators (RAOs) that are capable of producing estimates of the complete directional wave spectrum (Waals et al., 2002; Tannuri et al., 2003; Pascoal and Guedes Soares, 2009; Brodtkorb et al., 2018). These methods differ from our approach, which is signal-based (i.e., it requires no ship information) and built on regular harmonic waves, thus limiting it to information about the main (dominant) wave direction and wave number. It is currently unknown how well this method will work for more irregular wave patterns comprising many frequencies and directions. Hence, future investigations will aim at

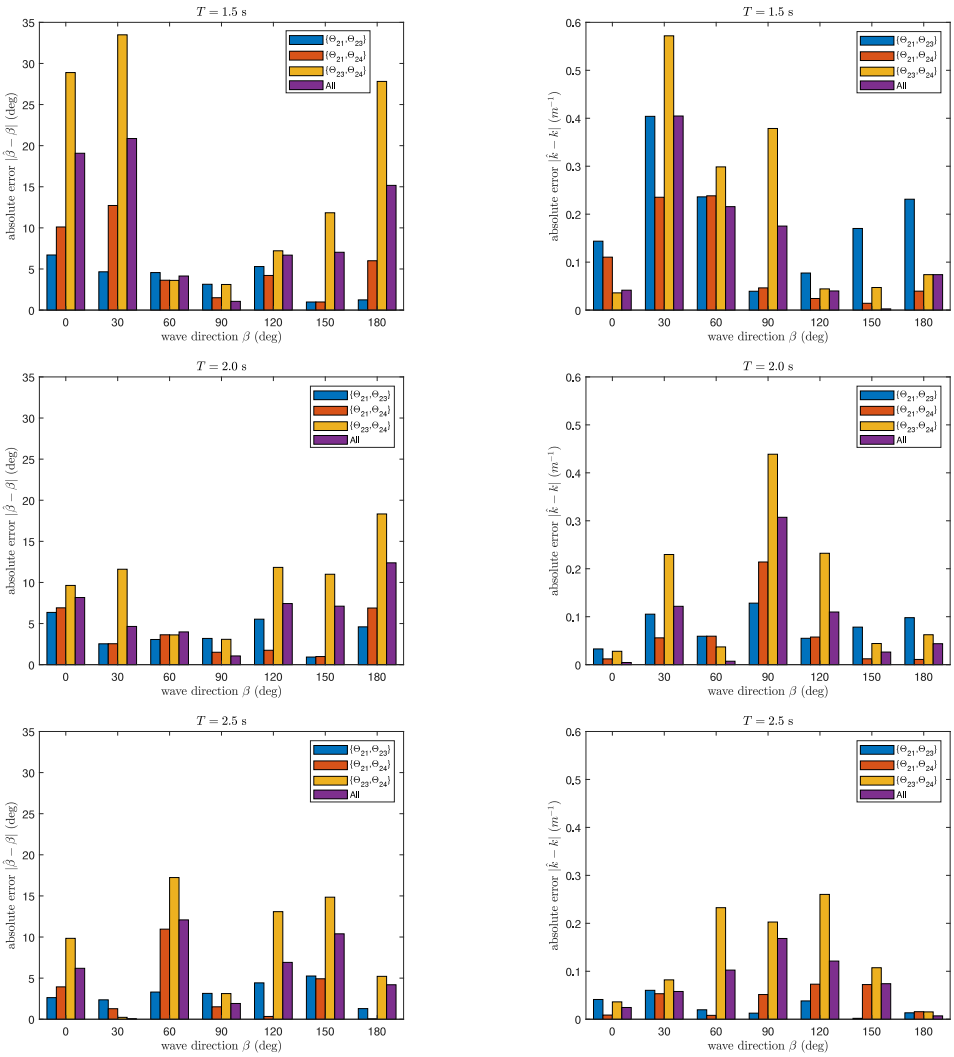

Fig. 13. Results from wave experiments with wave periods $T = 1.5$ s, 2.0 s, 2.5 s, and sampling time $T_s = 0.01$ s (100 Hz). The various sets of phase difference measurements are $\{\Theta_{21}, \Theta_{23}\}$, $\{\Theta_{21}, \Theta_{24}\}$, $\{\Theta_{23}, \Theta_{24}\}$, $\{\Theta_{12}, \Theta_{13}, \Theta_{14}, \Theta_{23}, \Theta_{24}, \Theta_{34}\}$ (all) corresponding to IMUs $\{s_1, s_2, s_3\}$, $\{s_1, s_2, s_4\}$, $\{s_2, s_3, s_4\}$, $\{s_1, s_2, s_3, s_4\}$, respectively, and are shown with different colors. For each set of IMUs, the bar plots show the absolute error between the wave estimates (after convergence) and the true values. (For interpretation of the references to color in this figure legend, the reader is referred to the web version of this article.)

experimental testing of the UKF in such wave environments, with the possibility of extending the algorithm to utilize the complete phase model (4) with roll-pitch compensation such that the UKF may be applied to all vessels in both moderate and higher sea states.

The transition from geographically fixed wave arrays to portable shipboard wave arrays has increased the practical usefulness of the PTPD approach. As a next research step, the possibility of using the PTPD approach for moving vessels with a non-zero forward speed shall be investigated. In order to accommodate this capability, the forward vessel speed should be considered in the PTPD model derivation, which generally causes frequency shifts in the measured vessel motions due to the Doppler effect. Hence, future work will also target wave direction estimation for underway vessels by extending our PTPD approach to consider the shifted wave (encounter) frequency.

6. Conclusions

This paper has added several extensions to the existing literature on shipboard and traditional wave arrays considering the phase-time-path-difference (PTPD) concept. We have shown (through observability analysis and experimental data) that *both* the wave direction and wave number can be obtained from a minimum of three noncollinear sensors (e.g., IMUs) measuring regular harmonic waves, assuming a dynamically positioned surface vessel with small roll and pitch angles. In this regard, we proposed a signal-based unscented Kalman filter (UKF) algorithm to estimate these wave quantities, which offers several benefits over the standard analytical solution (7) in terms of addressing uncertainties and incorporating multiple measurements. We have discussed and quantified several sources of error related to the sensors (e.g., sensor imperfections, insufficient sampling rate, and oscillations

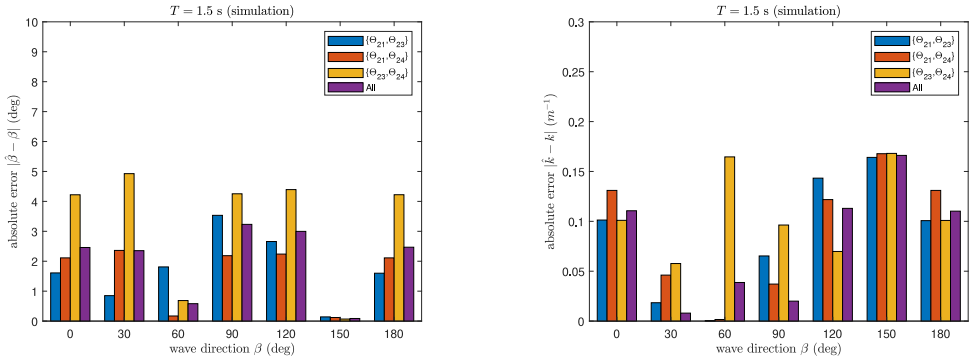

Fig. 14. Results from simulation with sensor positioning errors. The various sets of phase difference measurements are $\{\Theta_{21}, \Theta_{23}\}$, $\{\Theta_{21}, \Theta_{24}\}$, $\{\Theta_{23}, \Theta_{24}\}$, $\{\Theta_{21}, \Theta_{23}, \Theta_{24}\}$ (all) corresponding to IMUs $\{s_1, s_2, s_3\}$, $\{s_1, s_2, s_4\}$, $\{s_2, s_3, s_4\}$, $\{s_1, s_2, s_3, s_4\}$, respectively, and are shown with different colors. For each set of IMUs, the bar plots show the absolute error between the wave estimates (after convergence) and the true values. The respective phase differences $\{\Theta_{21}, \Theta_{23}, \Theta_{24}\}$ were simulated using (9) with $T = 1.5$ s, sampling time $T_s = 0.01$ s, and adding positioning errors to all sensors (configured according to Fig. 10). The errors were added as Gaussian random noise to the configuration matrix of (10) with variance given by (20) using $\sigma_{21} = 2$ cm, $\sigma_{23} = 10$ cm, and $\sigma_{24} = 10$ cm. (For interpretation of the references to color in this figure legend, the reader is referred to the web version of this article.)

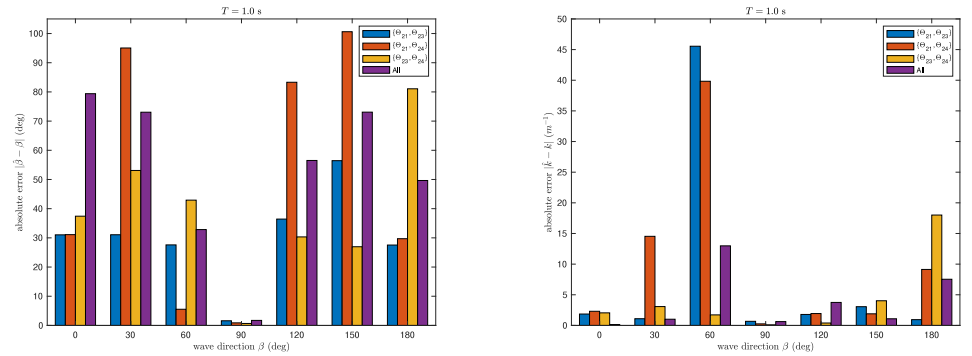

Fig. 15. Results from wave experiments with wave period $T = 1.0$ s and sampling time $T_s = 0.01$ s (100 Hz). The various sets of phase difference measurements are $\{\Theta_{21}, \Theta_{23}\}$, $\{\Theta_{21}, \Theta_{24}\}$, $\{\Theta_{23}, \Theta_{24}\}$, $\{\Theta_{12}, \Theta_{13}, \Theta_{14}, \Theta_{23}, \Theta_{24}, \Theta_{34}\}$ (all) corresponding to IMUs $\{s_1, s_2, s_3\}$, $\{s_1, s_2, s_4\}$, $\{s_2, s_3, s_4\}$, $\{s_1, s_2, s_3, s_4\}$, respectively, and are shown with different colors. For each set of IMUs, the bar plots show the absolute error between the wave estimates (after convergence) and the true values. (For interpretation of the references to color in this figure legend, the reader is referred to the web version of this article.)

and transient effects) and array construction (e.g., inexact sensor locations) and shown how some of these errors can be incorporated into the UKF to yield the estimated uncertainty in the wave estimates. Finally, we have shown how the Barber and Doyle criterion (22), together with some of the errors above, should be considered in the design of shipboard wave arrays.

Our proposed PTPD model and UKF algorithm hinge on regular harmonic waves, meaning that the practicality of this approach is currently restricted to ocean waves resembling such wave patterns (e.g., narrow-banded wave trains such as swell). It is presently unknown how well the UKF will work in more complex sea environments. Future study will aim at experimental testing of the UKF in such environments, with the possibility of extending the algorithm to estimate vessel roll and pitch motions, thus enabling the complete phase model (4) to be used instead. Such an extension will render the UKF algorithm appropriate to *any* surface vessel in moderate *and* higher sea states. Future work will also target wave direction estimation for underway vessels by extending our PTPD approach to consider the wave encounter frequency.

CRediT authorship contribution statement

Johann A. Dirdal: Conceptualization, Methodology, Software, Investigation, Formal analysis, Writing, Visualization. **Roger Skjetne:** Conceptualization, Writing – review & editing. **Jan Roháč:** Conceptualization, Writing – review & editing. **Thor I. Fossen:** Conceptualization, Writing – review & editing, Supervision.

Declaration of competing interest

The authors declare that they have no known competing financial interests or personal relationships that could have appeared to influence the work reported in this paper.

Acknowledgments

The work was sponsored by the Research Council of Norway (RCN) through the Centre of Excellence on Autonomous Marine Operations and Systems (NTNU AMOS, RCN project 223254), and partly through the Centre for Research-based Innovation, SFI MOVE (RCN project 237929). The research was also partially funded by the ESIF, EU Operational Programme Research, Development and Education, and from the Center of Advanced Aerospace Technology (CZ.02.1.01/0.0/0.0/16 019/0000826) carried out at the Faculty of Mechanical Engineering, Czech Technical University in Prague.

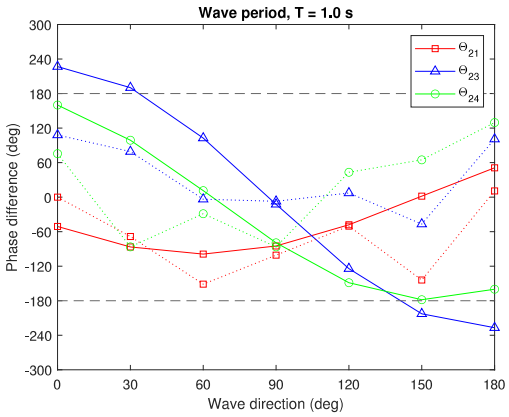

Fig. 16. The theoretical (solid) vs. estimated (dotted) phase differences $\{\Theta_{21}, \Theta_{23}, \Theta_{24}\}$ for wave period $T = 1.0$ s and sensor configuration given by Fig. 10 using $\{s_2\}$ as reference. The theoretical values were computed using (9), whereas the corresponding estimates were calculated from cross-correlations (Fig. 11) between the processed IMU data for $T = 1.0$ s.

Appendix A. Observability analysis

In this appendix, we show that the relative wave direction β and wave number k of a harmonic wave can be uniquely determined from a minimum of three noncollinear sensors, given a dynamically positioned surface vessel with small roll and pitch angles. In the following analysis, we consider two separate cases: wave number k known and wave number k unknown. As we shall see, the minimum sensor requirements stated in Theorem 1 apply in both cases. Theorem 1 shall be proven by showing that the nonlinear state–space model (10) is (locally) observable for a minimum of two phase difference measurements, which corresponds to three sensors. The forthcoming observability analysis hinges on the definitions of nonlinear observability (Nijmeijer, 1990; Marino and Tomei, 1996), which are stated below for convenience.

Definition 1. The system

$$\begin{aligned} \dot{\mathbf{x}} &= \mathbf{f}(\mathbf{x}), \quad \mathbf{x} \in \mathbb{R}^n, \\ \mathbf{z} &= \mathbf{h}(\mathbf{x}), \end{aligned} \tag{A.1}$$

is said to be locally observable in U_0, a neighborhood of the origin, if

$$\operatorname{rank}\{d\mathbf{h}, \dots, d(L_{\mathbf{f}}^{n-1}\mathbf{h})\} = n, \quad \forall \mathbf{x} \in U_0, \tag{A.2}$$

If (A.2) holds for every $\mathbf{x} \in \mathbb{R}^n$ we say that the system is observable.

Definition 2. The observation space $\mathbb{O}$ of the system (A.1) is the linear space (over $\mathbb{R}^n$)

$$\mathbb{O} = \operatorname{span}\{L_{\mathbf{f}}^{n-1} h_i\}, \quad i = 1, \dots, p.$$

The observability codistribution is given by the observation space by

$$d\mathbf{h} = \operatorname{span}\{d\mathbf{H}(\mathbf{x}) \ : \ \mathbf{H} \in \mathbb{O}\},$$

where

$$d\mathbf{H} = \frac{\partial \mathbf{H}}{\partial x_1} dx_1 + \frac{\partial \mathbf{H}}{\partial x_2} dx_2 + \cdots + \frac{\partial \mathbf{H}}{\partial x_n} dx_n.$$

Case A: Wave number known

Sensors $N = 2$

If we assume the wave number to be a known quantity, then the state–space model in (10) can be reduced to the following scalar system

$$\begin{aligned} \dot{x} &= 0, \\ z = h(x) &= k \begin{bmatrix} R_{12}\cos\alpha_{12} & R_{12}\sin\alpha_{12} \end{bmatrix} \begin{bmatrix} \cos x \\ \sin x \end{bmatrix}, \end{aligned} \tag{A.3}$$

where $z = \Theta_{12}$ and $x = \beta \in (-\pi, \pi]$. The measurement equation can be expanded and written more compactly as

$$z = kR_{12}\cos(x - \alpha_{12}),$$

which, for a single phase difference $z = \Theta_{12}$ (two sensors), has two solutions given by $\pm(x - \alpha_{12})$. Hence, (A.3) is not observable from a single pair of sensors.

Sensors $N = 3$

Adding an additional sensor, (A.3) now becomes

$$\begin{aligned} \dot{x} &= 0, \\ \mathbf{z} = \mathbf{h}(x) &= \begin{bmatrix} R_{12}\cos\alpha_{12} & R_{12}\sin\alpha_{12} \\ R_{13}\cos\alpha_{13} & R_{13}\sin\alpha_{13} \end{bmatrix} \begin{bmatrix} \cos x \\ \sin x \end{bmatrix}, \end{aligned} \tag{A.4}$$

where $\mathbf{z} = [\Theta_{12}, \ \Theta_{13}]^\top$ and $x = \beta \in (-\pi, \pi]$. The system above can be condensed by defining constants a_1, a_2, b_1, b_2 such that

$$\mathbf{h}(x) = \begin{bmatrix} h_1 \\ h_2 \end{bmatrix} = \begin{bmatrix} a_1 & b_1 \\ a_2 & b_2 \end{bmatrix} \begin{bmatrix} \cos x \\ \sin x \end{bmatrix} = \begin{bmatrix} a_1\cos x + b_1 \sin x \\ a_2 \cos x + b_2 \sin x \end{bmatrix}.$$

The observation space $\mathbb{O}$ (Definition 2) of (A.4) is determined by computing the Lie derivatives up to $n = 1$, i.e.,

$$L_f^0 \mathbf{h} = [h_1, \ h_2]^\top,$$

which yields the observation space

$$\begin{aligned} \mathbb{O} &= \operatorname{span}\{h_1, h_2\} \\ &= \operatorname{span}\{a_1 \cos x + b_1 \sin x, a_2 \cos x + b_2 \sin x\}. \end{aligned}$$

Using this result, the observability codistribution can be formed as

$$\begin{aligned} d\mathbf{H} = \frac{\partial \mathbf{h}}{\partial x} dx &= \begin{bmatrix} \frac{\partial h_1}{\partial x} & \frac{\partial h_2}{\partial x} \end{bmatrix}^\top dx \\ &= \begin{bmatrix} -a_1 \sin x + b_1 \cos x \\ -a_2 \sin x + b_2 \cos x \end{bmatrix} dx \\ &= \begin{bmatrix} -a_1 & b_1 \\ -a_2 & b_2 \end{bmatrix} \begin{bmatrix} \sin x \\ \cos x \end{bmatrix} dx, \end{aligned}$$

and, finally, we get

$$\begin{aligned} d\mathbf{h} &= \operatorname{span}\{d\mathbf{H}\} \\ &= \operatorname{span}\left\{ \begin{bmatrix} -a_1 & b_1 \\ -a_2 & b_2 \end{bmatrix} \begin{bmatrix} \sin x \\ \cos x \end{bmatrix} dx \right\}. \end{aligned}$$

The observability codistribution $d\mathbf{h}$ will have full rank as long as the above coefficient matrix is non-singular. This condition can easily be checked by evaluating when the determinant is zero, i.e.,

$$\det\left(\begin{bmatrix} -a_1 & b_1 \\ -a_2 & b_2 \end{bmatrix} \right) = -a_1 b_2 + b_1 a_2 = 0.$$

Inserting the expressions for a_1, a_2, b_1, b_2 into the above expression and simplifying it, yields

$$k^2 R_{12} R_{13} \sin(\alpha_{12} - \alpha_{13}) = 0.$$

Since $k, R_{12}, R_{13} > 0$, the above expression is zero only when the sensors lie on the same line, i.e., $\alpha_{12} = \alpha_{13}$. Hence, for $N = 3$ (three sensors) we have from Definition 1 that

$$\operatorname{rank}\{d\mathbf{h}\} = 1 = n \quad \forall x \in (-\pi, \pi] \subseteq \mathbb{R},$$

as long as the sensors are arranged in a noncollinear configuration. Since x is only defined between $(-\pi, \pi]$, which is a subset of $\mathbb{R}$, the system (A.4) is by definition *locally* observable.

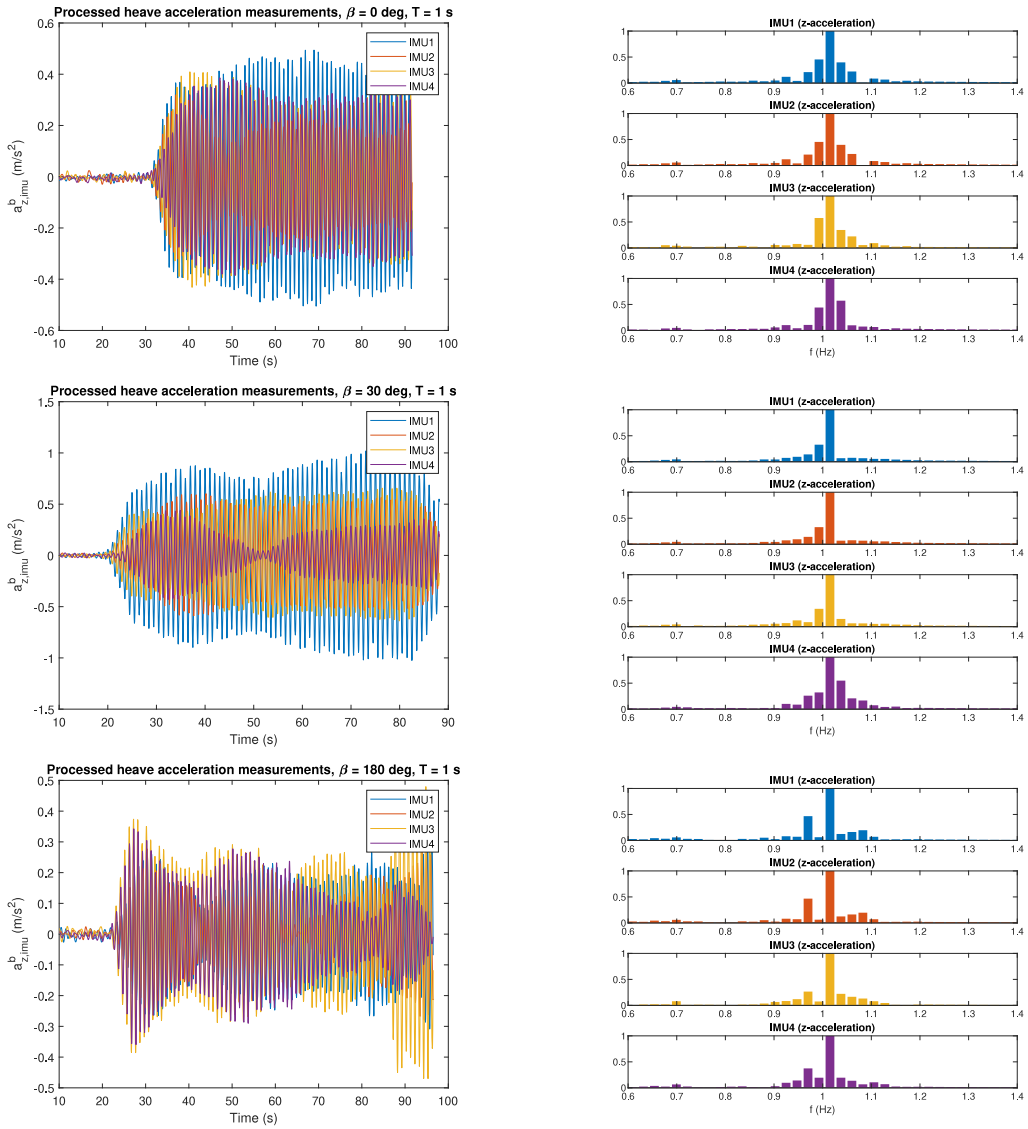

Fig. 17. (a) Heave accelerations (after processing) for wave experiments with period $T = 1.0$ s and wave directions $\{0°, 30°, 180°\}$, and (b) the corresponding FFTs. The FFTs were normalized by dividing all values in each respective plot by the corresponding maximum. The peak wave frequency in all the FFTs is located at $f = 1.015$ Hz, which corresponds to a wave period $T = 0.985$ s.

Case B: Wave number unknown

Sensors $N = 2$

If we assume the wave number to be an unknown quantity, then the state–space model in (10) reduces to

$$\dot{\mathbf{x}} = \mathbf{0},$$
$$z = h(\mathbf{x}) = \begin{bmatrix} R_{12}\cos\alpha_{12} & R_{12}\sin\alpha_{12} \end{bmatrix} \begin{bmatrix} x_2\cos x_1 \\ x_2 \sin x_1 \end{bmatrix}, \tag{A.5}$$

where $z = \Theta_{12}$, $\mathbf{x} = [x_1,\ x_2]^\top = [\beta,\ k]^\top$, and $x_1 \in (-\pi, \pi]$ and $x_2 \in \mathbb{R}^+$. The measurement equation can be expanded and written more compactly as

$$z = R_{12}x_2\cos(x_1 - \alpha_{12}),$$

which, for a single phase difference $z = \Theta_{12}$ (two sensors), has multiple solutions. Hence, the system (A.5) is not observable from a single pair of sensors.

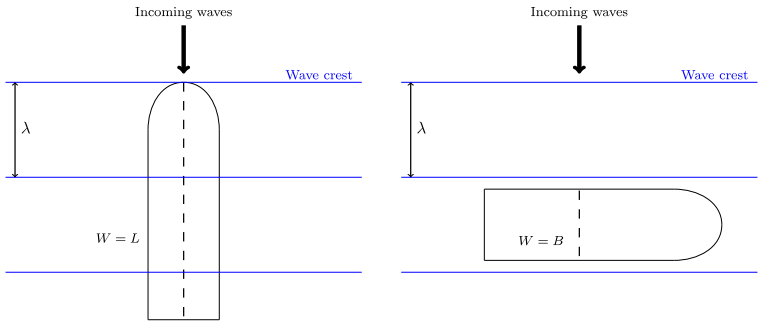

Fig. 18. The length of the wave trajectory W (represented by dashed lines) depends on the relative wave direction β. When $\beta = 180°$ (left), the vessel will filter the waves (shown in blue) passing through it as the wavelength $\lambda < W = L$, where L is the vessel length. However, when $\beta = 90°$ (right), the vessel motion responses will be unaffected by filtering as $\lambda > W = B$, where B is the vessel beam.

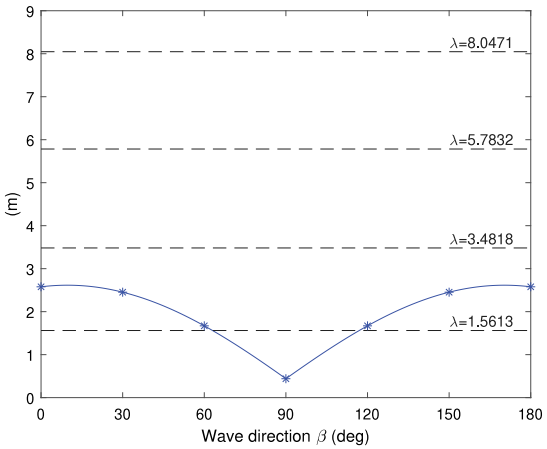

Fig. 19. The wave trajectory distance W (solid blue line) computed from (31) vs. experimental wavelengths λ (dashed lines). The value of W associated with each experimental wave direction β is indicated with an asterisk. The length and beam dimensions of the model ship used in the experiments are $L = 2.58$ m and $B = 0.44$ m, respectively. For each wave period $T = 1.0$ s, 1.5 s, 2.0 s, and 2.5 s, the corresponding wavelength $\lambda = 2\pi/k$ is computed using (21) with $d = 1.5$ m.

Sensors $N = 3$

Adding an additional sensor, (A.5) now becomes

$$\dot{\mathbf{x}} = \mathbf{0},$$
$$\mathbf{z} = \mathbf{h}(\mathbf{x}) = \begin{bmatrix} R_{12}\cos\alpha_{12} & R_{12}\sin\alpha_{12} \\ R_{13}\cos\alpha_{13} & R_{13}\sin\alpha_{13} \end{bmatrix} \begin{bmatrix} x_2\cos x_1 \\ x_2\sin x_1 \end{bmatrix}, \tag{A.6}$$

where $\mathbf{z} = [\Theta_{12},\ \Theta_{13}]^\top$, $\mathbf{x} = [x_1,\ x_2]^\top = [\beta,\ k]^\top$, and $x_1 \in (-\pi, \pi]$ and $x_2 \in \mathbb{R}^+$. The system above can be condensed by defining constants a_1, a_2, b_1, b_2 such that

$$\mathbf{h}(\mathbf{x}) = \begin{bmatrix} h_1 \\ h_2 \end{bmatrix} = \begin{bmatrix} a_1 & b_1 \\ a_2 & b_2 \end{bmatrix} \begin{bmatrix} x_2\cos x_1 \\ x_2\sin x_1 \end{bmatrix} = \begin{bmatrix} a_1x_2\cos x_1 + b_1x_2\sin x_1 \\ a_2x_2\cos x_1 + b_2x_2\sin x_1 \end{bmatrix}.$$

The observation space $\mathbb{O}$ (Definition 2) of (A.6) is then determined by computing the Lie derivatives up to $n = 2$, i.e.,

$$L_{\mathbf{f}}^0\mathbf{h} = [h_1,\ h_2]^\top,$$
$$L_{\mathbf{f}}^1\mathbf{h} = \frac{\partial \mathbf{h}}{\partial \mathbf{x}}\mathbf{f} = \mathbf{0}, \quad \text{since } \mathbf{f}(\mathbf{x}) = \mathbf{0},$$

which yields the observation space

$$\mathbb{O} = \text{span}\{h_1, h_2\}$$
$$= \text{span}\{a_1x_2\cos x_1 + b_1x_2\sin x_1, a_2x_2\cos x_1 + b_2x_2\sin x_1\}.$$

Using this result, the observability codistribution can be formed as

$$d\mathbf{H} = \frac{\partial \mathbf{h}}{\partial x_1}dx_1 + \frac{\partial \mathbf{h}}{\partial x_2}dx_2 = \underbrace{\begin{bmatrix} \frac{\partial h_1}{\partial x_1} & \frac{\partial h_1}{\partial x_2} \\ \frac{\partial h_2}{\partial x_1} & \frac{\partial h_2}{\partial x_2} \end{bmatrix}}_{\partial \mathbf{h}/\partial \mathbf{x}} \begin{bmatrix} dx_1 \\ dx_2 \end{bmatrix}$$
$$= \begin{bmatrix} -a_1x_2\sin x_1 + b_1x_2\cos x_1 & a_1\cos x_1 + b_1\sin x_1 \\ -a_2x_2\sin x_1 + b_2x_2\cos x_1 & a_2\cos x_1 + b_2\sin x_1 \end{bmatrix} \begin{bmatrix} dx_1 \\ dx_2 \end{bmatrix},$$

with

$$d\mathbf{h} = \text{span}\{d\mathbf{H}\}.$$

The observability codistribution $d\mathbf{h}$ will have full rank as long as the Jacobian $\partial\mathbf{h}/\partial\mathbf{x}$ is non-singular. This condition can easily be checked by evaluating the determinant, i.e.,

$$\det\left(\begin{bmatrix} -a_1x_2\sin x_1 + b_1x_2\cos x_1 & a_1\cos x_1 + b_1\sin x_1 \\ -a_2x_2\sin x_1 + b_2x_2\cos x_1 & a_2\cos x_1 + b_2\sin x_1 \end{bmatrix}\right)$$
$$= (-a_1x_2\sin x_1 + b_1x_2\cos x_1)(a_2\cos x_1 + b_2\sin x_1)$$
$$- (a_1\cos x_1 + b_1\sin x_1)(-a_2x_2\sin x_1 + b_2x_2\cos x_1)$$
$$= -a_1b_2x_2(\sin^2 x_1 + \cos^2 x_1)$$
$$+ b_1a_2x_2(\sin^2 x_1 + \cos^2 x_1)$$
$$= x_2(-a_1b_2 + b_1a_2).$$

Inserting the expressions for a_1, a_2, b_1, b_2 into the equation above, simplifying, and equating it to zero, yields

$$x_2R_{12}R_{13}\sin(\alpha_{12} - \alpha_{13}) = 0.$$

Since $x_2, R_{12}, R_{13} > 0$, the above expression is zero only when the sensors lie on the same line, i.e., $\alpha_{12} = \alpha_{13}$. Hence, for $N = 3$ (three sensors), we have from Definition 1 that

$$\text{rank}\{d\mathbf{h}\} = 2 = n \quad \forall x_1 \in (-\pi, \pi],\ \forall x_2 \in \mathbb{R}^+,$$

as long as the sensors are arranged in a noncollinear configuration. Since x_1 and x_2 are only defined in $(-\pi, \pi]$ and $\mathbb{R}^+$, respectively, which are both subsets of $\mathbb{R}$, the system in (A.6) is by definition *locally* observable.

Appendix B. Finding an expression of the wave trajectory distance

In this appendix, we derive an analytical expression of the wave trajectory distance through the vessel (i.e., the vessel length as seen by the waves) for a box-shaped vessel. With this expression, we can quantitatively assess when high-frequency filtering due to the vessel is likely to influence the measured motion responses for different wave periods and wave directions.

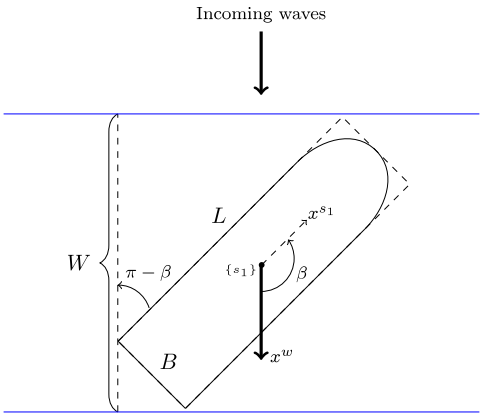

Fig. B.20. A vessel with length L and beam B dimensions measured at the waterline, oriented at an angle β relative to the incoming harmonic waves (wave crests shown in blue). The vessel hull has been approximated with a rectangle of length L and width B to simplify analysis. The definitions of the wave direction β, the tangent wave frame $\{w\}$ with wave propagation axis x^w, and reference sensor $\{s_1\}$ with sensor axis x^{s_1} are given in Fig. 1. The wave trajectory distance W is the distance the wave should travel across the vessel (i.e., the total distance in which the wave is in contact with the vessel).

Consider a vessel with length L and beam B measured at the waterline, oriented at an angle β relative to the incoming harmonic waves, as shown in Fig. B.20. In general, the first point on the vessel that the wave will affect is the corner closest to the initial wave, whereas the final exit point will be the diagonally-opposite corner. Using rudimentary trigonometric identities, the distance between these points along the wave propagation axis x^w can be expressed as

$$W = L|\cos\beta| + B|\sin\beta|, \tag{B.1}$$

where W is the wave trajectory distance and β is the relative wave direction. The maximum wave trajectory distance can be determined by taking the derivative of (B.1) with respect to β, which yields the following expression

$$\frac{dW}{d\beta} = L\left(\frac{-\cos\beta\sin\beta}{|\cos\beta|}\right) + B\left(\frac{\cos\beta\sin\beta}{|\sin\beta|}\right) = 0$$
$$\Rightarrow |\tan\beta| = \frac{B}{L},$$

and has four possible solutions

$$\beta = \pm\arctan(B/L) \text{ and } \beta = \pi \pm \arctan(B/L). \tag{B.2}$$

When the vessel is oriented at each of these wave directions, two of the corners will be furthest apart along the axis x^w. Hence, the wavelength λ should ideally be greater than W when β is given by (B.2) to avoid high-frequency filtering for all wave directions in the recorded motion responses.

References

Aranovskiy, S.V., Bobtsov, A.A., Kremlev, A.S., Luk'yanova, G.V., 2007. A robust algorithm for identification of the frequency of a sinusoidal signal. J. Comput. Syst. Sci. Int. 46 (3).

Barber, N., Doyle, D., 1956. A method of recording the direction of travel of ocean swell. Deep Sea Res. (1953) 3 (3).

Belleter, D.J., Galeazzi, R., Fossen, T.I., 2015. Experimental verification of a global exponential stable nonlinear wave encounter frequency estimator. Ocean Eng. 97.

Brodtkorb, A.H., Nielsen, U.D., Sørensen, A.J., 2018. Sea state estimation using vessel response in dynamic positioning. Appl. Ocean Res. 70.

Brown, R.G., Hwang, P.Y.C., 1997. Introduction to Random Signals and Applied Kalman Filtering: With MATLAB Exercises and Solutions, third ed. Wiley, New York, NY, URL: https://cds.cern.ch/record/680442.

de Souza, F.L., Tannuri, E.A., de Mello, P.C., Franzini, G., Mas-Soler, J., Simos, A.N., 2018. Bayesian estimation of directional wave-spectrum using vessel motions and wave-probes: Proposal and preliminary experimental validation. J. Offshore Mech. Arctic Engi. 140 (4).

Donelan, M.A., Drennan, W.M., Magnusson, A.K., 1996. Nonstationary analysis of the directional properties of propagating waves. J. Phys. Oceanogr. 26 (9).

Draycott, S., Davey, T., Ingram, D.M., Day, J.L.a., Johanning, L., 2015. Using a phase-time-path-difference approach to measure directional wave spectra in FloWave. In: EWTEC Conference Proceedings. pp. 1–7.

Draycott, S., Davey, T., Ingram, D.M., Day, A., Johanning, L., 2016. The SPAIR method: Isolating incident and reflected directional wave spectra in multidirectional wave basins. Coast. Eng. 114, 265–283.

Draycott, S., Noble, D.R., Davey, T., Bruce, T., Ingram, D.M., Johanning, L., Smith, H.C., Day, A., Kaklis, P., 2018. Re-creation of site-specific multi-directional waves with non-collinear current. Ocean Eng. 152.

Duz, B., Mak, B., Hageman, R., Grasso, N., 2019. Real time estimation of local wave characteristics from ship motions using artificial neural networks. In: 14th Int. Conf. of Practical Design of Ships and Other Floating Structures. Yokohama, Japan.

Esteva, D.C., 1976. Wave direction computations with three gage arrays. In: Proc. Fifteenth Coastal Engng. Conf., (Hawaii Univ., U.S.A.: Jul. 11-17, 1976), Vol. 1, New Yo. p. 349–367.

Esteva, D.C., 1977. Evaluation of the computation of wave direction with three-gauge arrays. Technical report, Technical Paper No. 77-7, CERC, U.S. Army Corps of Engineers.

Fernandes, A.A., Gouveia, A.D., Nagarajan, R., 1988. Determination of wave direction from linear and polygonal arrays. Ocean Eng. 15 (4), 345–357.

Fernandes, A.A., Menon, H.B., Sarma, Y.V., Jog, P.D., Almeida, A.M., 2001. Wavelength of ocean waves and surf beat at Duck from array measurements. In: Proceedings of the International Symposium on Ocean Wave Measurement and Analysis, Vol. 2.

Fernandes, A.A., Sarma, Y.V., Menon, H.B., 2000. Directional spectrum of ocean waves from array measurements using phase/time/path difference methods. Ocean Eng. 27 (4), 345–363.

Fossen, T.I., 2021. Handbook of Marine Craft Hydrodynamics and Motion Control, second ed. Wiley, Chichester, West Sussex, U.K..

Fu, T.C., Fullerton, A.M., Hackett, E.E., Merrill, C., 2011. Shipboard measurement of ocean waves. In: Proceedings of the International Conference on Offshore Mechanics and Arctic Engineering - OMAE, Vol. 6.

Hardisty, J., 1988. Measurement of shallow water wave direction for longshore sediment transport. Geo-Mar. Lett. 8 (1).

Haseltine, E.L., Rawlings, J.B., 2005. Critical evaluation of extended Kalman filtering and moving-horizon estimation. Ind. Eng. Chem. Res. 44 (8).

Heyn, H.M., Udjus, G., Skjetne, R., 2017. Distributed motion sensing on ships. In: OCEANS 2017 - Anchorage, Vol. 2017-January.

Holthuijsen, L.H., 2007. Waves in Oceanic and Coastal Waters. Cambridge University Press.

Julier, S., Uhlmann, J., 2004. Unscented filtering and nonlinear estimation. Proc. IEEE 92 (3).

Kandepu, R., Imsland, L., Foss, B.A., 2008. Constrained state estimation using the unscented Kalman filter. In: 2008 Mediterranean Conference on Control and Automation - Conference Proceedings, MED'08.

Luo, L., Liu, S., Li, J., Jia, W., 2020. Deterministic reconstruction and reproduction of multi-directional irregular waves based on linear summation model. Ocean Eng. 198, 106952.

Mak, B., Düz, B., 2019. Ship as a wave buoy: Using simulated data to train neural networks for real time estimation of relative wave direction. In: Proceedings of the International Conference on Offshore Mechanics and Arctic Engineering - OMAE, Vol. 9.

Marino, R., Tomei, P., 1996. Nonlinear Control Design: Geometric, Adaptive and Robust. Prentice Hall International (UK) Ltd, GBR.

Nielsen, U.D., 2006. Estimations of on-site directional wave spectra from measured ship responses. Mar. Struct. 19 (1).

Nielsen, U.D., 2007. Response-based estimation of sea state parameters - influence of filtering. Ocean Eng. 34 (13).

Nielsen, U.D., 2008. The wave buoy analogy - estimating high-frequency wave excitations. Appl. Ocean Res. 30 (2).

Nielsen, U.D., 2017. A concise account of techniques available for shipboard sea state estimation. Ocean Eng. 129.

Nielsen, U.D., Brodtkorb, A.H., Sørensen, A.J., 2019. Sea state estimation using multiple ships simultaneously as sailing wave buoys. Appl. Ocean Res. 83.

Nielsen, U.D., Dietz, J., 2020. Estimation of sea state parameters by the wave buoy analogy with comparisons to third generation spectral wave models. Ocean Eng. 216.

Nijmeijer, H., 1990. Nonlinear Dynamical Control Systems. Springer New York, New York, NY.

Pascal, R., Bryden, I., 2011. Directional spectrum methods for deterministic waves. Ocean Eng. 38 (13).

Pascal, R., Lucas, J., Ingram, D., Bryden, I., 2009. Assessing and improving the Edinburgh curved wave tank. In: Proceedings of the International Offshore and Polar Engineering Conference.

Pascoal, R., Guedes Soares, C., 2009. Kalman filtering of vessel motions for ocean wave directional spectrum estimation. Ocean Eng. 36 (6–7).

Price, W., Bishop, R., 1974. Probabilistic Theory of Ship Dynamics. Chapman and Hall, London.

Simon, D., 2010. Kalman filtering with state constraints: A survey of linear and nonlinear algorithms. IET Control Theory Appl. 4 (8).

Tannuri, E.A., Sparano, J.V., Simos, A.N., Da Cruz, J.J., 2003. Estimating directional wave spectrum based on stationary ship motion measurements. Appl. Ocean Res. 25 (5).

Udjus, G., 2017. Force Field Identification and Positioning Control of an Autonomous Vessel Using Inertial Measurement Units (MSc Thesis). Norwegian University of Science and Technology, Trondheim, p. 85.

Waals, O.J., Aalbers, A.B., Pinkster, J.A., 2002. Maximum likelihood method as a means to estimate the directional wave spectrum and the mean wave drift force on a dynamically positioned vessel. In: Proceedings of the International Conference on Offshore Mechanics and Arctic Engineering - OMAE, Vol. 4.

B A phase-time-path-difference approach for online wave direction and wave number estimation from measured ship motions in zero and forward speed using a single inertial measurement unit

Johann A Dirdal, Roger Skjetne, Jan Roháč, and Thor I Fossen. "A phase-time-path-difference approach for online wave direction and wave number estimation from measured ship motions in zero and forward speed using a single inertial measurement unit". *Ocean Engineering* 288 (2023). DOI: 10.1016/j.oceaneng.2023.116131

Ocean Engineering 288 (2023) 116131

Contents lists available at ScienceDirect

Ocean Engineering

journal homepage: www.elsevier.com/locate/oceaneng

A phase-time-path-difference approach for online wave direction and wave number estimation from measured ship motions in zero and forward speed using a single inertial measurement unit

Johann A. Dirdal [a,*], Roger Skjetne [b], Jan Roháč [c], Thor I. Fossen [a]

[a] Department of Engineering Cybernetics, Norwegian University of Science and Technology (NTNU), NO-7491 Trondheim, Norway
[b] Department of Marine Technology, Norwegian University of Science and Technology (NTNU), NO-491 Trondheim, Norway
[c] Department of Measurement, Faculty of Electrical Engineering, Czech Technical University in Prague, Prague, Czech Republic

ARTICLE INFO

Keywords:
Rigid body
Shipboard wave estimation
PTPD
Signal-based
Forward speed
IMU
Kalman filter

ABSTRACT

This study investigates the potential capability of a relatively new and unexplored signal-based approach for shipboard wave estimation. The approach uses the phase-time-path-differences (PTPDs) from an array of shipboard sensors to uniquely resolve the wave propagation direction and wave number. We derive a kinematic PTPD model accounting for forward vessel speed and assess its theoretical foundation to model the sensor delays on a rigid body. The forward-speed PTPD model is structurally equivalent to the zero-speed model considered in previous works, thus retaining the same observability results provided by a noncollinear array of a minimum of three sensors. Moreover, based on the outlined theory and PTPD model, we propose a methodology to estimate the main wave propagation direction and wave number online by employing a fast Fourier transform (FFT), an unscented Kalman filter (UKF), and a rigid-body measurement transformation based on a *single* inertial measurement unit (IMU). Provided that the vessel in question can be considered a rigid body, a single IMU is sufficient to obtain the desired wave quantities instead of three IMUs, as initially proposed in our previous work. Additionally, our methodology incorporates a novel frequency threshold to avoid distorted wave components caused by the effect of vessel filtering. The performance of our PTPD method is evaluated on data collected from a wave tank and full-scale experiments involving a vessel with zero and non-zero forward speed. The results show very good agreement with the reference wave values reported from a commercial wave radar and wave buoys operating in proximity to the vessel, indicating that our proposed method is competitive with existing wave measurement technology in terms of accuracy and online performance while being cheap, easy to install, flexible, and robust against environmental influences.

1. Introduction

Accurate information about the propagation direction and frequency characteristics of ocean waves is essential for various maritime activities. Ship captains rely on this data to chart safer and more efficient routes, reducing wave-related impacts and potential danger. Notably, the risk of wave-induced rolling – particularly parametric rolling – is a chief concern, capable of causing cargo loss and, in extreme cases, vessel capsizing. Additionally, in dynamic positioning (DP) applications, knowing the wave direction aids in aligning the vessel with the wave disturbance (a process known as weather-vaning (Kim and Kim, 2014)) to minimize control forces and increase stability and safety onboard. In the context of DP, the wave frequency also plays a crucial role for filtering out oscillatory motions from entering the feedback loop, thereby improving fuel efficiency and reducing actuator wear (Fossen, 2021). Moreover, knowledge about the wave propagation direction and wave number/frequency can, in general, serve as valuable input to several existing sea state estimation frameworks (e.g., Brodtkorb et al. (2018)) to improve the quality of wave estimations.

The physical distance between a pair of sensors situated on the ocean surface induces a delay between the wave elevation measurements recorded by them. This delay manifests itself as either a *phase*, *time*, or *path* difference (PTPD), which depends on the distance between the sensors, the propagation speed of the waves passing through the bodies containing the sensors, and the angle at which the waves approach them. Many studies have investigated the capabilities of using

* Corresponding author.
E-mail addresses: johann.a.dirdal@ntnu.no (J.A. Dirdal), roger.skjetne@ntnu.no (R. Skjetne), xrohac@fel.cvut.cz (J. Roháč), thor.fossen@ntnu.no (T.I. Fossen).

https://doi.org/10.1016/j.oceaneng.2023.116131
Received 5 June 2023; Received in revised form 28 September 2023; Accepted 21 October 2023

the PTPDs between a group of sensors to determine the main wave propagation direction (Esteva, 1976, 1977; Fernandes et al., 1988, 2000; Draycott et al., 2015, 2016, 2018; Luo et al., 2020). However, some practical drawbacks of these works are that they do not consider the wave number – although it can also be resolved from the same data (Donelan et al., 1996; Fernandes et al., 2001) – and they rely on a fixed stationary array of sensors, confining wave estimation to a specific geographical site. A more practical approach is to bring the sensors onboard a vessel and use the measured PTPDs to resolve the wave direction (and wave number) at any desired location, stationary or while moving. However, only a few studies have considered a shipboard PTPD approach (Fu et al., 2011; Udjus, 2017; Heyn et al., 2017; Dirdal et al., 2022). Hence, the capabilities of such an approach still need more exploration in the context of shipboard wave estimation (i.e., the field concerned with inferring statistics about ocean waves from sensor measurements taken onboard a ship) by considering more realistic wave conditions.

Most of the research on shipboard wave estimation is dominated by approaches based on the wave buoy analogy (Waals et al., 2002; Tannuri et al., 2003; Nielsen, 2006; Pascal et al., 2009; Nielsen, 2017a; Brodtkorb et al., 2018). However, a significant practical drawback of such approaches is that they rely on ship-dependent transfer functions known as response amplitude operators (RAOs), which should be determined for each ship using various hydrodynamic codes. Although some recent research activities have addressed this issue by proposing strategies for more accurate RAO tuning (Nielsen et al., 2021; Mounet et al., 2022), such transfer functions are not trivial to obtain and generally subject to many uncertainties. The fact that RAOs are transfer functions also limits the theoretical validity of these model-based approaches to linear systems, which for ships at sea, is only considered valid for mild and moderate wave conditions. In contrast, signal-based approaches (e.g., PTPD) are not constrained to any particular wave climate and require no ship information, rendering them considerably more practical as wave estimation is done directly from sensor measurements. However, only a handful of signal-based techniques are commercially available and hinge on wave radars and/or laser altimeters, which are expensive, sensitive to environmental influences, and challenging to install without expert help. Although shipboard wave estimation techniques based on machine learning (Mak and Düz, 2019; Duz et al., 2019; Han et al., 2022; Mittendorf et al., 2022) are also considered signal-based, they require ship-specific datasets, thus restricting generalization to other vessels.

The PTPD approach, on the other hand, is inherently signal-based and, when coupled with inertial measurement units (IMUs) as primary sensory devices, alleviate many of the practical concerns listed above by being inexpensive, robust against environmental impact, and easy to install; without requiring any detailed ship information. Despite the many advantages, current PTPD approaches using IMUs (Udjus, 2017; Heyn et al., 2017; Dirdal et al., 2022) have only been tested with stationary model ships in wave tanks involving regular waves. Consequently, the PTPD approach with IMUs needs further investigation in more realistic wave conditions and forward speed to solidify their potential. In this regard, extending the present PTPD framework to account for forward vessel speed will significantly improve the practical feasibility of the approach, which to our knowledge, is yet to be considered.

Accurate measurements of the PTPDs are a prerequisite for successful wave estimation using the PTPD approach. In general, the PTPDs are susceptible to several sources of error, including sensor noise, sensor imperfections (e.g., nonlinear sensitivity character and non-orthogonality and misalignment between inner sensitive axes), inexact sensor locations and alignments when installed, low data sampling rate, and modeling uncertainties. Although some of the literature above has acknowledged some of these errors, only one study (Dirdal et al., 2022) has attempted a quantitative analysis in the context of shipboard IMUs. However, the latter study does not account for modeling errors caused by mismatches in the PTPD dynamics when measured on a vessel (rigid body) rather than on the sea surface. The magnitude of such errors may be significant and can explain some of the deviations observed in the wave estimation results of the latter study. Hence, it is important to consider the properties of a rigid body in the theoretical foundation of the PTPD approach for shipboard sensors.

A practical disadvantage of current PTPD approaches is that they require much hardware in the form of multiple IMUs and cables that should be connected, synchronized in time, and distances between them measured before they can be applied. When multiple sensors are considered, a reduction in the sensors' sampling rate from their maximum possible value is usually required to accommodate the increased information load associated with multiple simultaneous measurements. However, decreasing the sensor sampling rate will inadvertently affect the accuracy of the measured PTPDs (Dirdal et al., 2022), which, in turn, will affect wave estimation quality. It is, however, possible to reduce the amount of hardware to a *single* IMU by employing a rigid body measurement transformation to generate the remaining (virtual) IMU measurements. Although such a measurement transformation is not novel (Zappa et al., 2001; Kjerstad and Skjetne, 2016), no work has yet attempted to use this transformation to facilitate PTPD wave estimation.

In general, implementing a methodology based on the PTPD concept requires two main procedures: estimating the PTPDs from the sensor measurements and estimating the wave direction and wave number from the PTPDs. Although there are numerous ways of realizing such a methodology, a practically feasible methodology must leverage two essential factors: accuracy and real-time/online estimation performance—the focal points of most studies considering shipboard wave estimation. However, another factor that needs to be addressed is the lowpass wave filtering characteristics of a ship, which occur whenever the waves passing through it are sufficiently short. When this happens, the waves become distorted by the vessel, and the measured vessel responses no longer accurately reflect the true wave conditions. Although many works have shown awareness of this problem (Nielsen, 2007, 2008; de Souza et al., 2018; Nielsen et al., 2019; Nielsen and Dietz, 2020), most of the discussions are qualitative, with the main remedy being to consider other responses measured by additional complementary sensors, which are less affected by filtering (Nielsen, 2008; de Souza et al., 2018). A quantitative measure is introduced in a recent study (Dirdal et al., 2022) showing when the effect of vessel filtering is likely to occur based on the length and breadth dimensions of the vessel and its orientation relative to the incoming waves. However, there currently does not seem to exist a procedure for avoiding the distorted portion of the measured vessel responses caused by high-frequency waves, which is inevitable for any irregular sea as some of the constituent wave components are naturally high in frequency.

In this study, we extend previous findings by the following contributions. First, the theoretical foundation of the PTPD approach is rigorously assessed. From this assessment, the circumstances under which the PTPD approach may be used to model the phase difference between a pair of sensors on a rigid body are carefully identified. These conditions are also verified experimentally from data collected during wave tank experiments with a model ship in regular and irregular waves. Second, we derive a new PTPD model for vessels with short-time constant forward speed and verify it experimentally on data collected from forward speed experiments in a wave tank involving regular and irregular waves. This PTPD model is structurally equivalent to our previous zero-speed model and, hence, observable for a minimum of three noncollinear-spaced sensors. Third, based on the theory outlined, we propose a methodology for resolving the wave propagation direction and wave number online, which comprises an FFT, UKF, and a rigid-body measurement transformation based on a single IMU. Our methodology incorporates a novel frequency threshold derived from the length and breadth dimensions of the vessel to avoid distorted wave components due to the filtering effect. Finally, we assess the capabilities of our proposed method in practice by considering data

Fig. 1. Two sensors denoted s_i and s_j situated on (a) the ocean surface and (b) a rigid body. The distance between the sensors is labeled d_{ij}.

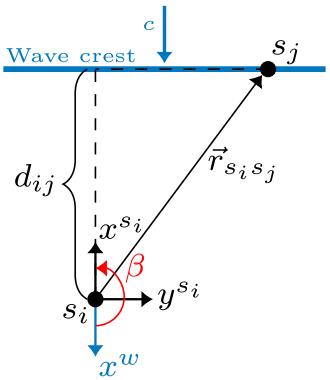

Fig. 2. A bird's-eye view of two sensors $\{s_i\}$ and $\{s_j\}$ positioned on the sea surface with a long-crested regular wave (shown in blue) passing through them with speed c. The wave should travel a distance d_{ij} to get from $\{s_j\}$ to $\{s_i\}$, which causes a constant delay between the wave elevation time series recorded in each sensor. The distance d_{ij} is expressed in the wave tangent frame $\{w\}$ with axes (x^w, y^w, z^w) and is attached to the (arbitrarily chosen) reference sensor $\{s_i\}$. The x^w axis points in the same direction as the propagating waves, z^w points upwards (out of the page), and y^w completes the right-handed coordinate system (not shown, but coincides with y^{s_i}). The relative wave direction β is defined as the counterclockwise angle from x^w to x^{s_i} (chosen arbitrarily as 180° in this example). The position of $\{s_j\}$ relative to $\{s_i\}$ is denoted by $\vec{r}_{s_i s_j}$.

gathered from a model wave tank and full-scale experiments. The full-scale experiments involve a research vessel equipped with multiple IMUs and a commercial wave radar, operating in proximity to several wave buoys on the west coast of Norway. The wave estimation results show that our proposed method is competitive with existing wave measurement technology in terms of accuracy and online performance while costing a fraction, being portable, flexible, and robust against environmental impact.

2. Theory

2.1. Main idea

A pair of spatially distributed sensors in the water will generally experience a different delay than those on a rigid body. On the ocean surface, the sensors are decoupled from each other, meaning that the delay between the wave elevation measurements is solely determined by the distance between the sensors and the propagation angle and speed of the waves passing through them (Fig. 1(a)). On a rigid body, however, the sensors are interrelated, meaning that as soon as the waves come in contact with the body, all sensor measurements will be affected simultaneously (Fig. 1(b)).

The differences between the sensor delays in the aforementioned situations can be shown quantitatively through some simple kinematics. Consider the situation in Fig. 1(a) but from a bird's-eye view later in time as illustrated in Fig. 2. The delay between the measurements in sensor $\{s_j\}$ and $\{s_i\}$ manifests itself as either a phase, time, or path difference (PTPD). The path difference d_{ij} is simply the distance along the wave propagation direction the wave must travel to get from $\{s_j\}$ to $\{s_i\}$. We obtain an expression for d_{ij} by decomposing the position vector $\vec{r}_{s_i s_j}$ in the wave tangent frame $\{w\}$, and extracting the resulting x-component. This operation is represented mathematically by

$$\mathbf{r}^w_{s_i s_j} = \mathbf{R}^w_{s_i} \mathbf{r}^{s_i}_{s_i s_j}, \tag{1}$$

where $\mathbf{r}^{s_i}_{s_i s_j} = [x_{ij}, y_{ij}, z_{ij}]^\top$ denotes the coordinate position vector of sensor $\{s_j\}$ relative to $\{s_i\}$ expressed in the sensor frame $\{s_i\}$ and $\mathbf{R}^w_{s_i}$ is a rotational transform between $\{s_i\}$ and $\{w\}$ given by

$$\mathbf{R}^w_{s_i} = \begin{bmatrix} \cos\beta & \sin\beta & 0 \\ \sin\beta & -\cos\beta & 0 \\ 0 & 0 & -1 \end{bmatrix}.$$

Carrying out the multiplication in Eq. (1) with the rotation matrix above, yields $\mathbf{r}^w_{s_i s_j} = [x_{ij}\cos\beta + y_{ij}\sin\beta, *, *]^\top$, where we have omitted the y and z components as they are not relevant. Hence, the path difference, which is the x-component of $\mathbf{r}^w_{s_i s_j}$, becomes $d_{ij} = x_{ij}\cos\beta + y_{ij}\sin\beta$, and the time it takes the wave to complete d_{ij} is simply

$$t_{ij} = \frac{d_{ij}}{c} = \frac{x_{ij}\cos\beta + y_{ij}\sin\beta}{c}, \tag{2}$$

where t_{ij} is the time difference between the measurements in $\{s_j\}$ and $\{s_i\}$, and c is the *wave celerity* or phase velocity, as it is also called. For a regular harmonic wave, the wave celerity is given by

$$c = \frac{\omega}{k}, \tag{3}$$

where ω and k denote the angular wave frequency and wave number, respectively. Substituting Eq. (3) into Eq. (2), yields

$$\Theta_{ij} = k(x_{ij}\cos\beta + y_{ij}\sin\beta), \tag{4}$$

where $\Theta_{ij} := \omega t_{ij}$ is the phase difference between the measurements in sensors $\{s_j\}$ and $\{s_i\}$.

Unfortunately, it is not straightforward to find a similar expression as Eq. (4) for the situation where the sensors are mounted on a rigid body (Fig. 1(b)). If the sensor output is evaluated as acceleration, the difference in acceleration between two arbitrary points (here labeled as s_j and s_i) on the rigid body is modeled by

$$\vec{a}_{ns_j} - \vec{a}_{ns_i} = \dot{\vec{\omega}}_{nb} \times \vec{r}_{s_i s_j} + \vec{\omega}_{nb} \times (\vec{\omega}_{nb} \times \vec{r}_{s_i s_j}), \tag{5}$$

where $\vec{a}_{ns_j}$ and $\vec{a}_{ns_i}$ are the accelerations of $\{s_j\}$ and $\{s_i\}$ relative to the navigational frame $\{n\}$,[1] $\vec{\omega}_{nb}$ represent the angular rates of the body frame $\{b\}$ relative to $\{n\}$, $\dot{\vec{\omega}}_{nb}$ is the angular acceleration, and $\vec{r}_{s_i s_j}$ is the position vector of $\{s_j\}$ relative to $\{s_i\}$. It is interesting to see from Eq. (5) that if the body simply oscillates up and down without any angular displacement (i.e., $\vec{\omega}_{nb} = \dot{\vec{\omega}}_{nb} = \vec{0}$), the accelerations in both sensors will be identical (i.e., zero delay). Hence, the measurement

[1] The navigational or North-East-Down frame $\{n\}$ is a local tangent frame with origin defined at the center of gravity of the navigated object and coordinates associated with Earth's reference ellipsoid. We consider the navigational frame to be Earth-fixed, which, for low-speed applications such as marine craft, enables $\{n\}$ to be approximated as an inertial frame of Ref. Fossen (2021).

delay perceived between sensors on a rigid body is caused by angular displacements about the body's roll, pitch, and yaw axes.

Although the cause of the sensor delays in Figs. 1(a) and 1(b) are inherently different (one is caused by the time it takes the wave to transit between the sensors, while the other is governed by the angular rates of the body induced by waves), they both share a common parameter, namely, the sensor separation distance $\vec{r}_{s_i s_j}$. If we decompose Eq. (5) in $\{b\}$ and introduce the coordinate vectors $\boldsymbol{\omega}^b_{nb} = [p, q, r]^\top$, $\dot{\boldsymbol{\omega}}^b_{nb} = [\dot{p}, \dot{q}, \dot{r}]^\top$, and $\mathbf{r}^b_{s_i s_j} = [x_{ij}, y_{ij}, z_{ij}]^\top$, we can rewrite Eq. (5) in terms of the sensor separation as

$$a^b_{ns_j,z} - a^b_{ns_i,z} = (pr - \dot{q})x_{ij} + (\dot{p} - qr)y_{ij} + (q^2 - p^2)z_{ij}, \tag{6}$$

where we have only considered the z-components of the accelerations as these are most relevant. As can be seen by studying Eqs. (4) and (6), the sensor separation $\mathbf{r}^b_{s_i s_j} = [x_{ij}, y_{ij}, z_{ij}]^\top$ and difference in acceleration (manifested as a difference in amplitude and phase between the signals) are *linearly* proportional. Using this fact, it is possible to apply the PTPD model to the situation in Fig. 1(b) by making the sensor separation sufficiently small. In this way, the sensor delays will become small enough that the models (4) and (6) almost yield the same result, and we can use the former to model the phase difference between a pair of sensors on a rigid body.[2]

2.2. A phase-time-path-difference model for surface vessels with constant forward speed

An important limitation of Eq. (4) is that it is based on a stationary pair of sensors, meaning that the model can only be applied to stationary vessels. As we shall see, we can generalize the phase difference model to account for speed such that it may be applied to situations in which the vessel is either stationary or moving.

In the following model derivation, consider the situation shown in Fig. 3, which depicts an underway vessel with a pair of distributed sensors, oriented at an angle relative to some incoming long-crested harmonic waves. Recall from Section 2.1 that the PTPD model was derived by projecting the relative sensor positions onto the wave tangent frame $\{w\}$ and extracting the resulting x-component to get the path difference d_{ij}. To carry out this operation for sensors on a rigid body, the rotational transform must be modified to account for the vessel roll and pitch angles induced by the waves (when the vessel oscillates due to the waves passing through it, the path difference d_{ij} changes, see Fig. 3(b)). Hence, a kinematic expression for d_{ij} can be obtained by transforming the body-fixed position vector $\vec{r}_{s_i s_j}$ from $\{s_i\}$ to $\{w\}$ using the rotational transform $\mathbf{R}^w_{s_i}$ according to Eq. (1), where $\mathbf{r}^{s_i}_{s_i s_j} = [x_{ij}, y_{ij}, z_{ij}]^\top$ denotes the body-fixed sensor coordinates expressed in $\{s_i\}$ and $\mathbf{R}^w_{s_i}$ is now defined by two sequences of intermediate rotations based on the zyx-convention (Fossen, 2021), i.e.,

$$\mathbf{R}^w_{s_i} = \mathbf{R}_{z,\beta}\mathbf{R}_{x,180^\circ}\mathbf{R}_{y,\theta}\mathbf{R}_{x,\phi} = \begin{bmatrix} c\beta c\theta & c\beta s\theta s\phi + s\beta c\phi & c\beta s\theta c\phi - s\beta s\phi \\ s\beta c\theta & s\beta s\theta s\phi - c\beta c\phi & s\beta s\theta c\phi + c\beta s\phi \\ s\theta & -c\theta s\phi & -c\theta c\phi \end{bmatrix}, \tag{7}$$

where $s\,\cdot = \sin(\cdot)$ and $c\,\cdot = \cos(\cdot)$. Inserting Eq. (7) into Eq. (1) and carrying out the multiplication, yields $\mathbf{r}^w_{s_i s_j} = [x_{ij}c\beta c\theta + y_{ij}(c\beta s\theta s\phi + s\beta c\phi) + z_{ij}(c\beta s\theta c\phi - s\beta s\phi), *, *]^\top$, where we have omitted the y and z components as they are not relevant. The path difference d_{ij} is simply the x-component of $\mathbf{r}^w_{s_i s_j}$ and the time it takes a wave to complete the distance d_{ij} is given by

$$t_{ij} = \frac{d_{ij}}{u_r} = \frac{x_{ij}c\beta c\theta + y_{ij}\big(c\beta s\theta s\phi + s\beta c\phi\big) + z_{ij}(c\beta s\theta c\phi - s\beta s\phi)}{u_r}, \tag{8}$$

where t_{ij} and u_r denote the corresponding time difference and x-component of the relative velocity between the waves and the vessel, respectively. In general, the velocity of the waves relative to the vessel can be expressed in the wave tangent frame $\{w\}$ as

$$\mathbf{v}^w_{bw'} = \mathbf{v}^w_{nw'} - \mathbf{v}^w_{nb} = \mathbf{v}^w_{nw'} - \mathbf{R}^w_b\mathbf{v}^b_{nb} = [c - U\cos\beta\cos\theta, *, *]^\top, \tag{9}$$

where $\mathbf{v}^w_{nw'} = [c,\ 0,\ 0]^\top$ and $\mathbf{v}^b_{nb} = [U,\ 0,\ 0]^\top$, respectively, represent the wave $\{w'\}$ and vessel $\{b\}$ velocities relative to the Earth-fixed navigational frame $\{n\}$, represented by the wave celerity c and forward vessel speed U. The rotational transform $\mathbf{R}^w_b$ is identical to Eq. (7) since $\{b\}$ and $\{s_i\}$ are aligned (see Fig. 3). Substituting u_r in Eq. (8) with the first component of Eq. (9), yields the time difference

$$t_{ij} = \frac{x_{ij}c\beta c\theta + y_{ij}\big(c\beta s\theta s\phi + s\beta c\phi\big) + z_{ij}(c\beta s\theta c\phi - s\beta s\phi)}{c - Uc\beta c\theta}. \tag{10}$$

The time difference can be converted to a phase difference Θ_{ij} by inserting Eq. (3) into Eq. (10), which gives

$$\Theta_{ij} = k\big(x_{ij}c\beta c\theta + y_{ij}(c\beta s\theta s\phi + s\beta c\phi) + z_{ij}(c\beta s\theta c\phi - s\beta s\phi)\big), \tag{11}$$

where $\Theta_{ij} := (\omega - kU\cos\beta\cos\theta)t_{ij}$. For well balanced vessels, the roll and pitch angles will on average be close to zero, i.e., $\bar{\phi} = \mathbb{E}[\phi(t)] \approx 0$ and $\bar{\theta} = \mathbb{E}[\theta(t)] \approx 0$, where $\mathbb{E}[\cdot]$ denotes the expected value. Based on this notion, we can derive the mean phase difference $\bar{\Theta}_{ij}$ by inserting the values $\bar{\phi} = 0$ and $\bar{\theta} = 0$ into Eq. (11), which yields

$$\bar{\Theta}_{ij} = k(x_{ij}\cos\beta + y_{ij}\sin\beta), \tag{12}$$

where the mean phase difference $\bar{\Theta}_{ij} := \omega_e t_{ij}$ is now defined in terms of the wave encounter frequency $\omega_e = \omega - kU\cos\beta$. By focusing on the average phase difference, we have conveniently circumvented the restrictive small-angle assumption considered in Dirdal et al. (2022). A quantitative assessment of the error impact due to the transition from Eq. (11) to Eq. (12) is given in Appendix. In the remainder of this study, we consider the phase difference as the principal sensor delay, as this quantity is most commonly treated in the literature.

2.3. Forward speed state-space model

The phase difference model (12) can be formulated into a state-space model by introducing the state vector $\mathbf{x} = [x_1,\ x_2]^\top = [\beta,\ k]^\top$ and polar coordinates ($x_{ij} = R_{ij}\cos\alpha_{ij}$, $y_{ij} = R_{ij}\sin\alpha_{ij}$), and rewriting Eq. (12) into the vector form

$$\bar{\Theta}_{ij} = \begin{bmatrix} R_{ij}\cos\alpha_{ij} & R_{ij}\sin\alpha_{ij} \end{bmatrix}\begin{bmatrix} x_2\cos x_1 \\ x_2\sin x_1 \end{bmatrix}.$$

For $N \geq 3$ number of sensors, the continuous-time state-space model can be written compactly as

$$\dot{\mathbf{x}} = \mathbf{0},$$

$$\mathbf{z} = \mathbf{h}(\mathbf{x}) = \underbrace{\begin{bmatrix} R_{12}\cos\alpha_{12} & R_{12}\sin\alpha_{12} \\ R_{13}\cos\alpha_{13} & R_{13}\sin\alpha_{13} \\ \vdots & \vdots \\ R_{1N}\cos\alpha_{1N} & R_{1N}\sin\alpha_{1N} \\ R_{23}\cos\alpha_{23} & R_{23}\sin\alpha_{23} \\ \vdots & \vdots \\ R_{2N}\cos\alpha_{2N} & R_{2N}\sin\alpha_{2N} \\ \vdots & \vdots \\ R_{(N-1)N}\cos\alpha_{(N-1)N} & R_{(N-1)N}\sin\alpha_{(N-1)N} \end{bmatrix}}_{\text{sensor configuration matrix}}\begin{bmatrix} x_2\cos x_1 \\ x_2\sin x_1 \end{bmatrix}, \tag{13}$$

[2] For sensors on a rigid body, the sensor separation and phase difference are only proportional in a limited distance range. When the sensor separation grows to infinity, the phase difference will converge to $\pm 180°$, at which point the sensor measurements will be anti-phase.

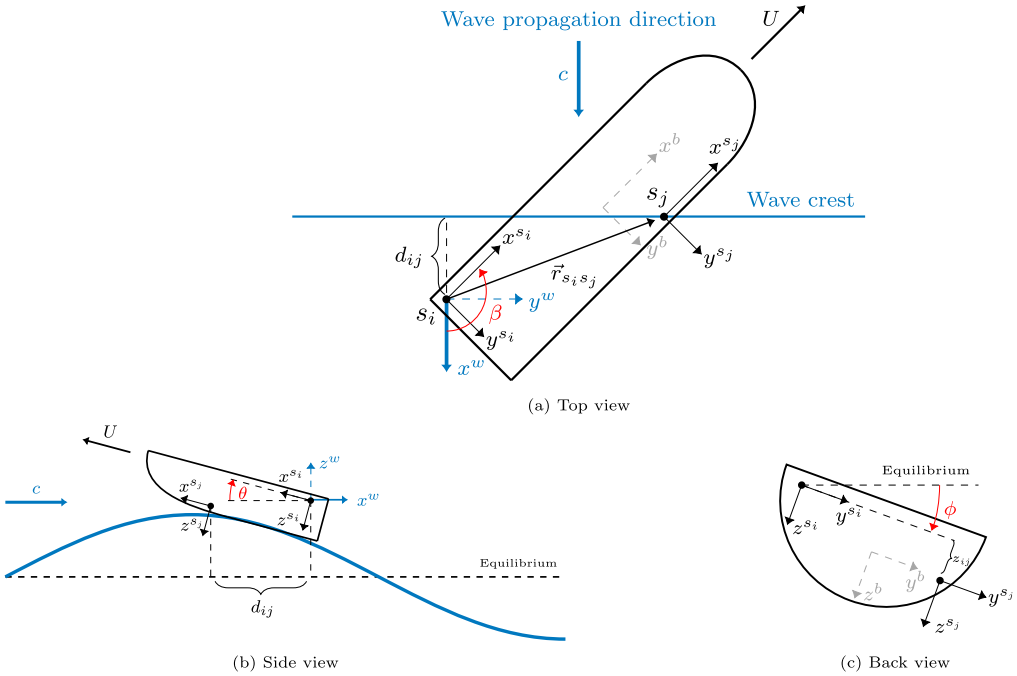

Fig. 3. Three independent situations of an underway vessel (rigid body) with constant forward speed U equipped with two sensors $\{s_i\}$ and $\{s_j\}$, oriented at an angle β relative to incoming long-crested harmonic waves with propagation speed c. The position of $\{s_j\}$ relative to $\{s_i\}$ is represented by $\vec{r}_{s_i s_j}$. The sensor axes point in the same direction as the vessel body frame $\{b\}$ (slightly faded). The tangent wave frame $\{w\}$ is attached to the vessel with axes (x^w, y^w, z^w) and origin coinciding with the (arbitrarily chosen) reference sensor $\{s_i\}$. The x^w axis points in the same direction as the propagating waves, z^w points upwards, and y^w completes the right-handed coordinate system. The distance the wave must travel to get from sensor $\{s_j\}$ to $\{s_i\}$ along the wave propagation direction is denoted d_{ij} and depends on the roll (ϕ), pitch (θ), and relative wave encounter (β) angles. The wave encounter angle β is defined as the angle from x^w to the projection of x^{s_i} onto the tangent plane $\{w\}$. Starboard incident waves are defined by $\beta \in (-180, 0]°$, whereas port incident waves are defined by $\beta \in (0, 180]°$. When $\beta = 0°$, the waves hit the stern first and we have following sea.

where $\mathbf{z} = [\bar{\Theta}_{12},\ \bar{\Theta}_{13},\ \ldots,\ \bar{\Theta}_{1N},\ \bar{\Theta}_{23},\ \ldots, \bar{\Theta}_{2N},\ \ldots, \bar{\Theta}_{(N-1)N}]^\top$. The dimension of $\mathbf{z}$ is $P_N \times 1$, where P_N is the maximum number of independent phase difference measurements associated with N, which, for nonlinear arrays, can be computed from

$$P_N = \frac{N(N-1)}{2}. \tag{14}$$

The state-space model (13) is observable for a minimum of two independent phase differences, i.e., three noncollinear sensors (see Dirdal et al. (2022) for proof). As we shall see, if the sensor is an IMU, it is sufficient to only consider a *single* IMU and use the rigid-body measurement transform (5) to generate the remaining measurements needed in Eq. (13) to uniquely resolve the wave encounter angle and wave number. It is worth emphasizing that the state-space model (13) is observable in shallow and deep waters as it only utilizes the general equation for wave celerity (phase velocity) in its derivation. Hence, the PTPD approach is valid for all water depths, provided that the vessel undergoes sufficient wave excitation.

2.4. High-frequency waves

The wave undulations on the sea surface will trigger a heave response from the vessel as they move through it. If the waves are sufficiently long, the heave response will be similar to the wave elevation, except scaled in amplitude. However, if the waves are very short, the heave response will be dissimilar from the waves due to the effect of vessel lowpass filtering (Nielsen, 2007, 2008; de Souza et al., 2018; Nielsen et al., 2019; Nielsen and Dietz, 2020; Dirdal et al., 2022). The effect of vessel filtering occurs whenever the wavelength of a particular wave is shorter than the projected wave trajectory distance through the vessel (Dirdal et al., 2022). When this happens, multiple wave crests will affect the vessel simultaneously, resulting in a distorted heave response. Hence, in order to avoid the effect of filtering, the wavelength λ should exceed the wave trajectory distance for a given wave direction β, i.e.,

$$\lambda > L|\cos\beta| + B|\sin\beta|, \tag{15}$$

where L and B represent the respective length and beam dimensions of the vessel. A quick and easy way to assess whether (15) holds for all β is to check if the given wavelength is larger than the diagonal length of the vessel (the maximum wave trajectory distance), i.e.,

$$\lambda > \sqrt{L^2 + B^2}. \tag{16}$$

If Eq. (16) holds, the effect of vessel filtering is avoided for all β and the vessel heave response will resemble the wave elevation (in other words, the vessel behaves like a buoy).

It is worth emphasizing that the effect of vessel filtering on sensor measurements is not accounted for by the PTPD model. As discussed in Section 2.1, the PTPD model merely uses the travel distance, propagation angle, and speed of the waves to quantify sensor delays and neglects any rigid body effects. It is, therefore, important to exercise caution when applying Eq. (13) to model the delay between shipboard sensors, especially if filtering is occurring. As we shall see in Section 3.3.3, this potential issue can be circumvented by employing criterion (16) in the estimation procedure.

2.5. Theoretical results

To summarize, a pair of sensors on the sea surface generally experience a different delay than those on a rigid body. However, the

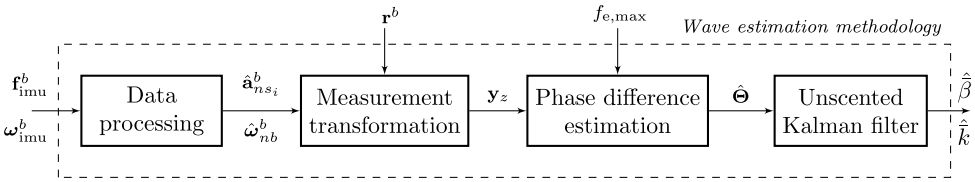

Fig. 4. A block diagram illustrating the four procedures involved in our wave estimation methodology. The input data comprises the specific force, $\mathbf{f}^b_{\mathrm{imu}}$, and angular rates, $\boldsymbol{\omega}^b_{\mathrm{imu}}$, from a shipboard IMU expressed in the vessel body frame $\{b\}$. The input data is processed to yield estimates of the linear acceleration, $\hat{\mathbf{a}}^b_{ns_i}$, and angular velocity, $\hat{\boldsymbol{\omega}}^b_{nb}$, which are then transformed to other locations on the vessel based on the desired lever arms $\mathbf{r}^b$. The z-components of the transformed accelerations are grouped into an acceleration matrix $\mathbf{y}_z$ and the phase differences $\hat{\boldsymbol{\Theta}}$ between them are estimated based on the frequency bandwidth $f_{\mathrm{e,max}}$. Finally, the phase differences are supplied to an unscented Kalman filter which yields estimates of the wave encounter angle $\hat{\bar{\beta}}$ and wave number $\hat{\bar{k}}$.

delays in both situations are proportional to the sensor separation up to a certain distance, although with different gradients. We conjecture that the forward speed PTPD model, which is simple, explicit, and observable in terms of the wave propagation direction and wave number, can be used to model the sensor delays on a rigid body given that the sensor separation distances are sufficiently small, and the waves are sufficiently long. These speculations can be compactly formulated into the following assumption:

Assumption 1. If Eq. (15) holds for a given λ and β and the separation distance between a pair of sensors on a rigid body is sufficiently small, then the state-space model (13) can accurately model the phase difference between the heave measurements in each sensor.

If Assumption 1 holds, then we are guaranteed by the observability proof of our state-space model that the relative wave propagation direction and wave number can be uniquely determined from phase differences between a group of sensors on a surface vessel (rigid body), which leads to the following theorem:

Theorem 1. *Consider a rigid body with constant forward speed $U \geq 0$, oriented at an angle β relative to the propagation direction of a regular wave (Fig. 3) with wave number k. If Assumption 1 holds, then β and k can be uniquely resolved from a minimum of three noncollinear sensors measuring the body's heave displacement or heave acceleration.*

Proof. See Dirdal et al. (2022).

It is worth mentioning that the vessel roll and pitch motion cannot be utilized with the PTPD approach as these motions do not exhibit any phase difference across various points on the body (recall that for a rigid body, angular motions are uniform for all points).

Suppose the sensors comprise a tri-axial accelerometer and gyroscope, such as an IMU. In that case, the minimum sensor requirements imposed by Theorem 1 can be relaxed to a single sensor by employing the acceleration transformation (5) to generate the other accelerations needed. This interesting result can be formulated into the following corollary:

Corollary 1.1. *If the sensor is an inertial measurement unit (IMU), then β and k can be uniquely resolved from a single IMU.*

Before we can assess the validity of these theoretical claims experimentally, we need to develop a methodology that enables us to transform the IMU measurements to different ship locations, extract the phase differences between the various measurements, and resolve the wave direction and wave number from the phase differences.

3. Methodology

Experimental verification of the theoretical results presented in Section 2.5 poses two crucial questions, namely, how to measure the phase difference between a pair of sensors and how to estimate the wave direction and wave number from the phase differences. In this section, we address these questions by proposing a methodology (Fig. 4) for estimating the desired wave quantities. As we shall see, our methodology comprises a sequence of procedures, each of which will be discussed in the following subsections.

3.1. Data processing

The data processing steps performed on the raw IMU data involve data segmentation, DC-removal, and lowpass filtering. These steps are necessary to preserve the time-localization of events and clean the data by mitigating unwanted biases and high-frequency noise.

3.1.1. Data segmentation

The ocean surface behavior is a non-stationary process, which implies that its statistical parameters, such as wave height, direction, and frequency, are time-varying. It is paramount to account for this time variability when computing these parameters to correctly assess the present ocean state. For instance, if we consider a very long data time series and apply an FFT to this data, it becomes difficult to associate which peak frequencies (and consequently which wave directions) correspond to the actual time instances in which the events took place. Hence, to preserve the time-localization of events using an FFT, it is necessary to divide the data series into (quasi-stationary) segments and process each data segment individually. This strategy is applied to the input IMU data in the estimation procedure (Fig. 4).

The specific force and angular velocity data are segmented by multiplying the developing time series with a (moving) Hanning window of a predefined length. The Hanning window alleviates the effect of spectral leakage by smoothly decreasing the input to zero near the endpoints, reducing potential discontinuities between the first and final data samples. However, since the lower and upper tails of the Hanning window are close to zero, a significant portion of the time series will effectively be ignored in the analysis. To ensure that all information is considered in the analysis, we use a 50% overlap between subsequent segments, which is common for Hanning windows.

When segmenting the data for FFT analysis, a compromise ultimately arises between the time and frequency resolution of the resulting periodograms. The compromise between time and frequency is regulated by the length of the window function considered (a long window generally implies good frequency resolution but uncertainty in the time resolution, and vice versa). An upper bound for the window length can be established if the time intervals where the waveforms are quasi-stationary are known. For ocean waves, stationarity is generally preserved for up to 15–30 min (Holthuijsen, 2007).

3.1.2. DC removal and lowpass filtering

In general, the IMU measurements are subject to several stochastic errors, which are typically separated and modeled as additive zero-mean Gaussian white noise and a time-varying bias term. Adhering to

this approach, we can use the standard three-axis accelerometer and gyroscope sensor models from Fossen (2021), which are given as

$$\begin{aligned}\mathbf{f}^b_{\text{imu}} &= \mathbf{a}^b_{ns_i} - \mathbf{g}^b + \mathbf{b}^b_{\text{acc}} + \mathbf{w}^b_{\text{acc}},\\ \boldsymbol{\omega}^b_{\text{imu}} &= \boldsymbol{\omega}^b_{nb} + \mathbf{b}^b_{\text{ars}} + \mathbf{w}^b_{\text{ars}},\end{aligned} \tag{17}$$

where $\mathbf{f}^b_{\text{imu}}$ and $\boldsymbol{\omega}^b_{\text{imu}}$ are the respective specific force and angular velocity measurements, $\mathbf{a}^b_{ns_i}$ and $\boldsymbol{\omega}^b_{nb}$ are the linear acceleration and angular velocity of the sensor frame $\{s_i\}$ with respect to $\{n\}$ (considered Earth-fixed and assumed inertial), $\mathbf{b}^b_{\text{acc}}$ and $\mathbf{b}^b_{\text{ars}}$ denote the respective sensor biases, $\mathbf{w}^b_{\text{acc}}$ and $\mathbf{w}^b_{\text{ars}}$ denote the respective sensor noises, and $\mathbf{g}^b$ denotes the gravitational acceleration. All quantities are expressed in $\{b\}$.

As can be seen by studying Eq. (17), the IMU measurements are generally centered around a non-zero value due to the sensor biases and force of gravity. If left unaccounted for, this non-zero value or DC-offset will show up in the first frequency bin of the FFT spectrum and may leak power into adjacent bins, affecting other low-frequency components. Hence, it is advantageous to remove the DC-offset before FFT processing. The latter can be achieved by simply averaging each measurement time series and subtracting the average from itself. In order to reduce the effect of high-frequency noise on the average and the angular velocity (which shall be differentiated later), we apply a lowpass filter with a cut-off frequency above the bandwidth of the considered waves (for how to select this cut-off frequency, see Section 3.3.3) to the IMU measurement segment. Hence, the final estimated acceleration and angular velocity segments are given by

$$\begin{aligned}\hat{\mathbf{a}}^b_{ns_i} &= \bar{\mathbf{f}}^b_{\text{imu}} - \mathbb{E}[\bar{\mathbf{f}}^b_{\text{imu}}],\\ \hat{\boldsymbol{\omega}}^b_{nb} &= \bar{\boldsymbol{\omega}}^b_{\text{imu}} - \mathbb{E}[\bar{\boldsymbol{\omega}}^b_{\text{imu}}],\end{aligned} \tag{18}$$

where $\bar{\mathbf{f}}^b_{\text{imu}}$ and $\bar{\boldsymbol{\omega}}^b_{\text{imu}}$ are the lowpass filtered signals and $\mathbb{E}[\cdot]$ denotes the expected value. The averaging operation in Eq. (18) tacitly assumes that the accelerometer and gyroscope biases in Eq. (17) remain more or less constant for the duration of each considered data segment. The validity of this assumption can be assessed by evaluating the accelerometer and gyroscope in-run bias stabilities found in the IMU datasheet for the time duration of the data segments. We assess the bias stability for the IMUs considered in the wave tank and full-scale experiments in Sections 4.1.3 and 5.1.2, respectively.

3.2. Measurement transformation

The acceleration at one specific point on a rigid body can be transformed to any other location, provided that the body's angular velocity and angular acceleration are known. This measurement transformation is given in Eq. (5) and can be decomposed in the body frame $\{b\}$ as follows

$$\mathbf{a}^b_{ns_j} = \mathbf{a}^b_{ns_i} + \dot{\boldsymbol{\omega}}^b_{nb} \times \mathbf{r}^b_{s_i s_j} + \boldsymbol{\omega}^b_{nb} \times (\boldsymbol{\omega}^b_{nb} \times \mathbf{r}^b_{s_i s_j}), \tag{19}$$

where $\mathbf{a}^b_{ns_j}$ is the transformed linear acceleration of virtual sensor $\{s_j\}$, $\mathbf{a}^b_{ns_i}$ is the physical linear acceleration of sensor $\{s_i\}$, $\dot{\boldsymbol{\omega}}^b_{nb}$ is the angular acceleration, and $\mathbf{r}^b_{s_i s_j}$ is the position of $\{s_j\}$ relative to $\{s_i\}$. If we replace $\mathbf{a}^b_{ns_i}$ and $\boldsymbol{\omega}^b_{nb}$ in Eq. (19) with our estimated quantities $\hat{\mathbf{a}}^b_{ns_i}$ and $\hat{\boldsymbol{\omega}}^b_{nb}$ from Section 3.1.2, we can use Eq. (19) to generate any virtual measurements needed by supplying the desired lever arms (sensor separation distances) $\mathbf{r}^b_{s_i s_j}$. The main challenge with this approach, however, is that it requires an accurate estimate of $\dot{\boldsymbol{\omega}}^b_{nb}$, which is not usually measured. In this study, we obtain estimates of the latter quantity by numerically differentiating $\hat{\boldsymbol{\omega}}^b_{nb}$. The data processing steps addressed in Section 3.1.2 ensure that the noise in $\hat{\boldsymbol{\omega}}^b_{nb}$ will not be significantly amplified by differentiation. After the desired amount of virtual accelerations have been generated, we extract the z-components of all of them and place them into an acceleration matrix $\mathbf{y}_z \in \mathbb{R}^{N\times L}$, consisting of N z-accelerations of length L.

Algorithm 1 Phase difference estimation

procedure PD($\mathbf{y}_z$, $f_{\text{e,max}}$)

$\hat{\mathbf{Y}}_z \leftarrow \text{fft}(\mathbf{y}_z)$ ▷ Compute the FFT

$\hat{\boldsymbol{\theta}}_z \leftarrow \text{atan2}\left(\text{imag}(\hat{\mathbf{Y}}_z), \text{real}(\hat{\mathbf{Y}}_z)\right)$ ▷ Compute the phase response

$\mathbf{f}_p \leftarrow \max_{0\le f\le f_{\text{e,max}}} |\hat{\mathbf{Y}}_z|$ ▷ Store the peak frequencies (within $f_{\text{e,max}}$) in a vector

for f in $\mathbf{f}_p$ **do**

$[\hat{\theta}_1, \hat{\theta}_2, \dots, \hat{\theta}_N]^\top \leftarrow \hat{\boldsymbol{\theta}}_z(f)$ ▷ Extract the phase values at frequency f

$\hat{\theta}_{ij} = \hat{\theta}_i - \hat{\theta}_j, \quad 1 \le i \le N-1, \ 2 \le j \le N, \ i < j$ ▷ Compute the phase differences for all i and j

$\hat{\boldsymbol{\theta}}(k) \leftarrow [\hat{\theta}_{12}, \hat{\theta}_{13}, \dots, \hat{\theta}_{(N-1)N}]^\top$ ▷ Store the phase differences for each f in a matrix

$k \leftarrow k + 1$

end for

return $\hat{\boldsymbol{\theta}}$

end procedure

3.3. Phase difference estimation

We estimate the phase differences between the measured waveforms by employing an FFT with a frequency threshold to avoid wave components potentially distorted by the vessel in question. The estimation procedure is shown in Algorithm 1 and compromises the following sequence of steps:

1. Compute the FFTs and phase responses of $\mathbf{y}_z$.
2. Find the peak frequency of each magnitude response within a maximum frequency threshold $f_{\text{e,max}}$.
3. Extract the phase values for each peak frequency.
4. Compute the phase differences.

In this procedure, it is tacitly assumed that the dominant frequency of the forced oscillation in heave aligns with the frequency of the external wave force. This assumption is generally valid when the ship encounters a fully developed sea with sufficiently large wave amplitude and wavelength (see Assumption 1). In the following subsections, we elaborate on additional implementation details not mentioned in Algorithm 1.

3.3.1. Zero padding

The input to Algorithm 1 is the acceleration matrix $\mathbf{y}_z \in \mathbb{R}^{N\times L}$. If L is a power of two, radix-2 FFT algorithms can be used to compute the frequency responses, which are very efficient and can reduce processing time. If L is not a power of two, radix-2 FFT algorithms may still be applied by appending zeros at the end of the time domain signals such that the total signal length becomes a power of two.

3.3.2. Tolerance threshold

The inverse tangent function used to obtain the phase response in Algorithm 1 is highly susceptible to rounding errors. As a result, the

rounding errors typically appear as noisy spikes in the computed phase response. A common strategy used to mitigate this problem is to define a tolerance threshold ϵ and zero out the values of $\hat{\mathbf{Y}}_z$ for which $|\hat{\mathbf{Y}}_z| < \epsilon$.

3.3.3. Frequency threshold

As discussed in Section 2.4, the vessel will distort wave components passing through it if the wavelengths are sufficiently short. In reality, an irregular sea comprises multiple wave components, some of which have wavelengths shorter than the wave trajectory distance through the vessel. It is, therefore, essential to avoid such wave components when processing the heave response. The latter can be achieved by only considering the frequency components within the upper threshold $f_{\text{e,max}}$ of the FFT spectrum. Apart from scaling, sinusoidal components within this range are deemed unaffected by the vessel.

For stationkeeping vessels (i.e., $U = 0$), the zero-speed upper threshold $f_{\max}$ is the frequency in which the right hand side (RHS) and left hand side (LHS) of Eq. (15) become equal, which occurs when

$$f_{\max} = \sqrt{\frac{g/2\pi}{\sqrt{L^2+B^2}} \tanh\left(\frac{2\pi d}{\sqrt{L^2+B^2}}\right)}, \tag{20}$$

where g is the gravitational constant and d is the water depth. The relationship above is derived by rewriting Eq. (15) in terms of the wave number (i.e., $k = 2\pi/\lambda$), and inserting the resulting expression for k into the dispersion relation

$$\omega^2 = kg \tanh(kd). \tag{21}$$

For underway vessels (i.e., $U > 0$), the frequency threshold (20) needs to be adjusted to account for the Doppler shift given by

$$\omega_e = |\omega - kU\cos\beta|, \tag{22}$$

where ω_e is the Doppler shifted encounter frequency. Rewriting Eq. (22) in terms of linear frequency and $f_{\max}$, yields the adjusted maximum frequency threshold $f_{\text{e,max}}$ given in terms of forward speed, i.e.,

$$f_{\text{e,max}} = \left| f_{\max} \pm \frac{UL}{L^2+B^2} \right|, \tag{23}$$

where we have used $k = 2\pi/\sqrt{L^2+B^2}$ and $\cos\beta = \pm L/\sqrt{L^2+B^2}$ (worst case scenario in which the wave trajectory distance is maximum). The latter component on the RHS of (23) should be added or subtracted depending on whether the vessel is following or moving against the waves, respectively.

3.4. Unscented Kalman filter

The state-space model (13) is inherently nonlinear, which requires nonlinear estimation techniques to resolve the desired wave quantities. Although it is possible to solve the wave direction analytically from Eq. (12), the Kalman filter framework offers several benefits over such an approach. With the Kalman filter, it is easy to incorporate uncertainties into the estimation procedure, handle multiple measurements, and simultaneously estimate the wave direction and wave number online (Dirdal et al., 2022). It is, however, necessary for the wave number to be positive, posing a constraint on the state estimate.

As discussed in Dirdal et al. (2022), the unscented Kalman filter (UKF) has certain advantages over the extended Kalman filter (EKF) when constraints are imposed on the state estimates. In short, the UKF accounts for constraints when updating the error covariance, which the EKF ultimately neglects. For this reason, the UKF was selected as our main algorithm and the following subsections explain how it may be applied to yield the desired wave quantities.

3.4.1. Algorithm

The UKF algorithm may be applied to discrete-time nonlinear dynamical systems of the form

$$\begin{aligned} \mathbf{x}_k &= \mathbf{f}(\mathbf{x}_{k-1}) + \mathbf{w}_k, \ \mathbf{w}_k \sim \mathcal{N}(\mathbf{0}, \mathbf{Q}) \\ \mathbf{z}_k &= \mathbf{h}(\mathbf{x}_k) + \mathbf{v}_k, \ \mathbf{v}_k \sim \mathcal{N}(\mathbf{0}, \mathbf{R}) \end{aligned} \tag{24}$$

where $\mathbf{x}_k := \mathbf{x}(kT_s)$ and $\mathbf{z}_k := \mathbf{z}(kT_s)$ constitute the sampled state and measurement vectors for sample time T_s and number k (not to be confused with the wave number), $\mathbf{f}$ and $\mathbf{h}$ represent nonlinear transition functions, and $\mathbf{w}_k$ and $\mathbf{v}_k$ denote white Gaussian process and measurement noise with covariance $\mathbf{Q}$ and $\mathbf{R}$, respectively. If we discretize the continuous-time state-space model (13) and compare it with Eq. (24), it is clear that the former fits the required model form with $\mathbf{f}(\mathbf{x}_{k-1}) = \mathbf{x}_{k-1}$ and $\mathbf{h}(\mathbf{x}_k)$ as before. The process and measurement noise $\mathbf{w}_k$ and $\mathbf{v}_k$ represent the expected deviation between reality and our process and measurement models. They are characterized statistically through their covariance matrices $\mathbf{Q}$ and $\mathbf{R}$, which are discussed in detail in Sections 3.4.2 and 3.4.3, respectively.

The UKF algorithm with state constraints is given in Algorithm 2; for relevant background material regarding the UKF and constraint handling, the reader is referred to Brown and Hwang (1997), Julier and Uhlmann (2004), Kandepu et al. (2008), and Simon (2010) and references therein. As a general rule, the UKF uses a deterministic sampling scheme to select its sigma points. In this paper, we have chosen the following set of sigma points

$$X_k^{(i)} = \begin{cases} \hat{\mathbf{x}}_k^-, & i = 0 \\ \hat{\mathbf{x}}_k^- + \sqrt{(M+\lambda)\hat{\mathbf{P}}_k^-}, & i = 1, \dots, M \\ \hat{\mathbf{x}}_k^- - \sqrt{(M+\lambda)\hat{\mathbf{P}}_k^-}, & i = M+1, \dots, 2M \end{cases} \tag{25}$$

where

$\lambda = \alpha^2(L+\kappa) - M$

M = dimension of state $\mathbf{x}_k$

α = spread of samples about the mean

κ = scaling factor

Sigma points outside the feasible region are projected onto the boundary using the projection

$$P(\hat{x}_2) = \begin{cases} \epsilon, & \hat{x}_2 < \epsilon \\ \hat{x}_2, & \text{otherwise} \end{cases} \tag{26}$$

where $\hat{x}_2$ is the wave number estimate and ϵ is a small positive number representing the boundary of the feasible region. The sigma points are then propagated through the nonlinear transform (13) to yield a new cloud of transformed points. The statistics of these points are then computed by weighting them together using the following sets of weights

$$W_\mu^{(0)} = \frac{\lambda}{\lambda+M}, \ W_\mu^{(0<i\leq 2M)} = \frac{1}{2(\lambda+M)}, \tag{27}$$

$$W_\sigma^{(0)} = W_\mu^{(0)} + 1 - \alpha^2 + \gamma, \ W_\sigma^{(0<i\leq 2M)} = \frac{1}{2(\lambda+M)}. \tag{28}$$

3.4.2. Process noise covariance

The conditions of the ocean environment, including wave direction and wave number, are generally time-varying. Assuming that the desired wave quantities are slowly varying, we can accommodate this variability by modifying the state-space model (13) to include white Gaussian noise with variance σ_w^2. The modified state-space model now becomes a Gaussian random walk process of the form

$$\dot{\mathbf{x}} = \mathbf{A}\mathbf{x} + \mathbf{G}\mathbf{w}, \quad \mathbf{w} \sim \mathcal{N}(\mathbf{0}, \mathbf{D}\delta(t-\tau)), \tag{29}$$

where $\mathbf{A} = \mathbf{0}_2$ (2×2 zero matrix), $\mathbf{G} = I_2$ (2×2 identity matrix), $\mathbf{D} = \sigma_w^2 I_2$, and $\delta(t-\tau)$ is the Dirac delta function. For simplicity, we

Algorithm 2 Unscented Kalman filter

procedure UKF($\hat{\mathbf{x}}_k^-, \hat{\mathbf{P}}_k^-, \mathbf{z}_k$)

$X_k^{(i)} \leftarrow \text{Sigma}(\hat{\mathbf{x}}_k^-, \hat{\mathbf{P}}_k^-)$ ▷ Compute sigma points using Eq. (25)

$X_c^{(i)} \leftarrow P(X_k^{(i)})$ ▷ Project sigma points using Eq. (26)

$\hat{\mathbf{x}}_k^- \leftarrow \sum_{i=0}^{2M} W_\mu^{(i)} X_c^{(i)}$ ▷ Compute the apriori state estimate with Eq. (27)

$\hat{\mathbf{P}}_k^- \leftarrow \{\sum_{i=0}^{2M} W_\sigma^{(i)}(X_c^{(i)} - \hat{\mathbf{x}}_k^-)(X_c^{(i)} - \hat{\mathbf{x}}_k^-)^\top\} + \mathbf{Q}$ ▷ Compute the apriori error covariance with Eq. (28)

$Z_k^{(i)} \leftarrow \mathbf{h}(X_c^{(i)})$ ▷ Propagation of sigma points using Eq. (13)

$\hat{\mathbf{z}}_k^- \leftarrow \sum_{i=0}^{2M} W_\mu^{(i)} Z_k^{(i)}$ ▷ Predicted measurement

$\hat{\mathbf{S}}_k \leftarrow \{\sum_{i=0}^{2M} W_\sigma^{(i)}(Z_k^{(i)} - \hat{\mathbf{z}}_k^-)(Z_k^{(i)} - \hat{\mathbf{z}}_k^-)^\top\} + \mathbf{R}$ ▷ Compute the innovation covariance

$\hat{\mathbf{P}}_k^{\mathbf{xz}} \leftarrow \sum_{i=0}^{2M} W_\sigma^{(i)}(X_c^{(i)} - \hat{\mathbf{x}}_k^-)(Z_k^{(i)} - \hat{\mathbf{z}}_k^-)^\top$ ▷ Compute the cross-covariance

$\mathbf{K}_k \leftarrow \hat{\mathbf{P}}_k^{\mathbf{xz}} \hat{\mathbf{S}}_k^{-1}$ ▷ Compute the Kalman gain

$\hat{\mathbf{x}}_k \leftarrow \hat{\mathbf{x}}_k^- + \mathbf{K}_k(\mathbf{z}_k - \hat{\mathbf{z}}_k^-)$ ▷ Compute posterior state estimate

$\hat{\mathbf{P}}_k \leftarrow \hat{\mathbf{P}}_k^- - \mathbf{K}_k \hat{\mathbf{S}}_k \mathbf{K}_k^\top$ ▷ Compute posterior error covariance

return $\hat{\mathbf{x}}_k, \hat{\mathbf{P}}_k$

end procedure

have used the same variance σ_w^2 to describe the variability of the wave direction and wave number. From basic control theory, it can be shown that the exact discretization of Eq. (29) is given by

$$\mathbf{x}_k = \mathbf{F}\mathbf{x}_{k-1} + \mathbf{w}_k,$$

where $\mathbf{F} = e^{T_s \mathbf{A}} = I_2$ and

$$\mathbf{w}_k = \int_{t_{k-1}}^{t_k} e^{(t_k-\tau)\mathbf{A}} \mathbf{G}\mathbf{w}(\tau) d\tau = \int_{t_{k-1}}^{t_k} \mathbf{w}(\tau) d\tau,$$

where we have simplified the latter expression by inserting the values for $\mathbf{A}$ and $\mathbf{G}$ into it. The process noise covariance $\mathbf{Q}$ is given by

$$\mathbf{Q} = \mathbb{E}[\mathbf{w}_k \mathbf{w}_k^\top] = T_s \mathbf{D} = T_s \sigma_w^2 I_2, \tag{30}$$

where $T_s = t_k - t_{k-1}$ denotes the sampling period.

3.4.3. Measurement noise covariance

Both the phase difference measurements $\mathbf{z}_k$ and measurement model $\mathbf{h}(\mathbf{x}_k)$ are subject to uncertainties that will cause discrepancies between them. The discrepancies are modeled by white Gaussian noise $\mathbf{v}_k$, which—if adequately designed (i.e., choosing the noise covariance $\mathbf{R}$ appropriately)—can account for prevalent errors. In this work, we deem errors caused by (i) submodeling and (ii) the FFT to be most fundamental to any deviations observed. It is important to address these errors to get an estimate of the uncertainties in the desired wave quantities, which, in turn, indicate whether they can be relied on or not.

The errors caused by (i) can be divided into two distinct groups: (a) errors due to the model simplification performed on Eq. (11) (i.e., averaging the instantaneous phase differences), and (b) errors resulting from the fact that we are applying a PTPD model to the phase differences on a rigid body. The phase difference error caused by (a) can be quantitatively assessed by evaluating the absolute difference between Eqs. (11) and (12), which, for an arbitrary pair of sensors, yields

$$\begin{aligned}|\Theta_{ij} - \bar{\Theta}_{ij}| = \Big| & k R_{ij}\big(c\beta c\alpha_{ij}(c\theta - 1) + c\beta s\theta s\phi s\alpha_{ij} \\ & + s\beta s\alpha_{ij}(c\phi - 1)\big) + k z_{ij}\big(c\beta s\theta c\phi - s\beta s\phi\big)\Big|.\end{aligned} \tag{31}$$

In all the wave tank experiments, the model error (31) was less than 1° for all experimental wave parameters and sensor pairs (see Appendix). We deem errors of this magnitude minor and, as we shall see, are also dominated by the error incurred from (ii). For these reasons, we neglect errors due to (a) in the measurement covariance.

In contrast to (a), model deviations caused by (b) are considerably more challenging to quantify. The challenge arises because we lack a model quantifying directly how the phase changes when a measurement is transformed using Eq. (19) (if we had such an explicit model this would render the PTPD approach redundant). In order to assess the impact of (b), we rely on experimental data to quantify the deviation between the true phase differences and those predicted by our PTPD model. The experimental results from the wave tank show that the model error caused by (b) depends on the separation distance between the sensors. Hence, if the sensors are sufficiently close, (b) can safely be neglected from the measurement noise covariance without incurring significant errors. A discussion of the sensor separation is given in Section 4.2.1.

The phase difference error associated with (ii) can be attributed to spectral leakage, which occurs whenever the considered waveform is not periodic within the given sample interval. In other words, if the actual waveform frequency is not an integer multiple of the frequency resolution, the former will not be in the exact center of an FFT frequency bin, causing a spread of power into neighboring bins. For waveforms of finite duration comprising multiple frequencies, spectral leakage will generally persist as all the frequency components will generally not be integer multiples of the frequency resolution. An analysis of the FFT phase error resulting from spectral leakage is given by Dishan (1995), who shows that the error can be quantified as

$$\tilde{\Theta} = \pi T \tilde{f}, \tag{32}$$

where $\tilde{\Theta} := \hat{\Theta} - \Theta$ is the phase error between the true and estimated phase (represented by a hat), T is the duration of the considered waveform, and $\tilde{f} := \hat{f}_n - f$ is the frequency error between the true frequency and estimated frequency bin $\hat{f}_n = n/T$ for $n = 0, 1, \ldots, L/2-1$, where L denotes the transform length. The maximum frequency error occurs whenever the true frequency resides in the exact middle of two frequency bins, i.e.,

$$\tilde{f}_{\max} = \frac{\Delta}{2},$$

where $\Delta = 1/T$ is the frequency resolution. Inserting the latter into Eq. (32), yields the maximum phase error, i.e.,

$$\tilde{\Theta}_{\max} = \frac{\pi}{2}. \tag{33}$$

Based on Eq. (33), the upper error bound of the computed phase difference $\Theta_{ij} = \Theta_i - \Theta_j$ becomes

$$|\tilde{\Theta}_{ij}| = |\hat{\Theta}_{ij} - \Theta_{ij}| = |(\hat{\Theta}_i - \Theta_i) - (\hat{\Theta}_j - \Theta_j)| = |\tilde{\Theta}_i - \tilde{\Theta}_j| \le |\tilde{\Theta}_i| + |\tilde{\Theta}_j| \le \pi. \tag{34}$$

Although the theoretical error bound (34) is significant and may dissuade the FFT for phase estimation, in practice, we see that employing a Hanning window with the FFT leads to very accurate phase difference estimates by reducing spectral leakage.[3] Moreover, the main focus of this study is not optimality but rather a proof of concept of the PTPD approach to rigid bodies. As we shall see, the FFT algorithm is sufficient to achieve the latter goal.

The error bound (34) indicates that the true phase difference can be located *anywhere* within $\pm\pi$ of the estimated phase difference. This

[3] Multiple regular wave experiments were considered, and the phase difference estimates produced by the FFT with a Hanning window and curve fitting (considered ground truth) agreed very well.

Table 1
A summary of the initial state estimates, covariances, and internal parameters used in the UKF.

UKF initialization	$\hat{\mathbf{x}}_0 = [0,\ 0.05]^\top$ $\hat{\mathbf{P}}_0 = \mathrm{diag}([\frac{1}{3}\pi^2,\ 2])$
Process and measurement covariance	Wave tank experiments $\mathbf{Q} = T_s\sigma_w^2 I_2, \quad \sigma_w = 1\times10^{-3}$ $\mathbf{R} = \frac{1}{3}\pi^2 I_{P_N}$ Full-scale experiments $\mathbf{Q} = T_s\sigma_w^2 I_2, \quad \sigma_w = 1\times10^{-1}$ $\mathbf{R} = \frac{1}{72}\pi^2 I_{P_N}$
UKF parameters	$M = 2, \quad \alpha = 0.01, \quad \gamma = 2, \quad \kappa = 0$

type of uncertainty is characteristic of a uniform distribution with zero mean and variance

$$\sigma^2_{\theta_{\text{fft}}} = \frac{1}{3}\pi^2. \tag{35}$$

However, the UKF algorithm requires the measurement noise $\mathbf{v}_k$ to be zero mean Gaussian distributed. To accommodate this requirement, we approximate the uniform distribution above by a Gaussian with variance (35).

It is worth highlighting that there are no uncertainties in the virtual sensor locations when using the measurement transformation (19) to generate the virtual measurements. Hence, by employing Eq. (19) we eliminate uncertainties in the sensor locations as an error source, which were considered prominent in our previous work (Dirdal et al., 2022).

3.4.4. Initial parameter settings

A summary of the initialization parameters, process and measurement covariances, and internal parameters used in Algorithm 2 are listed in Table 1. It is worth stressing that faster convergence may be achieved by initializing the wave number to the value given by the dispersion relation (21) using the frequency obtained from the FFT. In this paper, however, we chose the initial values in Table 1 to demonstrate the validity of Theorem 1.

The initially estimated error covariance $\hat{\mathbf{P}}_0$ was selected by modeling the initial wave direction error as a uniform distribution over the interval $(-\pi, \pi]$ and approximating it by a Gaussian distribution with the same variance. The wave number variance was chosen heuristically but relatively large, reflecting our uncertainty in the actual value. The process and measurement covariance, $\mathbf{Q}$ and $\mathbf{R}$, were selected based on our analysis in Sections 3.4.2 and 3.4.3. Note that the sets of values for $\mathbf{Q}$ and $\mathbf{R}$ were chosen slightly differently in the wave tank and full-scale experiments to represent the conditions of the wave environment considered. For instance, in the wave tank, the wave conditions were completely stationary (represented by a low σ_w), whereas, in the ocean, the wave conditions were considerably more variable (represented by a larger σ_w). In the full scale experiments, the measurement covariance was reduced as this yielded better estimation results. As discussed in Section 3.4.3, we deem this reduction acceptable as the FFT phase estimates were generally very close to the ground truths in the wave tank experiments.

3.5. Summary of methodology

Our complete wave direction and wave number estimation methodology is given in Algorithm 3, merging all the procedures discussed in this section into one algorithm that is recursively applied for each new data segment. The input to Algorithm 3 comprises a data segment of the raw specific force and angular velocity measurements expressed in the vessel body frame $\{b\}$ from a single IMU, the desired (virtual) locations of the other IMU measurements (i.e., sensor separation distances), and a maximum frequency threshold $f_{\max}$ denoting the bandwidth of the considered waves. The frequency threshold should not exceed the upper threshold given by Eq. (20) and, if the vessel is moving with speed U, should be adjusted to $f_{\text{e,max}}$ by considering Eq. (23) (when $U = 0$, $f_{\text{e,max}}$ reduces to $f_{\max}$). The length of the considered data segment and percentage overlap with consecutive segments are generally tunable parameters. As we shall see, these parameters regulate the trade-off between accuracy and online estimation performance and should be carefully selected.

The estimated phase differences matrix $\hat{\boldsymbol{\Theta}}$ from Algorithm 1 has dimension $P_N \times N$, which means there are N sets of phase differences pertaining to each peak frequency. For this reason, the UKF algorithm must be applied N times to account for each, potentially different, set of phase differences, which, in turn, yields N separate wave estimates. We take the average of all these estimates and report this as the final estimated wave direction and wave number.

Algorithm 3 Wave direction and wave number estimation algorithm

procedure WDN($\mathbf{f}^b_{\text{imu}}$, $\boldsymbol{\omega}^b_{\text{imu}}$, $\mathbf{r}^b$, $f_{\max}$)

$f_{\text{e,max}} \leftarrow$ Doppler($f_{\max}$) ▷ Compute the Doppler frequency threshold using (23) with vessel speed U

$\hat{\mathbf{a}}^b_{ns_i}$, $\hat{\boldsymbol{\omega}}^b_{nb} \leftarrow$ DP($\mathbf{f}^b_{\text{imu}}$, $\boldsymbol{\omega}^b_{\text{imu}}$, $f_{\text{e,max}}$) ▷ Data processing using (18) with $f_{\text{e,max}}$ as cut-off frequency

$\mathbf{y}_z \leftarrow$ MT($\hat{\mathbf{a}}^b_{ns_i}$, $\hat{\boldsymbol{\omega}}^b_{nb}$, $\mathbf{r}^b$) ▷ Measurement transformation using (19) with virtual sensor locations $\mathbf{r}^b$

$\hat{\boldsymbol{\Theta}} \leftarrow$ PD($\mathbf{y}_z$, $f_{\text{e,max}}$) ▷ Phase difference estimation given by Algorithm 1

for $i = 1 : \texttt{length}(\hat{\boldsymbol{\Theta}})$ **do**

$\hat{\mathbf{x}}$, $\hat{\mathbf{P}} \leftarrow \hat{\mathbf{x}}_0$, $\hat{\mathbf{P}}_0$ ▷ Initial state and covariance estimates given in Table 1

for $j = 1 : \texttt{length}(\mathbf{y}_z)$ **do**

$\mathbf{z} \leftarrow \hat{\boldsymbol{\Theta}}(i)$ ▷ Extract phase differences corresponding to each peak frequency

$\hat{\mathbf{x}}$, $\hat{\mathbf{P}} \leftarrow$ UKF($\hat{\mathbf{x}}$, $\hat{\mathbf{P}}$, $\mathbf{z}$) ▷ Wave direction and number estimation given by Algorithm 2

end for

$\hat{\mathbf{X}}(i) \leftarrow \hat{\mathbf{x}}$ ▷ Store final wave estimate from UKF

end for

$\hat{\bar{\beta}}$, $\hat{\bar{k}} \leftarrow \texttt{mean}\ (\hat{\mathbf{X}})$ ▷ Extract average wave direction and wave number estimates

return $\hat{\bar{\beta}}$, $\hat{\bar{k}}$

end procedure

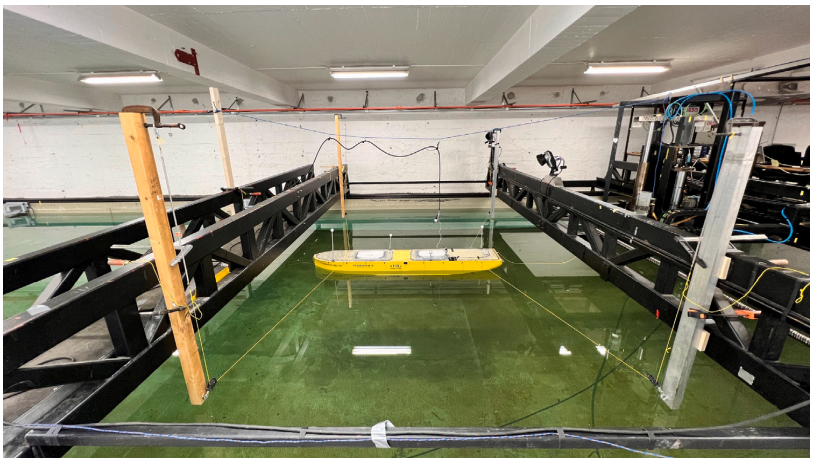

Fig. 5. The position and orientation of the model ship C/S Arctic Drillship (CSAD) were held fixed by a rope-pulley system.

4. Experimental validation of theory

4.1. Experimental design

The wave tank experiments were conducted in the NTNU marine cybernetics laboratory, which is a small wave basin with dimensions of 40 m × 6.45 m × 1.5 m. The laboratory is equipped with a wave maker, towing carriage, and real-time positioning system, making it an excellent playground for model-ship testing in regular and irregular waves.[4] We used the same model ship as in Dirdal et al. (2022), i.e., a 1:90 scaled model C/S Arctic Drillship (CSAD) equipped with several IMUs. In the following subsections, we explain the design measures taken to ensure that the assumptions of Section 2.5 were not significantly violated during data collection.

4.1.1. Constant heading and forward speed

The model ship heading and position were confined by a rope-pulley system connecting the ship to a towing carriage (Fig. 5). Each rope was attached to a spring, allowing almost free motions in heave, roll, and pitch while limiting the surge, sway, and yaw motions. The ropes were interchanged and adjusted to produce the desired boat headings.

Constant forward speed was achieved by using the towing carriage to pull the ship through the water. We considered three different carriage speeds, 0.5 m/s, 0.6 m/s, and 0.7 m/s, which, in full-scale, correspond to 9.1 knots, 11.1 knots, and 12.8 knots (using Froude scaling with 1:90 model scale), and are within the range of average transit speeds typical for drillships. Due to the limited length of the wave basin, these speeds could not be sustained by the towing carriage for more than 40 s in the slowest speed trial and less than 30 s in the highest speed trial. Consequently, the duration of all the recorded IMU data with forward speed is less than 40 s.

Due to the narrowness of the wave basin, only head sea ($\beta = 180°$) and following sea ($\beta = 0°$) conditions could be tested in the forward speed trials. Some oscillations in the heading angle of the ship were observed during experiments due to the towing carriage, impact of waves, and rope-pulley system. In order to assess the deviation caused by these oscillations, the real-time heading angle was measured using a separate camera-based positioning system called Qualisys. The measurements reported by Qualisys showed that the maximum error between the initial heading and heading during experiments was less than 5°. To ensure that the results were minimally affected by such deviations, the true wave encounter angle was based on the average heading angle computed from the Qualisys heading measurements.

4.1.2. Wave period and wave height

The experimental wave periods were generally selected above the CSAD lower wave period threshold $T_{\min} = 1/f_{\max} \approx 1.3$ s (computed by inserting the CSAD length and breadth dimensions, $L = 2.58$ m and $B = 0.44$ m, with a water pool depth of 1.45 m into Eq. (20)) to reduce the effect of vessel filtering on the IMU data. However, regular wave experiments were conducted with a wave period of $T_p = 1.0$ s to demonstrate the issues related to high-frequency waves.

In general, as long as the vessel can "feel" the waves passing through it, Theorem 1 is valid irrespective of how small or tall the waves are. In practice, however, higher waves imply a higher signal-to-noise ratio (SNR) in the IMU measurements, which can improve estimation results. Despite the advantage of a high SNR, considerable wave heights posed challenges to our rope-pulley system causing large oscillations in the heading angle of the CSAD. Moreover, significant waves caused more water exposure on deck, increasing the risk of water leaking into the vessel and damaging electronics. For these reasons, only slight, moderate, and (to some extent) rough sea states were considered in the experiments (Table 2).

4.1.3. Sensor configuration

We equipped the CSAD with four Bosch BMI160 IMUs to record the vessel motions caused by waves. The IMUs were fastened to the vessel using Velcro tape and the array configuration is illustrated in Fig. 6(a): The sensor array is noncollinear, with $\{s_1\}$, $\{s_2\}$, and $\{s_3\}$ being almost coplanar and $\{s_4\}$ significantly elevated compared to the rest. The IMUs are all connected to a Raspberry Pi 3 Model B+ through a common serial bus using the I2C communication protocol. The individual IMU measurements were time-synchronized based on the internal clock of the Raspberry Pi. The IMU sampling rate was set to 50 Hz for all experiments as the serial bus could not handle the increased information load associated with higher sampling rates.

Unfortunately, Bosch does not provide any information about the in-run bias stability of the accelerometers and gyroscopes in the BMI160 IMU, meaning it is difficult for us to assess whether the biases remain constant or not within the time frame of the recorded data segments. However, it is plausible that the IMU data collected during forward speed were not significantly affected by the bias due to the short time

[4] For details on the equipment, the reader is referred to the laboratory website: https://www.ntnu.edu/imt/lab/cybernetics.

Table 2
The peak wave periods (T_p) considered in the experiments, along with the corresponding wave height H (regular waves) and significant wave height H_s (irregular waves). Numbers outside parentheses represent the actual model-scale experimental parameters, whereas numbers inside parentheses represent the equivalent full-scale parameters (obtained using Froude scaling with scale factor 90). All scaled wave heights can be characterized as either a slight, moderate, or rough sea state (Price and Bishop, 1974) with wave periods within the frequency range of wind-generated waves. Wave periods and wave heights are given in seconds and meters, respectively.

T_p	1.0 (9.5)	1.4 (13.3)	1.5 (14.2)	1.6 (15.2)	1.8 (17.1)	2.0 (19.0)	2.5 (23.7)
H	0.040 (3.56)	–	0.027 (2.43)	–	–	0.017 (1.53)	0.011 (1.03)
H_s	–	0.027 (2.43)	–	0.018 (1.63)	0.017 (1.53)	0.014 (1.29)	–

Table 3
Absolute phase difference errors $\tilde{\Theta}_{ij}$ between our phase difference model (12) and the FFT estimated phase difference between the processed z-accelerations of IMUs $\{s_i\}$ and $\{s_j\}$ configured according to Fig. 6(a). The errors were evaluated for various sensor pairs exposed to regular waves with wave periods T_p = 1.0 s, 1.5 s, 2.0 s, and 2.5 s and vessel speeds U = 0.5 m/s, 0.6 m/s, and 0.7 m/s. The top and bottom tables show results for following sea ($\beta = 0°$) and head sea ($\beta = 180°$), respectively. All values are given in degrees.

T_p	U = 0.5 m/s				U = 0.6 m/s				U = 0.7 m/s			
	$\tilde{\Theta}_{12}$	$\tilde{\Theta}_{13}$	$\tilde{\Theta}_{24}$	$\tilde{\Theta}_{34}$	$\tilde{\Theta}_{12}$	$\tilde{\Theta}_{13}$	$\tilde{\Theta}_{24}$	$\tilde{\Theta}_{34}$	$\tilde{\Theta}_{12}$	$\tilde{\Theta}_{13}$	$\tilde{\Theta}_{24}$	$\tilde{\Theta}_{34}$
1.0 s	147.75	150.61	283.82	286.68	119.76	118.77	235.21	234.23	151.67	153.07	298.31	299.71
1.5 s	5.72	6.78	36.70	35.64	4.61	5.36	37.76	37.01	4.29	2.95	39.32	40.65
2.0 s	0.55	0.10	13.58	12.94	1.77	2.69	11.97	11.05	0.22	0.65	14.75	13.88
2.5 s	0.66	1.22	4.87	4.31	0.47	0.41	6.06	5.17	0.72	0.16	4.50	5.06

T_p	U = 0.5 m/s				U = 0.6 m/s				U = 0.7 m/s			
	$\tilde{\Theta}_{12}$	$\tilde{\Theta}_{13}$	$\tilde{\Theta}_{24}$	$\tilde{\Theta}_{34}$	$\tilde{\Theta}_{12}$	$\tilde{\Theta}_{13}$	$\tilde{\Theta}_{24}$	$\tilde{\Theta}_{34}$	$\tilde{\Theta}_{12}$	$\tilde{\Theta}_{13}$	$\tilde{\Theta}_{24}$	$\tilde{\Theta}_{34}$
1.0 s	103.35	108.24	230.45	235.33	106.01	108.75	230.45	233.19	108.01	106.72	234.41	233.12
1.5 s	0.33	0.22	37.77	37.22	2.49	2.43	34.34	34.40	4.35	4.29	30.53	30.60
2.0 s	1.95	1.55	15.23	14.83	3.13	2.59	16.78	16.23	5.27	4.48	21.21	20.43
2.5 s	2.21	2.20	9.91	9.90	1.38	0.93	9.10	8.65	2.19	2.57	9.29	9.68

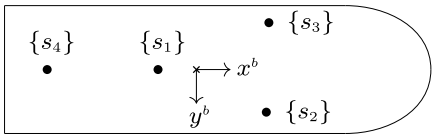

[mm]	x^b	y^b	z^b
s_1	-319	-9	93
s_2	409	156	113
s_3	418	-177	113
s_4	-1025	-13	-147

(a)

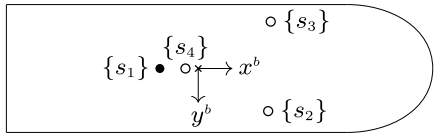

[mm]	x^b	y^b	z^b
s_1	-319	-9	93
s_2	409	156	113
s_3	418	-177	113
s_4	-103	-13	-147

(b)

Fig. 6. The IMU array configurations considered in the wave tank experiments. IMUs 1, 2, 3, and 4 are denoted $\{s_1\}$, $\{s_2\}$, $\{s_3\}$, and $\{s_4\}$, respectively. The location of each sensor is given in millimeters with respect to the vessel body frame $\{b\}$. The origin of $\{b\}$ is indicated by a cross and defined midships with the z-axis pointing down (into the page). The sensor configuration in (a) shows the original configuration of physically interconnected IMUs (filled circles), whereas (b) shows the virtual sensor configuration where only IMU 1 is physical and the locations of the other IMUs are virtual (hollow circles).

duration of all experiments (less than 40 s). On the other hand, the duration of the IMU data collected at zero speed was around 120 s, which may have been affected to a greater extent by the bias instability.

4.2. Results and discussion

In this section, we assess the validity of the theory developed in Section 2.5 by considering IMU data collected from experiments conducted in the wave basin where the model ship was stationary and underway in both regular and irregular waves. Since the time durations of the collected IMU data were short, we consider each complete time series as a single input data segment to our wave estimation algorithm (Algorithm 3). In the following results, the reference wave number was computed using the dispersion relation (21) along with the pool depth d = 1.45 m and the true peak wave period (i.e., the wave period used as input to the wavemaker machine). The peak wave period value was confirmed by examining the frequency content of the wave elevation data obtained from several wave probes placed around the tank. The reference wave propagation angle was obtained by fixing the ropes of the model ship to produce the desired boat headings (Fig. 5) and confirming this value with the Qualisys camera system. In the following results, we refer to the wave propagation angle relative to the boat heading as the wave encounter angle when the vessel moves and the wave direction when the vessel is stationary.

4.2.1. Experimental validation of Assumption 1

We can assess the validity of Assumption 1 by comparing the phase differences predicted by Eq. (12) with the actual phase differences measured between the sensors on the vessel for a range of vessel speeds, wave periods, and wave directions. The error between the phase differences (Table 3) reveal three interesting observations: (i) the phase errors associated with wave period T_p = 1.0 s are disproportionately large compared to the other wave periods, (ii) the sets of phase errors $\{\tilde{\Theta}_{12}, \tilde{\Theta}_{13}\}$ are smaller than $\{\tilde{\Theta}_{24}, \tilde{\Theta}_{34}\}$ for all experiments, and (iii) the errors generally decrease with increasing wave period.

The extreme deviations in observation (i) are caused by vessel filtering, which (in this case) occurs whenever the wave period is roughly

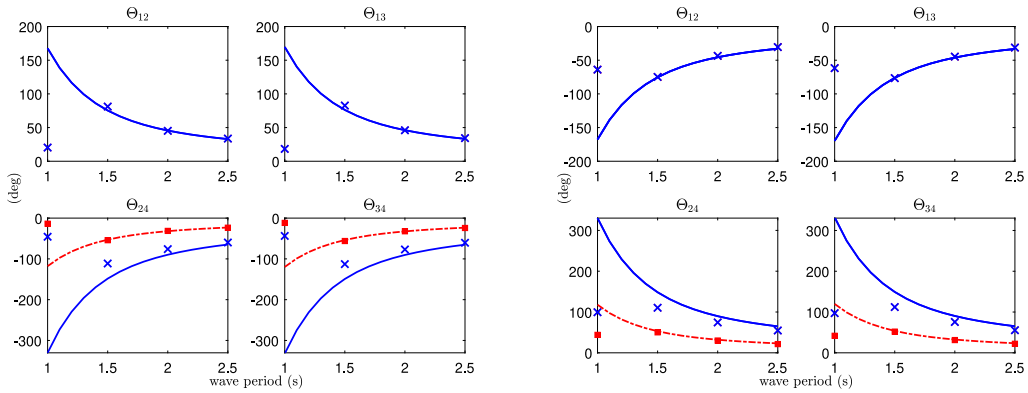

Fig. 7. The phase differences predicted by our model (12) (solid blue line) vs. the "true" phase differences (blue crosses) between respective sensor pairs as a function of wave period for vessel speed $U = 0.5$ m/s. The "true" phase differences were obtained by applying an FFT to the processed z-accelerations of each IMU to get the corresponding phase values. The results in red (dashed-dotted curves and squares) show the corresponding phase differences after virtually moving IMU 4 closer to the other IMUs. This virtual placement was achieved by employing the measurement transformation (19) and the modified sensor configuration in Fig. 6(b), together with the processed linear accelerations, angular rates, and angular accelerations of IMU 1. The dashed-dotted line shows the predicted phase differences (12) based on the new sensor location, whereas the squares show the corresponding "true" phase differences obtained using an FFT as before. Left and right-handed plots show results for following sea ($\beta = 0°$) and head sea ($\beta = 180°$), respectively. The phase difference results for $U = 0.6$ m/s and 0.7 m/s have been omitted as they were almost identical to the results displayed.

less than 1.3 s.[5] When the waves are sufficiently short, the vessel acts as a lowpass filter and attenuates the waves passing through it, resulting in a reduction in the angular rates of the body. A reduction in the angular rates causes the rigid-body accelerations to become increasingly similar (see Eq. (6)), which, in turn, implies that the phase differences approach zero. However, the phase differences predicted by Eq. (12) generally increase with decreasing wave period as it does not consider a rigid body. These opposite behaviors result in a growing deviation between the true phase difference dynamics and our proposed model (Fig. 7). As the wave period decreases, the true phase differences will approach zero due to vessel lowpass filtering becoming increasingly dominant, whereas the predicted phase differences continue to infinity.

The noticeable difference between the sets of phase errors in observation (ii) is mainly caused by a difference in the separation distance between sensors $\{s_1, s_2, s_3\}$ and $\{s_2, s_3, s_4\}$ (Fig. 6(a)). Specifically, the x-coordinate of $\{s_4\}$ is significantly larger than $\{s_2\}$ and $\{s_3\}$, which induces a larger deviation between the estimated and actual phase differences associated with $\{s_4\}$. However, if we bring $\{s_4\}$ closer to the other sensors, the deviation decreases to zero (Fig. 7). As explained in Section 2.1, we expect Eqs. (6) and (12) to yield roughly the same phase difference when the separation is sufficiently small since both models are proportional to the sensor separation. It is worth stressing, however, that there is generally a lower limit on how close the sensors may be separated before the state-space model loses observability. As the sensor separations decrease, there is an increasing risk that the measured phase differences all become zero, meaning there is no longer any guarantee that the UKF algorithm will find the correct solution. However, it is difficult to quantify the minimum sensor separation as it depends on the sensor sampling rate and speed/frequency of the waves passing through the sensors. Since the sampling rate is considered fixed for the system, a speed/frequency will always exist where the waves will appear without delay in all sensors, irrespective of the given sensor separation. Hence, the sensor separations should not be considered a fixed universal quantity but rather tunable parameters that can be adapted to different wave conditions. For instance, one possible strategy is to consider different sets of sensor separations, each of which should be applied depending on the measured wave frequency given by the FFT. However, a methodology based on such a strategy is outside the scope of the present study and left as a potential application for future work.

Observation (iii) can be understood by studying the effect of increasing the wave period on the models (6) and (12). The phase difference in Eq. (12) is proportional to the wave number, which, in turn, is inversely proportional to the wave period. Thus, as the wave period increases, the predicted phase difference generally decreases towards zero (Fig. 7). The effect of increasing the wave period on the angular rates and accelerations in Eq. (6) can be understood by considering the vessel roll and pitch responses in regular waves, which, for an underway vessel, can generally be expressed as

$$\begin{aligned} \phi(t) &= A_\phi \sin(\omega_e t + \epsilon_\phi), \\ \theta(t) &= A_\theta \cos(\omega_e t + \epsilon_\theta), \end{aligned} \tag{36}$$

where A_ϕ and A_θ denote the roll and pitch amplitudes, ω_e is the wave encounter frequency, and ϵ_ϕ and ϵ_θ represent the phase shifts. Assuming that the boat heading is fixed (i.e., $\dot{\psi} = 0$), the angular rates p and q can be written mathematically as $p = \dot{\phi}$ and $q = \dot{\theta}\cos(\phi)$ (Fossen, 2021). Computing the time derivatives of Eq. (36) we see that the amplitudes of p and q depend directly on ω_e. Hence, as the wave period increases, the angular frequencies ω and ω_e will be driven to zero, further implying that p, q, $\dot{p}$, and $\dot{q}$ will also converge to zero. The latter result makes intuitive sense as, for very long waves, the vessel will appear to oscillate up and down vertically, with little roll and pitch motion, causing the measurements in each sensors to be almost identical (i.e., zero phase difference). Therefore, it is clear that increasing the wave period will cause both models (6) and (12) to converge to zero, which, in turn, implies that the corresponding error between them will behave in a similar fashion.

Unfortunately, due to the size of the wave tank, it was not possible to assess the validity of Assumption 1 for other boat headings in forward speed. Nevertheless, we carried out similar experiments in regular waves for the stationary case (i.e., $U = 0$ m/s) with boat headings $\{0°, 30°, 60°, 90°, 120°, 150°, 180°\}$ and obtained similar results. Hence, based on these experimental results, it is reasonable to conclude that Assumption 1 is valid.

4.2.2. Experimental validation of Theorem 1

The experimental results associated with the set of phase differences $\{\Theta_{12}, \Theta_{13}\}$ (Tables 4 and 5) show that in 89% and 83% of experiments considered with the original IMU setup, the wave encounter

[5] This value was obtained by evaluating Eq. (15) with $\beta = 0°/180°$ and $L = 2.58$ m, equating it with $\lambda = 2\pi/k$, and finding corresponding the wave period.

Table 4
Wave encounter angle results associated with the pairs of phase differences $\{\Theta_{12}, \Theta_{13}\}$ and $\{\Theta_{24}, \Theta_{34}\}$, respectively, for wave periods $T_p = 1.5$ s, 2.0 s, and 2.5 s and vessel speeds $U = 0.5$ m/s, 0.6 m/s, and 0.7 m/s in regular waves. The numbers represent the absolute error between the wave angle estimates (after convergence) from our wave algorithm (Algorithm 3) and the true values. Numbers outside parentheses represent errors associated with the original sensor configuration (Fig. 6(a)), where all results are based on physical IMU data. Numbers inside parentheses represent errors associated with a single physical IMU. The latter errors were obtained by using the processed linear acceleration, angular rates, and angular acceleration of IMU 1 with the measurement transformation (19) and the virtual sensor configuration in Fig. 6(b) to generate the other IMU measurements. The top and bottom tables show the results for following sea ($\beta = 0°$) and head sea ($\beta = 180°$), respectively. All wave angle errors are given in degrees.

T_p	$U = 0.5$ m/s		$U = 0.6$ m/s		$U = 0.7$ m/s	
	$\{\Theta_{12}, \Theta_{13}\}$	$\{\Theta_{24}, \Theta_{34}\}$	$\{\Theta_{12}, \Theta_{13}\}$	$\{\Theta_{24}, \Theta_{34}\}$	$\{\Theta_{12}, \Theta_{13}\}$	$\{\Theta_{24}, \Theta_{34}\}$
1.5 s	4.92 (2.47)	7.26 (2.43)	1.34 (0.58)	1.15 (0.53)	3.94 (2.32)	3.29 (2.40)
2.0 s	2.06 (1.77)	2.70 (1.77)	4.37 (2.35)	5.91 (2.31)	6.43 (2.35)	7.14 (2.27)
2.5 s	0.14 (2.06)	0.41 (2.05)	4.36 (3.36)	6.26 (3.35)	2.63 (3.75)	3.86 (3.75)

T_p	$U = 0.5$ m/s		$U = 0.6$ m/s		$U = 0.7$ m/s	
	$\{\Theta_{12}, \Theta_{13}\}$	$\{\Theta_{24}, \Theta_{34}\}$	$\{\Theta_{12}, \Theta_{13}\}$	$\{\Theta_{24}, \Theta_{34}\}$	$\{\Theta_{12}, \Theta_{13}\}$	$\{\Theta_{24}, \Theta_{34}\}$
1.5 s	1.74 (0.91)	3.02 (1.03)	0.17 (0.16)	1.10 (0.03)	4.14 (0.09)	4.58 (0.14)
2.0 s	0.49 (1.23)	0.63 (1.27)	3.60 (1.76)	4.38 (1.80)	2.60 (2.72)	2.28 (2.71)
2.5 s	1.91 (0.22)	1.97 (0.21)	6.70 (1.86)	6.87 (1.83)	2.24 (1.30)	2.06 (1.29)

Table 5
Wave number results associated with the pairs of phase differences $\{\Theta_{12}, \Theta_{13}\}$ and $\{\Theta_{24}, \Theta_{34}\}$, respectively, for wave periods $T_p = 1.5$ s, 2.0 s, and 2.5 s and vessel speeds $U = 0.5$ m/s, 0.6 m/s, and 0.7 m/s in regular waves. The numbers represent the absolute error between the wave number estimates (after convergence) from our wave algorithm (Algorithm 3) and the true values. Numbers outside parentheses represent the wave number errors associated with the original sensor configuration (Fig. 6(a)), where all results are based on physical IMU data. Numbers inside parentheses represent the wave number errors associated with a single physical IMU. The latter errors were obtained by using the processed linear acceleration, angular rates, and angular acceleration of IMU 1 with the measurement transformation (19) and the virtual sensor configuration in Fig. 6(b) to generate the other IMU measurements. The top and bottom tables show the results for following sea ($\beta = 0°$) and head sea ($\beta = 180°$), respectively. All wave number errors are given in m^{-1}.

T_p	$U = 0.5$ m/s		$U = 0.6$ m/s		$U = 0.7$ m/s	
	$\{\Theta_{12}, \Theta_{13}\}$	$\{\Theta_{24}, \Theta_{34}\}$	$\{\Theta_{12}, \Theta_{13}\}$	$\{\Theta_{24}, \Theta_{34}\}$	$\{\Theta_{12}, \Theta_{13}\}$	$\{\Theta_{24}, \Theta_{34}\}$
1.5 s	0.17 (0.06)	0.40 (0.08)	0.09 (0.06)	0.46 (0.10)	0.10 (0.09)	0.48 (0.17)
2.0 s	0.02 (0.01)	0.14 (0.01)	0.10 (0.05)	0.13 (0.07)	0.07 (0.01)	0.14 (0.02)
2.5 s	0.02 (0.02)	0.03 (0.03)	0.05 (0.00)	0.07 (0.00)	0.04 (0.02)	0.08 (0.02)

T_p	$U = 0.5$ m/s		$U = 0.6$ m/s		$U = 0.7$ m/s	
	$\{\Theta_{12}, \Theta_{13}\}$	$\{\Theta_{24}, \Theta_{34}\}$	$\{\Theta_{12}, \Theta_{13}\}$	$\{\Theta_{24}, \Theta_{34}\}$	$\{\Theta_{12}, \Theta_{13}\}$	$\{\Theta_{24}, \Theta_{34}\}$
1.5 s	0.09 (0.00)	0.39 (0.08)	0.15 (0.06)	0.36 (0.04)	0.05 (0.07)	0.36 (0.08)
2.0 s	0.07 (0.04)	0.18 (0.05)	0.08 (0.07)	0.19 (0.08)	0.11 (0.11)	0.24 (0.11)
2.5 s	0.08 (0.05)	0.13 (0.05)	0.02 (0.03)	0.10 (0.02)	0.03 (0.06)	0.14 (0.06)

angle and wave number errors are less than 5° and 0.1 m^{-1}, respectively.[6] These numbers provide strong evidence in favor of Theorem 1 and extend previous findings by showing that the PTPD approach is valid for underway vessels and not only stationary ones (Udjus, 2017; Heyn et al., 2017; Dirdal et al., 2022). Unfortunately, due to the narrowness of the wave tank, it was not possible to assess Theorem 1 for other boat headings in forward speed. We refer to our previous work (Dirdal et al., 2022) for an assessment of Theorem 1 for boat headings $\{0°, 30°, 60°, 90°, 120°, 150°, 180°\}$ in the stationary case (i.e., $U = 0$ m/s). It is worth mentioning that we have omitted the results for wave period $T_p = 1.0$ s since Assumption 1 is violated for that period, as discussed in Section 4.2.1.

In contrast, the experimental results (Tables 4 and 5) also show that for the set of phase differences $\{\Theta_{24}, \Theta_{34}\}$, merely 83% and 22% of the total wave encounter angle and wave number errors are within 5° and 0.1 m^{-1}, respectively. The significant difference in quality (especially in the wave number) compared to the errors achieved using the set $\{\Theta_{12}, \Theta_{13}\}$ can be explained by a difference in the sensor positioning of $\{s_1, s_2, s_3\}$ and $\{s_2, s_3, s_4\}$. As discussed in Section 4.2.1, $\{s_4\}$ is displaced further from $\{s_2, s_3\}$ along the x^b axis than $\{s_1\}$, resulting in a greater deviation between our phase difference model and the actual phase difference dynamics. Bringing $\{s_4\}$ closer to the other sensors reduces the deviation between the models, resulting in 100% and 94% of the wave encounter angle and wave number errors for $\{\Theta_{24}, \Theta_{34}\}$ being within 5° and 0.1 m^{-1} (Tables 4 and 5), respectively. It is worth stressing that although the deviation can in theory be reduced to zero by bringing the sensors very close, doing so in practice may compromise the observability of Eq. (13), as discussed in Section 4.2.1.

The wave number estimation results (Table 5) also demonstrate another interesting and beneficial fact: We can retain the absolute frequency (through the dispersion relation (21)) from shipboard IMU measurements taken in the encounter frequency domain. This property is particularly useful for beam to following sea conditions (i.e., $\beta \in (-90°, 90°)$) in which the wave encounter frequency generally does not possess a unique solution (Fig. 8). Due to the observability of our state-space model, our approach directly maps the phase differences (which are based on the encounter frequency) to the absolute frequency domain, thereby circumventing the 1-to-3 mapping problem associated with underway vessels in following seas (Nielsen, 2017b, 2018).

4.2.3. Experimental validation of Corollary 1.1

The experimental results (Tables 4 and 5) show that for a *single* IMU in 100% and 94% of experiments considered, the wave encounter angle and wave number errors are within 5° and 0.1 m^{-1}, respectively. These numbers extend previous findings by showing that a single IMU is sufficient, as opposed to three, as initially proposed in Dirdal et al. (2022). This result increases the practical utility of the PTPD approach

[6] For comparison, standard commercial radars such as Miros SM-050 and Miros Wavex report wave direction accuracies of 7° and 20° and wave period accuracies of 5% and 10%—see Table 6 for how these values affect the accuracy of the wave number and why 0.1 m^{-1} was selected as the accepted error threshold.

Table 6
Theoretical wave number errors $\bar{k}$ (unit m^{-1}) resulting from a 5% and 10% error in the experimental wave periods T_p (unit seconds). The wave number errors were computed from Eq. (21) by adding and subtracting the percentage error to each respective wave period. In each calculation, the water pool depth of the wave basin ($d = 1.45$ m) was considered. Based on these numbers, we consider 0.1 m^{-1} a reasonable error threshold to assess the quality of the wave number estimation results.

T_p	1.0	1.4	1.5	1.6	1.8	2.0	2.5
$\bar{k}_{5\%}$	0.40	0.20	0.17	0.15	0.11	0.09	0.05
$\bar{k}_{10\%}$	0.82	0.41	0.35	0.30	0.23	0.18	0.11

significantly as many vessels already employ IMUs as part of their sensor suite, thus allowing the approach to be applied directly without the need for installing additional units and time synchronizing the measurements between them. It is worth emphasizing that the results presented here are only valid for IMUs, which can measure angular rates and specific force simultaneously—both of which Eq. (19) relies on.

However, an important drawback of Eq. (19) is that it depends on the angular acceleration $\dot{\boldsymbol{\omega}}_{nb}^{b}$, which is not usually measured. In this work, we have obtained estimates of the latter through numerical differentiation of $\boldsymbol{\omega}_{nb}^{b}$, which we argue is valid since each measurement data segment has been lowpass filtered (see Section 3.1.2). The validity of using numerical differentiation is further substantiated by our results, which are either similar in magnitude or outperform the results based on multiple physical IMUs. It is worth mentioning that there exist other methods for estimating $\dot{\boldsymbol{\omega}}_{nb}^{b}$ (Zappa et al., 2001; Kjerstad and Skjetne, 2016); however, these rely on an array of (minimum) four noncoplanar tri-axial accelerometers.

It is interesting to see that the wave estimates for $\{\Theta_{12}, \Theta_{13}\}$ from a single IMU, in many cases, produce lower errors than for three physical IMUs (Tables 4 and 5), despite the sensor coordinates being (in theory) the same. We speculate that one of the reasons for this behavior is that the application of Eq. (19) effectively eliminates any bias resulting from uncertainties in the sensor positioning. As discussed in Dirdal et al. (2022), uncertainties in the sensor positions can result in significant errors in the phase differences, especially for higher frequency waves. By employing Eq. (19) instead, the issues regarding sensor positioning are conveniently circumvented, as any virtual sensor coordinates specified as input to Eq. (19) represents the true location.

Up to now, we have used Eq. (19) to generate the *minimum* number of measurements needed to determine the wave encounter angle and wave number uniquely. However, it is worth pointing out that we could use Eq. (19) to spawn any arbitrary number of measurements. As discussed in Dirdal et al. (2022), increasing the number of phase differences will reduce the error variance of the estimates, but only up to a specific limit. Note that this will only work if the virtual sensor locations are noncollinear (Theorem 1) and sufficiently close to each other (Assumption 1).

4.2.4. Long-crested irregular waves

So far, we have established the theoretical foundation for determining the wave encounter angle and wave number from a train of regular harmonic waves. However, in reality, ocean waves are irregular, typically characterized by many wave components differing in amplitude, frequency, and wave direction. For *long-crested* irregular waves, each constituent wave component has the same propagation direction, meaning that it is, in theory, sufficient only to consider one such wave component to infer the general propagation direction. Hence, if we can extract only one wave component/frequency (e.g., using an FFT), we can apply Theorem 1 and Corollary 1.1 to determine the wave propagation direction of long-crested irregular waves from a single IMU.

In order to assess the validity of the approach mentioned above, two sets of experiments were conducted in the wave basin involving a stationary and underway vessel, respectively, subjected to long-crested irregular waves. In the stationary and forward speed trials, we considered the set of boat headings $\{0°, 30°, 60°, 90°, 120°, 150°, 180°\}$

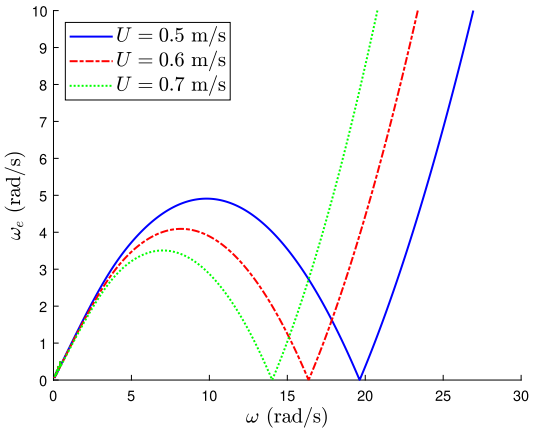

Fig. 8. Encounter wave frequency (ω_e) vs. absolute wave frequency (ω) in following waves ($\beta = 0°$) computed by Eq. (22) with water depth $d = 1.45$ m (results are almost identical for increasing d) and forward vessel speeds $U = 0.5$ m/s, 0.6 m/s, and 0.7 m/s to represent the test conditions of the wave basin. When $\omega_e < 1/4\psi$, where $\psi = U\cos\beta/g$, the wave encounter frequency maps to three different (absolute) wave frequencies. The latter situation applies for all our experiments conducted in following waves with (absolute) wave periods $T_p = 1.5$ s, 2.0 s, and 2.5 s.

and $\{0°, 180°\}$, respectively, with significant wave heights and peak wave periods given in Table 2. The experimental results (Tables 7 and 8) show that in 92% of the forward speed trials and 79% of the stationary trials, the wave encounter angle error is less than 5°. If we extend the error threshold to 10°, all wave direction estimates except one are within the latter. These results demonstrate that our phase difference model can also be applied to long-crested irregular waves to uniquely resolve the relative wave propagation direction from a single IMU. The application of our approach to long-crested irregular waves for stationary and underway vessels extends previous works (Udjus, 2017; Heyn et al., 2017; Dirdal et al., 2022), which are limited to a stationkeeping vessel and regular waves, and whose results are based on multiple physical IMUs.

Despite the good agreement between the wave direction results, the same level of agreement is not seen for the wave number, which, for underway and stationkeeping trials, yields 71% and 57% of errors less than 0.1 m^{-1} (Tables 7 and 8), respectively. It is difficult to state with certainty the exact reasons for the observed discrepancies; however, we speculate that they are caused by a combination of (i) poor frequency resolution in the FFT spectra, (ii) a growing mismatch between our phase prediction model and the true vessel dynamics due to increased angular vessel rates, and (iii) the UKF algorithm sometimes favoring a low wave direction error at the expense of a high wave number error. Each of these issues are addressed in the following paragraphs.

As mentioned in Section 4.1, the time duration of the recorded IMU data was less than 40 s for the forward speed trials and less than 120 s for the zero speed trials. Time durations of such magnitudes will invariably impact the attainable frequency resolution of the FFT spectra. As discussed in Section 3.4.3, a poor frequency resolution will make it more challenging to pinpoint the true frequency, causing it

Table 7
Wave encounter angle and wave number results, $\bar{\beta}$ and $\bar{k}$, respectively, from forward speed trials in following and head waves (i.e., $\beta = 0°$ and $\beta = 180°$) with vessel speeds $U = 0.5$ m/s, 0.6 m/s, and 0.7 m/s exposed to long-crested irregular waves with peak wave periods $T_p = 1.4$ s, 1.6 s, 1.8 s, and 2.0 s. The numbers show the absolute error between the wave estimates (after convergence) from our wave algorithm (Algorithm 3) and the true values by considering the set of phase differences $\{\Theta_{12}, \Theta_{13}, \Theta_{14}, \Theta_{23}, \Theta_{24}, \Theta_{34}\}$ and the virtual sensor configuration in Fig. 6(b). Note that in the results presented we have reduced the maximum frequency threshold in Algorithm 3 to $f_{\max} = 0.6$ Hz. The wave encounter and wave number errors are given in degrees and m^{-1}, respectively.

T_p	$U = 0.5$ m/s				$U = 0.6$ m/s				$U = 0.7$ m/s			
	$\beta = 0°$		$\beta = 180°$		$\beta = 0°$		$\beta = 180°$		$\beta = 0°$		$\beta = 180°$	
	$\bar{\beta}$	$\bar{k}$	$\bar{\beta}$	$\bar{k}$	$\bar{\beta}$	$\bar{k}$	$\bar{\beta}$	$\bar{k}$	$\bar{\beta}$	$\bar{k}$	$\bar{\beta}$	$\bar{k}$
1.4 s	0.19	0.47	1.95	0.03	0.37	0.49	7.44	0.05	2.28	0.08	6.35	0.06
1.6 s	0.39	0.15	0.14	0.06	0.40	0.24	0.47	0.15	4.18	0.71	2.30	0.01
1.8 s	1.88	0.06	0.05	0.06	1.68	0.12	1.86	0.05	2.93	0.00	0.19	0.09
2.0 s	0.11	0.06	0.11	0.02	0.91	0.02	4.61	0.02	3.13	0.07	2.40	0.06

Table 8
Wave direction and wave number results, $\bar{\beta}$ and $\bar{k}$, respectively, from a stationary vessel exposed to long-crested irregular waves with peak wave period $T_p = 1.4$ s, 1.6 s, 1.8 s, and 2.0 s and wave directions $\beta = 0°$, 30°, 60°, 90°, 120°, 150°, and 180°. The numbers show the absolute error between the wave estimates (after convergence) from our wave algorithm (Algorithm 3) and the true values by considering the set of phase differences $\{\Theta_{12}, \Theta_{13}, \Theta_{14}, \Theta_{23}, \Theta_{24}, \Theta_{34}\}$ and the virtual sensor configuration in Fig. 6(b). Note that in the results presented we have reduced the maximum frequency threshold in Algorithm 3 to $f_{\max} = 0.6$ Hz. The wave direction and wave number errors are given in degrees and m^{-1}, respectively.

T_p	$\beta = 0°$		$\beta = 30°$		$\beta = 60°$		$\beta = 90°$		$\beta = 120°$		$\beta = 150°$		$\beta = 180°$	
	$\bar{\beta}$	$\bar{k}$	$\bar{\beta}$	$\bar{k}$	$\bar{\beta}$	$\bar{k}$	$\bar{\beta}$	$\bar{k}$	$\bar{\beta}$	$\bar{k}$	$\bar{\beta}$	$\bar{k}$	$\bar{\beta}$	$\bar{k}$
1.4 s	1.89	0.20	3.45	0.03	2.06	0.26	2.46	0.01	3.85	0.05	6.51	0.08	0.87	0.17
1.6 s	0.92	0.24	7.56	0.01	1.72	0.42	3.83	0.08	3.14	0.19	10.47	0.06	0.18	0.10
1.8 s	1.57	0.11	6.91	0.28	4.00	0.11	2.90	0.13	3.55	0.22	5.56	0.06	0.90	0.07
2.0 s	0.41	0.10	3.10	0.04	3.13	0.09	2.92	0.06	2.80	0.01	9.58	0.14	0.92	0.02

to fall between two frequency bins and ultimately affecting the phase response. In order to improve FFT resolution, a longer FFT length must be considered, which may be fulfilled by increasing the duration of the measured data or by various interpolation techniques such as zero-padding.

Inspecting the wave estimation errors in Table 8 closely, it is clear that the most significant wave direction and wave number errors are associated with the experiments in which $\beta = 30°, 60°, 120°$ and $150°$. In those experiments, we expect the angular rates of the body to be quite high due to the vessel roll and pitch responses being active and large simultaneously (the waves are approaching the vessel diagonally as opposed to straight on or from the side). An increase in the angular rates will cause a growing mismatch between our phase prediction model and the actual phase difference dynamics. As discussed in Section 4.2.1, this mismatch can generally be reduced by tuning the sensor separations such that the virtual sensor positions become sufficiently close.

The issues raised above will manifest themselves as errors in the estimated phase differences. These errors tend to be reflected more in one of the wave quantities than the other and less often in both simultaneously. In other words, when significant errors are present, the UKF algorithm seems to favor a lower estimation error in one of the wave quantities at the expense of a higher error in the other. In order to assess this speculation, we have conducted a small simulation study investigating how individual estimation errors are affected by the UKF for a range of wave directions and frequencies when significant errors in the phase differences are present. In addition to confirming the speculation above, the results (Fig. 9) also show that the wave number error is generally more sensitive to changes in the wave period (compare the magnitudes of the wave direction and wave number errors in the plots in Fig. 9). This behavior can explain some of the opposing wave estimation results in Tables 7 and 8 and, in particular, why the wave number error in some cases appears to be affected more than the corresponding wave direction error.

It is worth mentioning that in the results presented (Tables 7 and 8), we have reduced the maximum frequency threshold $f_{\max}$ in Algorithm 3, which produced better results. As we have seen, lower frequencies (longer wave periods) tend to produce more accurate wave estimates due to a reduction in the angular rates of the body, thus yielding less mismatch between our model and the actual vessel dynamics. However, by reducing the frequency threshold, our algorithm may effectively select a frequency different from the spectrum's peak frequency. This operation poses no issue for long-crested seas as each wave component propagates in the same direction. However, for more short-crested seas where multiple propagation directions may exist, care must be exercised to maintain the frequency threshold so that the desired peak wave frequency and direction are addressed.

5. Full scale experiments

5.1. Experimental design

During spring 2022, an experimental campaign was carried out with the NTNU-owned research vessel Gunnerus (Fig. 10) in the vicinity of Ålesund, a small coastal city on the west coast of Norway, to collect full-scale IMU data in various sea states and to assess the practicality of our proposed PTPD method. The research vessel Gunnerus is equipped with an advanced dynamical positioning system and many other instruments, making it an excellent platform for measuring waves at zero and forward speed.[7]

5.1.1. Campaign description

The field experiments were conducted over the course of two days. On each of these days, experiments involving zero and forward speed were, respectively, considered. The zero-speed trials were carried out in two distinct locations (Fig. 11(a)) in which the vessel was exposed to open and sheltered waters, respectively. At each location, four heading angles were considered by orienting the vessel into the waves (head sea) and subsequently adjusting the heading angle by 30°. Each heading angle and vessel position was maintained for approximately 40 min by the dynamical positioning system onboard. However, the duration of some experiments is shorter since the data logging system had to be restarted for some experiments, resulting in a loss of data. The forward

[7] For more information and details about the vessel and the equipment onboard, the reader is referred to the official Gunnerus website: https://www.ntnu.edu/oceans/gunnerus.

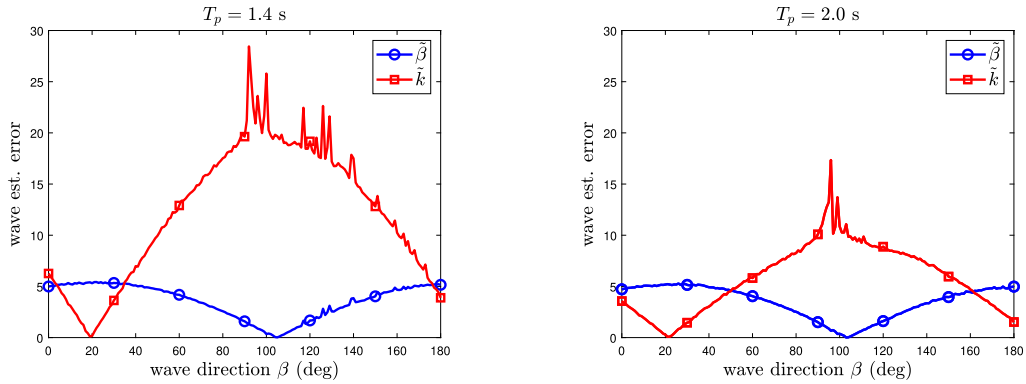

Fig. 9. Wave direction and wave number estimation results from our UKF algorithm (Algorithm 2) based on simulated phase differences with added random Gaussian noise. The phase differences were simulated using Eq. (12) with the sensor configuration in Fig. 6(b) and adding random Gaussian noise with mean 10° and standard deviation 5° to the computed values. The set of phase differences $\{\Theta_{12}, \Theta_{13}, \Theta_{14}, \Theta_{23}, \Theta_{24}, \Theta_{34}\}$ were considered in the simulation together with wave periods $T_p = 1.4$ s (left) and $T_p = 2.0$ s (right). The plots show the absolute error between the wave estimates (after convergence) and the true values. The wave direction error is given in degrees, whereas the wave number error is given in m^{-1} but multiplied by a factor of 100 to better highlight the overall trend.

Fig. 10. The research vessel Gunnerus considered in the full-scale experiments.

speed trials consist of a single experiment in head sea (Fig. 11(b)) lasting approximately 6 min. The short time duration and the limited number of trials for forward speed were due to ship operational issues.

5.1.2. IMU system and sensor configuration

Our data logging system comprises five ADIS16465 high-precision microelectric mechanical system (MEMS) IMUs (each of which includes a tri-axial accelerometer and gyroscope), a GPS receiver, a solid state drive, and a synchronization unit (Fig. 12). The IMUs and GPS receiver are all connected to the synchronization unit, which performs the synchronization of measurements using PPS time synchronization. All communication between the IMU nodes is done serially through the SPI protocol via cables of length 20 m. For all experiments, the IMU sampling rate was set to 100 Hz. We consider this sampling rate sufficient, as it is twice the rate used for the wave tank experiments as well as much higher than the bandwidth of wind-generated ocean waves.

The IMUs were rigidly attached to the vessel by clamping them onto the metal bars running across the roof of Gunnerus using screw clamps (Fig. 13). The metal bars run laterally across the vessel, making them an excellent reference to ensure that the gyroscope/accelerometer x-axis of each IMU is aligned with the vessel's longitudinal axis (thus minimizing potential misalignment errors). The distances between the IMUs were measured using a laser distance measure tool relative to a common and known reference point on the vessel.

The IMU configuration considered in experiments is illustrated in Fig. 14. The IMU array is noncollinear and coplanar. The former is necessary to ensure that the state-space model (13) is observable, whereas the latter reduces the deviation between Eqs. (11) and (12) when $z_{ij} = 0$ (see Appendix). The sensor positions were deliberately chosen to be near each other for three reasons. First, as established in Section 4.2.1, Assumption 1 is valid when the sensors are sufficiently close to each other. Second, the rigid-body assumption is preserved more for smaller regions on the vessel than positions on opposite ends (e.g., bow and stern), which are more susceptible to bending and other forms of deformation. Third, no other locations were as suitable as the roof for measuring distances and fastening the sensors to the vessel (drilling into the vessel to attach the sensors was not permitted).

The gyroscope and accelerometer sensor biases were assumed constant for the duration of each processed data segment. This assumption is substantiated by the gyroscope and accelerometer Allan variance curves found in the ADIS16465 datasheet, which states that for a 6 min integration period (the considered window length of each data segment; see Section 5.2.1 for discussion), the gyroscope and accelerometer in-run bias stability are less than 2°/hr and 4.5 μg, respectively.

5.1.3. Wave direction reference systems

Gunnerus possesses a commercial wave radar system comprising a Furuno X-band marine radar and a Miros Wavex computer. The Miros computer processes the raw Furuno radar images of backscattered light reflected off the sea surface to produce estimates of the directional wave spectrum. In the following results, we consider the main/dominant wave direction estimated by the wave radar system as the ground truth reference value. Moreover, we consider the accepted wave direction error threshold to be 20° when evaluating the performance of our wave estimation algorithm, as this number is the wave direction accuracy reported by the Miros Wavex system.

Some of the zero-speed experiments were performed near a Fugro Seawatch Wavescan buoy (Fig. 11(a)) owned and administered by the Norwegian Public Roads Administration, who has made the buoy data available to the public (Furevik et al., 2016). The buoy measures almost everything related to the sea surface, including directional information, rendering it an additional useful reference for wave assessment. Compared to the wave radar system, however, the update rate of the buoy is significantly lower, with updates given every 10 min as opposed to 1 min for the wave radar.

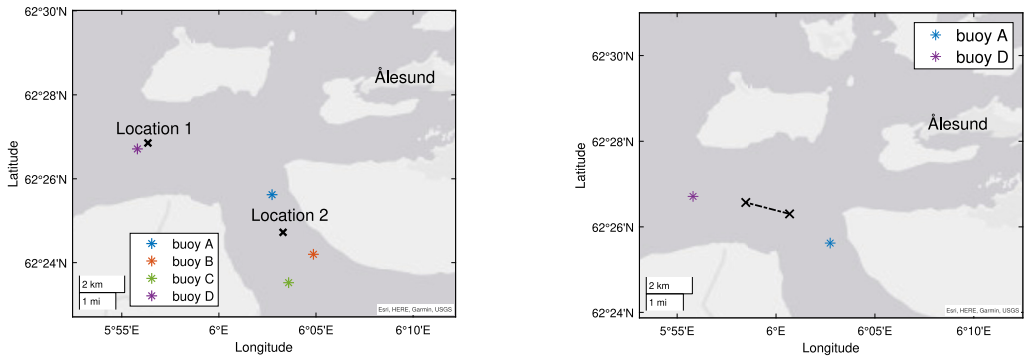

(a) Zero speed (b) Forward speed

Fig. 11. The zero-speed trials were conducted in two distinct locations: Breidsundet (Location 1) and Sulafjorden (Location 2). The forward speed trials comprise only one experiment because of ship operational issues, bringing the campaign to an abrupt end. Several directional wave rider buoys are stationed in the region, which the Norwegian Public Roads Administration operates. The wave conditions during experiments were relatively moderate, with significant wave heights generally less than 1.5 m.

Fig. 12. Our data logging system comprises five IMUs, a GPS receiver, a solid state drive, and a synchronization unit.

5.2. Results and discussion

In this section, we present and discuss the results from our PTPD approach when applied to full-scale experimental IMU data. All the wave radar and wave buoy values of the wave direction have been transformed to the wave tangent frame (Fig. 3) to be commensurate with the wave direction estimates given by our algorithm. The wave direction results are shown between 0° and 360° to avoid rapid jumps for values in proximity to 180°. For stationkeeping vessels, the wave number estimate is not particularly interesting as it is implicitly estimated by Algorithm 1 through the peak wave frequency used to generate the desired phase differences (we can use this frequency to calculate the wave number directly based on the dispersion relation for deep waters). For this reason, we consider the wave number redundant and have consequently omitted it from the zero-speed results.

The length and breadth dimensions of Gunnerus are 36.25 m and 9.90 m, respectively. Substituting these values into Eq. (20) with d arbitrarily large (deep waters) yields the maximum frequency threshold $f_{\max} = 0.2$ Hz. The latter value is substituted into Eq. (23) for the forward speed trials to get the adjusted frequency threshold $f_{\mathrm{e,max}}$ when the vessel moves with speed U.

5.2.1. Zero speed

The zero-speed experiments were conducted in two distinct locations (Fig. 11(a)) to assess the performance of our proposed method in two different sea states. Following the sea state code definitions by Price and Bishop (1974), the observed sea states in Location 1 and 2 were moderate and slight, with significant wave heights generally between 1.2 – 1.4 m and 0.7 – 0.8 m, respectively. The incident waves in Location 1 are generally larger than Location 2 as they come directly from the open sea, unobstructed by any landmass. In both locations, the swell was heavily dominant compared to the local wind.

Our experimental results (Figs. 15 and 16) show that in both locations, the estimates of the relative wave direction from our proposed method are generally very close to the corresponding values reported by the wave radar and wave buoy systems. Quantitatively, 91% and 71% of the total estimation errors are less than 20° and 10°, respectively, for the physical sensor configuration and, correspondingly, 92% and 70% for the virtual sensor configuration based on a single IMU. In addition to the high accuracy, the similarity of results between the physical and virtual sensor configurations further demonstrates that only a single IMU is indeed sufficient, thus rendering multiple physical IMUs redundant. This important result significantly increases the practical usefulness of our proposed method in addition to being accurate, cheap, portable, flexible, easy to install, and robust against various environmental conditions. In contrast, de facto standard wave buoy and wave radar systems are expensive and suffer from either being geographically confined, less flexible to changes, difficult to install (without expert help), and in some cases, sensitive to the external environment. For instance, during data collection, there were several losses from the wave radar due to precipitation and interference with the surrounding landmass (Fig. 16).

We suspect that uncertainties in the phase differences resulting from the FFT are likely one of the main culprits behind some of the observed deviations between the estimation results and the ground truths. By relying on the FFT, a compromise must be made between time and frequency resolution, which, in turn, translates to a compromise between real-time performance and accuracy—both of which must be present for practical feasibility. The compromise is reflected quantitively through the window length and percentage overlap between consecutive data segments, which for the presented results, were chosen after trial and error as 6 min and 50%, respectively. Collectively, these values produce estimate updates every third minute after initialization, which we consider a reasonable compromise between real-time performance and accuracy.

In the results presented, we reduced the frequency threshold to 0.13 Hz, which produced better results (recall that longer wave periods

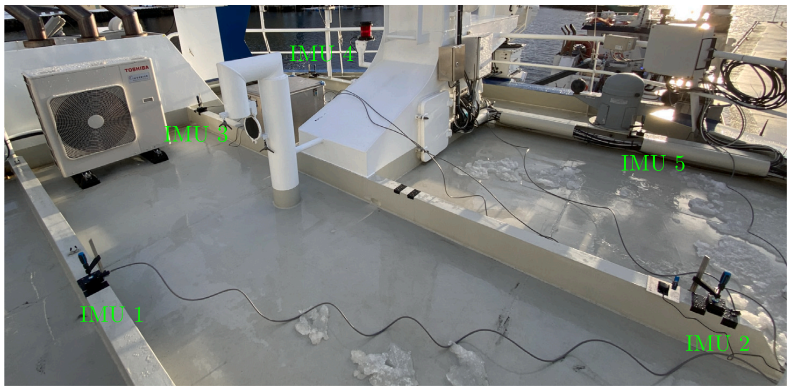

Fig. 13. The IMUs and GPS receiver were clamped to the roof of Gunnerus using screw clamps and connected to the synchronization unit, which was placed downstairs inside the bridge.

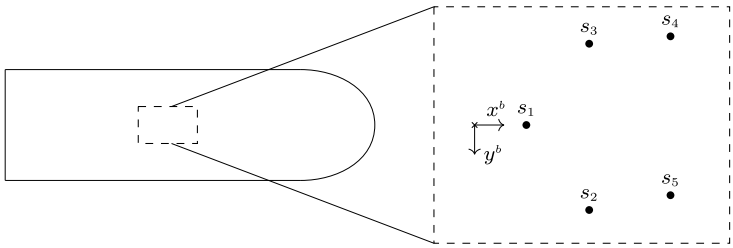

[m]	x^b	y^b	z^b
s_1	1.40	-0.02	1.58
s_2	3.12	2.28	1.58
s_3	3.13	-2.23	1.58
s_4	5.29	-2.45	1.58
s_5	5.28	1.87	1.58

Fig. 14. IMU array considered in the full-scale experiments. IMUs 1, 2, 3, 4, and 5 are denoted s_1, s_2, s_3, s_4, and s_5, respectively. The location of each sensor is given in meters with respect to the vessel body frame $\{b\}$. The origin of $\{b\}$ is indicated by a cross, where the z^b-axis (not shown) points down into the page. We have used the same configuration for the virtual sensor locations with IMU 1 considered as the only physical sensor. The virtual measurements from the other "sensors" were obtained by employing the measurement transformation (19) together with the processed linear accelerations, angular rates, and angular accelerations of IMU 1.

generally reduce model mismatch). As discussed in Section 4.2.4, such an adjustment is generally acceptable for unimodal seas where all wave components have the same propagation direction. Indeed, this was the case for both locations, which were largely swell-dominant. However, for a bimodal sea state consisting of swell and local wind-generated waves, our method (if left unmodified) will return the main wave direction and wave number corresponding to the most prominent wave system, assuming the wave systems are clearly distinguishable. This result follows from the current implementation of the method (see Algorithm 3), which assumes a single mode and concludes after finding the frequency associated with the largest peak. It is worth noting that if all the modal frequencies are known, the PTPD approach can be extended to work in multimodal environments by applying the method recursively for each modal frequency. The main challenge, however, is to identify the frequency of each unique mode in the heave acceleration spectrum. The latter can be achieved through various peak detection algorithms such as `findpeaks()` in MATLAB or more advanced techniques based on wavelet analysis (Du et al., 2006).

5.2.2. Forward speed

As mentioned earlier, the forward speed trials were abruptly ended due to ship operational issues shortly after commencing the first trial. For this reason, we consider the only forward speed experiment recorded that day, which lasted approximately 6 min. Despite the short duration, the results (Fig. 17) show great promise—91% of wave encounter angle errors and wave number errors are less than 20° and 0.01 m^{-1}, respectively, for the physical sensor configuration and, correspondingly, 82% and 73% for a single IMU. The wave number errors are particularly interesting as they suggest that it is indeed possible to retain the absolute wave frequency directly while moving with constant forward speed. Unfortunately, we were not able to test the latter in following sea conditions, thereby potentially circumventing the 1-to-3 mapping problem existing between encounter frequency and absolute frequency domains (Nielsen, 2017b, 2018).

6. Conclusions and further recommendations

A relatively new and exciting signal-based approach using the phase-time-path-differences (PTPDs) between a shipboard array of sensors to retrieve directional wave information has been explored in this study. We derived a new kinematic PTPD model accounting for forward vessel speed, thus generalizing the PTPD concept further to moving vessels. The theoretical foundation of this model in terms of modeling sensor delays on a rigid body was carefully assessed, and it was shown

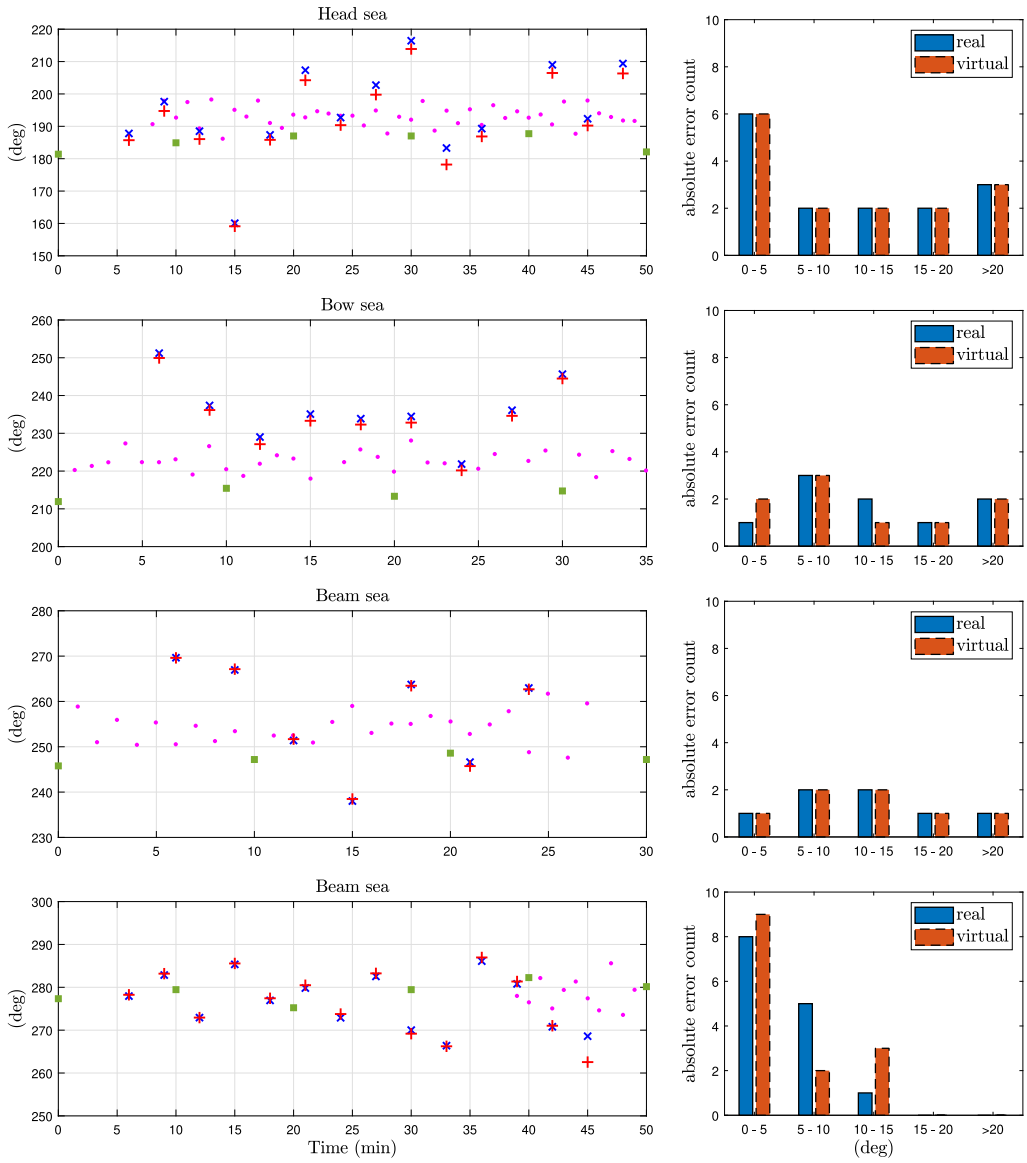

Fig. 15. Relative wave direction estimation results from our wave algorithm (Algorithm 3) from Location 1 (moderate sea with significant wave heights 1.2 – 1.4 m and water depth 339 m) for four different boat headings corresponding to head, bow, and beam seas. The estimates from the physical sensor configuration are indicated by crosses (blue), whereas the estimates from the virtual sensor configuration based on IMU 1 (Fig. 14) are indicated by plus signs (red). The corresponding wave direction values reported by the wave radar and wave buoy D are represented by dots (pink) and squares (green), respectively. The histograms next to each plot show the corresponding absolute error count for different error intervals for both sensor configurations (real and virtual). The wave radar values are considered as ground truth except for the bottom plot where it was mistakenly off and turned on again after 39 min. Hence, until 36 min, the wave buoy values were considered as reference. For each wave direction estimate (cross or plus sign), comparison was made with the ground truth by considering the value closest in time. All wave directions are given between $[0°, 360°)$ as the positive counterclockwise angle from the x-axis of the wave tangent frame to the vessel body x^b axis (Fig. 3). The window size, segment overlap, and frequency threshold $f_{\max}$ were set to 6 min, 50%, and 0.13 Hz, respectively.

that the model's accuracy relies on sufficiently short sensor separations and sufficiently long waves. Based on this theory and PTPD model, we proposed a methodology to resolve the wave propagation direction and wave number online from an array of IMUs and a single IMU by employing a rigid body measurement transform, an FFT, and a UKF. Our methodology incorporates a novel frequency threshold based on the main ship dimensions to avoid distorted wave components caused by vessel lowpass filtering. The wave estimation capabilities of our proposed method were tested on IMU data collected from a wave tank and full-scale experiments involving a research vessel equipped with a commercial wave radar operating in the proximity of several wave buoys outside the coast of Norway. The estimation results generally agreed very well with the reference wave values reported from both wave measurement systems, demonstrating that a single physical IMU is sufficient. Together, these results significantly increase the practical utility of the PTPD approach, rendering it a serious contender to other

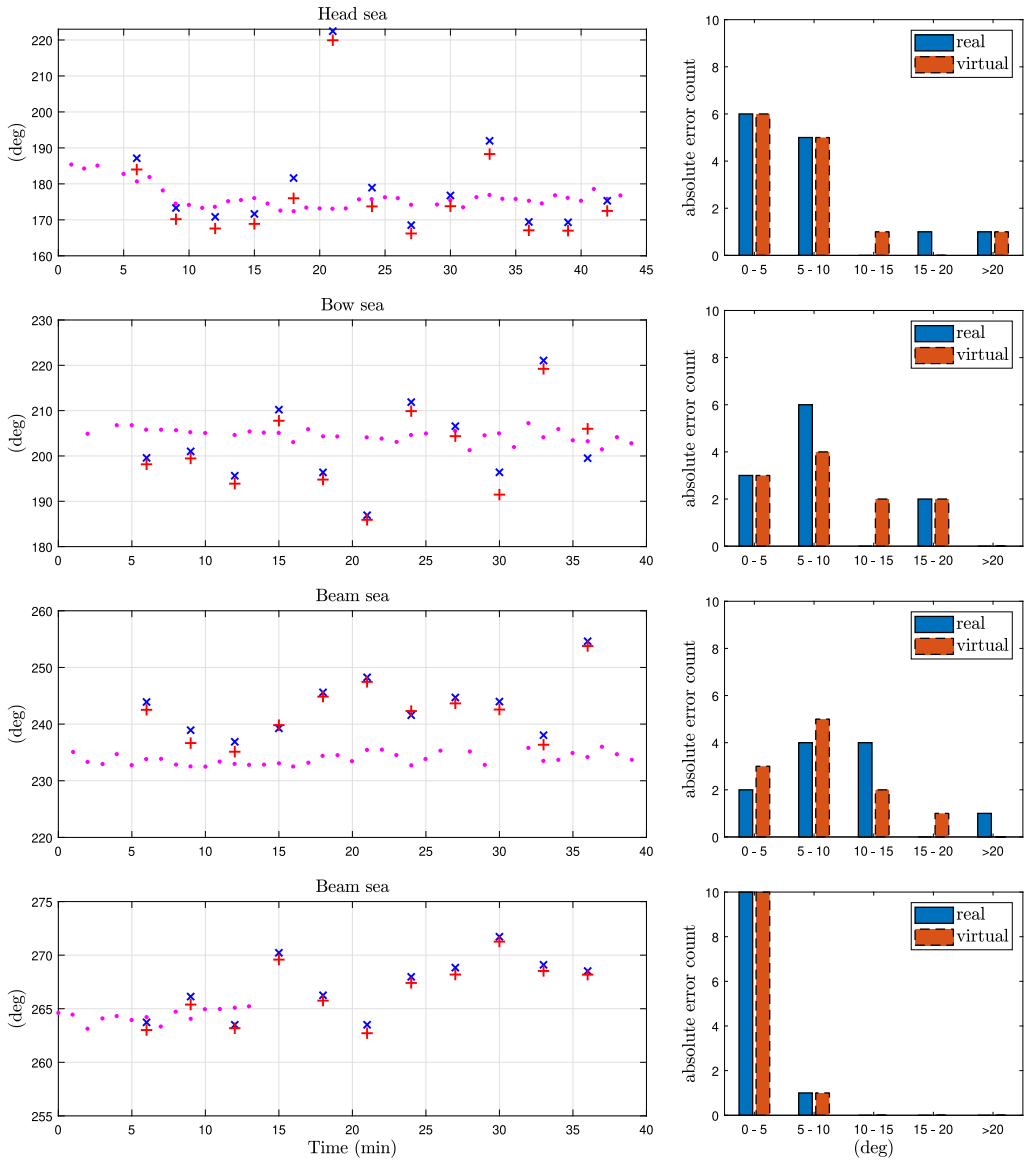

Fig. 16. Relative wave direction estimation results from our wave algorithm (Algorithm 3) from Location 2 (slight sea with significant wave heights $0.7-0.8$ m and water depth 442 m) for four different boat headings corresponding to head, bow, and beam seas. The estimates from the physical sensor configuration are indicated by crosses (blue), whereas the estimates from the virtual sensor configuration based on IMU 1 (Fig. 14) are indicated by plus signs (red). The corresponding wave direction values reported by the wave radar are represented by dots (pink). The histograms next to each plot show the corresponding absolute error count for different error intervals for both sensor configurations (real and virtual). For each wave direction estimate (cross or plus sign), comparison was made with the wave radar by considering the value closest in time. In the bottom plot, the wave radar dropped out due to significant interference with the surrounding landmass. For this reason, the remaining comparison with the other wave estimates was made based on the last recorded wave radar value. All wave directions are given between $[0°, 360°)$ as the positive counterclockwise angle from the x-axis of the wave tangent frame to the vessel body x^b axis (Fig. 3). The window size, segment overlap, and frequency threshold $f_{\max}$ were set to 6 min, 50%, and 0.13 Hz, respectively.

shipboard signal-based approaches in terms of accuracy and online performance while being cheap, flexible, easy to install, and robust against environmental influences.

As hinted in Section 5.2.1, our wave estimation procedure is currently limited by the FFT, which forces a trade-off between real-time performance and accuracy. In order to increase practical utility further, future studies should seek to optimize the estimation procedure by considering alternative methods to the FFT that are less stringent on the trade-off above. In this regard, there are, in particular, two approaches worth examining in greater detail, namely, the Hilbert-Huang transform (HHT) and a real-time phase difference tracking filter (Chen et al., 2019). The former approach can yield instantaneous frequency and phase information for non-stationary data, whereas the latter yields the same information in real time but is based on a single sinusoid. A comparison between these approaches (and potential others) and the FFT is left as an application for further studies.

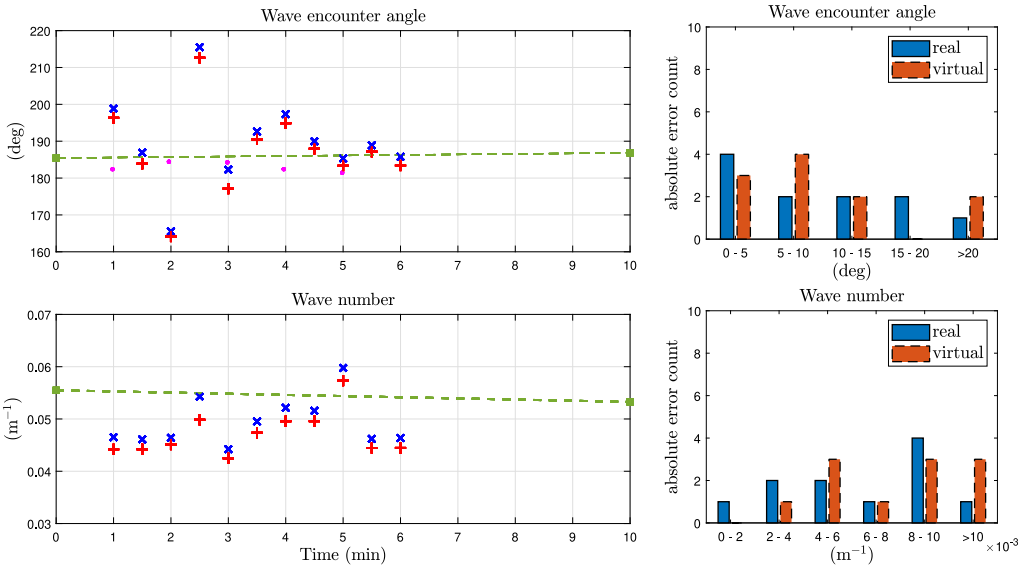

Fig. 17. Relative wave encounter angle and wave number estimation results from our wave algorithm (Algorithm 3) in head sea (moderate sea with significant wave height ~ 1.3 m and water depth 439 m) with forward vessel speed $U = 10.8$ knots (Fig. 11(b)). The estimates from the physical sensor configuration are indicated by crosses (blue), whereas the estimates from the virtual sensor configuration based on IMU 1 (Fig. 14) are indicated by plus signs (red). The corresponding wave direction values reported by the wave radar and wave buoy (A and D) are represented by dots (pink) and squares (green), respectively. The buoys A and D report the same wave direction and low frequency mean wave period, which has been converted to wave numbers using the dispersion relation (21) for deep waters, and are shown as squares (green) in the wave number plot. The histograms next to each plot show the corresponding absolute error count for different error intervals for both sensor configurations (real and virtual). The wave radar and wave buoy values are considered reference for the wave encounter angle and wave number, respectively. For each wave estimate (cross or plus sign), comparison was made with the ground truth by considering the value closest in time. A dashed line has been extended between the wave buoy values to make comparison easier. All wave directions are given between $[0°, 360°)$ as the positive counterclockwise angle from the x-axis of the wave tangent frame to the vessel body x^b axis (Fig. 3). The window size and segment overlap were set to 1 min and 50%, respectively. The frequency threshold was selected as the maximum default value based on the vessel length and beam dimensions.

The results from the forward speed trials presented in this work are promising but limited from further generalization due to the size of the wave basin (inhibiting other heading angles from being tested) and operational issues onboard RV Gunnerus. For this reason, future investigations should aim for additional forward speed testing in head, bow, beam, quartering, and following sea conditions to further validate our theory and proposed methodology. In particular, additional experimentation in beam to following seas is of interest to show that our approach can directly obtain the absolute true wave frequency, thereby circumventing the 1-to-3 mapping problem generally existing between the encounter and absolute frequency domains.

One of the conditions for the PTPD approach to model sensor delays on a rigid body is that the sensor separations be sufficiently close. However, a too-small sensor separation combined with the (fixed and finite) sensor sampling rate increases the risk of all measured phase differences becoming zero, resulting in a loss of observability of our state-space model. This phenomenon can happen for any given sensor configuration, provided that the propagation speed of the considered waves is sufficiently high. Hence, what constitutes a minimal sensor separation depends on the wave conditions, and finding a lower bound on the separation distance for all situations is difficult. We leave this as a potential topic for future inquiry.

In this study, the primary wave environment considered for practical assessment of the PTPD approach has been long-crested irregular waves. It is important to note that the PTPD method can be extended to work in more short-crested wave environments featuring multiple modes by recursively applying the method to each modal frequency. Identifying these modal frequencies, for instance through various peak detection algorithms based on wavelet analysis, is beyond the scope of the present study.

CRediT authorship contribution statement

Johann A. Dirdal: Conceptualization, Methodology, Software, Validation, Investigation, Formal analysis, Writing, Visualization. **Roger Skjetne:** Conceptualization, Writing – review & editing, Co-supervision. **Jan Roháč:** Conceptualization, Writing – review & editing. **Thor I. Fossen:** Conceptualization, Writing – review & editing, Supervision.

Declaration of competing interest

The authors declare that they have no known competing financial interests or personal relationships that could have appeared to influence the work reported in this paper.

Data availability

Data will be made available on request.

Acknowledgments

The work was sponsored by the Research Council of Norway (RCN) through the Centre of Excellence on Autonomous Marine Operations and Systems (NTNU AMOS, RCN project 223254), and partly through the Centre for Research-based Innovation, SFI MOVE (RCN project 237929).

Appendix. Model error analysis

In this section, the model deviations between the time-varying and average phase difference models, (11) and (12), respectively, are quantitatively assessed for different wave parameters and roll-pitch

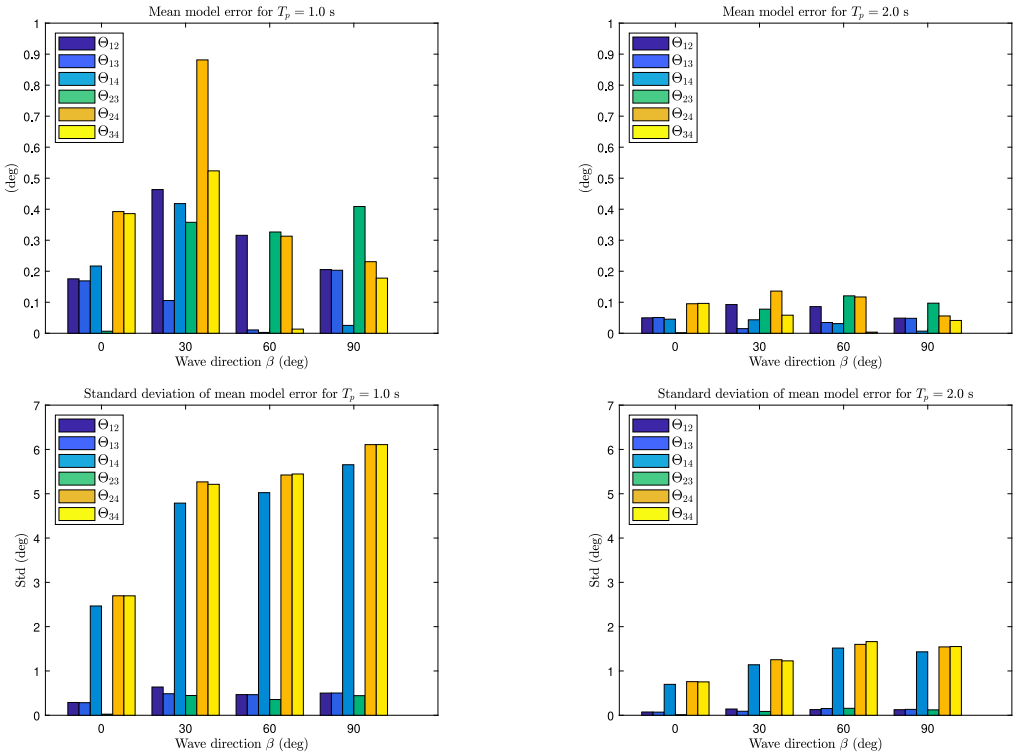

Fig. A.18. For each experimental wave period T_p and wave direction β, the absolute value of the mean error (top) and corresponding standard deviation (bottom) for all phase differences are shown in different colors. The mean error is computed by $1/N \sum$((11)–((12))) for a total of N roll and pitch samples based on the sensor configuration in Fig. 6(a), which for four sensors yields a total of six independent phase differences $\{\Theta_{12}, \Theta_{13}, \Theta_{14}, \Theta_{23}, \Theta_{24}, \Theta_{34}\}$. In all experiments, the roll and pitch response amplitudes were scaled to simulate the worst-case conditions of the pool experiments in Section 4. For $\beta = 0°$, the pitch response amplitude was scaled to 5° and, for $\beta = 90°$, the roll response amplitude was scaled to 10°. For $\beta = 30°$ and 60°, both the roll and pitch responses were scaled to 10° and 5°, respectively.

responses. To carry out such an assessment, we consider roll and pitch data from a model ship in regular waves with periods $\{1.0\,\text{s}, 2.0\,\text{s}\}$ and relative wave directions $\{0°, 30°, 60°, 90°\}$. The roll and pitch responses have been scaled to even larger amplitudes to see how increasingly rougher seas may impact the model differences. As we shall see, the model deviations are directly affected by the vessel roll and pitch offset, the height separation between the sensors onboard, and the period of the waves passing through the vessel. The experimental data considered in this analysis were collected as part of the Master's thesis of Udjus (2017).

A.1. Simulation results

The simulation results (Fig. A.18) show the total mean error between Eqs. (11) and (12) and the corresponding standard deviation computed from each roll-pitch sample for the duration of the considered responses. In the computation of these errors, the sensor configuration in Fig. 6(a) was considered, which consists of four sensors and gives access to a total of six independent phase differences in each experiment. The wave number was computed through the dispersion relation in (21), assuming a water depth of 1.5 m.

The following observations are made from the mean model errors and standard deviations in Fig. A.18:

(i) The mean model error for each phase difference is less than 1° for all experiments.

(ii) The standard deviation of each phase difference associated with sensor 4 is significantly larger than the rest.

(iii) The mean model error and standard deviation decrease for increasing wave periods.

Observations (i) and (ii) are discussed in the subsequent subsections, respectively. The downscaling effect (iii) is caused by the wave number k, which is inversely proportional to the wave period. Hence, longer waves imply smaller errors than shorter waves and vice versa.

A.2. Roll and pitch asymmetry

Regarding (i), we repeated the same simulations with roll and pitch responses scaled to 30° and 10°, respectively, and observed similar results (i.e., all errors were less than 1°). These results show that the average phase difference model is more or less independent of roll-pitch amplitude, thus eliminating the need for the small-angle assumption considered in our previous work (Dirdal et al., 2022).

However, if the roll and pitch responses can be asymmetric (e.g., due to uneven loading conditions and/or manufacturing errors), the average roll and pitch angles may no longer be centered close to zero (i.e., $\bar{\phi}(t) = \phi_0 \neq 0$ and $\bar{\theta}(t) = \theta_0 \neq 0$). If these offsets are left unaccounted for, they may cause a bias between the considered phase difference models (Fig. A.19). However, if the roll and pitch offsets are known, the deviation can be alleviated by inserting these values into Eq. (11) and applying this average model instead.

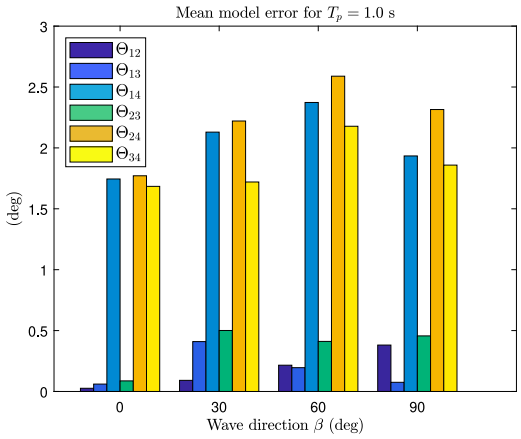

Fig. A.19. Repeated mean model error simulation for wave period $T_p = 1.0$ s (Fig. A.18) but with an offset value of 2° added to all roll and pitch responses.

A.3. Sensor height separation

A significant sensor height separation will amplify any differences between the considered phase difference models due to the latter term in the RHS of Eq. (11). When the roll and pitch responses are symmetric about zero, this amplification effect is manifested mainly in the standard deviations of mean model errors (Fig. A.18). However, if the roll and pitch responses are asymmetric about zero, the sensor height separation may also influence the mean model error (Fig. A.19). This amplification effect can be mitigated by only considering coplanar sensor measurements (i.e., all sensors on the same plane).

References

Brodtkorb, A.H., Nielsen, U.D., Sørensen, A.J., 2018. Sea state estimation using vessel response in dynamic positioning. Appl. Ocean Res. 70.

Brown, R.G., Hwang, P.Y.C., 1997. Introduction to Random Signals and Applied Kalman Filtering: With MATLAB Exercises and Solutions, third ed. Wiley, New York, NY, URL: https://cds.cern.ch/record/680442.

Chen, N., Fan, S., Zheng, D., 2019. A phase difference measurement method based on strong tracking filter for Coriolis mass flowmeter. Rev. Sci. Instrum. 90 (7).

de Souza, F.L., Tannuri, E.A., de Mello, P.C., Franzini, G., Mas-Soler, J., Simos, A.N., 2018. Bayesian estimation of directional wave-spectrum using vessel motions and wave-probes: Proposal and preliminary experimental validation. J. Offshore Mech. Arct. Eng. 140 (4).

Dirdal, J.A., Skjetne, R., Roháč, J., Fossen, T.I., 2022. Online wave direction and wave number estimation from surface vessel motions using distributed inertial measurement arrays and phase-time-path-differences. Ocean Eng. 249.

Dishan, H., 1995. Phase error in fast Fourier transform analysis. Mech. Syst. Signal Process. 9 (2).

Donelan, M.A., Drennan, W.M., Magnusson, A.K., 1996. Nonstationary analysis of the directional properties of propagating waves. J. Phys. Oceanogr. 26 (9).

Draycott, S., Davey, T., Ingram, D.M., Day, J.L.a., Johanning, L., 2015. Using a phase-time-path-difference approach to measure directional wave spectra in FloWave. In: EWTEC Conference Proceedings. pp. 1–7.

Draycott, S., Davey, T., Ingram, D.M., Day, A., Johanning, L., 2016. The SPAIR method: Isolating incident and reflected directional wave spectra in multidirectional wave basins. Coast. Eng. 114, 265–283.

Draycott, S., Noble, D.R., Davey, T., Bruce, T., Ingram, D.M., Johanning, L., Smith, H.C., Day, A., Kaklis, P., 2018. Re-creation of site-specific multi-directional waves with non-collinear current. Ocean Eng. 152.

Du, P., Kibbe, W.A., Lin, S.M., 2006. Improved peak detection in mass spectrum by incorporating continuous wavelet transform-based pattern matching. Bioinformatics 22 (17).

Duz, B., Mak, B., Hageman, R., Grasso, N., 2019. Real time estimation of local wave characteristics from ship motions using artificial neural networks. In: 14th Int. Conf. of Practical Design of Ships and Other Floating Structures. Yokohama, Japan.

Esteva, D.C., 1976. Wave direction computations with three gage arrays. In: Proc. Fifteenth Coastal Engng. Conf., Vol. 1. Hawaii Univ., U.S.A.: Jul. 11–17, 1976, pp. 349–367, New Yo.

Esteva, D.C., 1977. Evaluation of the Computation of Wave Direction with Three-Gauge Arrays. Technical Report, CERC, Technical Paper No. 77-7, U.S. Army Corps of Engineers.

Fernandes, A.A., Gouveia, A.D., Nagarajan, R., 1988. Determination of wave direction from linear and polygonal arrays. Ocean Eng. 15 (4), 345–357.

Fernandes, A.A., Menon, H.B., Sarma, Y.V., Jog, P.D., Almeida, A.M., 2001. Wavelength of ocean waves and surf beat at duck from array measurements. In: Proceedings of the International Symposium on Ocean Wave Measurement and Analysis, Vol. 2.

Fernandes, A.A., Sarma, Y.V., Menon, H.B., 2000. Directional spectrum of ocean waves from array measurements using phase/time/path difference methods. Ocean Eng. 27 (4), 345–363.

Fossen, T.I., 2021. Handbook of Marine Craft Hydrodynamics and Motion Control, second ed. Wiley, Chichester, West Sussex, U.K.

Fu, T.C., Fullerton, A.M., Hackett, E.E., Merrill, C., 2011. Shipboard measurement of ocean waves. In: Proceedings of the International Conference on Offshore Mechanics and Arctic Engineering - OMAE, Vol. 6.

Furevik, B.R., Lønseth, L., Borg, A.L., Neshaug, V., Gausen, M., 2016. Oceanographic observations for the coastal highway E39 project in mid Norway. http://dx.doi.org/10.21343/ef2d-jp97.

Han, P., Li, G., Skjong, S., Zhang, H., 2022. Directional wave spectrum estimation with ship motion responses using adversarial networks. Mar. Struct. 83.

Heyn, H.M., Udjus, G., Skjetne, R., 2017. Distributed motion sensing on ships. In: OCEANS 2017 - Anchorage, Vol. 2017-January.

Holthuijsen, L.H., 2007. Waves in Oceanic and Coastal Waters. Cambridge University Press.

Julier, S., Uhlmann, J., 2004. Unscented filtering and nonlinear estimation. Proc. IEEE 92 (3).

Kandepu, R., Imsland, L., Foss, B.A., 2008. Constrained state estimation using the unscented Kalman filter. In: 2008 Mediterranean Conference on Control and Automation - Conference Proceedings. MED'08'.

Kim, D.H., Kim, N., 2014. An auto weather-vaning system for a DP vessel that uses a nonlinear controller and a disturbance observer. Int. J. Nav. Archit. Ocean Eng. 6 (1).

Kjerstad, O.K., Skjetne, R., 2016. Disturbance rejection by acceleration feedforward for marine surface vessels. IEEE Access 4.

Luo, L., Liu, S., Li, J., Jia, W., 2020. Deterministic reconstruction and reproduction of multi-directional irregular waves based on linear summation model. Ocean Eng. 198, 106952.

Mak, B., Düz, B., 2019. Ship as a wave buoy: Using simulated data to train neural networks for real time estimation of relative wave direction. In: Proceedings of the International Conference on Offshore Mechanics and Arctic Engineering - OMAE, Vol. 9.

Mittendorf, M., Nielsen, U.D., Bingham, H.B., Storhaug, G., 2022. Sea state identification using machine learning—A comparative study based on in-service data from a container vessel. Mar. Struct. 85.

Mounet, R.E., Nielsen, U.D., Brodtkorb, A.H., Tannuri, E.A., de Mello, P.C., 2022. Simultaneous sea state estimation and transfer function tuning using a network of dynamically positioned ships. Appl. Ocean Res. 129.

Nielsen, U.D., 2006. Estimations of on-site directional wave spectra from measured ship responses. Mar. Struct. 19 (1).

Nielsen, U.D., 2007. Response-based estimation of sea state parameters - influence of filtering. Ocean Eng. 34 (13).

Nielsen, U.D., 2008. The wave buoy analogy - estimating high-frequency wave excitations. Appl. Ocean Res. 30 (2).

Nielsen, U.D., 2017a. A concise account of techniques available for shipboard sea state estimation. Ocean Eng. 129.

Nielsen, U.D., 2017b. Transformation of a wave energy spectrum from encounter to absolute domain when observing from an advancing ship. Appl. Ocean Res. 69.

Nielsen, U.D., 2018. Deriving the absolute wave spectrum from an encountered distribution of wave energy spectral densities. Ocean Eng. 165.

Nielsen, U.D., Brodtkorb, A.H., Sørensen, A.J., 2019. Sea state estimation using multiple ships simultaneously as sailing wave buoys. Appl. Ocean Res. 83.

Nielsen, U.D., Dietz, J., 2020. Estimation of sea state parameters by the wave buoy analogy with comparisons to third generation spectral wave models. Ocean Eng. 216.

Nielsen, U.D., Mounet, R.E., Brodtkorb, A.H., 2021. Tuning of transfer functions for analysis of wave–ship interactions. Mar. Struct. 79.

Pascal, R., Lucas, J., Ingram, D., Bryden, I., 2009. Assessing and improving the Edinburgh curved wave tank. In: Proceedings of the International Offshore and Polar Engineering Conference.

Price, W., Bishop, R., 1974. Probabilistic Theory of Ship Dynamics. Chapman and Hall, London.

Simon, D., 2010. Kalman filtering with state constraints: A survey of linear and nonlinear algorithms. IET Control Theory Appl. 4 (8).

Tannuri, E.A., Sparano, J.V., Simos, A.N., Da Cruz, J.J., 2003. Estimating directional wave spectrum based on stationary ship motion measurements. Appl. Ocean Res. 25 (5).

Udjus, G., 2017. Force Field Identification and Positioning Control of an Autonomous Vessel using Inertial Measurement Units (MSc thesis). Norwegian University of Science and Technology, Trondheim, p. 85.

Waals, O.J., Aalbers, A.B., Pinkster, J.A., 2002. Maximum likelihood method as a means to estimate the directional wave spectrum and the mean wave drift force on a dynamically positioned vessel. In: Proceedings of the International Conference on Offshore Mechanics and Arctic Engineering - OMAE, Vol. 4.

Zappa, B., Legnani, G., Van Den Bogert, A.J., Adamini, R., 2001. On the number and placement of accelerometers for angular velocity and acceleration determination. J. Dyn. Syst. Meas. Control Trans. ASME 123 (3).

References

[1] US Department of Commerce, N. O., and A. A. *National Data Buoy Center*. Nov. 1996. URL: https://www.ndbc.noaa.gov/.

[2] MarineTraffic. *Global Ship Tracking Intelligence: AIS Marine Traffic*. URL: https://www.marinetraffic.com/.

[3] US Department of Commerce, N. O., and A. A. *Voluntary observing ship program*. Nov. 1996. URL: https://www.vos.noaa.gov/.

[4] Ulrik D. Nielsen. "A concise account of techniques available for shipboard sea state estimation". *Ocean Engineering* 129 (2017), pp. 352–362. DOI: 10.1016/j.oceaneng.2016.11.035.

[5] Hamed Majidian, Lei Wang, and Hossein Enshaei. "Part. A: A review of the real-time sea-state estimation, using wave buoy analogy". *Ocean Engineering* 266 (2022). DOI: 10.1016/j.oceaneng.2022.111684.

[6] Ulrik D. Nielsen, Mikkel Bjerregard, Roberto Galeazzi, and Thor I. Fossen. "New concepts for shipboard sea state estimation". *OCEANS 2015 - MTS/IEEE Washington*. 2016, pp. 1–10. DOI: 10.23919/oceans.2015.7404386.

[7] Leo H. Holthuijsen. *Waves in Oceanic and Coastal Waters*. Cambridge University Press, 2007. DOI: 10.1017/CBO9780511618536.

[8] Willard J. Pierson, G. Neumann, and R. W. James. "Practical methods for observing and forecasting ocean waves by means of wave spectra and statistics". *Navy Hydrographic Office* (1955), p. 284.

[9] Michel K. Ochi. *Ocean Waves: The Stochastic Approach*. Cambridge Ocean Technology Series. Cambridge University Press, 1998. DOI: 10.1017/CBO9780511529559.

[10] M. J. Tucker. "A shipborne wave recorder". *Trans. Inst. Naval Architects* 98 (1956), pp. 236–250.

[11] E. G. Pitt. “A new empirically-based correction procedure for shipborne wave recorder data”. *Applied Ocean Research* 13.4 (1991), pp. 162–174. DOI: 10.1016/S0141-1187(05)80072-0.

[12] K. Takekuma and T. Takahashi. “On the evaluation of sea spectra based on the measured ship motions”. *Trans West-Jpn* 45 (1973), pp. 51–57. URL: https://www.scopus.com/inward/record.uri?eid=2-s2.0-84885299254&partnerID=40&md5=6c5231916d2575c0a87bd8eb848b7719.

[13] K. Lindemann, J. Odland, and J. Strengehagen. “On the Application of Hull Surveillance Systems for Increased Safety and Improved Structural Utilization in Rough Weather”. *Nor Veritas Publ* 105 (1978).

[14] Tsugukiyo Hirayama. “Real-time estimation of sea spectra based on motions of a running ship, 2nd report: Directional wave estimation”. *Journal of the Kansai Society of Naval Architects* 204 (1987).

[15] Toshio Iseki, Kohei Ohtsu, and Masataka Fujino. “A Study on Estimation of Directional Spectra Based on Ship Motions”. *The Journal of Japan Institute of Navigation* 86 (1992), pp. 179–188.

[16] Kimio Saito, Katsuya Maeda, Akihiko Matsuda, and Shirou Suzuki. “Directional Wave Spectrum Generated in the Experimental Tank”. *Journal of the Society of Naval Architects of Japan* 2000.187 (2000), pp. 77–83. DOI: 10.2534/jjasnaoe1968.2000.77.

[17] Toshio Iseki and Kohei Ohtsu. “Bayesian estimation of directional wave spectra based on ship motions”. *Control Engineering Practice*. Vol. 8. 2. 2000, pp. 215–219. DOI: 10.1016/S0967-0661(99)00156-2.

[18] Olaf J. Waals, A. B. Aalbers, and J. A. Pinkster. “Maximum likelihood method as a means to estimate the directional wave spectrum and the mean wave drift force on a dynamically positioned vessel”. *Proceedings of the International Conference on Offshore Mechanics and Arctic Engineering - OMAE*. Vol. 4. 2002, pp. 605–613. DOI: 10.1115/OMAE2002-28560.

[19] Eduardo A. Tannuri, Joao V. Sparano, Alexandre N. Simos, and José J. Da Cruz. “Estimating directional wave spectrum based on stationary ship motion measurements”. *Applied Ocean Research* 25.5 (2003), pp. 243–261. DOI: 10.1016/j.apor.2004.01.003.

[20] R. Pascoal, C. Guedes Soares, and A. J. Sørensen. “Ocean Wave Spectral Estimation Using Vessel Wave Frequency Motions”. *Journal of Offshore Mechanics and Arctic Engineering* 129.2 (May 2006), pp. 90–96. DOI: 10.1115/1.2426986.

[21] Alexandre N. Simos, João V. Sparano, Eduardo A. Tannuri, and Vinícius L.F. Matos. “Directional wave spectrum estimation based on a vessel 1st order motions: Field results”. *Proceedings of the International Offshore and Polar Engineering Conference*. 2007, pp. 81–89.

[22] João V. Sparano, Eduardo A. Tannuri, Alexandre N. Simos, and Vinicius L.F. Matos. “On the estimation of directional wave spectrum based on stationary vessels 1st order motions: A new set of experimental results”. *Proceedings of the International Conference on Offshore Mechanics and Arctic Engineering - OMAE*. Vol. 4. 2008, pp. 311–320. DOI: 10.1115/OMAE2008-57431.

[23] R. Pascoal and C. Guedes Soares. “Kalman filtering of vessel motions for ocean wave directional spectrum estimation”. *Ocean Engineering* 36.6-7 (2009), pp. 477–488. DOI: 10.1016/j.oceaneng.2009.01.013.

[24] R. Pascoal, L. P. Perera, and C. Guedes Soares. “Estimation of directional sea spectra from ship motions in sea trials”. *Ocean Engineering* 132 (2017), pp. 126–137. DOI: 10.1016/j.oceaneng.2017.01.020.

[25] Astrid H. Brodtkorb, Ulrik D. Nielsen, and Asgeir J. Sørensen. “Sea state estimation using vessel response in dynamic positioning”. *Applied Ocean Research* 70 (2018), pp. 76–86. DOI: 10.1016/j.apor.2017.09.005.

[26] Toshio Iseki and Daisuke Terada. “Bayesian estimation of directional wave spectra for ship guidance system”. *International Journal of Offshore and Polar Engineering* 12.1 (2002).

[27] Toshio Iseki. “Extended Bayesian estimation of directional wave spectra”. *International Conference on Offshore Mechanics and Arctic Engineering*. Vol. 37440. 2004, pp. 611–616.

[28] Ulrik D. Nielsen. “Estimations of on-site directional wave spectra from measured ship responses”. *Marine Structures* 19.1 (2006), pp. 33–69. DOI: 10.1016/j.marstruc.2006.06.001.

[29] Ulrik D. Nielsen and David C. Stredulinsky. “Sea state estimation from an advancing ship - A comparative study using sea trial data”. *Applied Ocean Research* 34 (2012), pp. 33–44. DOI: 10.1016/j.apor.2011.11.001.

[30] Ulrik D. Nielsen and Toshio Iseki. “A study on parametric wave estimation based on measured ship motions”. *The Journal of Japan Institute of Navigation* 126 (2012), pp. 171–177.

[31] Ulrik D. Nielsen, Ingrid Marie V. Andersen, and Jos Koning. “Comparisons of means for estimating sea states from an advancing large container ship”. *Proceedings of the PRADS* (2013).

[32] Najmeh Montazeri, Ulrik Dam Nielsen, and Jørgen Juncher Jensen. "Estimation of wind sea and swell using shipboard measurements - A refined parametric modelling approach". *Applied Ocean Research* 54 (2016), pp. 73–86. DOI: 10.1016/j.apor.2015.11.004.

[33] Ulrik D. Nielsen, Astrid H. Brodtkorb, and Asgeir J. Sørensen. "Sea state estimation using multiple ships simultaneously as sailing wave buoys". *Applied Ocean Research* 83 (2019), pp. 65–76. DOI: 10.1016/j.apor.2018.12.004.

[34] Ulrik D. Nielsen and Jesper Dietz. "Estimation of sea state parameters by the wave buoy analogy with comparisons to third generation spectral wave models". *Ocean Engineering* 216 (2020). DOI: 10.1016/j.oceaneng.2020.107781.

[35] Ulrik D. Nielsen. "Transformation of a wave energy spectrum from encounter to absolute domain when observing from an advancing ship". *Applied Ocean Research* 69 (2017), pp. 160–172. DOI: 10.1016/j.apor.2017.10.011.

[36] Ulrik D. Nielsen. "Deriving the absolute wave spectrum from an encountered distribution of wave energy spectral densities". *Ocean Engineering* 165 (2018), pp. 194–208. DOI: 10.1016/j.oceaneng.2018.07.046.

[37] Michel K. Ochi and E. Nadine Hubble. "Six-Parameter Wave Spectra". *Coastal Engineering*. 1976, pp. 301–328. DOI: 10.1061/9780872620834.018.

[38] N. Hogben and F. C. Cobb. "Parametric modelling of directional wave spectra". *Offshore Technology Conference*. 1986. DOI: 10.4043/5212-MS.

[39] Rémy Pascal, Jorge Lucas, David Ingram, and Ian Bryden. "Assessing and improving the Edinburgh curved wave tank". *Proceedings of the International Offshore and Polar Engineering Conference*. 2009.

[40] Zhengru Ren, Xu Han, Amrit Shankar Verma, Johann Alexander Dirdal, and Roger Skjetne. "Sea state estimation based on vessel motion responses: Improved smoothness and robustness using Bézier surface and L1 optimization". *Marine Structures* 76 (2021). DOI: 10.1016/j.marstruc.2020.102904.

[41] Ulrik D. Nielsen. "Response-based estimation of sea state parameters - influence of filtering". *Ocean Engineering* 34.13 (2007), pp. 1797–1810. DOI: 10.1016/j.oceaneng.2007.03.002.

[42] Ulrik D. Nielsen. "The wave buoy analogy - estimating high-frequency wave excitations". *Applied Ocean Research* 30.2 (2008), pp. 100–106. DOI: 10.1016/j.apor.2008.07.002.

[43] Felipe Lopes de Souza et al. “Bayesian Estimation of Directional Wave-Spectrum Using Vessel Motions and Wave-Probes: Proposal and Preliminary Experimental Validation”. *Journal of Offshore Mechanics and Arctic Engineering* 140.4 (Dec. 2018), p. 41102. DOI: 10.1115/1.4039263. URL: https://doi.org/10.1115/1.4039263.

[44] Johann A. Dirdal, Roger Skjetne, Jan Roháč, and Thor I. Fossen. “Online wave direction and wave number estimation from surface vessel motions using distributed inertial measurement arrays and phase-time-path-differences”. *Ocean Engineering* 249 (2022). DOI: 10.1016/j.oceaneng.2022.110760.

[45] Johann A Dirdal, Roger Skjetne, Jan Roháč, and Thor I Fossen. “A phase-time-path-difference approach for online wave direction and wave number estimation from measured ship motions in zero and forward speed using a single inertial measurement unit”. *Ocean Engineering* 288 (2023). DOI: 10.1016/j.oceaneng.2023.116131.

[46] I. R. Young, W. Rosenthal, and F. Ziemer. “A three-dimensional analysis of marine radar images for the determination of ocean wave directionality and surface currents.” *Journal of Geophysical Research* 90.C1 (1985), pp. 1049–1059. DOI: 10.1029/JC090iC01p01049.

[47] José Carlos Nieto Borge, Konstanze Reichert, and Jürgen Dittmer. “Use of nautical radar as a wave monitoring instrument”. *Coastal Engineering* 37.3-4 (1999), pp. 331–342. DOI: 10.1016/S0378-3839(99)00032-0.

[48] Weimin Huang, Xinlong Liu, and Eric W. Gill. “Ocean wind and wave measurements using X-band marine radar: A comprehensive review”. *Remote Sensing* 9.12 (2017). DOI: 10.3390/rs9121261.

[49] Kai Håkon Christensen et al. “Surface wave measurements using a ship-mounted ultrasonic altimeter”. *Methods in Oceanography* 6 (2013), pp. 1–15. DOI: 10.1016/j.mio.2013.07.002.

[50] Trygve K. Løken et al. “Wave measurements from ship mounted sensors in the Arctic marginal ice zone”. *Cold Regions Science and Technology* 182 (2021). DOI: 10.1016/j.coldregions.2020.103207.

[51] Fangwen Tu, Shuzhi Sam Ge, Yoo Sang Choo, and Chang Chieh Hang. “Sea state identification based on vessel motion response learning via multi-layer classifiers”. *Ocean Engineering* 147 (2018), pp. 318–332. DOI: 10.1016/j.oceaneng.2017.08.047.

[52] Bart Mak and Bülent Düz. “Ship as a wave buoy: Estimating relative wave direction from in-service ship motion measurements using machine learning”. *Proceedings of the International Conference on Offshore Mechanics and Arctic Engineering - OMAE*. Vol. 9. 2019. DOI: 10.1115/OMAE2019-96201.

[53] Bart Mak and Bülent Düz. “Ship as a wave buoy: Using simulated data to train neural networks for real time estimation of relative wave direction”. *Proceedings of the International Conference on Offshore Mechanics and Arctic Engineering - OMAE*. Vol. 9. 2019. DOI: 10.1115/OMAE2019-96225.

[54] Bulent Duz, Bart Mak, Remco Hageman, and Nicola Grasso. “Real Time Estimation of Local Wave Characteristics From Ship Motions Using Artificial Neural Networks”. *14th Int. Conf. of Practical Design of Ships and Other Floating Structures*. Yokohama, Japan, 2019, pp. 657–678. URL: https://doi.org/10.1007/978-981-15-4680-8_45.

[55] Ina Bjørkum Arneson, Astrid H. Brodtkorb, and Asgeir J. Sørensen. “Sea State Estimation Using Quadratic Discriminant Analysis and Partial Least Squares Regression”. *IFAC-PapersOnLine*. Vol. 52. 21. 2019, pp. 72–77. DOI: 10.1016/j.ifacol.2019.12.285.

[56] Xu Cheng et al. “Modeling and analysis of motion data from dynamically positioned vessels for sea state estimation”. *Proceedings - IEEE International Conference on Robotics and Automation*. Vol. 2019-May. 2019, pp. 6644–6650. DOI: 10.1109/ICRA.2019.8794069.

[57] Xu Cheng et al. “A Novel Densely Connected Convolutional Neural Network for Sea-State Estimation Using Ship Motion Data”. *IEEE Transactions on Instrumentation and Measurement* 69.9 (2020), pp. 5984–5993. DOI: 10.1109/TIM.2020.2967115.

[58] Xu Cheng, Guoyuan Li, Robert Skulstad, Houxiang Zhang, and Shengyong Chen. “SpectralSeaNet: Spectrogram and Convolutional Network-based Sea State Estimation”. *IECON Proceedings (Industrial Electronics Conference)*. Vol. 2020-October. 2020, pp. 5069–5074. DOI: 10.1109/IECON43393.2020.9254890.

[59] Toshiki Kawai, Yasumi Kawamura, Tetsuo Okada, Taiga Mitsuyuki, and Xi Chen. “Sea state estimation using monitoring data by convolutional neural network (CNN)”. *Journal of Marine Science and Technology (Japan)* 26.3 (2021), pp. 947–962. DOI: 10.1007/s00773-020-00785-8.

[60] Peihua Han, Guoyuan Li, Stian Skjong, and Houxiang Zhang. “Directional wave spectrum estimation with ship motion responses using adversarial networks”. *Marine Structures* 83 (2022). DOI: 10.1016/j.marstruc.2022.103159.

[61] Malte Mittendorf, Ulrik Dam Nielsen, Harry B. Bingham, and Gaute Storhaug. “Sea state identification using machine learning—A comparative study based on in-service data from a container vessel”. *Marine Structures* 85 (2022). DOI: 10.1016/j.marstruc.2022.103274.

[62] Nathan K. Long, Daniel Sgarioto, Matthew Garratt, and Karl Sammut. "Response component analysis for sea state estimation using artificial neural networks and vessel response spectral data". *Applied Ocean Research* 127 (2022). DOI: 10.1016/j.apor.2022.103320.

[63] Gustavo A. Bisinotto et al. "Sea state estimation based on the motion data of a moored FPSO using neural networks: An evaluation with multiple draft conditions". *Ocean Engineering* 276 (2023). DOI: 10.1016/j.oceaneng.2023.114235.

[64] Don H. Johnson and Dan E. Dudgeon. *Array signal processing: concepts and techniques*. Prentice Hall, 1993.

[65] D. Esteva. "Wave direction computations with three gage arrays". *Coastal Engineering Proceedings* 1.15 (Jan. 1976), pp. 349–367. DOI: 10.9753/icce.v15.19.

[66] D. C. Esteva. *Evaluation of the computation of wave direction with three-gauge arrays*. Tech. rep. CERC, Technical Paper No. 77-7. U.S. Army Corps of Engineers, 1977.

[67] A. A. Fernandes, A. D. Gouveia, and R. Nagarajan. "Determination of wave direction from linear and polygonal arrays". *Ocean Engineering* 15.4 (Jan. 1988), pp. 345–357. DOI: 10.1016/0029-8018(88)90050-9.

[68] A. A. Fernandes, Y. V.B. Sarma, and H. B. Menon. "Directional spectrum of ocean waves from array measurements using phase/time/path difference methods". *Ocean Engineering* 27.4 (Apr. 2000), pp. 345–363. DOI: 10.1016/S0029-8018(99)00024-4.

[69] S. Draycott et al. "Using a Phase-Time-Path-Difference Approach to Measure Directional Wave Spectra in FloWave". *EWTEC Conference Proceedings*. 2015, pp. 1–7.

[70] S. Draycott, T. Davey, D. M. Ingram, A. Day, and L. Johanning. "The SPAIR method: Isolating incident and reflected directional wave spectra in multidirectional wave basins". *Coastal Engineering* 114 (Aug. 2016), pp. 265–283. DOI: 10.1016/j.coastaleng.2016.04.012.

[71] S. Draycott et al. "Re-creation of site-specific multi-directional waves with non-collinear current". *Ocean Engineering* 152 (2018), pp. 391–403. DOI: 10.1016/j.oceaneng.2017.10.047.

[72] Li Luo, Shuxue Liu, Jinxuan Li, and Wei Jia. "Deterministic reconstruction and reproduction of multi-directional irregular waves based on linear summation model". *Ocean Engineering* 198 (Feb. 2020). DOI: 10.1016/j.oceaneng.2020.106952.

[73] A. A. Fernandes, H. B. Menon, Y. V.B. Sarma, Pankti D. Jog, and A. M. Almeida. "Wavelength of ocean waves and surf beat at Duck from array measurements". *Proceedings of the International Symposium on Ocean Wave Measurement and Analysis*. Vol. 2. 2001, pp. 1809–1818. DOI: 10.1061/40604(273)182.

[74] Thomas C. Fu, Anne M. Fullerton, Erin E. Hackett, and Craig Merrill. "Shipboard measurement of ocean waves". *Proceedings of the International Conference on Offshore Mechanics and Arctic Engineering - OMAE*. Vol. 6. 2011, pp. 699–706. DOI: 10.1115/OMAE2011-49894.

[75] Guttorm Udjus. *Force Field Identification and Positioning Control of an Autonomous Vessel using Inertial Measurement Units (MSc thesis)*. Trondheim: Norwegian University of Science and Technology, 2017.

[76] Hans-Martin Heyn, Guttorm Udjus, and Roger Skjetne. "Distributed motion sensing on ships". *OCEANS 2017 - Anchorage*. 2017, pp. 1–9.

[77] Thor I. Fossen. *Handbook of marine craft hydrodynamics and motion control*. 2nd Edition. Chichester, West Sussex, U.K.: Wiley, 2021.

[78] Jørgen Juncher Jensen, Alaa E. Mansour, and Anders Smærup Olsen. "Estimation of ship motions using closed-form expressions". *Ocean Engineering* 31.1 (2004), pp. 61–85. DOI: 10.1016/S0029-8018(03)00108-2.

[79] Joel Reis, Pedro Batista, Paulo Oliveira, and Carlos Silvestre. "Discrete-time Kalman filter for heave motion estimation". *Ocean Engineering* 277 (2023). DOI: 10.1016/j.oceaneng.2023.114240.

[80] Nan Chen, Shangchun Fan, and Dezhi Zheng. "A phase difference measurement method based on strong tracking filter for Coriolis mass flowmeter". *Review of Scientific Instruments* 90.7 (2019). DOI: 10.1063/1.5086714.

[81] Pan Du, Warren A. Kibbe, and Simon M. Lin. "Improved peak detection in mass spectrum by incorporating continuous wavelet transform-based pattern matching". *Bioinformatics* 22.17 (2006), pp. 2059–2065. DOI: 10.1093/bioinformatics/btl355.